Silicon Nanostructures for Photovoltaics

Dissertation

zur Erlangung des Doktorgrades

der Technischen Fakultät

der Albert-Ludwigs-Universität Freiburg im Breisgau

vorgelegt von

Philipp Löper

Fraunhofer Institut für

Solare Energiesysteme (ISE)

Freiburg

März 2013

Dekan:

Prof. Dr. Yiannos Manoli

Referenten:

Prof. Dr. Margit Zacharias

Prof. Dr. Eicke Weber

Tag der mündlichen Prüfung:

16. Juli 2013

Erklärung

Ich erkläre, dass ich die vorliegende Arbeit ohne unzulässige Hilfe Dritter und ohne Benutzung anderer als der angegebenen Hilfsmittel angefertigt habe. Die aus anderen Quellen direkt oder indirekt übernommenen Daten und Konzepte sind unter Angabe der Quelle gekennzeichnet. Insbesondere habe ich hierfür nicht die entgeltliche Hilfe von Vermittlungs- oder Beratungsdiensten (Promotionsberaterinnen oder Promotionsberater oder anderer Personen) in Anspruch genommen. Niemand hat von mir unmittelbar oder mittelbar geldwerte Leistungen für Arbeiten erhalten, die im Zusammenhang mit dem Inhalt der vorgelegten Dissertation stehen. Die Arbeit wurde bisher weder im In- noch im Ausland in gleicher oder ähnlicher Form einer anderen Prüfungsbehörde vorgelegt.

Ich erkläre hiermit, dass ich mich noch nie an einer in- oder ausländischen wissenschaftlichen Hochschule um die Promotion beworben habe oder gleichzeitig bewerbe.

Ort und Datum: Unterschrift:

Abstract

The basic motivation of this thesis is to explore a path beyond the 29% fundamental efficiency limit [1] of crystalline silicon (c-Si) through a reduction of the spectral losses of single-junction solar cells. The overall concept envisages a c-Si tandem solar cell by implementing band gap engineered Si NCs as a high band gap absorber of the top solar cell.

The first necessary step towards a Si NC solar cell is the demonstration of a high open-circuit voltage (higher than with bulk Si). The feasibility of a high open-circuit voltage is demonstrated in this thesis by means of a theoretical model in combination with experimental data for the optical properties.

Experimental investigations were performed with Si nanocrystals (Si NCs) embedded in silicon dioxide (SiO_2) or silicon carbide (SiC), both prepared according to a superlattice approach and high-temperatures thermal annealing (up to 1150°C).

Calibrated absorption- and photoluminescence spectra of Si NCs in SiO_2 are analyzed according to the generalized Planck law of radiation to determine the open-circuit voltage by optical means, i.e. without the need of selective contacts to the Si NC film. It is shown that the generalized Planck law is not valid to describe the luminescence of Si NCs embedded in SiO_2, but the spectrum is rather a superposition of single luminescence centers which is broadened by the size distribution.

Si NCs in a SiC matrix were investigated motivated by the poor electrical transport through the SiO_2 matrix. An electrical characterization is presented and related to the structural properties.

In previous Si NC solar cell test devices, either the performance was adversely affected by the fabrication processes, or the structure did not allow for a separation of the Si NC and substrate contributions to the measurement.

To remedy this shortcoming, a novel, membrane-based device structure has been developed in the framework of this thesis. This device structure permits to decouple the high-temperature annealing needed to form Si NCs from the preparation of the selective contacts and thus enables for the first time an unambiguous characterization of Si NC films in a minority carrier device.

Membrane-based p-i-n solar cells were prepared with Si NCs embedded in SiC as the absorber layer and doped amorphous silicon carbide (a-Si_xC_{1-x}:H) and indium tin oxide (ITO)

as selective contacts. Based on a detailed general device analysis, illumination-dependent IV measurements were employed to determine the fundamental transport and recombination properties, the effective mobility lifetime product, on device level.

Table of contents

1 Introduction

1.1 Motivation

Today's world energy demand is met predominantly by the fossil primary energy sources oil, gas and coal. The combustion of the fossil primary energy sources has provoked a global climate change through a mean temperature increase of 0.87°C [2] since the pre-industrial era. Under the impression of the nuclear catastrophe in Fukushima, general agreement was reached in several societies to end nuclear power and to build on a sustainable future. After decades of political inertia to accept and take measures against climate change, a goal of 2°C maximum mean temperature increase was agreed on by 194 countries of the United Nations Framework Convention on Climate Change in 2010 [3]. The growth of renewable energies has strengthened hopes for a carbon-free future energy supply. However, the unlocking of light tight oil and shale gas is likely to profoundly change global energy flows, lower the oil price, and thus also to dampen the financial incentives for renewable energies. Only two years after the definition of the 2°C goal, the international energy agency (IEA) has arrived at the distressing conclusion that a 3.6°C mean temperature increase will be inevitable if climate policies are not changed radically [4]. In addition to the current climate bill is the fact that another 14 gigantic fossil fuel projects that are still being planned so that Greenpeace [5] foresees a global warming of even 6°C.

"The world is clearly at a Point of No Return: either replace coal, oil and gas with renewable energy, or face a future turned upside down by climate change … To avoid locking us into catastrophic warming, the building of new fossil fuel infrastructure needs to stop within five years – placing the planned dirty energy projects in direct conflict with a livable climate." [5]

At a time, when the global temperature has increased by only 0.87°C [2], but the climate change manifests itself in hurricanes, droughts, and heat waves, urgent action is required to prevent a climatic catastrophe.

It is not too late, yet. A decisive policy of a consistent transition to renewable energies and a strong support for the development of future technologies can still avoid a climatic catastrophe [4, 5]. Special significance among the range of renewable technologies is attached to photovoltaics because it combines several strategic advantages. The modularity of photovoltaic (PV) systems offers scalability of applications as well as

production facilities. The same components are used for off grid applications in developing countries, grid-connected roof top installations or large area power plants. Up-scaled production therefore serves a broad range of market segments, and impressive price reductions have been reached. According to the "International technology roadmap for photovoltaics" published by SEMI [6], the average selling price decreases by 20% for every doubling of the cumulative PV module shipments. However, the price reductions that can be reached by up-scaling the production are limited in the long run by the raw material costs. The key to long term cost competitiveness is therefore the development of novel solar cell concepts that go beyond the fundamental efficiency limits of present silicon (Si) solar cells. Fig. 1.1 depicts the air mass 1.5 global (AM1.5G) solar spectrum and illustrates the energy that can be converted theoretically by a Si solar cell. The theoretical efficiency limit arises from two loss mechanisms. Photons with an energy of less than the band gap energy are not absorbed by the solar cell (red arrow in Fig. 1.1, right), giving rise to transmission losses. The band gap is the region between the conduction and the valence band, denoted in Fig. 1.1 as E_C and E_V respectively, and is a fundamental material property. High-energy photons, on the other hand, create a high-energy electron hole pair in the solar cell (blue arrows in Fig. 1.1, right). However, the excess energy is dissipated to the crystal lattice (thermalization), and only a fraction of the incident solar radiation energy is converted to electricity. Ideal energy conversion is only possible for photons whose energy just matches the band gap energy, indicated by the green arrows in Fig. 1.1.
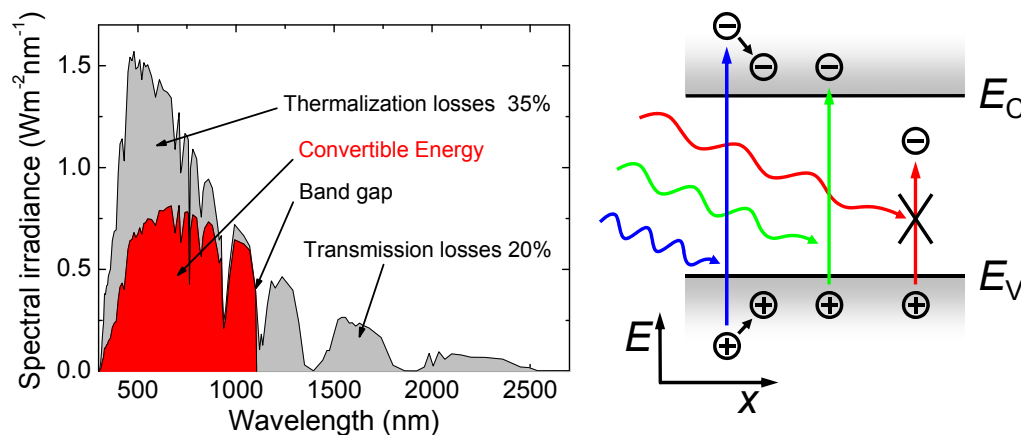
Fig. 1.1: The air mass 1.5 global (AM1.5G) solar spectrum (left) and the maximum convertible energy of a silicon solar cell after [7]. The fundamental efficiency limit arises from the spectral losses, which are (right) the thermalization of high-energy charge carriers (blue arrow) and transmission of photons with less than band gap energy (red arrow).

Matching the band gap to the incident photon flux is the basic idea of tandem solar cells.

1.2 Silicon nanocrystals for a crystalline silicon tandem solar cell

An optimized conversion of radiation into electrical energy through mitigation of the losses depicted in Fig. 1.1 is possible by a spectral customization of the solar cell to the spectrum. This can be reached by stacking multiple solar cells, each optimized to a certain spectral region. Fig. 1.2 depicts the principle of such a multi junction or tandem solar cell. Each sub cell absorbs only a certain spectral region, thereby minimizing the transmission and thermalization losses. Tandem solar cells are already commercially available and efficiencies of 37.7% have been reached with compound semiconductors from the third and fifth main group of the periodic system (III-V) [8]. However, III-V solar cells are only of limited use for large area power generation as several involved elements are toxic (arsenic), rare (indium) and expensive. Silicon (Si) is the second most abundant element in the earth crust [9], is not toxic, and solar cell manufacturers can build on the highly developed Si technology from microelectronics. Advanced solar cell concepts are thus desirable that are based on Si materials and compatible with Si technology. Tandem solar cells have been realized with amorphous and microcrystalline Si with a record efficiency of 13.4% [8]. However, amorphous and microcrystalline Si suffers from a metastable degradation effect [10, 11] which reduces the efficiency by up to 30%. The effect has not been fully explained yet [12], but is frequently related to the structural disorder of amorphous Silicon.
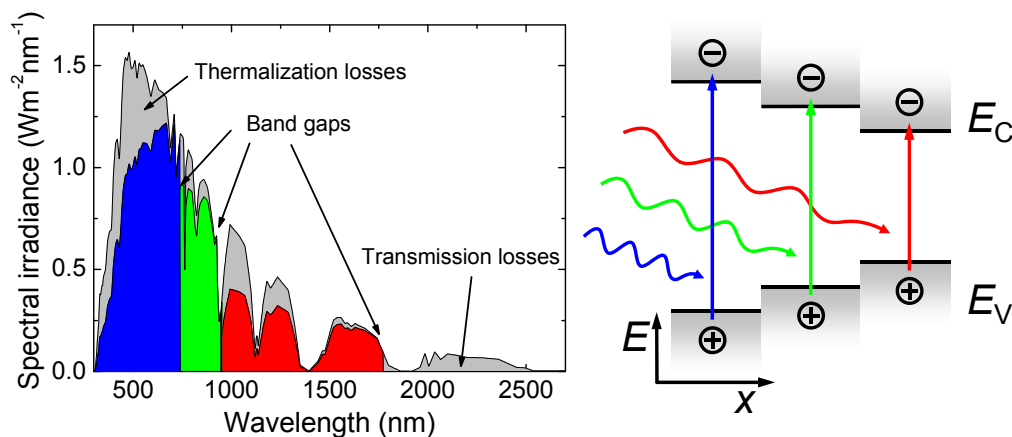
Fig. 1.2: *The combination of multiple solar cells with different band gaps enables a better spectrum utilization (left) compared to a solar cell with one band gap. The band gaps are optimized to a certain spectral region for minimized thermalization and transmission losses (right).*

Crystalline silicon does not show such metastabilities and does not degrade. The objective of a high band gap in a crystalline Si material can be met by utilizing quantum confinement effects in Si nanostructures. Since the first observation of visible photoluminescence from anodically etched Si [13], nanostructured Si has received a lot of attention for providing a high band gap that is compatible with Si technology. In this context, a "high band gap" refers to a band gap value higher than in the extended Si crystal (bulk). The band gap has since been shown to be well controllable by carefully tuning the quantum confinement in the Si nanocrystals (NCs). Possible applications of Si NCs include solid state lighting [14], laser applications [15], or charge storage devices [16]. Moreover, Si quantum dots (QDs) with a tunable band gap enable the realization of a crystalline Si tandem solar cell. The principle of a crystalline Si tandem solar cell is sketched in Fig. 1.3. The high-energy photons (blue arrow) are absorbed in the Si NC top solar cell, while photons with less energy are transmitted by the latter and absorbed in the bottom solar cell. The bottom solar cell is made of bulk Si, e.g. a Si wafer or thin film crystalline Si. The band gap of the Si NC top solar cell can be tuned by controlling the Si NC size to adapt the top solar cell to the incident spectrum.
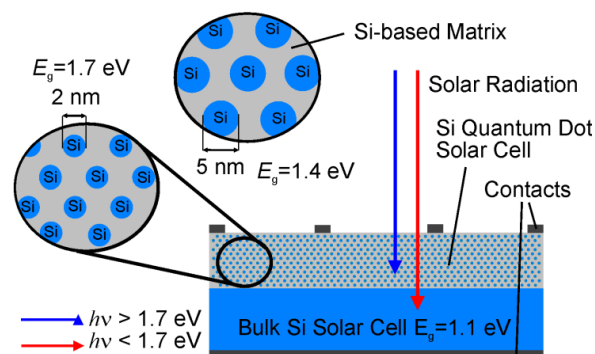
Fig. 1.3: *Diagram of a crystalline silicon tandem solar cell after [17]. The top solar cell consists of Si nanocrystal QDs that absorb only the high-energy photons. The band gap of the Si nanocyrstal QDs can be tuned by controlling the nanocrystal size.*
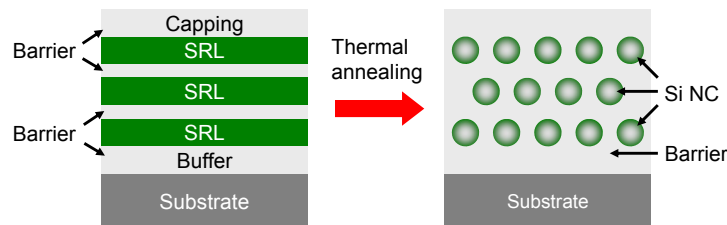
Fig. 1.4: *Diagram for the fabrication of a Si nanocrystal (NC) superlattice by the multilayer approach after Zacharias [18]. Silicon-rich layers (SRL) are sandwiched between stoichiometric layers (Barrier). The barrier layers restrict the Si NC growth and thereby enable a narrow size distribution. Si NC formation is induced by thermal annealing at high temperatures, usually >1000°C.*

Large area fabrication of size controlled Si NCs is achieved by depositing an amorphous precursor in a multilayer configuration which is then thermally annealed to form the Si NCs [18]. The multilayer is prepared as a stack of alternating Si-rich and stoichiometric layers of a Si compound as shown in Fig. 1.4. Upon annealing, the Si excess in the Si-rich layers precipitates and crystallizes at temperatures around 1100°C. The stoichiometric layers act as barriers towards crystallite growth and thus restrict the Si NC size distribution.

1.3 Main objectives of this work

This work aims at the development of a Si NC solar cell. While the understanding of Si NC growth in a SiO_2 matrix is already at an advanced stage, their formation mechanisms in alternative matrices such as Si_3N_4 or SiC is still a matter of debate. A SiC matrix is especially promising as it offers electrical conduction through the matrix itself. For this reason, the present thesis covers two material systems: Si NCs in SiO_2 with a controlled band gap and luminescent properties, and Si NCs in SiC, providing electrical conduction but with less understood structural properties. Considerable progress has been achieved towards the implementation of Si NCs to a solar cell [19-22]. However, a characterization of Si NC materials in a high-voltage device, i.e. as a solar cell absorber with appropriately designed selective contacts, has not yet been reported. Most studies were either restricted to structural and optical investigations, or the devices were limited by inherent shortcomings. Therefore, a systematic characterization of the Si NC top cell is identified as the first step towards the realization of a crystalline Si tandem solar cell.

In the light of these challenges, the principal objective of this thesis is to explore the general feasibility of a Si NC solar cell. The main objectives are

- an assessment of the voltage potential of Si NC materials,
- an enhanced understanding of Si NC formation in SiC,
- a characterization of the electrical properties of Si NCs in SiC,
- the development and characterization of test devices for the experimental demonstration of the voltage potential of Si NCs, and
- a Si NC material characterization on photovoltaic device level

1.4 Outline

In **chapter 1**, the topic of this thesis is motivated and the concept of a crystalline Si tandem solar cell is introduced. The main objectives of the research project are defined and the structure of the thesis is outlined.

Chapter 2 introduces the theoretical concepts underlying the discussions in the following chapters. The theory of the envelope function approximation for the description of Si NC superlattices is introduced. Subsequently, illuminated semiconductors are considered to derive a theoretical description of luminescence and the current-voltage curve of a solar cell. Finally, the basic concepts of amorphous semiconductors are introduced with an emphasis on the differences to their crystalline counterparts.

Chapter 3 examines the open-circuit voltage potential of various Si NC materials. A band structure calculation for an idealized system is combined with experimental data to derive estimates for the maximum open-circuit voltages of ideal Si NC solar cells.

Chapter 4 discusses the properties of Si NCs in a SiO_2 matrix. The chapter focusses on the optical spectra of Si NCs embedded in SiO_2. Optical absorption and photoluminescence spectroscopy are employed to investigate the size-dependence of the band gap. The decisive parameter for a Si NC solar cell, the open-circuit voltage, is assessed by an analysis of the optical spectra.

Chapter 5 treats the preparation of SiC multilayers and an analysis of their structural transformations upon thermal annealing. An experiment is presented for the optimization of the structural material properties based on the results of previous studies. The structural and electrical properties of the solid phase crystallized films are characterized and related to each other.

Chapter 6 summarizes the current status of material development with regard to the SiO_2 and SiC host matrices. The material properties are related to the overall goal of the crystalline Si tandem solar cell with special emphasis on the flaws of the two materials.

In **Chapter 7,** Si NC devices that have been realized so far are reviewed and shown to be inadequate for a Si NC material characterization. A newly developed membrane-based device is introduced which meets the requirements for a Si NC high-voltage solar cell and enables a systematic Si NC material characterization.

The implementation of SiO_2- and SiC-based Si NC films into the membrane-based device is presented in **chapter 8**. A general characterization of the device functionality is presented along with a procedure to identify device failure. Several different SiC/Si NC layers are employed as the solar cell absorber and a detailed characterization of their photovoltaic properties is carried out.

Chapter 9 revisits the concept of the crystalline tandem solar cell and puts to debate various realization possibilities. Requirements to the Si NC material are formulated based on the possibilities and challenges of the tandem cell concepts.

Chapter 10 summarizes the thesis and draws conclusions.

2 Theory

This chapter introduces the basic concepts that are needed to understand photovoltaic operation of a Si NC material. The first part covers the description of an ideal Si NC superlattice with the envelope function approximation. The second part describes the generation and recombination of electrons and holes in a semiconductor and explains the generalized Planck law of radiation. Consequently, the current-voltage curve is then derived from the charge carrier generation and recombination rates. Special emphasis is given to p-i-n thin film devices and their typical voltage-dependent photocurrent collection. The presentation of semiconductor and solar cell theory in this chapter follows in large parts the text book of Würfel [23].

2.1 Quantum confinement in a cubic silicon nanocrystal superlattice

The energy band structure of an idealized Si NC superlattice was calculated within the framework of this thesis with the envelope function approximation. This method utilizes the band structures of the single materials represented by their valence and conduction band energies and the effective masses. The advantage of the envelope function approximation is that for special choices of the confining potential, reasonable simplifications permit analytical expressions of the solutions. In the following, the Si nanocrystal system is modelled as an idealized superlattice of periodically arranged cubic QDs embedded in a matrix of dielectric material. A sketch of the superlattice is shown in Fig. 2.1. Each cube represents a nanocrystal of size L, and the space between the cubes is filled with matrix material. The periodicity P is the same along the orthogonal spatial axis x, y and z so that the distance between the nearest cubes is $S = P - L$. Because of its higher band gap in comparison to silicon, the dielectric matrix forms a potential barrier for charge carriers. The band structure is thus a periodic array of rectangular potential barriers in each spatial dimension as introduced by Kronig and Penney [24].

The charge carriers within the potential are described by the Schrödinger equation [25]

$$\left(-\frac{\hbar}{2} \nabla \frac{1}{m^*(\boldsymbol{r})} \nabla + V(\boldsymbol{r}) \right) \psi(\boldsymbol{r}) = E\psi(\boldsymbol{r}), \qquad (2.1)$$

with the reduced Planck's constant $\hbar$, effective mass m^*, wave function ψ, position vector $\boldsymbol{r}$ and
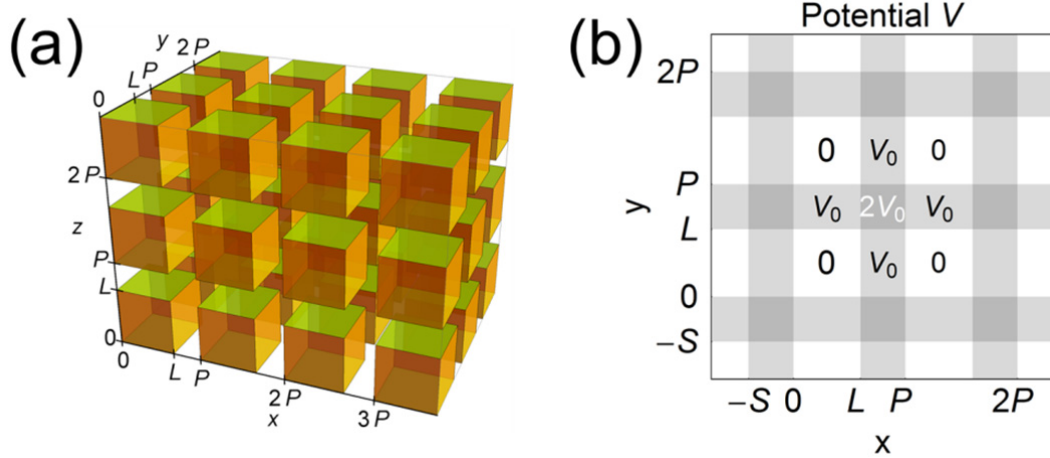
Fig. 2.1: (a) Ideal superlattice of cubic quantum dots with size L and periodicity P along each spatial direction and (b) Potential arising from Eqs. (2.2) and (2.3). The figures were adapted from [25].

energy E. The potential $V(\boldsymbol{r})$ is assumed to be the superposition [25]

$$V(\boldsymbol{r}) = V_x(x) + V_y(y) + V_z(z) \tag{2.2}$$

of the three periodic potentials $V_i(i)$ for the coordinates $i = x, y, z$ with periodicity P. Each one-dimensional potential $V_i(i)$ is a periodic array of rectangular potentials [25]:

$$V_i(i) = \begin{cases} V_0 \text{ for } |x - iP| > {L}/{2} \\ \\ 0 \text{ else} \end{cases} \tag{2.3}$$

With this choice of potential the Schrödinger equation decouples into three identical one dimensional (1D) superlattice equations. The enveloped function can thus be expressed as the sum of three 1D eigenfunctions [25]

$$\varphi_{n_x n_y n_z}(\boldsymbol{r}) = \psi_{n_x}(x) + \psi_{n_y}(y) + \psi_{n_z}(z). \tag{2.4}$$

The eigenvalue of the total Schrödinger equation is the sum [25]

$$E_{n_x n_y n_z} = E_{n_x} + E_{n_y} + E_{n_z}, \tag{2.5}$$

with the eigenvalues E_{n_i} of the 1D Schrödinger equation. It has to be noted that this approach overestimates the confining potential along the face diagonal and the space diagonal, where it amounts to $2V_0$ and $3V_0$, respectively (Fig. 2.1, right). However, this corner potential introduces only a minor correction, which is particularly small for states within the well, i.e. below the potential barrier [25].

The solution of Eq. (2.1) with the potential of Eqs. (2.2) and (2.3) was presented by Bastard *et al.* [26]:

$$cos(kP) = cos(\kappa_{QP}L)\,cosh(\kappa_M S)$$

$$+ \frac{1}{2}\left(\frac{m_{QP}^*\kappa_M}{m_M^*\kappa_{QP}} - \frac{m_M^*\kappa_{QP}}{m_{QP}^*\kappa_M}\right) sin(\kappa_{QP}L)\,sinh(\kappa_M S) \text{ for } 0 < E < V_0 \qquad (2.6)$$

The reciprocal lattice vector is denoted as k, the effective masses in the quantum dot and the matrix as m_{QP}^* and m_M^*, respectively, and the abbreviations

$$\kappa_{QP} = \frac{1}{\hbar}\sqrt{2m_{QP}^*E} \text{ and } \kappa_M = \frac{1}{\hbar}\sqrt{2m_M^*(V_0 - E)} \qquad (2.7)$$

are used. These solutions give a relation between the wave vector $\boldsymbol{k}$ and the energy E, resulting in the electronic band structure $E(\boldsymbol{k})$. The right hand side of Eq. (2.6) is plotted in Fig. 2.2 for an exemplary parameter set. Valid solutions to Eq. (2.6) are all values between -1 and 1, indicated by the grey bar in Fig. 2.2.
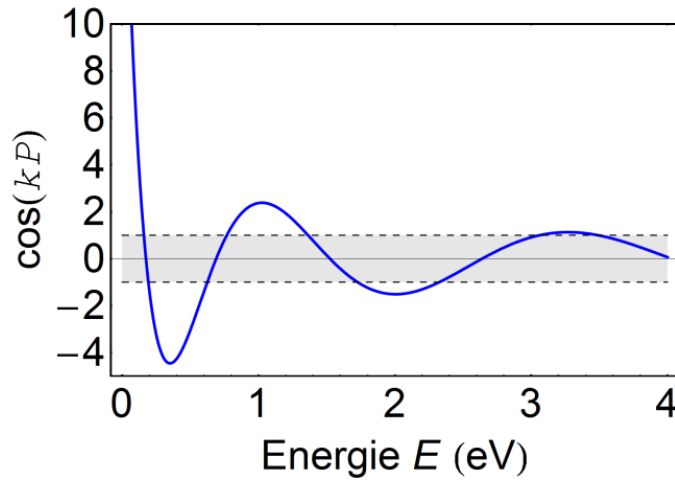
Fig. 2.2: Plot of the right hand side of Eq. (2.6), the solution to the Schrödinger equation (Eq. (2.1)). The parameters $L = 2$ nm, $S = 0.5$ nm, $V_0 = 1.9$ eV, $m_{QP}^* = 0.33\,m_0$ and $m_M^* = 0.4\,m_0$ were used. The figure was adapted from [27].

2.2 Charge carrier generation and recombination

Solar cells convert radiation energy to electrical energy. Common solar cell realizations make use of semiconductors as the photon absorber and the conversion process is mediated by the electrons and holes in the semiconductor. The electrons and holes in the semiconductor can be considered the "working gas" in analogy to a Carnot machine. In an undoped, so-called intrinsic semiconductor, the only free charge carriers are electrons from the valence band that are thermally excited to the conduction band. This can be changed by introducing dopant impurities to the semiconductor. A fundamental property of a semiconductor is the equilibrium relation between the intrinsic charge carrier density n_i, and the concentrations of electrons, n_e^0, and holes, n_h^0 [23],

$$n_{\mathrm{i}}^2 = n_{\mathrm{e}}^0 n_{\mathrm{h}}^0 = N_{\mathrm{C}} N_{\mathrm{V}} \, exp\left(-\frac{E_{\mathrm{G}}}{k_{\mathrm{B}} T}\right). \tag{2.8}$$

The notations N_{C} and N_{V} are used for the effective density of states in the conduction and the valence band, respectively, the temperature T and k_{B} denotes the Boltzmann constant. The band gap is written E_{G}. This relation is valid irrespective of the doping. Equilibrium refers to thermodynamic equilibrium with the environment radiation, i.e. without illumination. For the second equal sign in Eq. (2.8), the Boltzmann approximation was used.

The absorption of photons by a semiconductor creates a population of electrons in the conduction band and a hole population in the valence band (Fig. 2.2) . Immediately after absorption, the two distributions have the temperature of the sun. Due to collisions with the crystal lattice, the electrons and holes lose their kinetic energy to the lattice until they are in thermal equilibrium with the latter. This process is called thermalization and occurs within about 10^{-12} s after absorption. After the cooling, the electron and hole populations are in chemical equilibrium with respect to transitions between states in their respective band, each carrying a mean kinetic energy of $3/2 \times k_{\mathrm{B}} T$. The particle density of each charge carrier type is described by its chemical potential, $\varepsilon_{\mathrm{F,e}}$ for the electrons in the conduction band and $\varepsilon_{\mathrm{F,h}}$ for the holes in the valence band. As the thermalization does not change the number of electrons and holes, the particle density is higher than in the dark. In analogy to the dark, the particle density is described with the Fermi distribution and the chemical potential is also called the "quasi-Fermi energy" of the respective charge carrier type. The term "quasi" is used to mark the difference to the dark, where the Fermi energy ε_{F} applies.
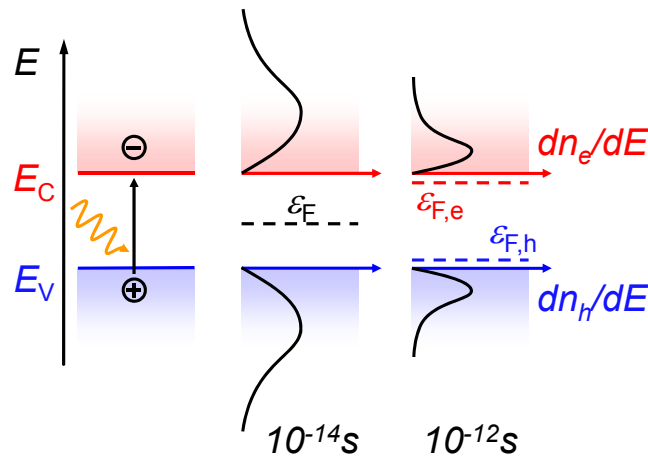
Fig. 2.3: *The absorption of a photons create an electron distribution in the conduction band and a hole distribution in the valence band. Thermal equilibrium with the lattice is reached after about 10^{-12} s. The figure was drawn after [23].*

The number of electrons per volume n_e in an illuminated semiconductor is the integral over the density of states $N(E)$ times the electron distribution described by its quasi-Fermi energy $\varepsilon_{F,e}$ and its temperature T [23],

$$n_e = \int_{E_C}^{\infty} N(E) \frac{1}{exp\left(\frac{E - \varepsilon_{F,e}}{k_B T}\right) + 1}. \qquad (2.9)$$

The creation of electron hole pairs happens with a generation rate G. The mean generation rate in a semiconductor with absorptance A and thickness d, irradiated with a photon current density dj_γ, is

$$G = \frac{1}{d} \int_0^{\infty} A(E) dj_\gamma(E)\, dE. \qquad (2.10)$$

The generation rate and the excess carrier density $\Delta n = n_e - n_e^0$ define the effective charge carrier lifetime τ_{eff} [28],

$$G = \frac{\Delta n}{\tau_{eff}}. \qquad (2.11)$$

Excess charge carriers can be injected by illumination with light, but also electrically through contacts to the semiconductor or by an electron beam. For the rest of this section, an infinitesimally thin semiconductor is considered. As long as the quasi-Fermi level is further than $3k_B T$ apart from the band edge, i.e. $\varepsilon_{F,e} < E_C - 3k_B T$ holds, the Fermi-Dirac of Eq.(2.9) distribution can be approximated with the Boltzmann distribution. The integral can be evaluated provided the density of states is known to derive the simplified expression [23]

$$n_e = N_C\, exp\left(-\frac{E_C - \varepsilon_{F,e}}{k_B T}\right). \qquad (2.12)$$

An analogous expression is valid for the hole concentration n_h and the hole quasi-Fermi level $\varepsilon_{F,h}$. [23],

$$n_h = N_V\, exp\left(-\frac{\varepsilon_{F,h} - E_V}{k_B T}\right). \qquad (2.13)$$

The quantities N_C and N_V arise from the integration of Eq. (2.9) and denote the effective densities of states in the two respective bands. The product of the electron and hole concentration in the illuminated semiconductor is thus given by

$$n_e n_h = N_C N_V\, exp\left(\frac{-E_G}{k_B T}\right) exp\left(\frac{\varepsilon_{F,e} - \varepsilon_{F,h}}{k_B T}\right). \qquad (2.14)$$

A comparison with the quantities of the unilluminated semiconductor (Eq. (2.8)) illustrates an important link between the quasi-Fermi level splitting and the intrinsic charge carrier density [23],

$$n_e n_h = n_e^0 n_h^0 \, exp\left(\frac{\varepsilon_{F,e} - \varepsilon_{F,h}}{k_B T}\right) = n_i^2 \, exp\left(\frac{\varepsilon_{F,e} - \varepsilon_{F,h}}{k_B T}\right). \tag{2.15}$$

The inverse process to generation is recombination. The rate or radiative recombination U is proportional to the concentrations of electrons and holes [23],

$$U = \beta n_e n_h. \tag{2.16}$$

The proportionality constant β is the material-specific coefficient of radiative recombination. In equilibrium with the environment, the rates of radiative recombination U^0 and generation G^0 are balanced [23],

$$U^0 = \beta n_e^0 n_h^0 = G^0. \tag{2.17}$$

The equilibrium rates are written U^0 and G^0 to distinguish from the rates in a semiconductor with excess charge carriers, $n_e \neq n_e^0$ and $n_h \neq n_h^0$. The equilibrium generation rate can be calculated from the absorptance and the incident equilibrium photon current density $dj_\gamma^0(E)$. Without illumination, the incident photo current density is the thermal radiation of temperature T [23],

$$G^0 = \int_0^\infty A(E) dj_\gamma^0(E) \, dE = \frac{\Omega}{4\pi^3 \hbar^3 c^2} \int_0^\infty A(E) \frac{E^2}{exp\left(\frac{E}{k_B T}\right) - 1} dE. \tag{2.18}$$

Now, we reconsider the recombination rate in the illuminated semiconductor (Eq. (2.16)), but describe the increased carrier concentrations with the quasi-Fermi level splitting Eq. (2.15). Using the identity between recombination and generation in equilibrium (Eq. (2.17)), finally leads to [23]

$$U = \beta n_e n_h = \beta n_e^0 n_h^0 \, exp\left(\frac{\varepsilon_{F,e} - \varepsilon_{F,h}}{k_B T}\right) = G^0 \, exp\left(\frac{\varepsilon_{F,e} - \varepsilon_{F,h}}{k_B T}\right). \tag{2.19}$$

This equation illustrates the enhanced radiative recombination due to an excess carrier density, or quasi-Fermi level splitting.

According to the theory of detailed balance, the equilibrium $U^0 = G^0$ described by Eq. (2.17) is fulfilled for each interval dE. This means that in equilibrium an identity between the emitted and the absorbed photon current densities holds for each interval dE [23],

$$dj_{\gamma,em}^0(E) = dj_{\gamma,abs}^0(E) = A(E) dj_\gamma^0(E). \tag{2.20}$$

The emitted and the absorbed photon current densities are written $dj^0_{\gamma,\text{em}}(E)$ and $dj^0_{\gamma,\text{abs}}(E)$, respectively. The detailed balance argument is central to the thermodynamic consideration of absorption and emission. It was derived for thermal radiation by Kirchhoff [29] and generalized by Weinstein [30] to the cases in which the grey body is not in thermal equilibrium with the black body radiation. Because the detailed balance is valid in every interval dE, the same factor $n_e n_h / n_i^2$ that enlarges the radiative recombination rate (Eq. (2.19)) applies also to describe the emitted photon current density [23],

$$dj_{\gamma,\text{em}}(E) = A(E)dj^0_\gamma(E)\frac{n_e n_h}{n_i^2}. \qquad (2.21)$$

As $dj^0_\gamma(E)$ is the already known equilibrium radiation of temperature T, we obtain with the help of Eq. (2.18)

$$dj_{\gamma,\text{em}}(E) = A(E)\,exp\left(\frac{\varepsilon_{\text{F,e}} - \varepsilon_{\text{F,h}}}{k_\text{B}T}\right)\frac{\Omega}{4\pi^3\hbar^3 c^2}\frac{E^2}{exp\left(\frac{E}{k_\text{B}T}\right) - 1}dE. \qquad (2.22)$$

This equation has been derived using the Boltzmann distribution and is only approximately valid for $\varepsilon_{\text{F,e}} < E_C - 3k_\text{B}T$. The exact result is [23]

$$dj_{\gamma,\text{em}}(E) = A(E)\frac{\Omega}{4\pi^3\hbar^3 c^2}\frac{E^2}{exp\left(\frac{E - \left(\varepsilon_{\text{F,e}} - \varepsilon_{\text{F,h}}\right)}{k_\text{B}T}\right) - 1}dE. \qquad (2.23)$$

This equation includes the Planck law of radiation for the equilibrium case, i.e. $\varepsilon_{\text{F,e}} - \varepsilon_{\text{F,h}} = 0$. As Eq. (2.23) describes luminescence as well as thermal radiation, in is called the generalized Planck law of radiation. It was derived by Lasher [31] and later in more generality by Würfel [32] who also proved its validity for indirect transitions [33].

2.3   Charge carrier separation

The quasi-Fermi levels in an illuminated semiconductor are shown schematically in Fig. 2.4 (a). The electrons and holes recombine at the surface, and the quasi-Fermi levels merge there.
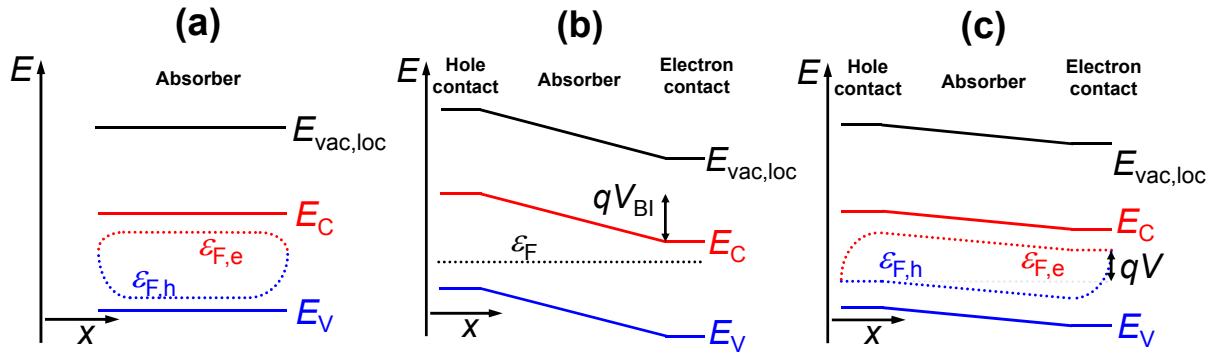
Fig. 2.4: Quasi-Fermi level distribution and band alignment in an illuminated semiconductor with surface recombination (a), a p-i-n structure in the dark (b) and an illuminated p-i-n structure (c).

Fig. 2.4 (b) depicts a band structure in which the absorber has been contacted with a p-doped region (hole contact) at the left and a n-doped region (electron contact) at the right. The energy bands align according to the requirement of a constant Fermi level and balanced charges at each interface, giving rise to the built-in potential V_{BI}. Under illumination, the Fermi level in the solar cell structure in Fig. 2.4 (b) splits into an electron and a hole quasi-Fermi level as depicted in Fig. 2.4 (c). Within the electron contact, the electron concentration is constant towards the external leads and the Fermi level is thus horizontal in Fig. 2.4. Consequently, the electron-contact extracts the quasi-Fermi level to the external leads. The holes do not recombine at the absorber/electron contact interface, and the hole quasi-Fermi level therefore does not drop within the absorber at the electron contact. Owing to their characteristic to contact only one charge carrier type, the doped regions are called "selective contacts". The potential difference between the two sides of the structure is the photovoltage at the external leads. An intrinsic absorber was assumed for Fig. 2.4 (b) and (c). The electric field qV_{BI}/d that arises from the built-in potential therefore drops over the entire absorber thickness d.

For the following consideration, ideal selective contacts and ideal charge carrier transport within the absorber is assumed. This is equivalent to vanishing gradients of the quasi-Fermi levels in Fig. 2.4. The external current J can be calculated by integrating the (hole) particle current J_h generated by illumination over an effective collection length L_{coll}

$$J = -q \int_0^{L_{coll}} div J_h \, dx. \tag{2.24}$$

The elementary charge is written q. As photon absorption generates the same number of electrons and holes, the calculation can as well be done with the electron quantities. The continuity equation under steady state conditions [23],

$$\frac{\partial n_h}{t} = G_h - R_h - \operatorname{div} J_h = 0, \tag{2.25}$$

yields

$$\operatorname{div} J_h = G_h - R_h. \tag{2.26}$$

The time is denoted as t. The generation rate is the sum of the equilibrium (dark) generation rate G_h^0 and the excess carrier generation by illumination ΔG_h. Moreover, we express the recombination rate R according to Eq. (2.19) as the equilibrium rate enhanced by the Boltzmann factor due to the quasi-Fermi level splitting. This results in

$$\operatorname{div} J_h = G_h^0 + \Delta G_h - G_h^0 \, exp\left(\frac{\varepsilon_{F,e} - \varepsilon_{F,h}}{k_B T}\right). \tag{2.27}$$

Integration of the particle current (Eq. (2.24)) thus results in

$$J = -q \int_0^{L_{coll}} \left\{ G_h^0 \left(1 - exp\left(\frac{\varepsilon_{F,e} - \varepsilon_{F,h}}{k_B T}\right)\right) + \Delta G_h \right\} dx. \tag{2.28}$$

Due to the assumptions of ideal contacts and transport, the external voltage V is given by the quasi-Fermi level separation $qV = (\varepsilon_{F,e} - \varepsilon_{F,h})$. Integration leads to the current-voltage (IV) curve of the device [23],

$$J(V) = J_0 \left(exp\left(\frac{qV}{k_B T}\right) - 1 \right) - J_{SC}. \tag{2.29}$$

In this equation, the saturation current density

$$J_0 = q G_h^0 L_{coll}, \tag{2.30}$$

and the current at short-circuit conditions ($\varepsilon_{F,e} - \varepsilon_{F,h} = 0$),

$$J_{SC} = -q \int_0^{L_{coll}} \Delta G_h \, dx. \tag{2.31}$$

were used. Current transport in real solar cells is not ideal, but is mediated by the finite absorber and contact conductivity. Moreover, a fraction of the voltage provided by the junction drops over the metallization between the semiconductor and the measurement tip. These resistance effects are commonly described as a global series resistance R_S. An accurate description of the externally measured IV curve also has to account for conduction paths in parallel to the junction, e.g. by shunts via the cell rims. The shunts are modeled with a parallel resistance parameter R_P. Moreover, defect recombination in the

junction enhances the recombination rate. A defect band in the middle between the electron and hole quasi-Fermi levels gives rise to a square dependence between the radiative recombination rate and the current, $R \propto J^2$. This behavior is modeled by the junction ideality factor n. These parameters define the one-diode model [23],

$$J(V) = J_0 \left(exp \left(\frac{q(V - R_S J)}{nk_B T} \right) - 1 \right) + \frac{(V - R_S J)}{R_P} - J_{SC}. \qquad (2.32)$$

This equation illustrates that the series resistances results in a voltage loss of $R_S J$. In contrast, the implied photovoltage refers to the voltage provided by the junction, i.e. free of external series resistances. As long as the solar cell absorber and selective contact materials are sufficiently conductive, gradients of the quasi-Fermi levels can be neglected and the implied photovoltage equals $(\varepsilon_{F,e} - \varepsilon_{F,h})/q$. It has to be noted, however, that the implied voltage can be lower than the quasi-Fermi level splitting in materials with very low transport.

2.4   Voltage-dependent photocurrent collection

In general, photocurrent collection is not independent of the applied voltage because the collection length can be a function of the applied voltage. For devices with voltage-dependent photocurrent collection the photocurrent is expressed as the product of a voltage-dependent current collection function $\xi(V)$ and the optically generated current

$$J_{gen} = -q \int_{Cell} \Delta G_h \, dx. \qquad (2.33)$$

This leads to an IV curve of the form

$$J(V) = J_0 \left(exp \left(\frac{q(V - R_S J)}{nk_B T} \right) - 1 \right) + \frac{(V - R_S J)}{R_P} - J_{gen} \xi(V). \qquad (2.34)$$

Recombination in thin film p-i-n solar cells can be described by the ratio of drift length and absorber thickness. Under the assumption of a uniform electrical field over the absorber, Crandall [34] derived for the collection function

$$\xi(V) = \frac{L_D}{d} \left(1 - exp \left(-\frac{d}{L_D} \right) \right), \qquad (2.35)$$

where d is the thickness of the intrinsic absorber and L_D the drift length as defined below. With further restriction of the model to small voltages and thin absorbers Merten *et al.* [35] derived an even simpler model. He models the recombination within the absorber with an additional recombination current and derives

$$\xi(V) = 1 - \frac{d}{L_D}, \tag{2.36}$$

Recombination in thin film p-i-n solar cells is thus described by the ratio of drift length L_D and absorber thickness. In both models, Eq. (2.35) and Eq. (2.36), L_D is the effective charge carrier drift length within the internal electrical field:

$$L_D = (\mu\tau)_{\text{eff}}(V_{\text{BI}} - V)/d. \tag{2.37}$$

The electrical field results from the potential difference of the built-in voltage V_{BI} and the applied voltage V, which drops over the absorber thickness d. Independent measurements of charge carrier mobility and lifetime are not possible in many thin film materials and devices. As their product, $(\mu\tau)_{\text{eff}}$ is easier to extract experimentally, it constitutes an important material parameter which summarizes both the recombination and transport properties in one effective value.

When the externally applied voltage equals V_{BI} in Eq. (2.37), the drift length is zero and the photogenerated current is not collected any more. As at this value of the external voltage the dark diode current equals the current under illumination (cf. Eq. (2.34), and the dark and light IV curves cross over. In more realistic cases the field is distorted due to e.g. space charges at the interfaces or traps, and the electric field therefore smaller than V_{BI}/d. The condition of vanishing photocurrent collection is thus better modeled by the flat band voltage $V_{\text{FB}} < V_{\text{BI}}$, for which $\xi(V_{\text{FB}}) = 0$. Inserting Eq. (2.36) to the IV curve (Eq. (2.34)) and differentiation of the latter leads to the short-circuit resistance

$$R_{\text{SC}} = \left(\frac{dJ}{dV}\right)^{-1}\Bigg|_{V=0V} = \frac{1}{J_{\text{SC}}}\frac{(\mu\tau)_{\text{eff}}V_{\text{BI}}^2}{d^2} = \frac{L_D(V=0V)V_{\text{BI}}}{J_{\text{SC}}d} \tag{2.38}$$

within the model of Merten *et al.* [35]. This equation permits to determine the value $(\mu\tau)_{\text{eff}}V_{\text{BI}}^2/d^2$ from the experimental parameters R_{SC} and J_{SC}.

2.5 Basic concepts of amorphous semiconductors

The Si NC preparation technique employed in the framework of this thesis relies on solid phase crystallization of the excess Si in amorphous precursor layers. The crystallized volume fraction depends on the solid phase crystallization conditions and the precursor properties, as will be described in detail in chapter 5. A description of the partially amorphous samples requires a basic understanding of amorphous semiconductors.

The main difference to crystalline semiconductors arises from the lacking long range order of the lattice. The atoms are coordinated according to their valency, and the short range order is thus similar to corresponding crystal. The overall electronic structure of an

amorphous semiconductor is thus similar to its crystalline counterpart, and both phases tend to have a similar band gap. However, the bond lengths and bond angles are not clearly defined like in a crystalline solid. The variations of the bond lengths and bond angles introduces a randomly varying disorder potential additionally to the potential of the lattice atoms. The periodicity of the crystalline lattice gives rise to wave functions (Bloch functions) with the periodicity of the lattice, modulated by an enveloped function. The envelope function defines a constant phase relation $\boldsymbol{k} \cdot (\boldsymbol{r_1} - \boldsymbol{r_2})$ between lattice sites $\boldsymbol{r_1}$ and $\boldsymbol{r_2}$ and also the momentum quantum number $\boldsymbol{k}$. The disorder potential perturbs the crystal potential, and is strong enough to destroy the constant phase relation between the wave functions at different lattice sites. The phase coherence is lost over one or two atom spacings, inducing an uncertainty to the momentum of $\Delta |\boldsymbol{k}| \approx \boldsymbol{k}$. Consequently, the momentum is not a good quantum number any more to describe the wave function, and is not conserved in electronic transitions. The loss of momentum conservation fundamentally changes the description of the electronic band structure. In spite of the $E(\boldsymbol{k})$ dispersion relation, the band structure is described in real space by a density of states $N(E)$. An increasing disorder potential causes strong electron scattering and above a certain threshold full localization (so-called Anderson localization [36]). It has been shown that the disorder potential in amorphous semiconductors is not strong enough for complete localization. However, some of the states are localized due to the disorder perturbation to the crystal potential, and lie at the edges of the extended states energy bands. The band structure of an amorphous solid is sketched in Fig. 2.5.
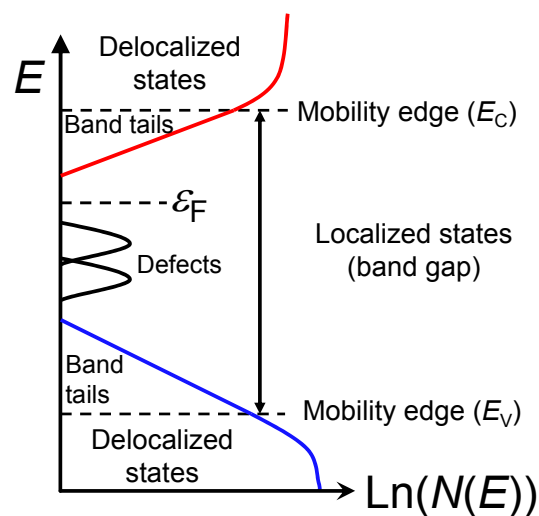
Fig. 2.5: Distribution of the density of states N(E) in an amorphous semiconductor, drawn after [12]. The region between the delocalized states of the conduction and the valence band is characterized by localized states arising from the band tails and defects.

The localized edge or band "tail" states extend exponentially to the band gap. The center of the bands are formed by extended states, separated from the localized band tails by a mobility edge E_C (for the valence band E_V). The lack of long range order of the amorphous network is also expressed in the fact that some atoms are not fully coordinated. The simplest coordination defect is an unpaired electron, or dangling bond. These and other defects cause electronic states deep in the band gap (mid-gap defects), illustrated by the two Gaussian distributions in Fig. 2.5.

The region between the extended states in the valence band and the extended states in the conduction band is called band gap in analogy to the crystalline semiconductor. However, a unequivocal definition of the band gap is not possible for amorphous solids as the mobility edges are not exactly defined. The strength of the optical transitions in the amorphous semiconductors is determined by the spatial overlap of the wave functions rather than by the momentum conservation as in crystalline semiconductors. In the case of the indirect semiconductor silicon, the absorption of the amorphous material is orders of magnitude stronger than the absorption due to the indirect band gap crystalline phase. The band gap of amorphous solids is mostly determined by optical means such as the methods after Tauc [37] or Cody [38, 39], and called optical band gap. As these methods are based on physical models, the magnitude of the optical band gap depends on the assumptions made. In order to quantify the optical band gap independently of any model assumptions, the quantities E_{03} (or E_{04}) are used. They refer to the photon energy at which the absorption coefficient is 10^3 cm^{-1} (or 10^4 cm^{-1}).

Conduction through the extended states is a thermally activated process. The activation energy is the difference of the Fermi energy and the mobility edge, $E_C - \varepsilon_F$, and the dark conductivity through extended states is thus [12]

$$\sigma_{\text{ext}} = \sigma_{\text{ext,0}} exp\left(-\frac{(E_C - \varepsilon_F)}{k_B T}\right). \tag{2.39}$$

The average conductivity above the mobility edge is $\sigma_{\text{ext,0}}$. Material parameters such as the mobility or the charge carrier lifetime are not experimentally accessible in most amorphous materials. However, their product, referred to as the effective mobility lifetime product, can be determined from conductivity measurements in dark and under illumination (photoconductivity) if the optical properties of the film are known. The photoconductivity σ_{photo} is the conductivity due to an excess charge carrier density Δn in a material with mobility μ [153],

$$\sigma_{\text{photo}} = e\Delta n\mu. \tag{2.40}$$

The excess carrier density is related to the generation rate G by an effective lifetime τ_{eff} [28]

$$\Delta n = G\tau_{\mathrm{eff}}, \tag{2.41}$$

The generation rate is calculated from the incident photon current density dj_γ and the optical properties of the film [153],

$$G = \frac{dj_\gamma\{1 - exp(-\alpha d)\}(1 - R)}{d}\eta. \tag{2.42}$$

The absorption coefficient α and the reflectance R characterize the optical properties of the film, and η denotes the excess charge carrier generation ratio. Inserting Eq. (13.6) in Eq. (13.5) and Eq. (13.4) yields the product $\eta\mu\tau_{\mathrm{eff}}$. The excess charge carrier generation ratio is assumed to be $\eta = 1$. As the mobility and the lifetime are both effective values, acounting also for trapping, recombination etc., the notation "effective mobility lifetime product", $(\mu\tau)_{\mathrm{eff}}$ is commonly used, [153]

$$(\mu\tau)_{\mathrm{eff}} = \frac{\sigma_{\mathrm{photo}}}{eG}. \tag{2.43}$$

The effective mobility product constitutes a global mean value of the recombination and transport properties and thus an important material parameter. It has to be noted that conductivity measurements are majority carrier measurements and the deduced $(\mu\tau)_{\mathrm{eff}}$ value thus only valid for the respective charge carrier type.

3 Quasi-Fermi level splitting in an idealized silicon nanocrystal superlattice

In this chapter the maximum open-circuit voltage of Si nanocrystals in a dielectric matrix is estimated. The maximum open-circuit voltage is approximated by the quasi-Fermi level splitting, which is calculated based on a band structure model for an idealized cubic Si NC superlattice and experimental charge carrier density values. For a superlattice of 3.5 nm large and 2 nm separated Si NC, quasi-Fermi level splittings of 1.24 V, 1.2 V and 1.12 V are calculated for a SiO_2, Si_3N_4 and SiC host matrix, respectively, at an excess charge carrier density of $\Delta n = 10^{16}$ cm^{-3}. The band structure calculation was performed within the M.Sc. thesis of Ralph Müller [27]. The results of this chapter were published in [40].

3.1 Description of the model

The first step towards the realization of a Si NC solar cell is the demonstration of a photovoltage higher than for bulk Silicon. In this chapter, the maximum open-circuit voltage of ideal Si NCs in SiO_2, Si_3N_4 and SiC is assessed to show the feasibility of a Si NC solar cell. The calculation is done based on experimental data of carrier generation and recombination and a band structure model of an idealized cubic Si NC superlattice.

The open-circuit voltage of a solar cell with perfect charge separation can be approximated by the quasi-Fermi level splitting in the illuminated absorber. The quasi-Fermi levels can be calculated from Eq. (2.9) given the density of states and the charge carrier density for each carrier type. In the following, the density of states of an idealized Si NC superlattice is calculated for several Si NC sizes, distances and host matrices. The excess carrier density is estimated based on experimental data. Both quantities are then used to calculate the quasi-Fermi level separation. The generation rate G was calculated from experimental absorption spectra and the AM1.5G solar spectrum according to Eq. (2.10) and the effective lifetime was determined with transient photoluminescence measurements. As the material is not doped, $n = n_e = n_h \approx \Delta n$ holds and the excess charge carrier density Δn can be obtained as the product of the generation rate G and the effective lifetime τ_{eff} according to Eq. (2.11).

3.2   Band structure and quasi-Fermi levels

In this chapter, the Si NC layer is modeled as an ideal cubic superlattice as shown in Fig. 2.1 (a) with the approximated potential given by Eqs. (2.2) and (2.3). The energy spectrum to this potential is calculated with Eq. (2.7), see the grey area in Fig. 2.2. The periodicity P is the sum of the NC edge length L and separation S, $P = L + S$. The barrier heights V_0 for the three matrixes was taken from the literature [41] to ensure comparability of the results and is given in Tab. 3.1.

The effective masses of electrons and holes in the matrix are assumed to be $m_M^* = 0.4\, m_0$. This value is reasonable for all the three dielectric matrix materials [41]. m_0 is the electron invariant mass. Within the nanocrystals, the effective mass m_{QP}^* is set to $0.33\, m_0$ for electrons and $0.28\, m_0$ for holes which are the geometric averages of the anisotropic effective masses in bulk silicon [42]. The valence band structure of a superlattice with 2 nm silicon quantum dots in a Si_3N_4 matrix and 0.5 nm spacing is shown in Fig. 3.1.

Tab. 3.1: Barrier height V_0 for electrons and holes in the modeled superlattice for the three prominent matrix materials SiC, Si_3N_4 and SiO_2 [41].

|	SiC	Si_3N_4	SiO_2
Barrier height for electrons (eV)	0.5	1.9	3.2
Barrier height for holes (eV)	0.9	2.3	4.7
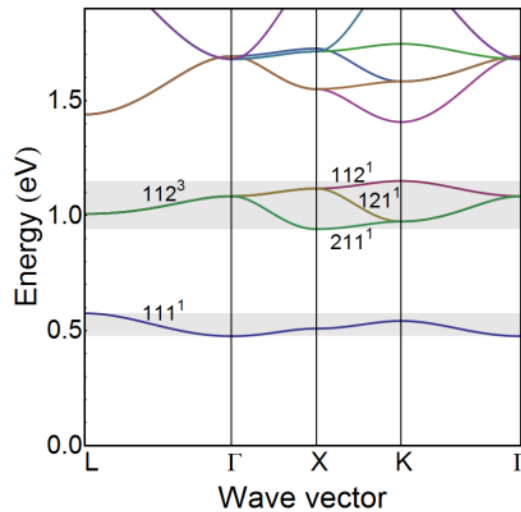
Fig. 3.1: Band structure calculated for 2 nm Si QDs with a distance of 0.5 nm embedded in a silicon nitride matrix. The conduction band edge of bulk silicon is set as the reference point for the energy axis with E=0. The energy bands are denoted by their quantum numbers and degeneracy (superscript). The figure was taken from [40].

The energy bands are denoted by their quantum numbers and degeneracy (superscript). A Si_3N_4 matrix is chosen to illustrate the energy bands because the structure of each contribution is well visible. The energy bands in SiO_2 are relatively flat due to the large confining potential barrier. Because the energy bands range over narrow energy domains separated from each other by energy intervals without states and they arise from wave function coupling of different QDs, they are called mini bands. The energy range between the first miniband for holes and the first miniband for electrons is the band gap of the entire material. Depending on the NC separation, the charge carriers are not mobile. Furthermore, a Si NC size variation leads to a band gap distribution and introduces localized states in analogy to amorphous semiconductors. In the framework of this thesis, band gap therefore does not strictly refer to an energy gap between extended states like in a crystalline semiconductor, but rather to the more general concept of the energy interval between the highest occupied molecular orbital (HOMO) and the lowest unoccupied molecular orbital (LUMO). Depending on the context it is also called optical band gap hereinafter to stress to determination by an optical method and in keeping with the terminology of amorphous semiconductors.

The density of states $N(E)$ for electrons in the superlattice is given by an integral over the surface of constant energy $S(E)$ [24]:

$$N(E) = \frac{2}{(2\pi)^3} \oint_{S(E)} \frac{\mathrm{d}S}{\nabla E(\boldsymbol{k})}. \qquad (3.1)$$

The integral was computed by a finite element method [27, 43] dividing the first Brillouin zone into 24576 tetrahedrons. In each tetrahedron a linear function was used to approximate the band structure $E(\boldsymbol{k})$. The density of states for different superlattices and geometries was calculated for a variation of dot size, inter-dot distance and matrix material. Fig. 3.2 shows the calculated density of states above the band gap for 2 nm Si QDs with 0.5 nm spacing in a Si_3N_4 matrix. The dashed lines represent the contribution of the single energy bands whereas the full lines stand for the complete minibands. The dependence of miniband position and width on dot size, inter-dot distance and matrix material is depicted in Fig. 3.3. The dot size mainly affects the position of the minibands in the energy diagram, shown in Fig. 3.3 (a) for a SiO_2 matrix. A pronounced shift of the first miniband towards higher energies is observed for smaller QDs (0.5 nm distance). Fig. 3.3 (a) also illustrates how the quantum dot size affects the width of the miniband.

However, the miniband width is much more strongly influenced by the inter-dot distance, as illustrated in Fig. 3.3 (b). A reduction from 1 nm to 0.25 nm inter-dot distance changes
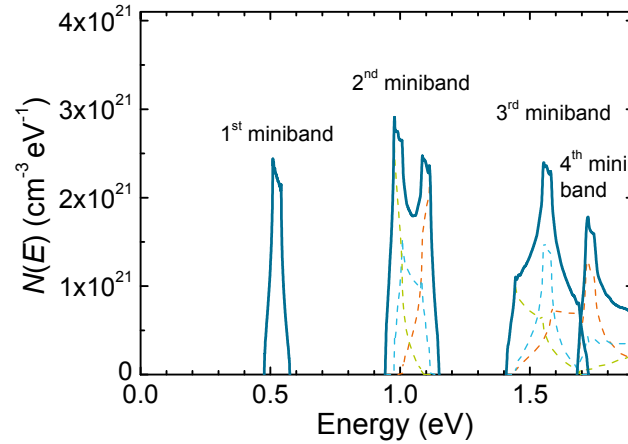
Fig. 3.2: *Density of states calculated for 2 nm Si QDs with a distance of 0.5 nm embedded in a Si$_3$N$_4$ matrix. The origin of the abscissa equals the conduction band edge of bulk silicon. The figure was adapted from [40].*
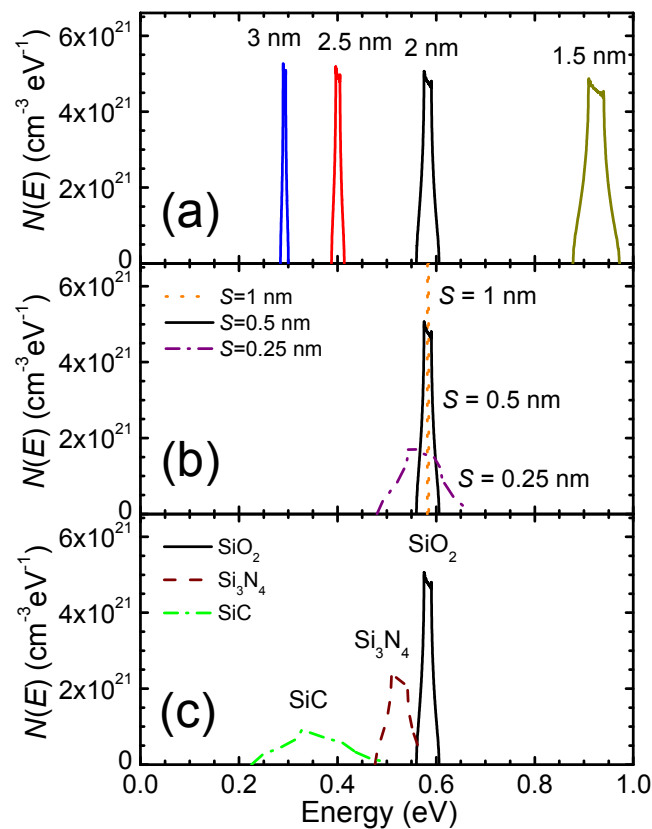
Fig. 3.3: *Calculated density of states in the first miniband above the Si band gap for a superlattice of Si QDs in SiO$_2$, Si$_3$N$_4$ and SiC. (a) Size variation for 0.5 nm separated Si QD in SiO$_2$. (b) Distance variation for 2 nm Si QD in SiO$_2$. (c) 2 nm Si QD with 0.5 nm spacing in various matrices. The figure was taken from [40].*

the shape of the first miniband from a narrow needle to wider distribution. Also, a slight shift towards lower energies occurs as the dots are closer to each other. The band gap of

the matrix material influences both the width and the position of the minibands. This is shown for the three technologically relevant matrices SiC, Si_3N_4 and SiO_2 in Fig. 3.3 (c). A SiO_2 matrix results in a strong quantum confinement due to the high energy barrier (see Tab. 3.1). The first miniband of Si QD in SiO_2 is far away from the bulk Silicon conduction band edge, and narrow in comparison with Silicon quantum dots in matrices with lower barriers. The matrix material (Fig. 3.3 (c)) is also responsible for the miniband width and height, but does not affect the area defined by the graph because the total number of electronic states remains the same.

In summary, the density of states in the modeled superlattice can be controlled by a set of three parameters, namely quantum dot size, inter-dot distance and the matrix material. The matrix material does not alter the integrated density of states in the respective miniband. But the integrated density of states depends on the dot size and the inter-dot distance because the number of states per unit volume is a function of the Si NC volume concentration. The NC volume concentration also also called NC density hereinafter. The integrated density of states in the first miniband, N_1, is shown in Fig. 3.4 for dot sizes relevant for quantum confinement (between 1.5 and 5 nm) and reasonable distances (between 0.5 and 4 nm). The density of states calculation was done in order to obtain a relation between the charge carrier concentration and the quasi-Fermi-level of one charge carrier type, given by Eq. (2.9). Fig. 3.5 exemplarily depicts this relation for electrons in the case of 2 nm quantum dots with 2 nm spacing in SiO_2. As long as the carrier concentration n is much smaller than the integrated density of states in the first miniband N_1, it rises logarithmically with the quasi-Fermi-level $\varepsilon_{F,e}$. Once the first miniband is filled, $\varepsilon_{F,e}$ jumps
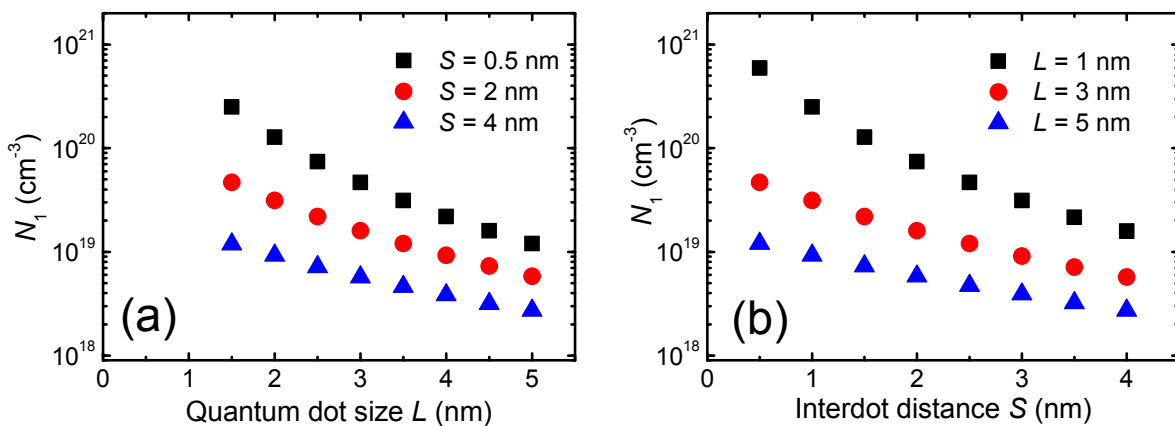
Fig. 3.4: *Integrated density of states in the first mini band (N_1) above the band gap for Si QDs in SiO_2. (a) Variation of the quantum dot size, and (b) variation of the quantum dot distance. The figure was taken from [40].*
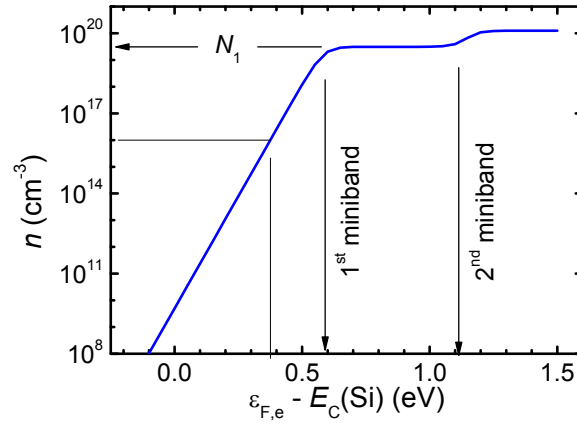
Fig. 3.5: Relation between the charge carrier concentration n and the quasi-Fermi level for electrons $\varepsilon_{F,e}$ for 2 nm Si QDs with 2 nm spacing in SiO$_2$. When the first miniband is full ($n = N_1$), the Fermi rises towards the second miniband. The thin lines indicate the quasi-Fermi level splitting for a carrier density of 10^{16} cm^{-3}. The figure was taken from [40].

towards the second miniband and the latter is populated. The effects for holes and the corresponding quasi-Fermi level $\varepsilon_{F,h}$ are analogous and not discussed here.

3.3   Quasi-Fermi level splitting

The excess carrier density Δn was calculated from experimental data on optical absorption and luminescent lifetime using Eqs. (2.10) and (2.41). Among the three prominent host matrices (SiO$_2$, Si$_3$N$_4$ and SiC), SiO$_2$ is the best understood and the most reliable material system. Only for Si NC in SiO$_2$, light emission has been proven to originate from quantum confined states within the NCs. Therefore, the absorptance and charge carrier lifetime were measured for Si NCs in SiO$_2$, and used for all material systems. The absorption spectra are discussed in section 4.2.1 (Fig. 4.2). The excess carrier density Δn was calculated under the assumption that every absorbed photon with a wavelength λ smaller than 600 nm creates one electron hole pair. The charge carrier lifetime was measured by time-resolved photoluminescence after a forming gas anneal for defect passivation, see Fig. 4.4 (chapter 4). The resulting excess charge carrier densities are reported in Tab. 3.2 and lie between 0.15×10^{16} cm-3 for the 2 nm NCs and 1.66×10^{16} cm-3 for 5 nm NCs. The integral density of states in the first miniband exceeds Δn by approximately three orders of magnitude, cf. Fig. 3.5. Hence it is clear that the quasi-Fermi levels lie between the bulk Si band gap and the first minibands and no saturation effects occur for the Δn values and the Si NC geometry considered here.

As long as the quasi-Fermi level lies below the first miniband, the quasi-Fermi level depends approximately logarithmically on the respective charge carrier density (see Fig. 3.5). But as its dependence on the position of the first miniband ($N(E)$ in Eq. (2.9)) is much more prominent as discussed below, the exact effects of the charge carrier density are neglected and the latter is set to a fixed mean value of $\Delta n = 10^{16}$ cm^{-3} for the following discussion. The quasi-Fermi level for electrons $\varepsilon_{F,e}$ in 2 nm NC in SiO$_2$ with 2 nm spacing and $n \approx \Delta n = 10^{16}$ cm^{-3} is about 0.375 eV above the conduction band edge of bulk silicon. This case is illustrated in Fig. 3.5 by thin black lines. The quasi-Fermi level for holes, $\varepsilon_{F,h}$, is

Tab. 3.2: Estimated excess carrier density Δn in different NC samples under illumination with the AM1.5G solar spectrum. Approximate NC sizes are 2 nm, 3.5 nm and 5 nm.

	2 nm	3.5 nm	5 nm
Δn (cm^{-3})	0.15×10^{16}	0.65×10^{16}	1.66×10^{16}
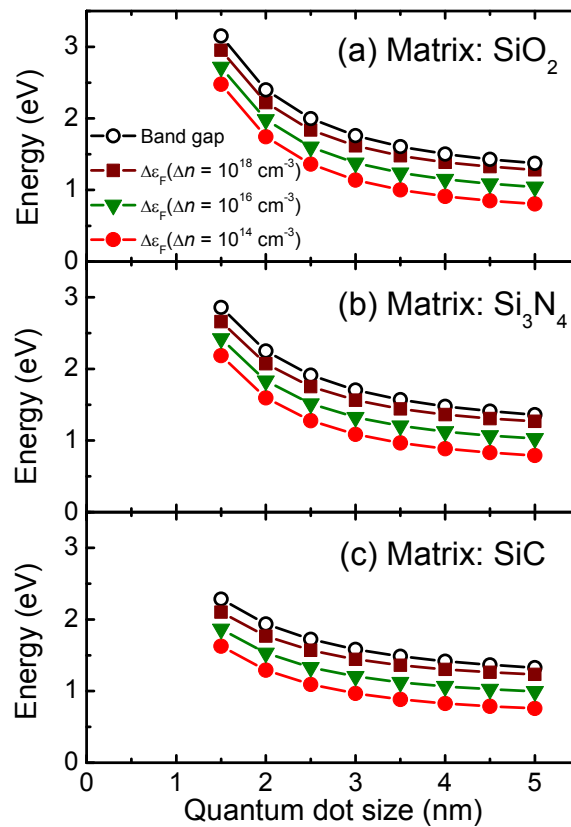
Fig. 3.6: Calculated band gap (black) and splitting of the quasi-Fermi levels ΔE_F for silicon quantum dots in a SiO$_2$ (a), Si$_3$N$_4$ (b) and SiC (c) matrix, all of them with an inter-dot distance of 2 nm. Illumination with the AM1.5G solar spectrum corresponds to $\Delta n = 10^{16}$ cm^{-3}. The figure was taken from [40].

determined in the same way (not shown here) and lies in this case about 0.495 eV below the valence band edge of bulk silicon. The splitting of the quasi-Fermi levels $\Delta\varepsilon_F$ then results in

$$\Delta\varepsilon_F = \varepsilon_{F,e} - \varepsilon_{F,h} = E_{G,Si} + 0.375 \text{ eV} + 0.495 \text{ eV}, \qquad (3.2)$$

with the band gap of bulk silicon $E_{G,Si} = 1.12$ eV. The density of states was calculated as described before for various cases, including variations of the Si NC size, their distance and the matrix (SiC, Si_3N_4 and SiO_2). Subsequently, for every case the splitting of the quasi-Fermi levels was calculated for the excess carrier densities $\Delta n = 10^{16}$ cm^{-3}, 10^{14} cm^{-3} and 10^{18} cm^{-3}. The results are shown in Fig. 3.6. The band gap strongly depends on the quantum dot size for all three matrices. The smaller the dots are, the stronger the quantum confinement and therefore the larger the band gap. However, the difference between the band gap and the quasi-Fermi level splitting, $E_G - \Delta\varepsilon_F$, depends only slightly on the dot size, the inter-dot distance and the matrix material. For illumination with the AM1.5G solar spectrum, the difference increases from 0.33 eV for 5 nm dots to 0.44 eV for 1.5 nm dots. The observation that $\Delta\varepsilon_F$ mainly follows the band gap can be explained with the integrated density of states in the first miniband, N_1, which is always several orders of magnitude larger than the excess carrier density Δn, and the fact that the first miniband is very narrow. Fig. 3.6 also shows how the quasi-Fermi level splitting depends on the charge carrier density. A higher excess carrier concentration can be achieved by means of light trapping [44] or increased lifetime. A 100fold higher carrier concentration would increase the quasi Fermi-level splitting by 0.24 eV (Fig. 3.6). Another way to achieve a higher excess carrier density are more densely packed Si NCs (higher volume density), because more light is absorbed per volume. The quasi-Fermi level splitting as a function of the Si NC separation is depicted in Fig. 3.7. A slight decrease of the quasi-Fermi level can be seen, but the quantum confinement is still preserved even for 0.5 nm spaced NCs. By means of atomistic calculations it was shown that even in the case of touching Si NCs the confinement is not lost [45].

It has to be noted that the procedure presented here involves several simplifications and relies on the idealized case of a cubic superlattice with monodisperse NCs. To check consistency with other band gap related data, we compare the quasi-Fermi level splitting with the optical gap E_{03} measured by spectrophotometry (see section 13.2.3) and the position of the photoluminescence maximum E_{PL}.
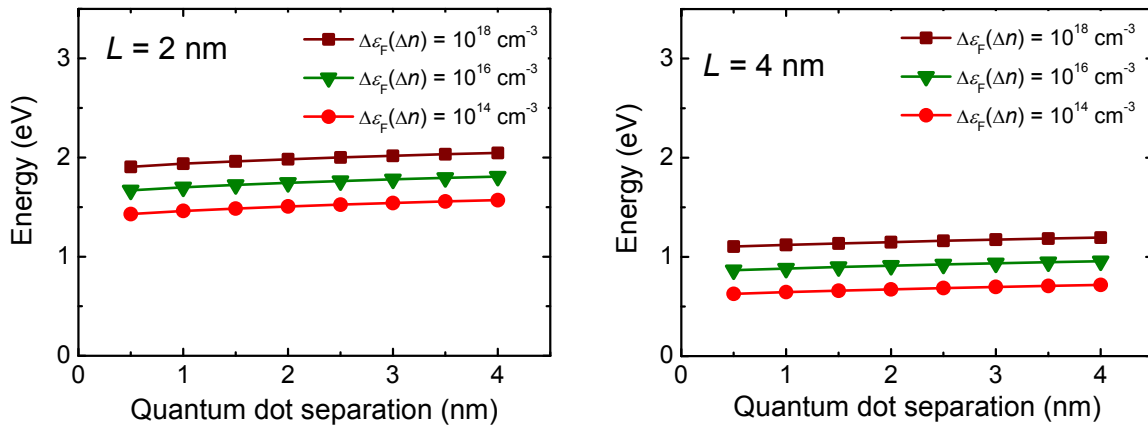
Fig. 3.7: *Quasi-Fermi level splitting* $\Delta\varepsilon_F$ *as a function of the Si NC separation and a variation of the excess carrier density for Si NC sizes of 2 nm (left) and 4 nm (right). The figure was adapted from [27].*

The three values show similar size dependence and the same sequence except for the smallest NC size (2 nm), see Fig. 3.8. However, bearing in mind the severe simplifications made (cubic shape, perfect size distribution etc.), the discrepancy for very small NC is no surprise. For sizes larger than approximately 2.5 nm, the calculation of the quasi-Fermi level splitting seems to be reasonable. The results are transferable to the other matrices provided they yield comparable absorption and charge carrier lifetimes.
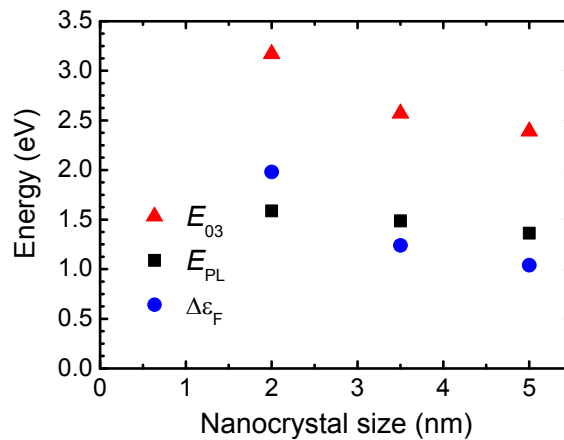
Fig. 3.8: *Experimental values of the photoluminescence maximum* E_{PL} *and the optical gap* E_{03} *of Si NCs in SiO$_2$ in comparison with the calculated quasi-Fermi level splitting. The quasi-Fermi level splitting was calculated for a Si NC separation of 2 nm and an excess carrier density of* 10^{16} *cm^{-3}. The figure was taken from [40].*

3.4   Chapter summary

The most fundamental criterion to a Si NC solar cell material is a higher photovoltage than achievable with bulk c-Si. In order to estimate the maximum open-circuit voltage, the quasi-Fermi level splitting in a Si NC material has been investigated under the assumption of ideal charge separation.

The splitting of the electron and hole quasi-Fermi levels in the Si NC absorber was modeled in a combined approach using theoretical band structure calculations and experimental values for the excess charge carrier density. The band structure was calculated for the idealized case of cubic Si NCs arranged in a simple cubic superlattice using the envelope function approach. The calculation was done for various cases, including variations of the NC size, the NC separation, the matrix material and the illumination level. As matrix materials SiO_2, Si_3N_4 and SiC were considered.

The superlattice arrangement of the Si NCs was found to result in split energy levels extending through the reciprocal space. The energy level splitting is a sign for wave function coupling between different NCs. The energy level manifolds are separated by each other by regions without states and are thus called minibands. A reduced barrier height was found to manifest itself in an increase miniband width due to the stronger NC-NC interaction. The integrated density of states of the first miniband ($\approx 10^{20}$ cm^{-3}) was calculated to be about three orders of magnitude larger than the excess carrier concentration ($\approx 10^{16}$ cm^{-3}). The quasi-Fermi levels thus follows the band gap as the Si NC size is reduced. For the three host matrices SiO_2, Si_3N_4 and SiC, quasi-Fermi level splittings of 1.24 V, 1.2 V and 1.12 V were calculated, respectively, for the case of 3.5 nm large and 2 nm separated Si NC and $\Delta n = 10^{16}$ cm^{-3}. Moreover it was shown that the quasi-Fermi level splitting can be increased by 0.24 eV by means of a 100fold higher illumination level. The size dependence of the quasi-Fermi level splitting was found to be in qualitative agreement with the size dependencies of the band gaps measured by photoluminescence spectroscopy or spectrophotometry. Based on the model presented here, quasi-Fermi level splittings above 1 eV can be attained for Si NCs embedded in one of the three host matrices.

4 Silicon nanocrystals in SiO$_2$

In this chapter a detailed analysis of the optical spectra of Si NCs in SiO$_2$ is presented with the objective to investigate the quasi-Fermi level splitting experimentally. Band gap control is shown by absorption and photoluminescence spectroscopy using size-controlled Si NCs embedded in SiO$_2$ prepared in our group. A brief review of the optical properties of Si NCs is presented with an emphasis on the influence of the Si NC chemical environment. The photoluminescence and absorption spectra of the samples size-controlled Si NCs discussed here are then analyzed in the framework of the generalized Planck law of radiation. The spectra do not agree with miniband formation but indicate that the Si NC array cannot be seen as a superstructure and the spectra are merely a superposition of single Si NC spectra. The electrical properties are reviewed briefly on the background of the implementation as a solar cell absorber.

4.1   Introduction

Si NC in SiO$_2$ can be obtained by a wide range of different methods, ranging from liquid phase processes [46] over gas phase approaches like pyrolysis of silane in a laser beam [47] or synthesis in a non-thermal plasma [48] [49] to solid phase crystallization of amorphous precursors. A good overview of liquid and gas phase processes was given by Bapat *et al*. [48] and the references therein. For the preparation of Si NCs by solid phase crystallization, an amorphous precursor with Si excess is fabricated in a first step by ion implantation, evaporation, sputtering or plasma enhanced chemical vapour deposition (PECVD). In a second step, the precipitation and the crystallization of Si the excess is induced by thermal, laser or electron beam annealing.

As a solar cell absorber, the Si NC material should have a tunable band gap, low absorptance at photon energies below the band gap and also exhibit extended states throughout the Si NC network. Furthermore, a narrow Si NC size distribution is required. According to atomistic calculations, electronic coupling between NCs critically depends on the size dispersion [45]. A similar effect is known from amorphous solids, whose band tails are explained with local potential fluctuations (section 2.5). As the band tail states do not couple to an energy band, transport is poor and the band tails act as trap and recombination centers. A smart way of producing Si NCs with a narrow size distribution

was developed by Zacharias and co-workers [18] [50]. The authors developed the superlattice approach depicted in Fig. 1.4 for the formation of Si NCs in SiO$_2$ with a narrow size distribution. Material fabrication takes place in two steps. First, a multilayer of alternating amorphous silicon-rich oxide (SRO) and SiO$_2$ layers is deposited onto a high-temperature stable and flat substrate. Then, thermal annealing leads to phase separation and solid phase crystallization around 1100°C. The phase separation is described by the formula

$$\mathrm{SiO_x} \xrightarrow{1100°C} \frac{x}{2}\mathrm{SiO_2} + \left(1 - \frac{x}{2}\right)\mathrm{Si.} \qquad x < 2 \qquad\qquad (4.1)$$
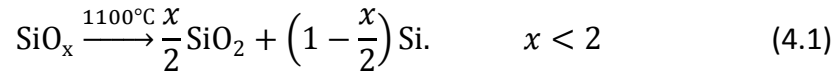
Here and in the following, SiO$_2$/SiO$_x$ refers to a multilayer made of SiO$_2$ and SiO$_x$ layers. When referring more generally to a Si nanocrystal array in a SiO$_2$ matrix, the notation SiO$_2$/Si NC is used. Fig. 4.1 depicts a transmission electron micrograph of a SiO$_2$/SiO$_x$ multilayer. Well separated
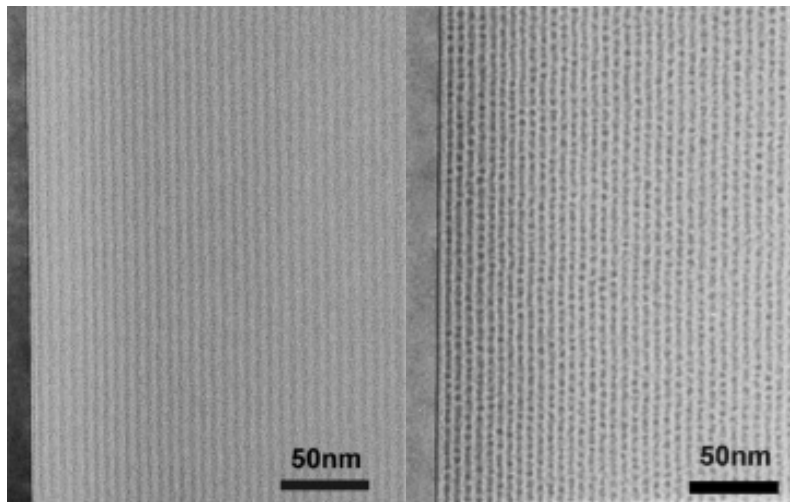
Fig. 4.1: *Transmission electron micrograph of the (left) amorphous SiO$_2$/SRO precursor multilayer and (right) Si NCs in SiO$_2$ in the annealed state. The images were taken from [50].*

SiO$_2$/SRO layers in the amorphous precursor can be distinguished. In the annealed state (Fig. 4.1, right),Si NCs are seen with apparently spherical shape in a regular arrangement. Alternatively to spatially separated Si NC, crystalline Si quantum well layers can be obtained by using pure Si in spite of SRO in the multilayer stack. From a historical point of view this material can be seen as the forerunner of Si NC in SiO$_2$ [51]. Si quantum wells in SiO$_2$ have been used for solar cell applications among others by Rölver and Berghoff *et al*. [52] and Stegemann *et al*. [53].

In the framework of this thesis, Si NCs in SiO$_2$ by the superlattice approach of Zacharias are used because this method yields a superior size control and two orders of magnitude

higher luminescence compared to Si NC from bulk SiO films [54]. Furthermore, the band gap is controlled more easily with quantum confinement in three dimensions in contrast to Si quantum wells.

4.2   Sample preparation

The samples discussed in this chapter were fabricated in our group by thermal evaporation of SiO powder to synthetic quartz glass (Suprasil 1) as substrate. The Si content x was adjusted by the evaporation ambient. Si-rich films (SiO$_x$, x=1.2) were evaporated in high vacuum and SiO$_2$ films in a controlled oxygen ambient. Prior to deposition, the substrate was annealed in N$_2$ to reduce the concentration of OH-groups within the substrate. Underneath and on top of the multilayer, 10 nm SiO$_2$ serves as buffer and encapsulation. Annealing was performed for 1 hour at 1100°C in Ar or N$_2$ atmosphere. Details of the sample preparation were reported in [55]. An overview over the samples is reported in Tab. 4.1. Amorphous precursor layer thicknesses were tuned by the deposition rate. The NC size was deduced from the PL peak position and a previously established

Tab. 4.1: Overview of the SiO$_2$/Si NC samples used in this work. All samples comprise a 10 nm SiO$_2$ buffer underneath and on top. The nominal thickness (as-deposited) of the SiO$_2$ barrier and the SRO well are referred to as d_{SiO_2} and d_{SRO}.

Sample	$d_{\mathrm{SiO_2}}$	d_{SRO}	NC size	Bilayers	High-T annealing	H-passivation
5N					N$_2$	-
	3	6	5	50		
5Ar					Ar	FGA
3.5N					N$_2$	-
	3	4	3.5	50		
3.5Ar					Ar	FGA
2N					N$_2$	-
	3	2	2	50		
2Ar					Ar	FGA

calibration relation based on high-resolution transmission electron micrographs of a large range of samples [56]. Several samples received an additional hydrogen treatment after high-temperature annealing. The hydrogen treatment consisted of a forming gas anneal (FGA, 95% N$_2$, 5% H$_2$,) at 420°C for 20 min.

4.2.1 Optical absorption

The absorption of Si NCs in SiO$_2$ was determined to characterize the optical band gap and its dependence on the Si NC size. The absorption spectra were furthermore used to

calculate the generation rate in a Si NC superlattice and to model the luminescence spectra with the generalized Planck law (section 4.3). The absorption coefficient was calculated from reflectance and transmittance spectra measured with a spectrophotometer and an integrating sphere as described in section 13.2.3. Each layer stack was prepared once with Ar and once with N_2 annealing to assess the influence of the different annealing atmospheres on the optical properties.

Fig. 4.2 (left) shows the absorption coefficient of Si NCs in SiO_2 with 5 nm, 3.5 nm and 2 nm size. The film thickness was measured in a scanning electron microscope for identical superlattices on a Si wafer substrate. A shift of the optical band gap to higher photon energy (blue shift) can be identified in Fig. 4.2 (left) as the Si NC size decreases. Si NCs annealed in N_2 absorb more strongly than NCs annealed in Ar. A detailed review of the early experiments on the absorption of Si NCs was published by Kovalev *et. al.* [57]. For more recent studies please refer to [58]. Decisive for solar cell applications is the charge carrier generation rate in the Si NC film, which is defined by the overlap integral of the absorptance spectrum and the AM1.5G solar spectrum (Eq. (2.10)). The absorptance is depicted with a linear scale and a function of the wavelength in Fig. 4.2 (right) together with the AM1.5G solar spectrum. The bigger the nanocrystals are, the stronger is their absorption. The resulting charge carrier density for the samples investigated here was approximately 10^{16} cm^{-3} as reported in chapter 3.
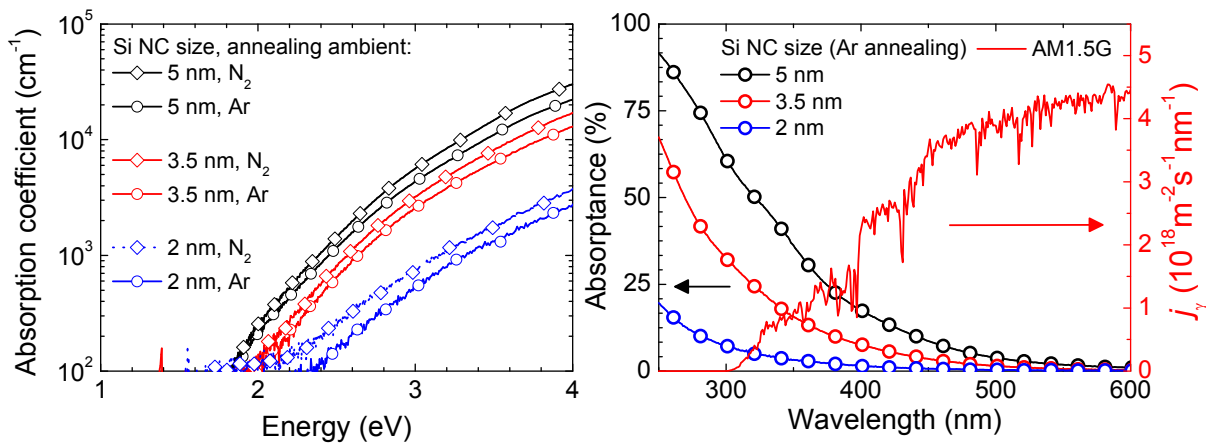
Fig. 4.2: *(Left) Absorption coefficient spectra of Si NCs with sizes of 2 nm, 3.5 nm and 5 nm annealed in N_2 and Ar (cf. Tab. 4.1). (Right) Absorptance on linear scale for the Si NCs prepared with Ar annealing and the AM1.5G solar spectrum. The overlap integral defines the mean charge carrier generation rate. The figure was adapted from [40].*

4.2.2 Photoluminescence

Photoluminescence (PL) spectroscopy utilizes the spontaneous emission of photons and thus provides information on the radiative and non-radiative decay rates and the band structure. The spectra yield complementary information to absorption spectroscopy, which will be further exploited in section 4.3 to model the photoluminescence with the generalized Planck law of radiation. This section presents a characterization of the sample series under investigation in this chapter (see Tab. 4.1) by PL and briefly reviews the mechanisms governing the photoluminescence properties of Si NCs embedded in SiO_2.

The PL peak position is frequently used as a measure for the band gap, and the PL intensity is a measure of the radiative efficiency (see Eq. (2.23)). Photoluminescence spectra of the sample series whose absorption was discussed in the previous section are shown in Fig. 4.3. The peak position shifts from 1.36 eV for 5 nm NC to 1.59 eV for 2 nm NC annealed in N_2. Comparison with Fig. 4.2 demonstrates that the PL peak positions are at longer wavelengths than the absorption onset, as was expected because of the Stokes shift. The PL peak of nitrogen annealed samples is slightly blue-shifted compared to the corresponding sample annealed in argon. Hiller [56] observed this nitrogen-induced blue shift along with a reduction of the defect density measured by electron spin resonance (ESR). They showed that N enriches in the silicon-rich layer and interpreted the occurrence of the ESR signal as evidence that N atoms were incorporated at the Si NC interface. According to their calculations, the N areal density on the NC interface is $5 \times 10^{14} \, cm^{-2}$. The defect passivating effect of nitrogen is well known from planar SiO_2/Si interfaces, which exhibits comparable defect areal densities [56]. The N-related blue shift can be explained
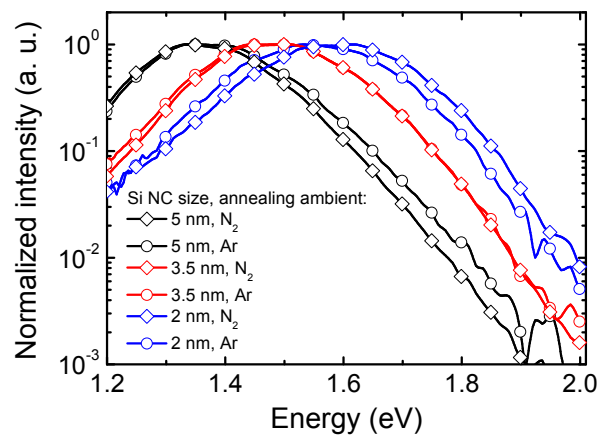
Fig. 4.3: *Normalized photoluminescence spectra of Si NC with 2 nm, 3.5 nm and 5 nm size annealed in N_2 and Ar.*

with the polarity of the Si NC interface termination. König *et al*. [59] investigated the effect of -F, -OH, -NH$_2$, -CH$_3$ and -H interface groups theoretically and found that owing to the bond polarity a charge transfer towards the interface group occurs which lowers the HOMO-LUMO gap. As the bond polarity decreases within the series -O, -N, -C, -H, the band gap for -NH$_2$-terminated NC is higher than that of -OH-terminated NC. The origin of PL from Si NC has been under discussion for over a decade. While the PL size-dependence was accepted since the pioneering work on porous Si, it has not been clear whether luminescence occurs from defect states at the Si NC surface or from quantum confined states in the Si NC bulk. Quantum confined states as the origin of PL were given evidence for by Godefroo *et al*. [60]. This work stressed the role of hydrogen at the Si NC interface and demonstrated how the origin of PL could be switched from defect-related to quantum confined states by a hydrogen treatment. The SiO$_2$/Si NC interface without H passivation was shown by Jivanescu *et al*. [61] to be very similar to the bulk SiO$_2$/Si interface and governed by the same defects. Hydrogen passivation has two effects on the PL spectrum. The PL shifts slighty towards lower photon energies (red shift) [62] and the intensity increases by an order of magnitude upon hydrogen passivation [62]. The reaction mechanism of H at the SiO$_2$/Si NC interface was investigated by Wilkinson *et al*. [63], who reported reaction rate parameters in good agreement with results from planar SiO$_2$/Si interfaces by Stesmans [64].

Defect states can also give rise to radiative transitions. Sub-band gap luminescence or absorption is therefore a sign for defect states. Furthermore, even if the electronic properties were not affected, sub-band gap absorption in a Si NC top solar cell is detrimental for tandem solar cell operation as it reduces the irradiance on the bottom solar cell. Especially interesting is the occurrence of bulk Si band gap luminescence, as this would be a sign for large NCs exhibiting bulk properties. For the sample series of Tab. 4.1, sub-band gap photoluminescence could not be evidenced. It is furthermore noted, that a very low sub-band gap absorption was reported by Lee *et al*. using photothermal deflection spectroscopy [58].

As H passivates the defects at the SiO$_2$/Si NC interface, the effective charge carrier lifetime is longer. Fig. 4.4 shows the luminescence decay of samples before and after hydrogen passivation of samples annealed in Ar (cf. Tab. 3.1). The effective lifetime was obtained by a single exponential fit. Due to the hydrogen passivation the effective lifetime increases from 30% to 50%.
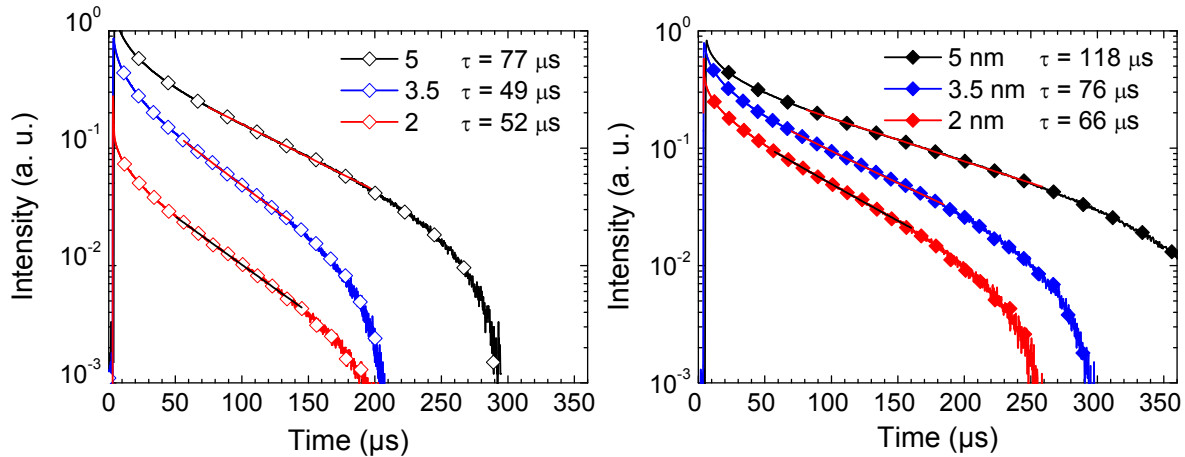
Fig. 4.4: *Time-resolved photoluminescence of Si NCs with 2 nm, 3.5 nm and 5 nm size in SiO$_2$ annealed in Ar before (left) and after (right) hydrogen passivation (adapted from [40]).*

4.3   Investigation of miniband formation

The luminescence spectrum of a semiconductor is theoretically described by the generalized Planck law of radiation (or generalized Planck law, Eq. (2.23)). It relates the luminescence and absorption spectrum to the chemical potential of the emitted photons. As the chemical potential of the emitted photons equals the quasi-Fermi level splitting in the semiconductor, the generalized Planck law constitutes an elegant way to probe the quasi-Fermi level splitting by purely optical means. In this section, the generalized Planck law is applied to calibrated PL spectra to extract the quasi-Fermi level splitting and to evidence the formation of minibands in a SiO$_2$/Si NC superlattice. The generalized Planck law (see section 2.2) describes the radiation emitted from a material with energy bands, whose occupations are described by their respective quasi-Fermi levels and the temperature of the charge carrier system. The concept of an energy band is tightly connected in this context to the thermodynamic description of the charge carrier population with a chemical potential.

The assignment of a chemical potential and a single temperature to the charge carrier population implies in detail [32]

- chemical equilibrium of electrons and holes within their respective bands with regard to transitions between states of different energy, and
- thermal equilibrium with the crystal lattice.

Chemical equilibrium with regard to transitions between the conduction band and the valence band is explicitly not required, i.e. $\varepsilon_{F,e} \neq \varepsilon_{F,h}$.

The description of the electron and hole population by chemical potentials presumes that the electronic states of different Si NCs couple sufficiently strong for the chemical equilibrium to establish, i.e. to form minibands through the Si NC network. In that case, the quasi-Fermi level splitting within the Si NC network can be extracted from the luminescence and absorption spectra by use of (2.23). Another applications are charge carrier temperature measurements [65], or absorption measurements in case the quasi-Fermi level splitting is known (light emitting diodes) [66]. If, however, the interaction is not sufficiently strong for a chemical equilibrium to establish for each charge carrier type, the generalized Planck law is not valid and the luminescence spectrum is merely a superposition of many single emitter spectra.

It is important to note that no assumption of electron or hole mobility is needed for the derivation of the generalized Planck law. For this reason it opens an elegant way to probe the quasi-Fermi level splitting of a material with low mobility. Technological implications of selective contacts are avoided because it is a purely optical measurement.

Calibrated photoluminescence spectra were measured using excitation by an Ar ion laser at 488 nm and 10 mW/mm² irradiance (see section 13.2.4). The Si NC temperature increase due to illumination was estimated to be less than 30 K based on a comparison of the thermal conductivities of the embedding media SiO_2 (1.4 $Wm^{-1}K^{-1}$) and air (0.0262 $Wm^{-1}K^{-1}$) and can thus be neglected. Absorption spectra were measured with a spectrophotometer (see section 13.2.3).

Fig. 4.5 shows photoluminescence spectra of NCs with 2 nm, 3.5 nm and 5 nm size, together with the spectra calculated with Eq. (2.23). The photoluminescence spectra are the same as shown in Fig. 4.3. The absorption spectra shown in Fig. 4.2 were used to calculate the theoretical spectra after Eq. (2.23). The calculated spectra are noisy in the spectral region of low absorptance, because here the absorption spectra become increasingly prone to errors. The only two parameters that can be varied in the generalized Planck law are the chemical potential $\Delta\varepsilon_F$ and the charge carrier temperature T. In the semi-logarithmic plots shown in Fig. 4.5, the temperature determines the slope of the high-energy wing, while the chemical potential translates the entire spectrum to higher photon fluxes. Two calculated curves are shown in Fig. 4.5 for each sample: For the red curves, the temperature was varied to achieve the best fit of the generalized Planck
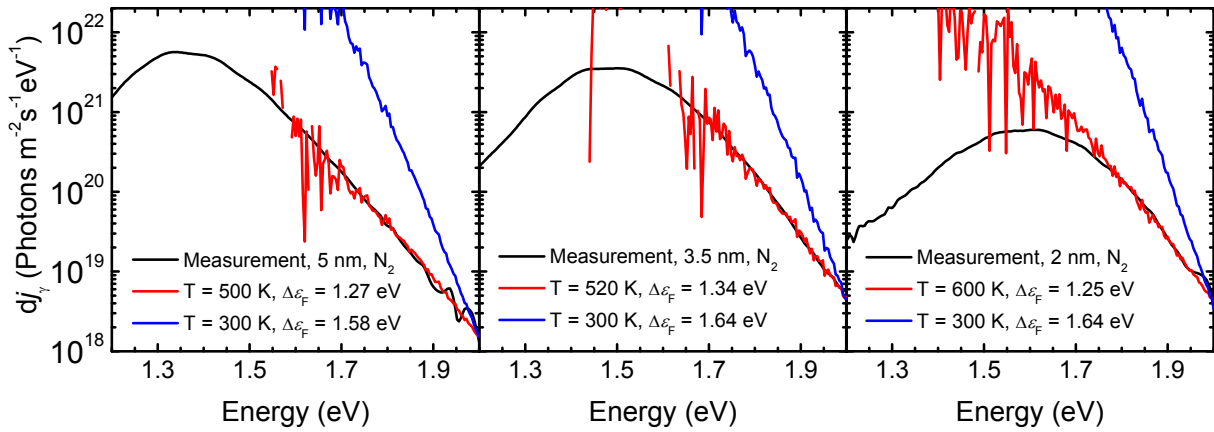
Fig. 4.5: *Calibrated PL spectra (black) for Si NCs in SiO$_2$ with 2 nm, 3.5 nm and 5.5 nm size (cf. Tab. 4.1). The curves shown in red and blue were calculated from optical absorption spectra (Fig. 4.2) according to Eq. (2.23) for 300K (blue), and for the temperature giving best agreement with the experimental data (red). The figure was adapted from [27].*

law to the experimental data. The blue curves were calculated with a charge carrier temperature of 300 K. The spectra can obviously not be fitted with a sample temperature of 300 K, because the high-energy slope of the measured spectrum is too shallow. The same analysis was also performed for samples with the same size variation that were annealed in Ar instead of N$_2$, yielding a very similar result.

As mentioned in the previous section, the luminescence increases drastically when the Si NC interface defects are passivated by hydrogen. The defect passivation might also alter the electronic coupling of adjacent NCs and thus also the luminescence and absorption spectra. Therefore, the analysis was extended to H-passivated Si NCs. The H-passivated samples belonged to the same sample set as the samples discussed above (Fig. 4.5) and also the size variation was the same as before (2 nm, 3.5 nm and 5 nm).

The optical spectra were measured and published by Lee *et al*. [58]. In that work, photoluminescence excitation (PLE) was employed for a most accurate determination of the optical absorption spectra taking into account only radiative transitions (see section 13.2.5). The PL spectra are shown together with the fit of the generalized Planck law (Eq. (2.23)) in Fig. 4.6. Like for Si NCs without H passivation, the theoretical function does not fit the experimental data well when a temperature of 300 K is assumed. Temperatures of 450 K to 550 K are necessary also in this case to achieve good agreement with the experimental data. The same result was also obtained with Si NCs annealed in Ar (not shown here).
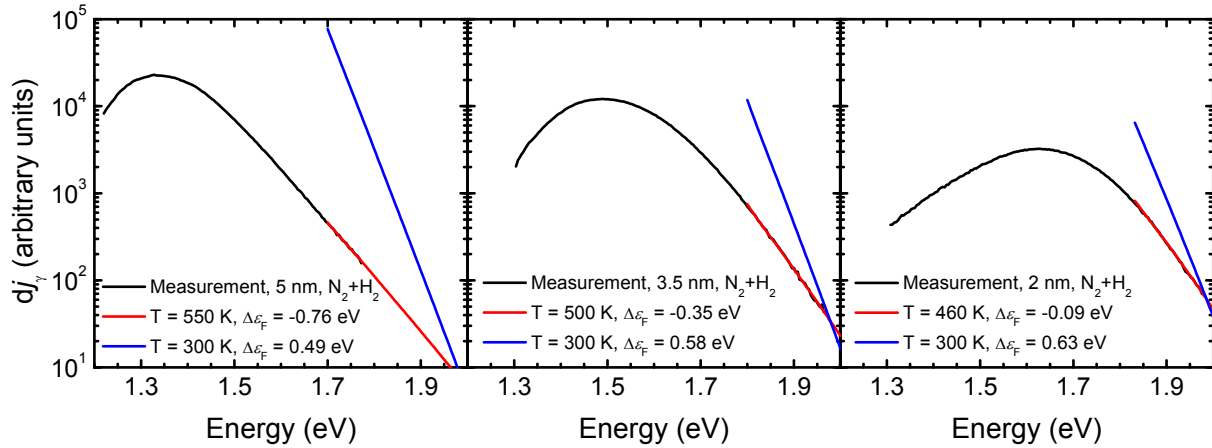
Fig. 4.6: *Experimental photoluminescence spectra and plot of the theoretical function for a series of H$_2$ passivated Si NCs with 2 nm, 3.5 nm and 5 nm size (cf. Tab. 4.1). PL and absorption data were taken from [58]. The theoretical function was calculated for 300 K (blue) and for the temperature giving best agreement with the experimental data (red). The figure was adapted from [27].*

Irrespective of the NC size, the annealing atmosphere and an additional defect passivation with hydrogen, the measured luminescence spectra are much broader than the spectra calculated with the generalized Planck law for a charge carrier temperature of 300 K. Provided that the generalized Planck law is valid, the experimental data imply a hot charge carrier population with carrier temperatures between 450 K and 600 K. The reverse argument, the generalized Planck law not being valid for this material, leads to the conclusion that the spectrum is a superposition of many single luminescence emitters. Simultaneous investigations of comparable samples by other techniques support this conclusion, namely single luminescence emitters. In this case the luminescence spectral shape would be directly related to the Si NC size distribution.

By means of TEM tomography, Fitting Kourkoutis and Hiller [55] gave evidence of spatially only sparsely distributed Si NCs [56]. Furthermore, conductivity measurements both in dark and under illumination lead to the conclusion that transport takes place only via tunneling, if at all, and that wave function coupling between the NCs is very weak. Hiller furthermore determined a Si NC areal density of 2.1×10^{12} cm^{-2} [56] for Si NC with a diameter of 3.5 nm. These two values imply a mean distance of 11.5 nm under the assumption of a 2D hexagonal arrangement, far too large for miniband formation. Insightful results were recently presented by Luo *et al.* [45] who employed atomistic calculations to model Si NC arrays. The authors report that miniband formation ceases already at separations >0.5 nm, and that even at intimate contact of two neighboring dots

quantum confinement is reduced by only 50 meV. Moreover, they elucidate the critical role of NC size variations and state that for size differences of 10% the quantum confinement is already affected severely.

Guerra *et al*. [67] report the absorption and luminescence spectra calculated with ab-initio methods in a recent publication. The authors consider Si NCs ensembles and calculate the optical spectra as a superposition of the spectra of individual Si NCs taking the Si NC size distribution into account. The excellent agreement with experimental results further supports the interpretation that the NC-NC interaction in experimentally realized Si NCs is too low for electronic coupling.

The luminescence intensity and the absorption depend on the interface termination, indeed. The SiO_2/Si NC interface can be altered with the high-temperature annealing ambient (Ar or N_2) and by hydrogen passivation. However, the spectral shape of photoluminescence and absorption does not change upon a different Si NC interface termination. Rather, the spectra can be explained with a superposition of the respective properties of single Si NCs with a certain size distribution. In conjunction with TEM and theoretical studies [45], the most reasonable interpretation is an array of non-interacting Si NC. Summing up, Si NCs in SiO_2 as described above cannot be considered as a superstructure with energy bands extending through the entire material system.

4.4   Electrical properties of Si nanocrystals in SiO_2

Besides appropriate optical properties, electrical conduction through the Si NC network is an indispensable prerequisite for the objective of a working solar cell. A broad range of studies have been carried out on the electrical properties of Si NCs. According to the very different motivations ranging from an electrically pumped light emitter over a charge storing device to a solar cell absorber, various experimental approaches have been employed. So far, most studies were motivated by fundamental questions or were targeting light emitting devices and were performed using MOS structures with a Si substrate. It will be explained in chapters 7 and 8 that such structures are not practical for a photovoltaic characterization of Si NC films. As the project presented here aims at the photovoltaic exploration of Si NCs, it was focused on the development of a photovoltage device. As the exact conduction mechanisms are beyond the scope of this thesis, but of importance for the overall goal of a c-Si tandem solar cell, only a very brief review on the electrical properties of Si NCs in SiO_2 is given here.

The most successful attempts for light emitting devices were realized with metal oxide semiconductor (MOS) structures with Si NCs in the (oxide) gate layer stack under alternating current (AC) excitation [68-70]. This approach relies on the subsequent injection of electrons and holes from the same electrode, which is in most cases the substrate wafer, and their radiative recombination. In most studies, however, large electric fields were employed to achieve electroluminescence (EL). Comparatively low electroluminescence turn on voltages of 1.4 V to 1.7 V were reported by Anopchenko et al. [70] who used a SiO_2/Si NC multilayer stack similar to the one used in this thesis. Charge carrier injection was achieved by Fowler-Nordheim tunneling in most cases. But apart from Fowler-Nordheim tunneling, the same authors also achieved bipolar charge injection under direct current (DC) excitation [71]. The bipolar injection was shown for a multilayer with 3 nm Si NCs and 2nm SiO_2 barrier layers by comparison to samples with thicker barrier layers at either the top or the bottom electrode. Bipolar injection is associated with direct tunneling, which is much more efficient than Fowler-Nordheim tunneling. However, even direct tunneling is too resistive for solar cell operation. A modified Si NC configuration was used by Rölver et al. [20]. Due to the very poor transport perpendicular to the SiO_2 barrier layers, they prepared multilayer stacks consisting of Si quantum wells (2D instead of 3D confinement) between SiO_2 barriers and studied the lateral charge carrier transport. They reported a current increase by 3 orders of magnitude for a multilayer with 3 nm Si layers between 3 nm SiO_2 barriers. In a further study, Berghoff et al. [72] introduced the concept of partially conductive SiO_x barriers instead of SiO_2 between the Si quantum well layers. He reported a current increase by 10 orders of magnitude compared to the SiO_2 barrier for a multilayer sample with 2 nm Si wells sandwiched between 3 nm SiO_x barriers [72]. However, the current increase was accompanied with a loss of quantum confinement. By comparison of the PL peaks of the multilayer and a bulk Si sample, a quantum confinement of 0.06 eV was evidenced at 9 K.

In conclusion, electrical transport through Si NCs embedded in a SiO_2 matrix has proven to be very poor. A possibility to render a Si NC solar cell absorber possible are ultra-thin SiO_2 or SiO_x barrier layers that assure growth confinement while enabling electrical conduction.

4.5   Chapter summary

Quantum confinement in Si NCs embedded in a SiO_2 matrix has been investigated with optical methods. For this means, Si NCs with a narrow size distribution were prepared by the superlattice approach on quartz glass substrates. The absorption spectra were

analyzed with spectrophotometric measurements and photoluminescence spectroscopy was employed to probe the spontaneous emission. A size-dependent blue shift of the absorption onset and the photoluminescence peak position was demonstrated, in agreement with QC predicted by theory. The luminescence or absorption from sub-band gap states was found to be below the detection limit.

According to the optical absorption and photoluminescence spectra, Si NCs in SiO_2 exhibit excellent optical properties to be implemented as the absorber in a high-band gap solar cell. In order to show not only the high optical band gap, but also the possibility for a high photovoltage, the quasi-Fermi level splitting in the material was examined.

For this means, calibrated photoluminescence and absorption spectra were recorded and modeled with the generalized Planck law of radiation. The application of the generalized Planck law yielded charge carrier temperatures in the Si NC ensemble around 500 K and quasi-Fermi level splittings of about 1.3 eV. It was pointed out that the generalized Planck law should be valid provided the Si NC interaction is sufficiently strong for a chemical equilibrium of each charge carrier type. However, if contrariwise the interaction is too weak, the system has to be considered as an ensemble of single Si NCs, whose properties are merely a superposition of single NC properties rendered by the size distribution. In this case the generalized Planck law would not be valid.

As a sample temperature rise of 200 K could be excluded, the fact that the experimental spectra were not in agreement with the theory at a charge carrier temperature of 300 K led to the conclusion that the generalized Planck law is not valid for the Si NCs under investigation. Therefore, wave function coupling in the Si NC network appears to be much weaker than assumed at the outset of the project. This interpretation is also supported by recent theoretical work [45, 73] and comparison to experimental results [67] which state that for NC separations larger than 0.2 nm [73] the NC-NC interaction is not sufficient for miniband formation and that the optical spectra are a superposition reflecting the Si NC size distribution.

The literature on the electrical properties of Si NC in SiO_2 was briefly reviewed in order to assess the feasibility of a SiO_2/Si NC solar cell at the present stage. The electrical properties are essentially determined by direct or Fowler-Nordheim tunneling through the SiO_2 barriers. However, attempts have already been made to exploit the quantum confinement beyond the multilayer approach. With the use of SiO_x barriers, Berghoff *et al.* [72] could show a current increased by a factor of 10^{10} while not completely losing the quantum confinement.

5 Silicon nanocrystals in SiC

This chapter discusses the development of Si NCs embedded in a SiC matrix. The basic properties of SiC and the preparation of amorphous SiC precursor films by PECVD are introduced. The composition of the amorphous precursor films and their structural properties are analyzed. Previous studies on the structural properties of solid-phase crystallized SiC multilayers are briefly reviewed. Based on these previous results, an experiment is presented with the scope of further optimizing the formation of Si NCs in SiC and systematically characterizing the electrical and luminescent properties. Finally, the electrical properties are related to the SiC multilayer structure and it is shown that the electrical properties are determined by the overall Si content and the annealing temperature. Some of the results presented in this chapter formed part of the Diploma thesis of Anke Witzky [74]. The foregoing results contained in the Diploma thesis of Rena Gradmann [75] and published by Gradmann et al. [76] also contributed to the general comprehension.

5.1 Introduction

Research on porous Si and Si NCs in SiO_2 has largely been motivated by the prospect of light-emitting Si. However, the scanty electrical transport through Si NC networks in SiO_2 has triggered the search for alternative, preferably conductive, host matrices for Si NCs to be used in high-band gap solar cells. One candidate is silicon carbide, as it combines many advantageous properties compared to silicon dioxide. Silicon carbide occurs in many polytypes, which differ by their crystal structures and therefore also by their electronic properties. The SiC polytypes exhibit band gap values between 2.39 eV (3C-SiC) and 3.33 eV (2H-SiC) at 2K [77]. Silicon carbide exhibits considerable room temperature conductivity and it can be doped. Due to the lower band gap, the band offsets towards silicon are much smaller than for a SiO_2 host matrix. The most prominent SiC polytypes are 3C, 6H and 4H. The polytype of the SiC used in this thesis was determined to be 3C by Künle *et al*. [78]. 3C-SiC is the only cubic SiC polytype and is also referred to as β-SiC in the literature. The crystal structure (zinc blende) of 3C-SiC is shown in Fig. 5.1. The Si crystal structure is easily derived from the 3C-SiC be replacing the C atoms with Si atoms. The basic properties of 3C-SiC are summarized and compared to silicon in Tab. 5.1.
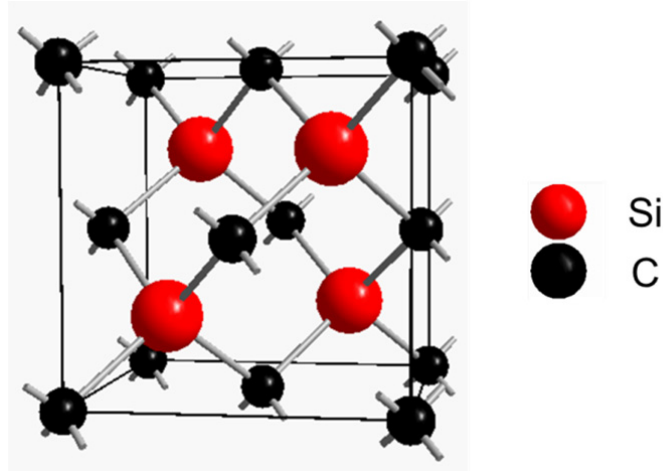
Fig. 5.1: Unit cell of the 3C-SiC crystal (taken from [79]).

Tab. 5.1: Basic properties of crystalline Si [42] and the crystalline silicon carbide polytype 3C-SiC ([77] with values for the band gap, mobility and ionization energies from [80]) at 300 K.

Quantity	Si	3C-SiC
Space group	$Fd\overline{3}m$	$F\overline{4}3m$
Lattice constant (Å)	5.43102	4.3596
Number of atoms in unit cell	8	8
Atoms/cm^3 (cm^{-3})	5.02×10^{22}	4.83×10^{22} (Si and C each)
Density (gcm^{-3})	2.329	3.166
Linear thermal expansion coefficient (°C^{-1})	2.59×10^{-6}	4.8×10^{-6}
Thermal conductivity (Wcm^{-1}K^{-1})	1.31	3.2
Band gap (eV)	1.12	2.3
Refractive index	3.42	2.65
Mobility (cm^{2}V^{-1}s^{-1})	1450 (electrons)	750 (electrons)
	505 (holes)	40 (holes)
Impurity ionization energy (meV)	45 (B, p-type)	50 (N, n-type)
Impurity ionization energy (meV)	45 (P, n-type)	270 (Al, p-type)

The development of Si NC in a SiC host matrix was mainly guided by the analogy to Si NC in SiO_2. A multilayer of alternating stoichiometric and silicon-rich layers is deposited and then annealed to provoke Si crystallization. In analogy to the SiO_2/Si NC system, the stoichiometric barrier layers act as diffusion barriers and restrict crystallite growth.

Depending on the annealing conditions, both the SiC matrix and the Si excess are still partly amorphous. Within the framework of this thesis, the notation "SiC" refers to silicon carbide in a general sense without specifying its structure or composition. For a distinction between extended crystals, nanocrystals and amorphous phases the terms c-SiC, SiC NCs and a-SiC are applied. Subscripts are used in "Si_xC_{1-x}" to explicitly indicate a variable or non-stoichiometric composition. According to this terminology, SiC/Si NC refers to the material consisting of a partially crystalline SiC matrix with embedded Si nanocrystals.

5.2 Preparation of a-Si_xC_{1-x} by PECVD

Amorphous silicon carbide belongs to the ample family of amorphous silicon (a-Si) alloys. After strong research interest in amorphous semiconductors in the 1950s and 1960s [81], amorphous silicon in its common hydride form (a-Si:H) was first prepared by Chittick *et al*. [82] in the late 1960s. Research on hydrogenated amorphous silicon carbide (a-Si_xC_{1-x}:H) began roughly a decade later [83] [84]. Hydrogen plays a key role for the deposition and the electronic properties of a-Si_x:H and a-Si_xC_{1-x}:H. Common deposition techniques are sputtering and plasma enhanced chemical vapor deposition (PECVD). PECVD is superior to sputtering for the preparation of very thin films with high electronic quality because lower deposition rates and a better film homogeneity can be realized. PECVD refers to plasma decomposition of the precursor molecules and subsequent deposition from the plasma phase on a substrate. The most common PECVD reactor type, sketched in Fig. 5.2 (a), is composed of two parallel electrodes between which the plasma is confined. The power is capacitively coupled to the plasma. The industrially available
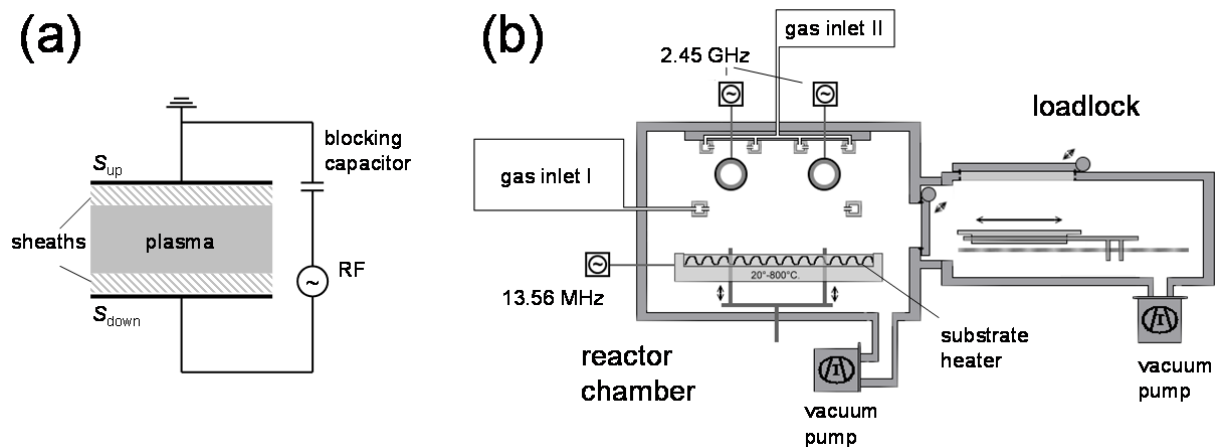

Fig. 5.2: *(a) Principle of a parallel plate PECVD reactor (adapted from [85]). (b) Scheme of the batch type reactor AK400M from Roth&Rau used to fabricate all samples discussed in this chapter (draft from Roth&Rau company).*

radio frequency (RF) 13.56 MHz is very commonly found for parallel plate reactors. Characteristic for RF capacitive discharges are the plasma sheaths that evolve next to the electrodes. As a consequence of their mass inertia, the ions within the plasma cannot follow the RF electric field. But as the electrons alternate with the electric field between the electrodes, some are collected by the latter resulting in an electron depleted region next to the electrodes. In conjunction with a blocking capacitor, this leads to a time averaged electric field between the plasma and the electrodes. The time-averaged electric field can be used to accelerate the ions to the substrate (sputtering).

The amorphous precursor layers for all samples discussed in this chapter were prepared in an AK400M PECVD reactor from the company Roth&Rau. Precursor refers to the film in the as deposited state, before any annealing treatment is carried out. The reactor is sketched in Fig. 5.2 (b). It features a microwave and a RF plasma source. Within the framework of this thesis, exclusively the RF plasma source was used. The samples are located on a graphite plate to which the RF power is coupled. The counter electrode is formed by the reactor walls on ground potential. The temperature of the substrate plate can be controlled between 20°C and 800°C. The relation between the set plate temperature and the real sample temperature had been determined in previous works [85] to be

$$T_{\text{real}} = 0.52 \times T_{\text{set}}(°C) + 67°C \qquad (5.1)$$

at the process pressure used in this work (0.3 mbar). The real temperature calculated according to this calibration is used hereinafter. As each deposition also coats the reactor walls, the reactor has to be cleaned in regular intervals. At the time of the material investigation discussed in this chapter, the reactor was cleaned mechanically. A back etch process was developed at a later stage, enabling an excellent reactor quality without the need to open the chamber. After cleaning, the reactor was purged with N_2 and evacuated repeatedly and then conditioned with the process for stoichiometric SiC (see Tab. 5.2 below). The reactor quality was assessed with FZ c-Si wafers as lifetime samples. For the lifetime samples, the a-Si_xC_{1-x} surface passivation and heterojunction layer (see section 7.2.1) was deposited on both sides of the wafers. As the charge carrier lifetime in the wafer is very sensitive to an imperfectly passivated surface, this procedure provides a readily available reactor quality control method.

The deposition processes employed in this work had been developed by Rothfelder [86] and Künle [79]. The processes were optimized for homogeneous and compact (i.e. no columnar, grainy or porous) film growth, spatial homogeneity and a low depositon rate. All processes are done at 65 W RF power, 0.3 mbar pressure, and a substrate temperature of

280°C. Silane (SiH_4), methane (CH_4) and hydrogen (H_2) were used as precursor gases. The hydrogen flow was 100 sccm throughout this work, and the layer composition was controlled by varying the silane and methane gas flows. A summary over all gas flows and the resulting stoichiometry is given in Tab. 5.2.

Prior to every deposition series, the reactor chamber was conditioned with the deposition process to be used afterwards and the reactor quality was assessed with FZ c-Si lifetime samples as described above. As soon as a good lifetime (>1 ms) was reached, the growth rates of the single processes were measured with trial depositions on FZ c-Si substrates. If a deposition series was continued on the following day, the entire procedure was repeated. The spatial homogeneity of the deposition rate was characterized for the different processes in by Rothfelder [86]. Only the central region of the reactor was used, providing a maximum variation of the deposition rate of 5%.

Tab. 5.2: Gas flows and resulting a-Si_xC_{1-x}:H film composition determined by RBS. The films were deposited with 65 W RF power, 0.3 mbar pressure, and 280°C substrate temperature.

Gas Flow	Silicon content
[SiH_4 / CH_4 / H_2]	x
(sccm)	(%)
[10 / 10 / 100]	77
[7 / 15 / 100]	67
[7 / 20 / 100]	63
[7 / 45 / 100]	54
[7 / 60 / 100]	51
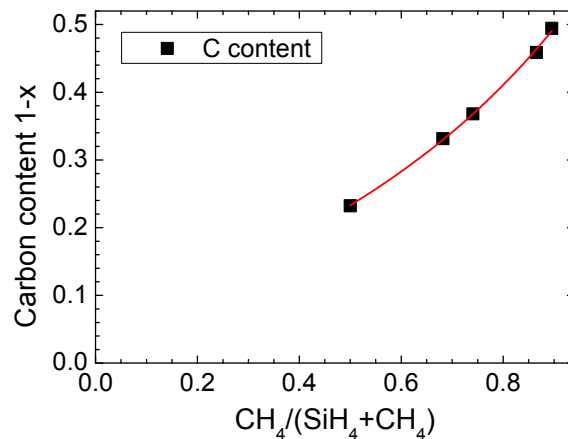
Fig. 5.3: Carbon content of a-Si_xC_{1-x} films as a function of gas phase composition $CH_4/(SiH_4+CH_4)$ for the processes in Tab. 5.2. The line is just a guide to the eye.

5.3 Compositional analysis with Rutherford backscattering spectrometry

A powerful tool to measure the chemical composition is rutherford backscattering spectrometry (RBS) as described in section 13.2.8. The heavier the target atoms, the higher is the energy of the backscattered ions. Furthermore, the electronic stopping of the projectile ions implies an additional backscatter energy loss. This leads to a continuous large background signal for energies less than the substrate loss energy. The RBS spectrum

of a SiC thin film on a Si substrate would therefore consist only of a small peak due to the C atoms on top of a large background signal due to the Si atoms in the film and the Si substrate. A more accurate determination of the composition requires an appropriate sample setup. The composition of the a-SiC films was determined using a carbon substrate with a Ge stopping layer on which the SiC film was deposited. An exemplary RBS spectrum is shown in Fig. 5.4. The substrate background is shifted towards lower energies (<300 keV) because of the Ge stopping layer and is thus separated from the peak of the C atoms in the SiC films which occurs around 400 keV. The Si peak appears at 850 keV and is well separated from the Ge peak of the stopping layer at 1100 keV. Thus, the RBS spectrum in Fig. 5.4 demonstrates that the sample setup is eligible for an accurate determination of the SiC film composition. The samples were prepared by magnetron sputtering of a 150 nm thick Ge film on a glassy carbon substrate (SIGRADUR®). Subsequently, the a-SiC film was prepared by PECVD as described in setion 5.2. The gas flows are listed in Tab. 5.2 together with the results. Because Ge forms a native oxide on the surface upon air exposure, a backscatter peak due to oxygen ions appears between 400 keV and 450 keV in the spectrum in Fig. 5.4 and is superposed with the C peak. The C and Si peaks are shown in detail in Fig. 5.5. The spectra demonstrate very clearly the increasing C content and decreasing Si content as the gas flows are changed from 10 SiH_4, 10 sccm CH_4 and 100 sccm H_2 to 7 sccm SiH_4, 60 sccm CH_4 and 100 sccm H_2. A detailed data analysis was done in two steps. In a first step, a reference sample consisting of the Ge film on the glassy carbon substrate was measured and simulated to determine the exact Ge and Ge oxide thicknesses. In a second step, the a-SiC spectra were simulated accounting for the Ge and
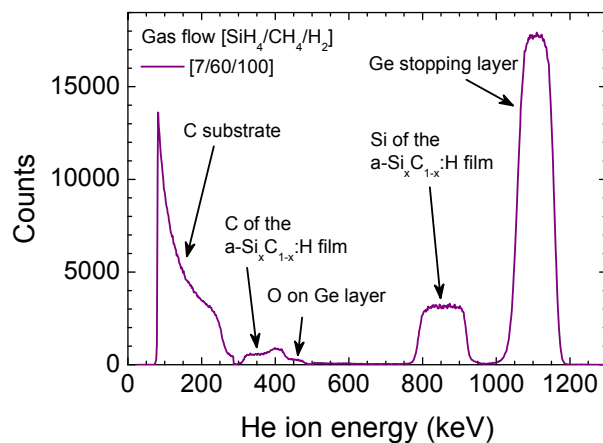
Fig. 5.4: Rutherford backscatter spectrum from a sample consisting of a glassy carbon substrate, a 150 nm Ge stopping layer and the a-Si$_x$C$_{1-x}$:H film under investigation.

Ge oxide previously determined. The simulations were performed with the computer code SIMNRA [87]. The results are shown in Tab. 5.2. It is noted that the results are in good agreement with the values reported in the review by Bullot *et al.* [84]. According to the RBS results, the a-Si$_x$C$_{1-x}$:H composition can be tuned between x=0.77 and x=0.51 by changing the gas flows from SiH$_4$=10 sccm, CH$_4$=10 sccm, to SiH$_4$=7 sccm, CH$_4$=60 sccm (H$_2$=100 sccm for both). The error on the film composition is estimated to be 1%. The results are rounded to %. As the film prepared with SiH$_4$=7 sccm, CH$_4$=60 sccm, H$_2$=100 sccm has a stoichiometric composition within the error, the layer is called stoichiometric hereinafter even if the x-value is rounded to x=0.51.
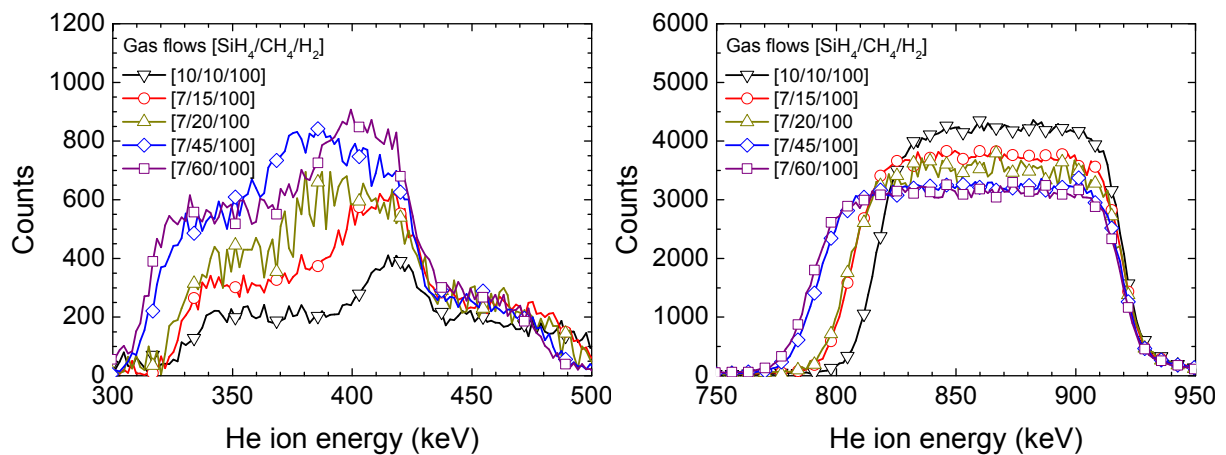
Fig. 5.5: Details of the RBS spectra around the backscatter energy peaks due to the C atoms (left) and the Si atoms(right) in the a-SiC film. The C peak is superposed with a peak due to O from the Ge native oxide.

5.4   Infrared absorption spectra

The bond of Si with C or with N and H has characteristic vibrational absorption modes in the infrared (IR) spectral range. As the vibrational modes depend on the bond network structure and therefore change upon thermal annealing, infrared absorption spectroscopy yields valuable information on the structural transformations. In the framework of this thesis, spectra in the mid-IR between 400 cm^{-1} and 4000 cm^{-1} were used as many Si-related bonds and bonds of atoms in Si-based dielectrics exhibit vibrational frequencies in this spectral range. All FTIR spectra were measured on samples with a shiny etched p-type floatzone (FZ) c-Si wafer as substrate. The substrate wafers were 250 μm thick, doped with boron and had a resistivity of 10 Ωcm. A FZ substrate was chosen because of its high purity, which reduces artefacts from non-uniform absorption in the substrate.

A detailed analysis of FTIR spectra requires careful data preprocessing and an adequate assignment of the various absorption peaks to the particular vibration modes. The reference subtraction and baseline correction is presented in section 13.2.2. This section discusses the existing literature to assign the spectral features to the particular vibrational modes.

The FTIR spectra of a-Si:H and its alloys have been investigated intensively since the early stages of research in these materials. Fundamental studies on the Si-H vibrational modes in a-Si:H were done by Brodsky *et al*. [88] and Lucovsky *et al*. [89]. Brodsky *et al*. [88] identified the peak at 640 cm^{-1} with the Si-H wagging vibration, a doublet feature around 845 cm^{-1} and 890 cm^{-1} with Si-H$_2$ bending vibrations and the peak at 2000 cm^{-1} with Si-H and Si-H$_2$ stretching vibrations. The authors established a relation between the integrated absorption and the concentration of the respective bonds for the Si-H$_2$ bending modes and the Si-H stretching mode. The nature of the Si-H$_2$ bending modes and its relation to the Si-H stretching modes was resolved by Lucovsky *et al*. [89]. Wieder *et al*. [90] investigated carbon incorporation, identified additional carbon-related peaks and pointed out that a frequency shift of the Si-H bonds occurs. He reported in agreement with Catherine *et al*. [91] that the Si-H peak at 2000 cm^{-1} shifts to 2090 cm^{-1} if the Si atom is back bonded to a C atom. Furthermore, he related the broad peak around 2900 cm^{-1} to several C-H$_n$ stretching modes.

The FTIR spectra of SiC multilayers before and after thermal annealing at 900 °C are shown in Fig. 5.6 (left). Before thermal annealing, peaks between 500 cm^{-1} and 1100 cm^{-1}, around 2100 cm^{-1} as well as a broad feature around 2900 cm^{-1} and several small peaks at 1240 cm^{-1}, 1340 cm^{-1} and 1396 cm^{-1} are seen. According to the literature described above, the peak at 2100 cm^{-1} is identified with the Si-H stretching vibration, the peak around 2900 cm^{-1} with C-H$_n$ stretching modes and the small peaks at 1240 cm^{-1}, 1340 cm^{-1} and 1396 cm^{-1} are related to Si-CH$_3$ (1240 cm^{-1}) and antisymmetric SiH$_3$-CH$_3$ bending modes [90] [92].

The most prominent feature in the FTIR spectra of a-Si$_x$C$_{1-x}$:H is the broad peak between 500 cm^{-1} and 1100 cm^{-1}. It consists of the above mentioned Si-H wagging mode around 640 cm^{-1}, the Si-H$_2$ bending modes at 900 cm^{-1}, the -CH$_3$ wagging mode at 1000 cm^{-1} and the Si-C stretching mode at 780 cm^{-1}. The assignment of the latter peak is not straight forward and contradicting results have been discussed in the literature. Several authors reported a Si-C stretching mode at 670 cm^{-1} [90]
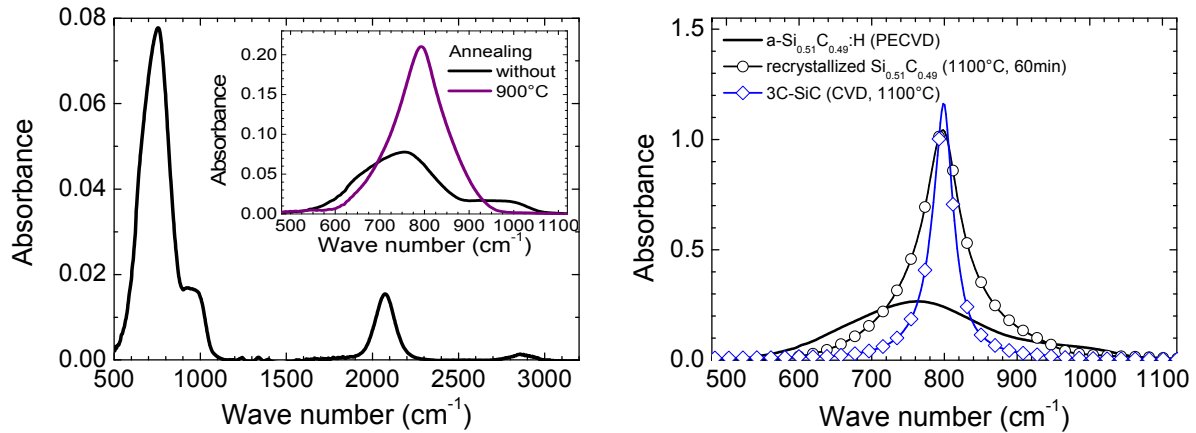
Fig. 5.6: *(Left) FTIR spectrum of a SiC/Si$_x$C$_{1-x}$ multilayer before annealing and in comparison to the spectrum of an annealed film (inset). (Right) FTIR spectra of nearly stoichiometric SiC films prepared by PECVD (black circles) and 3C-SiC (blue diamonds). The film prepared by PECVD has a composition of x=0.51 and was crystallized by thermal annealing at 1100°C for 60 min. The spectrum of the amorphous (as deposited) film is shown for comparison. The 3C-SiC film was prepared by chemical vapor deposition at 1100°C.*

or 720 cm^{-1} [93] [85] and related the peak at 780 cm^{-1} to the Si-CH$_3$ stretching vibration [90] [93] [85]. However, other authors [94] [95] [91] came to the conclusion that the peak at 780 cm^{-1} is indeed to be ascribed to the Si-C stretching mode as the peak does not vanish upon thermal annealing and thus hydrogen effusion. Finally, McKenzie *et al.* [96] compared the occurrences of the peaks between 700 cm^{-1} and 800 cm^{-1} in his samples with results from Borders *et al.* [97] and pointed out that the frequency shift from 720 cm^{-1} to 780 cm^{-1} could be explained with a compositional effect. He referred to SiC prepared by C ion implantation in Si [97], and the statement is also supported by comparing the results of Suwito [85] with the results of Künle *et al.* [79] and the present work. Suwito [85] employed a-Si$_x$C$_{1-x}$:H films with x=0.95 using the same deposition process as used in the present work apart from changed gas flows and reported the Si-C stretching mode to occur at 720 cm^{-1}.

For the samples analyzed here the Si-C peak is found at 760 cm^{-1} to 780 cm^{-1} depending on the annealing condition, thus following the trends previously reported by Beyer *et al.* [94] and Rovira *et al.* [95]. Upon annealing, the peak shifts towards 800 cm^{-1} as also reported in the literature [98]. For the experiment carried out here, the amorphous spectra are analyzed to understand the bonding microstructure of the amorphous precursor layers. The relevant information, however, are deduced from the spectra of annealed and partially crystallized films. Therefore, the spectra of the a-Si$_{0.51}$C$_{0.49}$:H film before annealing

and after solid phase crystallization are shown in Fig. 5.6 in comparison to the spectrum of crystalline 3C-SiC as a reference. The 3C-SiC film was prepared by chemical vapor deposition (CVD) at 1100°C as reported in [99]. The peak positions of the CVD and the solid phase crystallized film are in very good agreement with the results of Spitzer *et al*. [100]. These authors measured and calculated the IR transmission and reflection of cubic crystalline SiC and reported a transmission minimum at 790 cm^{-1}. As the trends found here for the amorphous films agree with the results of Catherine *et al*. [91], Beyer *et al*. [94] and Rovira *et al*. [95], and the spectrum of the recrystallized film agrees with the literature on crystalline SiC, the peak at 780 cm^{-1} is attributed the Si-C stretching vibration in the framework of this thesis. It is denoted Si-C(s) hereinafter. The hydrogen-related peaks are not analyzed in detail in the further course of this work because they are not present in the annealed films. However, their classification is important for a fundamental understanding of the spectra. The peak assignments used in the framework of this thesis are summarized in Tab. 5.3. Fig. 5.7 (left) shows the 500-1100 cm^{-1} spectral region and the decomposition of the measured spectrum into the different modes. A good fit is obtained with 4 Gaussians at 654 cm^{-1} (Si-H wagging), 760 cm^{-1} (Si-C stretching), 914.5 cm^{-1} (Si-H$_2$ bending) and 989 cm^{-1} (-CH$_3$ wagging), cf. Tab. 5.3. In the spectra of the annealed film, shown in Fig. 5.7 (right), the hydrogen-related peaks are not present any more. Furthermore, the peak features a larger amplitude, is found at higher wave number, and exhibits Lorentzian shape.

Tab. 5.3: FTIR peaks observed in this work and their assignment to vibrational modes.

Wave number (cm^{-1})	Mode	References
640	Si-H wagging (w)	[88], [89]
760-780	Si-C stretching (s)	[91], [94], [95]
900	Si-H$_2$ bending (b)	[90]
1000	-CH$_3$ wagging (w)	[90], [91], [94], [95]
1075	Si-O	[101]
2100	Si-H$_n$, n=1, 2, 3, stretching (s)	[90]
2900	C-H$_n$, n=1, 2, 3, stretching (s)	[90]
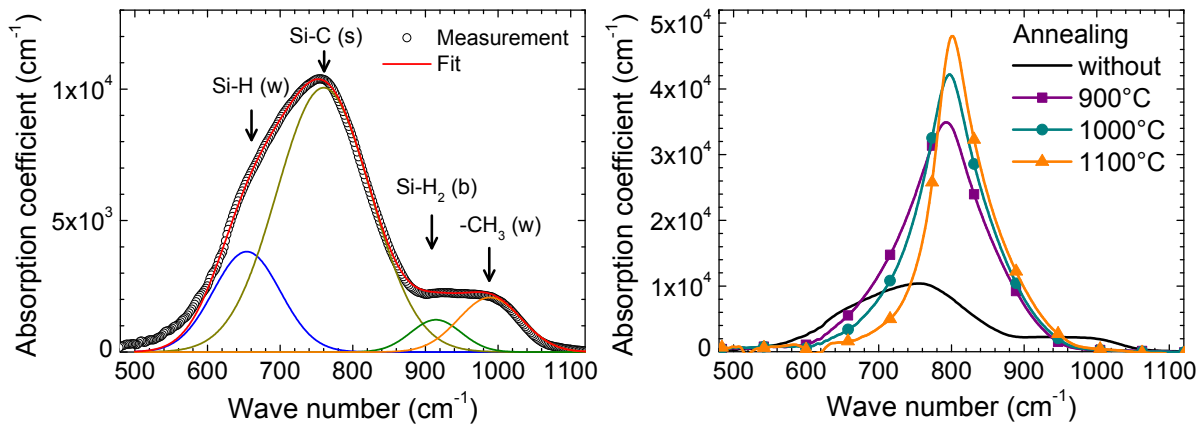
Fig. 5.7: (Left) Detail of the FTIR absorption spectrum shown in Fig. 5.6 and assignment of the vibration modes in the region 500 cm^{-1} to 1100 cm^{-1}. The figures were adapted from [74].

The FTIR peaks have Gaussian shape in the amorphous state due to the random distribution of bond lengths and angles. As the film is annealed, hydrogen effuses, the amorphous network reorganizes and more Si-C bonds form. The transformation of the network to the crystalline state is accompanied by a transition to a Lorentzian peak shape and a shift of the peak to higher wave numbers. As long as the material is only partially crystalline, the peak is a convolution of a Gaussian peak, due to the amorphous fraction, and a Lorentzian peak arising from the already crystallized volume (Voigt profile). For an easier fit procedure, the peak was modeled as a linear superposition of a Gaussian and a Lorentzian peak. The shift to higher wavenumbers is due to the higher force constants in the crystalline lattice and thus stiffer environment [102, 103] than in the amorphous, randomly bonded network. Oxygen-related modes are not detected, neither before nor after thermal annealing. It is noted however, that a small Si-O peak occurs in cases when oxygen leaks in the oven [104].

5.5 Review of solid phase crystallization in SiC/Si$_x$C$_{1-x}$ multilayers

The structural transformations of Si$_x$C$_{1-x}$ single layers as well as Si$_x$C$_{1-x}$ multilayers during thermal annealing were reported by Song *et al.* [105, 106], Künle *et al.* [78, 79, 107], Kurokawa *et al.* [108], Lopez-Vidrier *et al.* [109] and Summonte *et al.* [110, 111]. The multilayer system developed by Künle was further analyzed in the framework of this thesis and therefore constitutes an important reference. The following summary of the material development is guided by the results reported by Künle [79] for the SiC/Si$_x$C$_{1-x}$ multilayer system with complementing references to other authors. In general, good agreement is

found between the results of different authors. However, it has to be borne in mind that the deposition technique determines the structure of the amorphous precursor layer and thus also the crystallization properties. Certain deposition regimes produce columnar growth resulting in void-rich films as reported e.g. in the early works of Künle and co-workers [78, 112]. Hydrogen dilution of the precursor gases plays a vital role for obtaining homogeneous films. PECVD permits to grow films with a low deposition rate and excellent homogeneity and was therefore chosen to prepare all samples discussed in this thesis. The development of the Si_xC_{1-x} deposition processes is documented in detail in [86].

Amorphous Si_xC_{1-x} films deposited by PECVD contain a large hydrogen volume fraction as discussed before. The effusion of hydrogen upon thermal annealing leads to film shrinkage, which is around 30% [79] for the films investigated within the framework of this thesis. Hydrogen effusion depends on the film compositon and bond structure and occurs approximately between 200°C and 800°C [85, 94]. As hydrogen effuses, the amorphous network rearranges and Si crystallites form at annealing temperatures between 700°C and 900°C in Si_xC_{1-x} single layers [107]. This is 200 °C higher than in thick a-Si films, which are transformed into the crystalline phase already as the temperature exceeds 500°C [113]. In SiC/Si_xC_{1-x} multilayers, Si crystallizes at higher temperature than in Si_xC_{1-x} single layers and experimentally observed values are around 800°C-900°C [106, 114].

Summonte *et al*. reported that a higher Si content in the Si-rich layer [115] as well as a higher total Si volume concentration [111] lead to a larger Si crystalline volume fraction [115]. It can be inferred that the crystallization temperature decreases for a higher Si content, but this relation has not yet been shown explicitly.

The nanostructure of annealed SiC/Si_xC_{1-x} multilayers was characterized by energy-filtered transmission electron microscope (EFTEM) by Künle [79]. Fig. 5.8 shows an EFTEM ratio image of a multilayer in the as-deposited state, after annealing at 900°C and after annealing at 1000°C. The samples were annealed in a conventional tube furnace for 30 min in N_2 atmosphere. The EFTEM ratio image uses the difference in the plasmon energy loss peaks of Si (16.7 eV [116] and SiC (22.6 eV [117]). Two images, recorded at the plasmon loss peaks of Si and SiC respectively, are divided by each other. In the resulting ratio image, the Si appears in bright contrast and the SiC in dark contrast.

Intensity profiles of the EFTEM ratio images are shown as inserts (black graph). The multilayer structure is clearly visible before annealing (Fig. 5.8 (a)) and well preserved after annealing at 900°C for 30 min, though with a more irregular intensity profile. After annealing at 1000°C for 30 min, the substructure is still recognizable but appears grainy

due to the crystallization of the film. Details of the images are shown in Fig. 5.9. After annealing at 1000°C the SiC (dark contrast) appears to have clustered and to be surrounded by Si phases (bright contrast). Thus, the barrier layers were not effective in restricting the growth of Si NCs. Rather, the Si-rich phases joined across the SiC barriers. Therefore, the material depicted in Fig. 5.8 has to be regarded to consist of a Si matrix with embedded SiC NCs, as opposed to the initial objective. Fig. 5.8 (a) also disclosed the multilayer waviness that evolves after a number of bilayer repetitions. For the SiC/Si$_x$C$_{1-x}$ layers discussed here, the waviness prevails over the multilayer after 20 to 30 bilayers.

The polytype was determined to be 3C-SiC by virtue of the radial intensity distribution of electron-diffraction patterns by Künle *et al.* [78]. Furthermore, high-resolution TEM showed the formation of Si crystallites not only within the Si-rich layers, but also at the interfaces to the stoichiometric barrier layers [79]. Künle [79] also used stripe scanning transmission electron microscope (stripeSTEM) electron energy loss spectroscopy (EELS) to resolve the structure of the single nm-thin layers within the multilayer stack and to analyze compositional effects. This study was done on the SiC/Si NC multilayer annealed at 900°C (EFTEM image in Fig. 5.8 (b)).
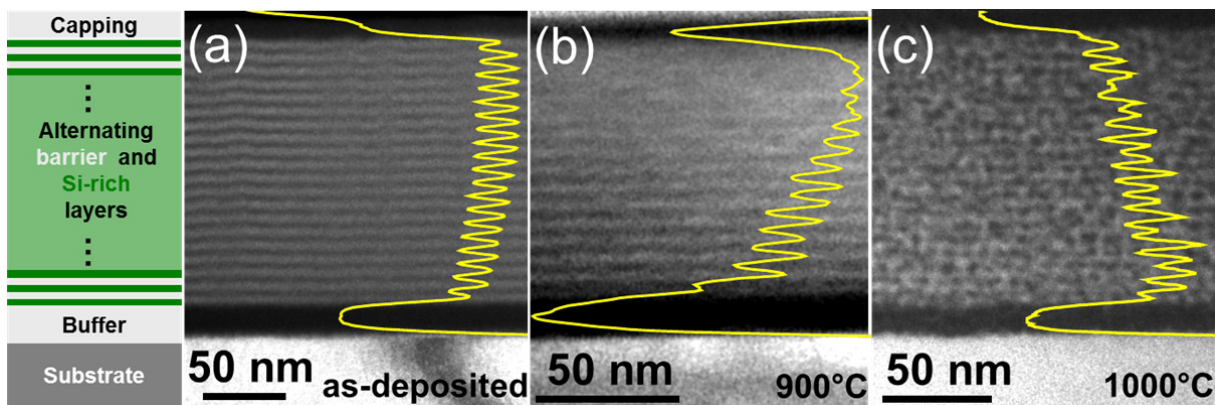
Fig. 5.8: EFTEM ratio image from SiC/Si$_x$C$_{1-x}$ multilayers in (a) the amorphous state and after annealing (b) at 900°C and (c) at 1000°C for 30 min. Si appears in bright and SiC appears in dark contrast here. The graphs are intensity profiles averaged over 50 nm. The TEM images were taken from Künle [79].
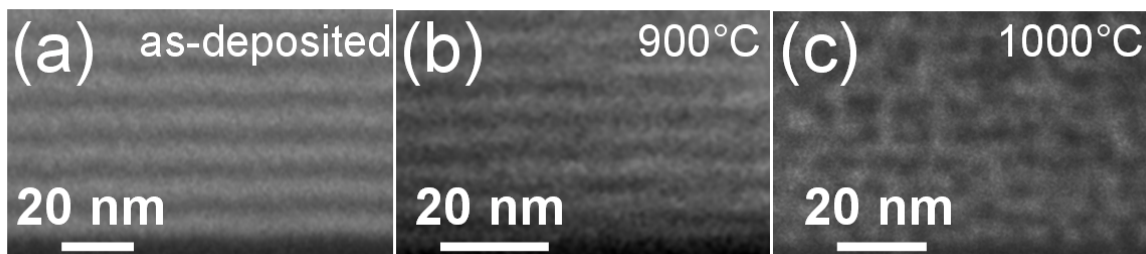
Fig. 5.9: Detail of the images shown in Fig. 5.8. All images were taken from Künle [79].

It had been shown previously that the EELS spectrum of stoichiometric amorphous bulk SiC shifts from 19.9 eV to 22.3 eV upon crystallization [78]. The EELS spectrum peak of annealed bulk Si-rich layers was shown to be around 17.7 eV [78], close to the plasmon energy of bulk Si of 16.8 eV [116]. The multilayer annealed at 900°C showed the following stripeSTEM EELS spectra: The plasmon peak of the $Si_{0.5}C_{0.5}$ buffer layer between the substrate Si wafer and the multilayer stack is detected at 20.5 eV. However, in the $Si_{0.5}C_{0.5}$ barrier layers within the multilayer stack it appears at 18.2 eV. Furthermore, the peak energy shifts within the buffer layer as the distance to the multilayer stack (the first Si-rich layer) decreases. The peak shift is interpreted as a chemical effect, caused by diffusion. During thermal annealing, C diffuses out of the stoichiometric layers into the Si layers, and Si diffuses from the Si-rich layer to the stoichiometric layers. The barrier layers are thus also Si-rich and their EELS spectrum is shifted to smaller energy.

In order to achieve size-controlled NCs exhibiting quantum confinement, the NCs should be growth-confined to the Si-rich layer and be laterally separated. Considering monodisperse hexagonally close packed Si crystals of radius r surrounded by SiC within a layer of thickness 2r results in a total Si concentration of the Si-rich layer of 59.2%. In the previous studies of Song *et al.* [106] and Künle *et al.* [114], Si concentrations of around x=95% were used to achieve the formation of Si NCs. However, no lateral separation of Si NCs within the same layer can be expected for such high Si content. Even though the experiments were designed to show the formation of Si NCs, and to separate Si NC formation from the formation of SiC NCs, almost all works also report the crystallization of SiC. An overview is given in Tab. 5.4, summarizing the multilayer configuration, the Si content of the well and the temperature at which Si and SiC crystallites were observed by

Tab. 5.4: *Comparison of the observation of Si NC and SiC NC formation in previous experiments. The thicknesses of the barrier and the well layer in the multilayer stack are denoted as $d_{Barrier}$ and d_{Well}. Conventional tube furnaces were used for annealing.*

Reference	Anneling conditions	$d_{Barrier}$ / d_{Well} (nm)	Well Si content x (%)	Total Si content (%)	Si NC detection (°C)	SiC NC detection (°C)
Künle [114]	30 min, N_2	3 / 5 (asdep)	95	79	900	900
Song [106]	25 min, N_2	2.5±1 / 5.5±1	96	82	800	900
Song [106]	25 min, N_2	2.5±1 / 5.5±1	90	78	900	900

GIXRD. Crystallization of Si but not SiC was only reported by Song *et al*. [106] for one sample with a very high ($x =$0.96) Si content in the well and a total multilayer Si contentration of $x =$0.82. In summary, the separated formation of Si NCs from SiC crystallization for reasonable Si concentrations has not yet been shown.

The material has to be treated as a mixture of Si and SiC. Depending on the annealing conditions, they are both present in the crystalline as well as the amorphous state. While the multilayer structure is well visible in the as deposited layers and also up to annealing temperatures of 900°C, it deteriorates at higher temperatures.

5.6 Multilayers with silicon-rich barriers

5.6.1 Scope of the experiment and experimental details

It has been pointed out in the previous section that previous studies were successful in demonstrating the formation of Si NCs in SiC under the condition that also the SiC matrix crystallized. This fact rendered a clear phase separation of Si and SiC within a multilayer structure impossible. Furthermore, the simultaneous crystallization of Si and SiC implies a very high SiC/Si grain boundary density. As the crystalline SiC/Si interface has been reported to be very recombination active [118], grain boundaries are expected to be detrimental to the solar cell absorber performance. However, the experiments on Si NC formation in SiC were restricted to a structural characterization and a systematic study of the electrical properties had not yet been done.

In this chapter, an experiment is presented which aims at the separation of Si NC formation from the crystallization of SiC in conjunction with a systematic characterization of the electrical and electro-optical properties. To prevent the C out-diffusion as reported by Künle [79] and to investigate this effect more in detail, the C content of the barrier layers was varied. As this might also affect the crystallization temperature, all samples were annealed at several temperatures while maintaining a constant annealing plateau time of 30 min.

All a-Si$_x$C$_{1-x}$ layers discussed in this chapter were deposited using the processes summarized in Tab. 5.2. Shiny-etched 250 µm thick c-Si FZ (100) wafers were used as substrates for FTIR and GIXRD characterization. For electrical measurements, reflection and transmission measurements, and photoluminescence and Raman spectroscopy, we used quartz glass (SUPRASIL®) substrates. The samples were cleaned in hot HNO$_3$ followed by a HF-dip to remove the surface oxide as described in section 13.3. Prior to the deposition of a-Si$_x$C$_{1-x}$ all quartz glass substrates were pre-annealed to effuse hydroxyl

groups. Multilayers were prepared with a 15 nm barrier as buffer layer to prevent epitaxial growth, followed by 20 bilayers of 4 nm barrier and 6 nm Si-rich carbide, and a 15 nm thick barrier layer as encapsulation. The Si-rich carbide was always prepared with a Si content of x=0.77. For the barrier layers, the Si content was varied in three steps, x=51%, x=54% and x=58%, see Tab. 5.5. After deposition, the samples were annealed in a tube furnace at 900°C, 1000°C and 1100°C for 30 min in N_2 at a pressure of 1050 mbar. Heating and cooling ramps were 10 K/min. Before annealing, the furnace was evacuated to a residual pressure of 3×10^{-6} mbar at 150°C and held for 30 min to desorb surface adsorbates.

After deposition, annealing and measurement of the reflection and transmission spectra, the samples were cleaned in a Piranha solution followed by an dip in 50% HF. They were then treated with a remote hydrogen plasma (RPHP) to re-introduce hydrogen into the SiC/Si NC film for defect passivation. The RPHP treatment was performed at 450°C for 45 min. Afterwards, indium tin oxide (ITO) with a resistivity of 4×10^{-4} Ωcm was sputtered through a shadow mask to define electrical contacts. Immediately before ITO sputtering, the samples were dipped in 1% HF (60 s) to remove the surface native oxide. All electrical and optical measurements except the transmission and reflection spectra were done after the hydrogen treatment. All electrical measurements were performed with the device structure sketched in Fig. 13.3. IV curves were recorded from -1 V to +1 V for six different electrode distances, see section 13.2.1. All IV curves used for further evaluation were linear throughout the entire measurement range. The resistivity was extracted from the total resistance measured as a function of the electrode distances as described in section 13.2.1. Photoconductivity and temperature dependent IV curves were measured using two electrodes with known IV curves and a reference measurement at standard dark conditions was performed immediately before. An Ar+ ion layer was used as light source for photoconductivity measurements and the light intensity was monitored with a

Tab. 5.5: Deposition processes used for the sample discusses in this chapter. The well layer was prepared with x=77% in all samples, see Tab. 5.2 for the process parameters.

Barrier Si content x (%)	Barrier gas flow [SiH_4 / CH_4 / H_2] (sccm)	Well Si content x (%)	Total Si content (%)
51	[7 / 60 / 100]	77	66
54	[7 / 45 / 100]	77	68
58	[7 / 30 / 100]	77	70

reference solar cell at the sample position. The reflectance and the absorption coefficient used in the calculation of the effective mobility lifetime product were calculated from reflection and transmission spectra recorded with a spectrophotometer (section 13.2.3).

5.6.2 Structural analysis

The variation of the structural properties with the nanolayer composition and the annealing temperature was analyzed with gracing incidence X-ray diffraction (GIXRD), Raman spectroscopy and Fourier transform infrared spectroscopy (FTIR).

Fig. 5.10 displays the IR spectral region of the Si-C stretching vibration (Si-C(s), see section 5.4) as a function of the annealing temperature and for varied Si content of the SiC barrier layer. It can be observed that the amplitude of the Si-C(s) mode rises and the peak becomes narrower as the film is annealed at higher temperature. Furthermore, the peak amplitude increases as the barrier contains more carbon. A larger peak amplitude can be explained with more Si-C bonds. Apparently, a composition closer to 50% carbon in the barrier facilitates the formation of Si-C bonds in the film.

The formation of Si and SiC nanocrystals can by monitored by grazing incidence X-ray diffraction (GIXRD). Fig. 5.11 (left) depicts the diffractograms of the sample series of Tab. 5.2. The diffraction peaks at 28.5°, 47.3° and 56.1° stem from reflexes at the Si (111), Si (220) and Si (311) crystal lattice planes [79]. The diffraction peaks at 35.6° and 60°C can be attributed to reflexes from the (111) and (220) lattice planes of 3C-SiC [79]. As some of the Si-related GIXRD peaks are very weak,
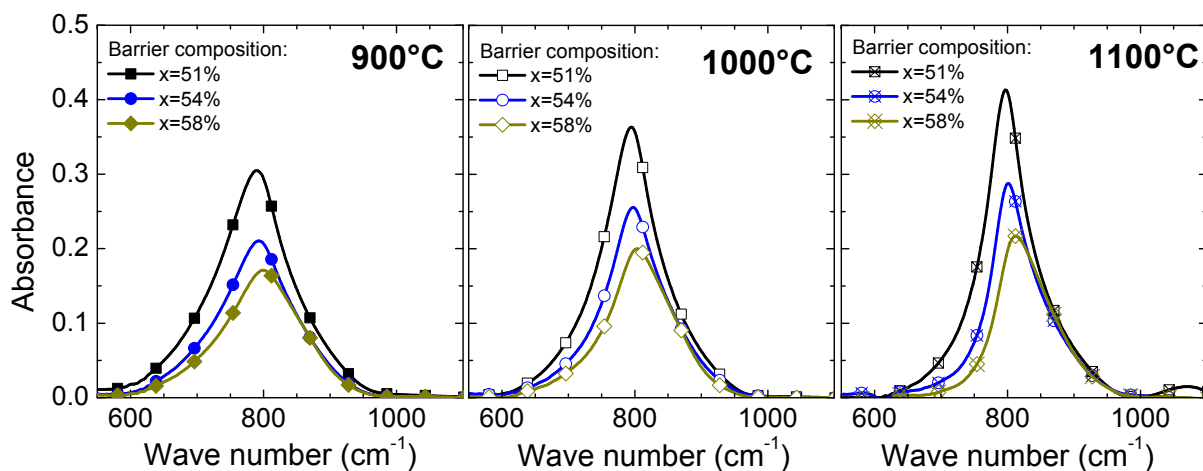
Fig. 5.10: FTIR spectra of the SiC/Si$_x$C$_{1-x}$ multilayers described in Tab. 5.2. The figures were adapted from [74].
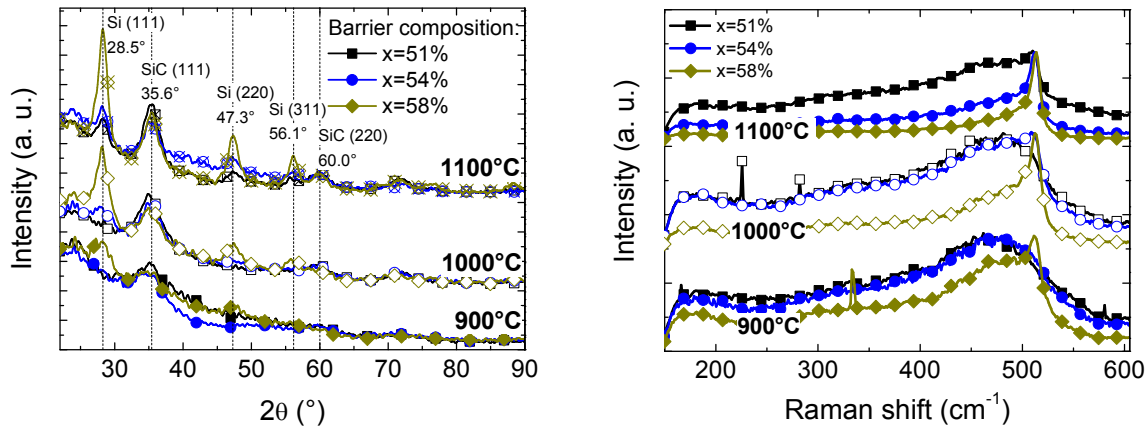
Fig. 5.11: (Left) Grazing incidence X-ray diffractograms and (right) Raman spectra of the sample set described in Tab. 5.2. The figures were adapted from [74].

Raman spectroscopy was used as a complementary tool to investigate Si crystallization. The Raman spectra for the sample series from Tab. 5.2 are depicted in Fig. 5.11 (right). As no peaks related to SiC modes [119] were measured, Fig. 5.11 (right) shows only the spectral region around the Si TO phonon mode. The Raman spectrum of crystalline Si exhibits a narrow peak due to the transversal optical (TO) phonon at 520 cm^{-1} [120]. This mode shifts to lower wave numbers as the crystallite size is reduced and appears as a broad Gaussian peak at 480 cm^{-1} for amorphous Si [121]. Furthermore, amorphous Si exhibits a longitudinal acoustic mode at 300 cm^{-1} and a longitudinal optical mode at 400 cm^{-1} [122, 123]. The Raman spectrum of micro- or nanocrystalline silicon is closely related to the spectrum of single crystalline Si but exhibits the TO phonon peak at smaller wave numbers. Furthermore, a shoulder is usually seen in the low wave number side (around 500 cm^{-1}) of the TO phonon peak and attributed to the defective part of the crystalline network [120, 121]. The spectra shown in Fig. 5.11 (right) were described as a superposition of the mentioned Raman modes as described in section 13.2.6 and the "Raman crystallinity" was calculated from the integrated peak intensities according to Eq. (13.5). The occurrence of the Raman c-Si TO mode and its development with Si content and annealing temperature follows the same trend as the Si (111) GIXRD peak. The structural transformations are discussed in the following with reference to the X-ray diffractograms as GIXRD yields information on both components, Si and SiC. It has to be noted, however, that all conclusions can also be derived from the Raman spectra as long as Si crystallization is concerned.
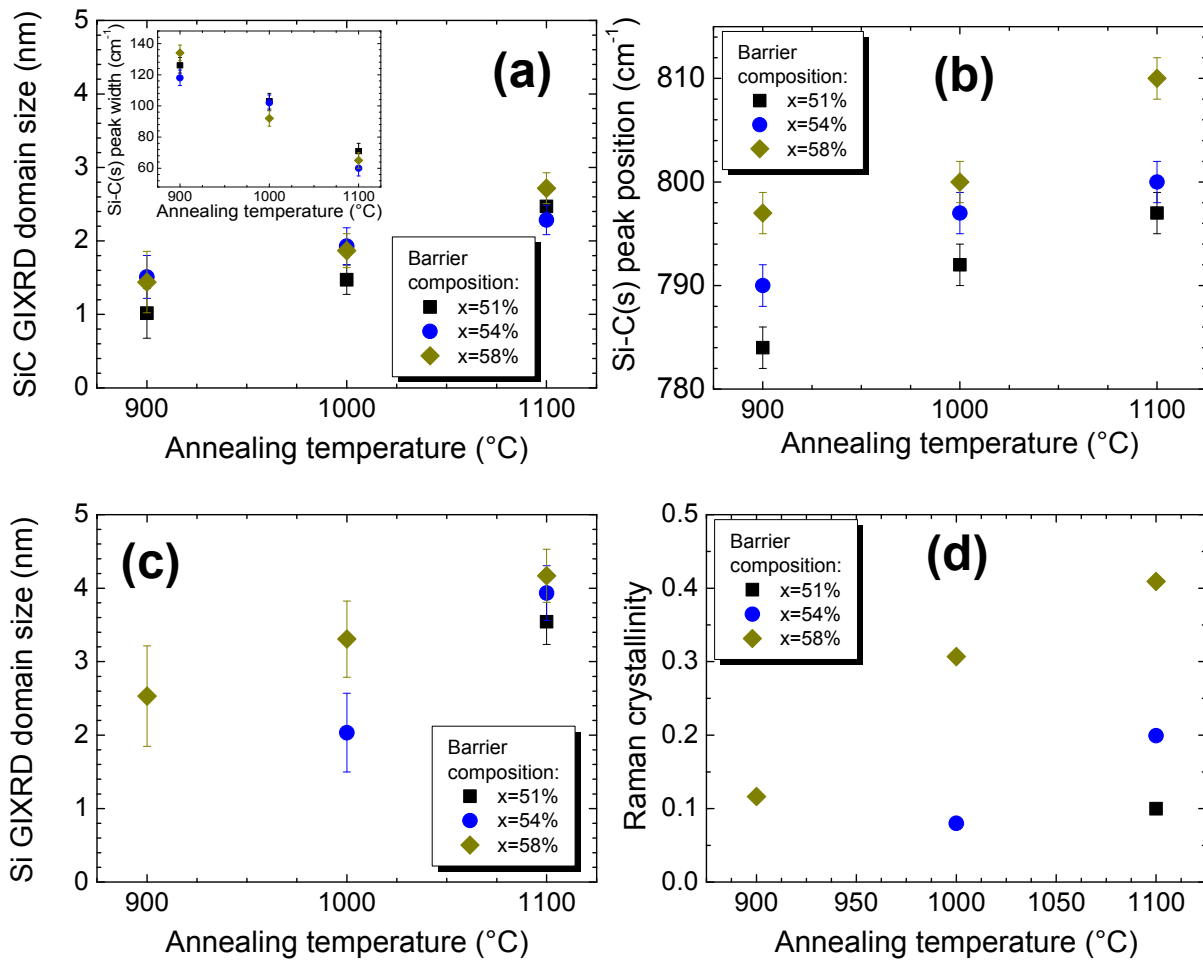
Fig. 5.12: (a) SiC GIXRD crystalline domain sizes and the Si-C(s) peak width (inset), (b) FTIR Si-C(s) peak position, (c) Si GIXRD domain size and (d) Si Raman crystallinity. The GIXRD domain sizes were calculated with the Scherrer formula Eq. (13.6), and the Raman crystallinity was calculated according to Eq. (13.5).

SiC crystallites are found after all annealing treatments for all barrier layer carbon contents (Fig. 5.11 (left)). Distinct evidence for Si crystals, however, is only found in sample 3. Here, the Si (111) peak is already present after annealing at 900°C. In the samples with x=51% and x=54%, only a very small Si peak evolves at higher temperatures. As the GIXRD peak width is determined by the spatial coherence of the diffracted beam, the diffraction peak width is a measure of the grain size. A GIXRD mean crystalline domain size can be calculated by means of the Scherrer formula Eq. (13.6). "Nanocrystal size" or "GIXRD domain size" refers to the GIXRD mean crystalline domain size for the rest of this chapter. Fig. 5.12 depicts the annealing temperature dependence of the Si and SiC crystallite sizes calculated by the Scherrer formula, along with the Raman crystallinity and the spectral width and the position of the FTIR Si-C(s) mode. The GIXRD SiC crystallite size (Fig. 5.12 (a))

clearly depends on the annealing temperature but is only slightly affected by the barrier C content 1-x. A positive correlation between SiC crystallite size and temperature is also confirmed by the decreasing FTIR Si-C(s) peak width (Inset Fig. 5.12 (a)) and the peak position (Fig. 5.12 (b)). The Si-C(s) peak position (Fig. 5.12 (b)), however, exihibts another trend which does not appear in the SiC GIXRD domain size or the Si-C(s) peak width (Fig. 5.12 (a)). The FTIR Si-C(s) peak shifts towards higher wave numbers not only as the annealing temperatures increased, but also for higher Si content. A compositional effect is also clearly visible from the Si GIXRD domain size (Fig. 5.12 (c)) and the Si Raman crystalline volume fraction (Fig. 5.12 (d)). Fig. 5.12 (c) demonstrates that a higher Si content in the barrier fosters Si crystallization by lowering the Si crystallization temperature from 1100°C for x=51% to 900°C for x=58%.

To illustrate the compositional effect, the discussed quantities are replotted in Fig. 5.13 as a function of the Si content. The Si GIXRD crystallite size and also the Raman crystallinity
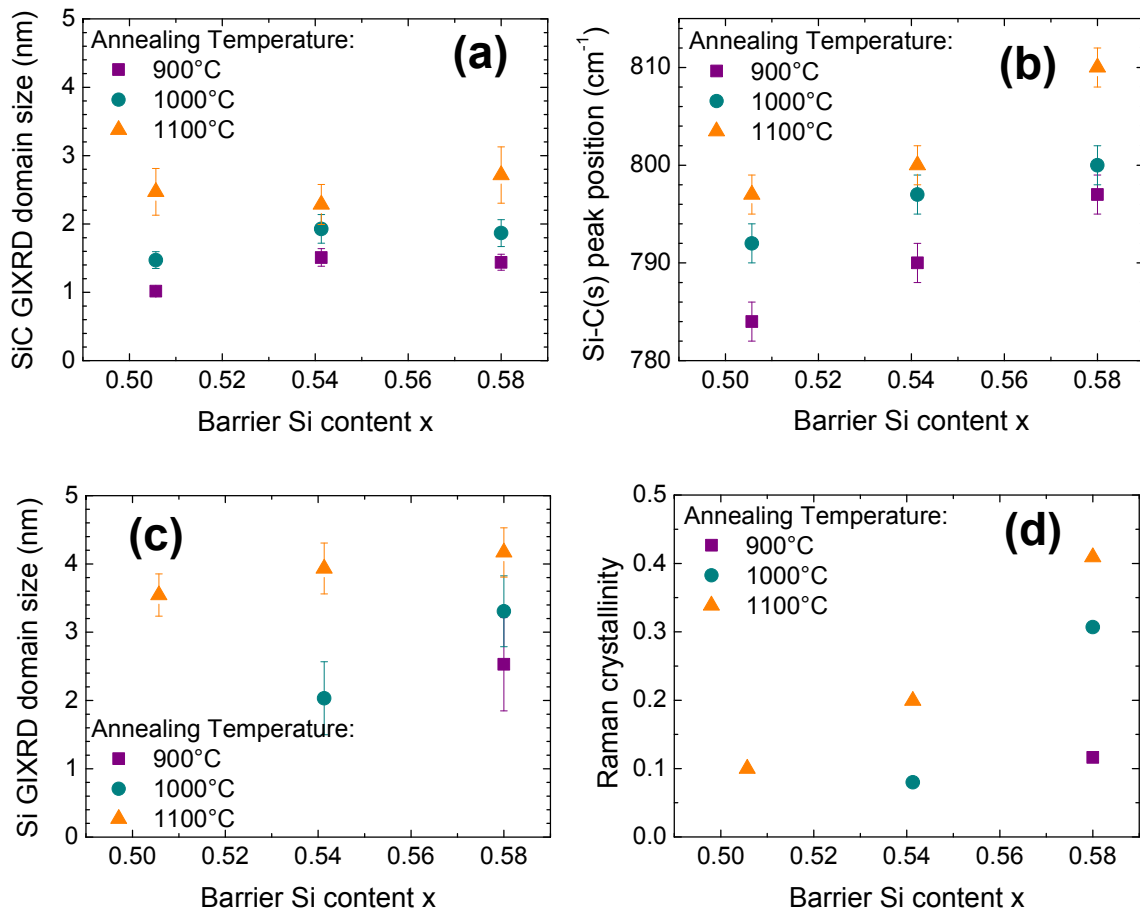
Fig. 5.13: *Compositional dependence of (a) the SiC GIXRD crystalline domain sizes, (b) the FTIR Si-C(s) peak position, (c) the Si GIXRD domain size and (d) the Si Raman crystallinity.*

clearly increase with the Si content, but the SiC GIXRD crystallite size is almost independent of the Si content. It was shown in Fig. 5.10 that more C (less Si) within the well leads to the formation of more Si-C bonds (larger FTIR Si-C(s) amplitude). As apparently the SiC crystallites do not grow larger (Fig. 5.12 (a)), the number of SiC crystallites has to increase as the C content is raised to explain the larger Si-C(s) amplitude. It is noteworthy that even for x=58% in the barrier layer, SiC crystallites form.

A higher Si excess fosters Si crystallization and leads to a higher Si crystalline volume fraction (Fig. 5.13 (c) and Fig. 5.13 (d)). Thus, it would result in a higher total crystalline volume fraction of the layer even if the SiC crystalline volume fraction was constant. As the Si-C bonds that are not surrounded by SiC are embedded in either amorphous or crystalline Si phases, the Si-C(s) vibration is sensitive to a more crystalline and thus stiffer Si network. The compositional shift of the Si-C(s) stretching vibration seen in Fig. 5.12 (b) and Fig. 5.13 (b) can thus be explained with the higher total crystallinity due to the higher Si crystallinity of the material.

Künles [79] conclusion that upon thermal annealing C and Si inter-diffuse (C out of the barrier layer to the Si-rich layer and Si vice versa) is supported by the results presented in this chapter. Inter-diffusion leads to partial or full deterioration of the multilayer structure, more homogeneously distributed Si excess and thus less Si excess in the Si-rich regions. A stoichiometric barrier would, compared to a Si-rich barrier, imply that crystallization of Si occurs only at higher temperature, and the Si crystalline domains are expected to be smaller. This reasoning is in full agreement with the experimental results discussed in this chapter, i.e. less C in the barrier promotes Si crystallization, as seen in Fig. 5.13 (c) and (d).

In addition, large amorphous volume fractions are present even in most SiC/Si NC multilayers annealed at temperatures up to 1100°C, cf. Fig. 5.11 (right). Therefore, the material has to be considered as a mixture of amorphous and crystalline phases of both Si and SiC. The crystallite sizes and crystalline volume fraction of each phase depend on the deposition parameters, the composition and thickness of each layer as well as the annealing conditions. As the Si-C(s) mode is sensitive to the structural transformation of both phases, and furthermore accessible for all
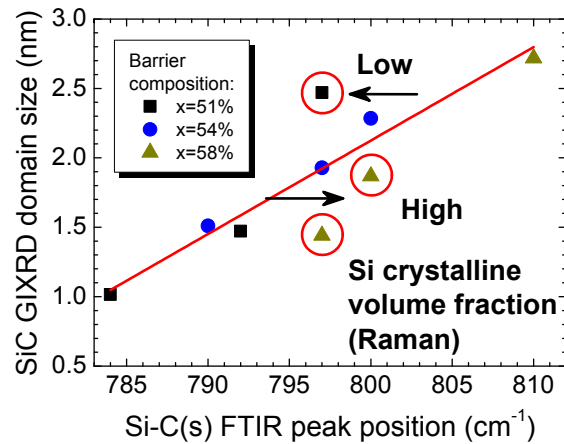
Fig. 5.14: *Correlation between the SiC GIXRD domain size and the peak position of the Si-C stretching vibration. The deviation of the three encircled samples can be explained with the Si Raman crystallinity. Comparison with Fig. 5.11 demonstrates that in these samples the Raman crystallinity deviates considerably from the isothermally annealed samples. The line is just a guide to the eye.*

samples, it constitutes a valuable parameter representing the overall crystallinity of the entire material. This is stressed by Fig. 5.14, which illustrates the correlation of the SiC GIXRD crystallite size to the Si-C(s) vibration peak position. A linear correlation of the two quantities is seen for all data points except three (encircled red). The latter correspond to the samples with considerably higher (dark yellow triangles) or lower (black square) Si Raman crystallinity compared to the isothermally annealed samples with lower or higher Si content. Therefore, the Si-C(s) FTIR peak position represents the structural changes of the entire network, i.e. the SiC and the Si phases. As it is the only parameter available for all samples, it will be used in the following to represent the overall crystallinity of the film.

SiC/Si NC multilayers show completely distinct structural properties in comparison with the SiO_2/Si NC material. The deviating structural properties can be explained with the fundamentally different crystallization mechanisms. Thermal annealing of SiO_x induces a phase separation into Si and SiO_2. At more elevated temperatures, Si crystallizes but SiO_2 remains amorphous. In Si_xC_{1-x} layers, a phase separation to Si+SiC is indeed observed upon crystallization. Before the material crystallizes, however, C diffusion compensates the Si excess in the Si-rich layer. Furthermore, the crystallization temperature depends on the Si excess and is lower for a higher Si excess. Once Si crystallites form, the crystallization of SiC is also observed.

5.6.3 Electrical characterization

The multilayer structure of SiC/Si NC multilayers prepared by PECVD and thermal annealing is only partially preserved upon solid phase crystallization (see Fig. 5.8). Therefore, the material has rather to be considered as a bulk material mix instead of a superlattice structure. Nonetheless, reference to the superlattice structure is made, because the structural properties of the final material are related to the superlattice structure of the amorphous precursor multilayer. Moreover, the NC size distribution and spatial positions are still better defined in the multilayer structure than in bulk single layers.

This section covers the electrical properties of the samples presented in Tab. 5.5, whose structural properties were discussed in the previous section. The samples mainly differ with regard to the degree of crystallinity and the Si content. The electrical properties are related to the FTIR Si-C(s) peak position, as this parameter was shown to be sensitive to the structural changes of both phases (Si and SiC) and thus represents an ordering parameter for the overall material.

The electrical properties of the SiC/Si NC films were characterized with conductivity measurements in dark, under illumination (photoconductivity) and in dependence of the sample temperature. The methods are described in section 13.2.1. The SiC/Si NC multilayers with a barrier composition of 51% and 54% Si cracked upon annealing at 1100°C. These samples are therefore omitted in the further discussion.

The dark conductivity is shown in Fig. 5.15 plotted against the Si-C(s) FTIR peak position. The annealing temperatures are indicated additionally to permit an univoqual identification with the samples as described in Tab. 5.5.

For the samples with x=51% and x=54% in the barrier the conductivity increases with the annealing temperature and is approximately proportional to the Si-C(s) peak position, i.e. the total crystallinity. The conductivity is about one order of magnitude higher per 100°C increase of the annealing temperature. For the samples annealed at 900°C, an increase of the conductivity by three orders of magnitude due to the higher Si content can be seen. However, a different pattern is observed for the samples with x=58% annealed at higher temperature. The conductivity decreases about 3.5 orders of magnitude as the annealing temperature increases from 900°C to 1100°C. This effect is discussed below. The temperature dependence of the dark conductivity is shown in Fig. 5.16. The dark conductivity follows the Arrhenius law for T>300 K. At low temperatures, the data exhibit a curvature when displayed as Arrhenius plot. Both behaviours are usually found in amorphous Si and amorphous SiC [84] and explained with temperature activated
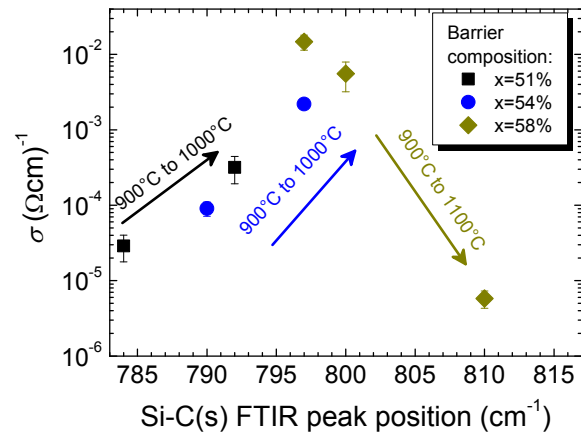
Fig. 5.15: Dark conductivity of SiC/Si NC multilayer with varying barrier layer Si content x.
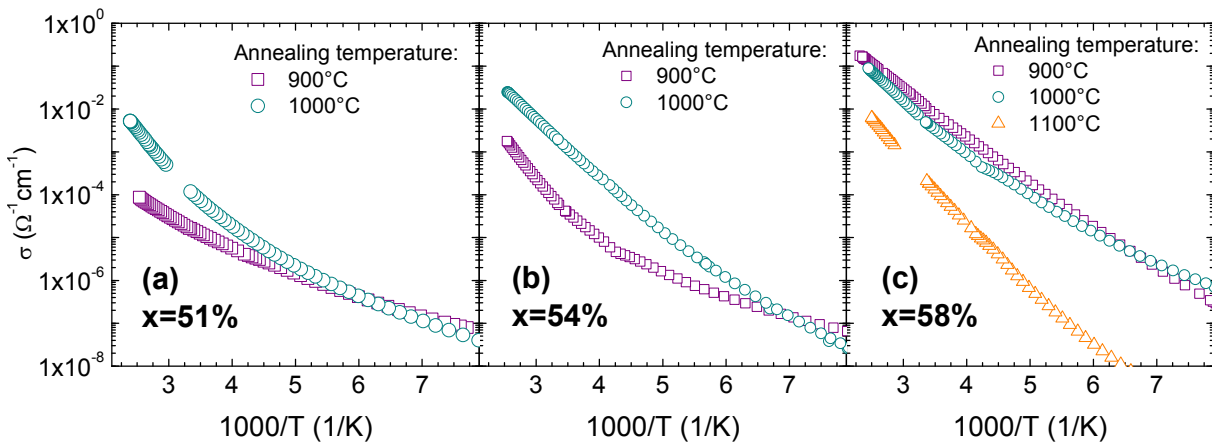
Fig. 5.16: Temperature-dependence of the dark conductivity. As the films with barrier compositions of x=51% and 54% cracked upon annealing at 1100°C, they are omitted for further analysis. The figures were adapted from [74].
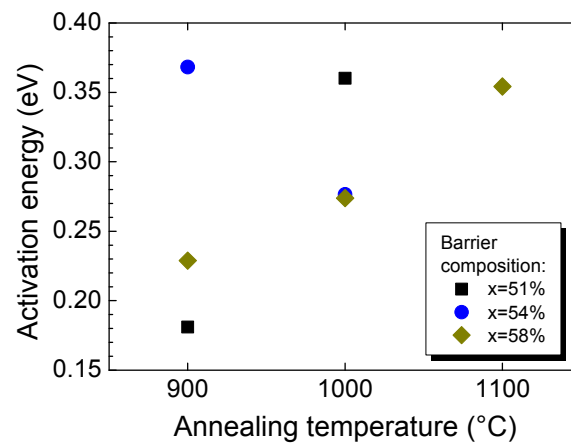
Fig. 5.17: Activation energy of the dark conductivity extracted from the Arrhenius plots in Fig. 5.16 for T>300 K.

conductivity through extended band states and hopping conduction through mid gap or band tail defect states [124]. At room temperature and above, conduction takes mainly place through extended states [84] and the activation energy is therefore the difference between the Fermi level and the mobility edge (see section 2.5, Eq. (2.39)). The activation energy was calculated according to Eq. (2.39) from the slope of a linear regression to $\ln(\sigma_{\mathrm{dark}})$ between 305 K and 425 K. All samples exhibit an activation energy between 181 meV and 361 meV, summarized in Fig. 5.17. While the activation energy increases for the samples with 51% and 58% Si in the barrier, the samples with 54% Si in the barrier show the opposite trend.

5.6.4 Discussion of the structural and electrical properties

Research on epitaxial 3C-SiC was for a long time concerned with unintentional background doping [125, 126]. The most common candidates for background doping in 3C-SiC are oxygen and nitrogen [126]. Eickhoff *et al.* [126] studied the origin of doping in not intentionally doped and nitrogen doped 3C-SiC. He compared single crystalline, polycrystalline and nanocrystalline material grown by CVD at 1200°C, 1170°C and 1100°C. The single and poly crystalline 3C-SiC was epitaxially grown on a Si wafer, while the nanocrystalline material was deposited on a thermally oxidized Si wafer. As the grain size of the nanocrystalline material was reported to be <100 nm, it constitutes a good approximation to crystallized stoichiometric SiC films from PECVD. The three different materials all exhibited a high oxygen concentration. While the oxygen was located mainly at the SiC/Si interface in single crystalline 3C-SiC, it was present with constant concentration throughout the entire SiC bulk in the nanocrystalline material. By means of cross-sectional TEM oxygen was related to structural defects such as grain boundaries. It was shown that nitrogen was responsible for background doping in single crystalline material, resulting in carrier densities of 10^{17} cm^{-3} with 56 meV activation energy. In the nanocrystalline material, however, a carrier density of $2{\times}10^{19}$ cm^{-3} was measured and attributed to the oxygen background. Gali *et al.* [127] previously had predicted theoretically an oxygen deep donor level 200 meV below the conduction band and an activation energy of 200 meV had been measured by Suzuki *et al.* [128]. Eickhoff *et al.* [126] also observed 200 meV activation energy and related this behaviour to the oxygen background.

Based on these studies, the incorporation of background dopants to SiC deposited by PECVD and then crystallized in the solid phase is very likely. The activation energies (Fig.

5.17) are similar to those observed for oxygen background doping in 3C-SiC, but still vary considerably.

The positive correlation of the dark conductivity with the crystallinity seen in Fig. 5.15 for x=51% and 54% can be readily explained with conduction through the progressively more crystalline material. However, it is not obvious why this trend should be reversed for 58% Si content in the well layer. Therefore, the chemical microstructure of the annealed samples was further analyzed. A detailed analysis of the FTIR peak around 800 cm^{-1} reveals a hump in the high-wave number shoulder, which is not yet explained with the structural transformations outlined before. The hump is clearly seen in Fig. 5.10, which depicts the FTIR spectrum of the sample with the highest Si content in the barrier layer (x=58%) and annealed at 1100°C along with the FTIR spectrum of stoichiometric SiC by PECVD. Due to the spectral positon of the hump, nitrogen bonded to silicon can be inferred to cause the additional absorption, as the dominant Si-N feature is an asymmetric streching vibration found at 860 cm^{-1} [129]. The Si-H$_2$ bending mode at 900 cm^{-1} is not eligible as the sample was annealed at 1100°C and any hydrogen has effused. The IR absorption of silicon nitride was quantified by Bustarret et al. [130], who reported a calibraton factor of 1.3×10^{19} cm^{-2} for this mode. An excellent fit of the experimental FTIR spectrum is obtained when accounting for a Si-N mode at 860 cm^{-1} as illustrated in Fig. 5.18. Using the calibration factor from Bustarret et al. [130] a Si-N bond density of 1.4×10^{22} cm^{-3} is calculated. Assuming threefold coordinated nitrogen, this value corresponds to a nitrogen atomic volume concentration of 4.7×10^{21} cm^{-3}. Secondary ion mass spectrometry (SIMS) was measured on the same sample to confirm the incorporation of nitrogen. The SIMS depth profile is shown in Fig. 5.19. The nitrogen concentration was found to be around 10^{21} cm^{-3}, decaying exponentially from 3×10^{21} cm^{-3} at the surface to 7×10^{20} cm^{-3} at the wafer interface. Given the very different matrix material in the experiment of Bustarret et al. [130], and the calibration of the SIMS measurement using a monocrystalline N-doped SiC standard, the agreement between with the value of 4.7×10^{21} cm^{-3} measured by FTIR is excellent. The hump at 860 cm^{-1} was only found in the FTIR spectra of samples annealed at 1100°C and the sample with the highest barrier Si content annealed at 1000°C. The nitrogen atomic volume concentration was calculated for all mentioned samples with the calibration factor from Bustarret et al. [130] under the assumption of threefold coordination and is depicted in Fig. 5.18.

Nitrogen was not expected beforehand to react with SiC/Si NC multilayers as most comparable studies [106, 108, 114] were performed with a N$_2$ annealing atmosphere and

the incorporation of nitrogen was not reported. However, the mentioned studies were restricted to structural investigations, mostly based on FTIR, Raman, GIXRD and TEM.
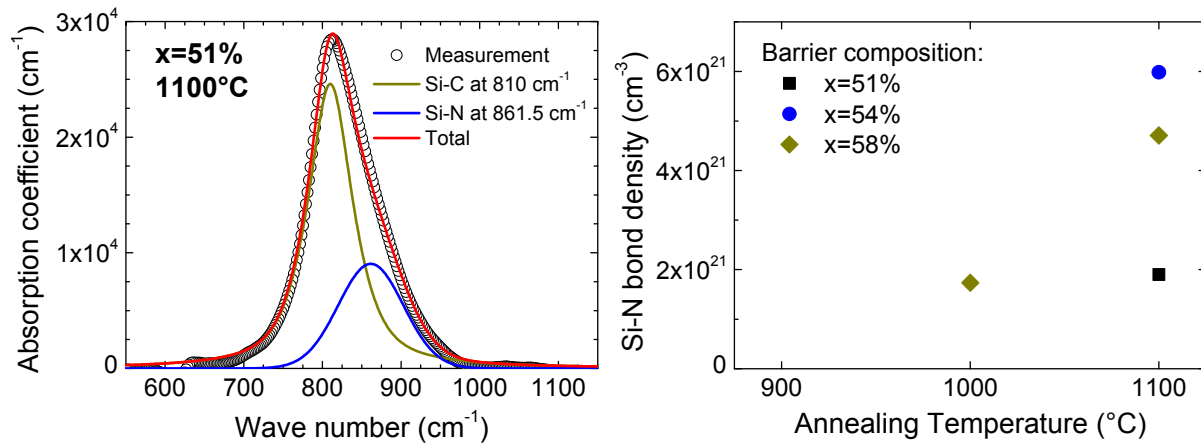
Fig. 5.18: (Left) FTIR spectrum of the multilayer with a Si barrier content of x=58% that was annealed at 1100°C. An excellent fit is obtained when additionally to the Si-C(s) mode a Si-N asymmetric stretching vibration is accounted for. (Right) Si-N bond density calculated with the calibration constant from Bustarret et al. [130] under the assumption of threefold coordinated N atoms.
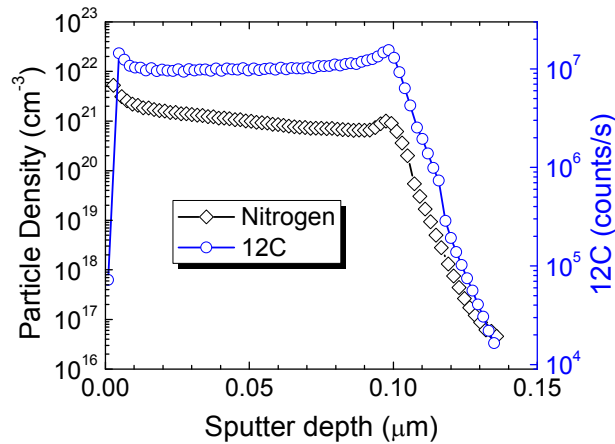
Fig. 5.19: Secondary ion mass spectrometry depth profile of the sample discussed in Fig. 5.18.

In the following, the literature on high-temperature reactions of nitrogen with Si and SiC is briefly reviewed to identify possible Si-N bond formation mechanisms in Si-rich SiC. A broad literature exists on the preparation of silicon carbo nitride (SiCN), as well as nitrogen doping of crystalline SiC during epitaxial growth and also high-temperature reactions of SiC and Si surfaces with nitrogen. SiCN compounds are usually fabricated by chemical or physical vapor deposition using Si-, C- and N-containing precursors. However, the existing results do not allow to draw conclusions   on the high-temperature behaviour of PECVD

deposited SiC with N_2. Several authors presented nitrogen doped a-SiC films prepared by PECVD, but the incorporation of nitrogen to Si-rich a-Si_xC_{1-x} films *after* deposition during e.g. thermal annealing is not covered by the literature. Nitrogen (as well as aluminum) doping of epitaxially grown SiC is controlled by competition of the dopant atoms with the Si or C atoms for the respective lattice site [131]. As nitrogen is incorporated to the C lattice site, doping can be controlled by adjusting the Si/C ratio in the reactor. An excessive C supply suppresses the incorporation of N. SiC is usually grown at temperatures above 1100°C, but nitrogen doping has also been achieved at 800°C by e.g. Wijesundara *et al*. [132]. A review on SiC technology, including doping, was given e.g. by Neudeck [80].

Miyagawa *et al*. [133] reported the formation of a buried Si_3N_4 by N_2^+ ion implantation into SiC at 1100°C. The authors compared implantation at 1100°C with implantation at lower temperature and subsequent annealing at 1100°C for 60 min. They observed that β-Si_3N_4 formed upon implantation at 1100°C, but not for implantation below 930°C followed by annealing at 1100°C. Furthermore, they inferred a preferential migration of free C atoms produced by the N bombardement out of the N enriched layer due to the strong Si-N bonds.

The nitridation of SiC surfaces was pursued by Elsbergen *et al*. [134] and Bermudez *et al*. [135]. Elsbergen *et al*. [134] exposed Si-terminated 6H-SiC surfaces to a nitrogen RF plasma and observed the formation of Si_3N_4. The authors reported a thickness increase with temperature up to a maximum of 1.4 nm at 800°C. At temperatures >800°C they observed thinner layers. In order to obtain thicker Si_3N_4, they deposited Si on Si-terminated SiC surfaces before plasma exposure.

Nitridation of Si surfaces in N_2 is much more efficient than nitridation of SiC surfaces and can be regarded as the historical precessor of Si_3N_4 growth. A summary can be found in a review on Si surface chemistry by Waltenburg *et al*. [136] and references therein. Uniform 10 nm thick Si_3N_4 layer were reported by Ito [137] at temperatures between 1200°C and 1300°C. Formation of Si_3N_4 in the temperature range relevant for the work presented here was reported by Schrott *et al*. [138, 139] and Zhu *et al*. [140]. While according to Zhu *et al*. [140] Si_3N_4 forms only above 1100°C under annealing in high-purity N_2, Schrott reported Si_3N_4 formation on a Si (111) surface at 1000°C<T<1050°C [138] and on a Si (100) surface at 850°C<T<1050°C [139]. Furthermore, he observed decomposition into Si_2N at temperatures exceeding 1200°C. Jennings [141] pointed out that the reaction of nitrogen with Si powders is not a solid state reaction, but merely a gas phase reaction with the previously evaporated Si. FTIR spectra very similar to those reported here were presented

by Barbadillo *et al*. [142] [143] who coimplanted C[+] and N[+] ions into a Si wafer and found a segregation into Si_3N_4 and SiC.

According to these results, the formation of Si_3N_4 on c-Si surfaces has to be expected for temperatures above approximately 900°C. In SiC crystals, N reacts only with the uppermost atom layers by replacing C atoms, but not with the SiC bulk. Moreover, these reactions take place only with N_2 in an excited state, e.g. using plasma or hot wire techniques. Nitrogen is thus unlikely to react with the SiC phases in the SiC/Si_xC_{1-x} multilayers to extended Si_3N_4 clusters. However, the incorporation as dopant impurity during the amorphous-to-crystalline phase transition of SiC appears to be reasonable and would even enable doping of the SiC barrier. As based on the literature the nitridation or penetration by nitrogen of stoichiometric SiC is not plausible, a stoichiometric SiC encapsulation layer prevents the formation of Si_3N_4.

As pointed out above, the growth of Si_3N_4 is indeed to be expected at Si interfaces, and is even likely to proceed into the Si domains within the SiC/Si_xC_{1-x} multilayer. While "domain" refers to the crystalline and the amorphous phases, Si_3N_4 growth is more likely to occur with the unpaired electrons in the amorphous Si than with crystalline phases. This suggests that temperatures >900°C and Si domains that extend from the film surface into the bulk of the film are the conditions for Si_3N_4 growth by annealing of SiC/Si_xC_{1-x} multilayers in N_2. As Si_3N_4 forms at the Si domain interfaces, it grows as a shell around the latter interrupting the conduction path. If the nitrogen does not penetrate the entire film, the Si_3N_4 shell may be expected to grow around the Si crystallites at least within the first 10 nm beneath the film surface. A Si_3N_4 phase around the Si clusters therefore forms a barrier to electrical transport, explaining the decreasing dark conductivity.

5.6.5 Photoconductivity

To assess the electronic quality of the SiC/Si NC multilayers, the photoconductivity was measured as described in section 13.2.1 and the effective mobility lifetime product was calculated according to Eq. (2.43). As the effective mobility lifetime product $(\mu\tau)_{eff}$ takes the charge carrier generation rate into account, it is suited for material comparison. The photoconductivity was measured for one contact spacing and a reference measurement at dark conditions was made immediately before. The results are shown in Fig. 5.20 (a) and (b). The effective mobility lifetime product as well as the photoconductivity exhibit the same trend as the dark conductivity. They increase with the overall crystallinity for Si

contents of the well of 51% and 54%. For 58% Si, however, a decrease with the crystallinity (higher annealing temperature) is observed.

The charge carrier mobility is supposed to change upon thermal annealing as the material
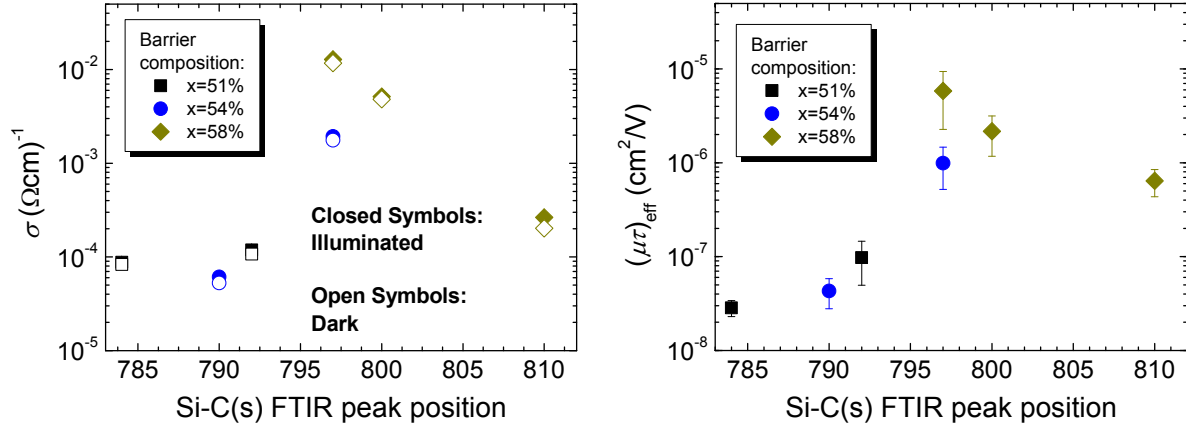
Fig. 5.20:(Left) Conductivity under illumination with an Ar ion laser and in dark for comparison. (Right) Effective mobility lifetime product. The figures were adapted from [74].

crystallizes, but the results obtained so far do not permit to draw conclusions on the charge carrier lifetime. However, as the photoconductivity resembles the structural dependence of the dark conductivity it can be inferred that the photoconductivity is dominated by the latter. As the mobility can be assumed to be not illumination-dependent, the charge carrier concentration in the dark is comparable to the charge carrier concentration under illumination. This argument allows to narrow down the range of possible charge carrier lifetime values. The experimental values of $\sigma_{\mathrm{photo}} \approx 0.1 \times \sigma_{\mathrm{dark}}$ in conjunction with the assumption of a constant mobility leads to $\Delta n \approx 0.1 \times n_{\mathrm{dark}}$. With an approximate generation rate of $G = 10^{21}\,\mathrm{cm^{-3}}$,

$$\frac{n_{\mathrm{dark}}}{\tau} = 10^{22}\,\frac{1}{\mathrm{cm^3 s}} \tag{5.2}$$

follows from Eq. (2.11). An upper limit of $n_{\mathrm{dark}} = 10^{19}\,\mathrm{cm^{-3}}$ can be estimated assuming a background doping comparable to nanocrystalline 3C-SiC [126] grown by CVD. This implies an upper limit for the effective charge carrier lifetime of $\tau_{\mathrm{eff}} = 10^{-2}\,\mathrm{s}$. Moreover, a lower limit for the mobility of $10^{-4}\,\mathrm{cm^2/(Vs)}$ can be deduced using the $(\mu\tau)_{\mathrm{eff}}$ value of $10^{-6}\,\mathrm{cm^2/V}$. Consequently, an estimated lower limit of $n_{\mathrm{dark}} = 10^{17}\,\mathrm{cm^{-3}}$ leads to a lower limit of $\tau_{\mathrm{eff}} = 10^{-5}\,\mathrm{s}$ and an upper mobility limit of $10^{-1}\,\mathrm{cm^2/(Vs)}$.

5.6.6 Photoluminescence

Photoluminescence (PL) spectroscopy was carried out to evaluate the effect of the different barrier composition and the annealing temperature on the luminescence properties. The experiment was done with the same samples that were used for IV measurements (see section 5.6.1). As described above, photoluminescence was measured after the remote hydrogen plasma treatment on the samples described in Tab. 5.5. Moreover, PL on another sample series was measured to evaluate the effect of different hydrogen treatments for defect passivation. In general, the PL intensity from SiC/Si NC films is very low. For wavelengths <900 nm the intensity is in the range of a very thin (<10 nm) SiO_2 on a c-Si wafer. In fact, a positive influence of the reactor temperature and the duration of the hydrogen treatment on the intensity of a luminescence peak between the excitation laser wavelength and 800 nm was measured on a different sample series (not shown here). However, no PL was measured any more after an HF dip to etch off the surface oxide. Therefore, an eventual surface oxide was etched off in HF before the PL measurement for the sample series discussed here (Tab. 5.5).

The PL spectra are shown in Fig. 5.21 for the varying annealing temperature (x=0.51) and varying barrier layer composition (T_{anneal}=1000°C). The PL spectra exhibit mainly three features. A broad peak at 560 nm, which is very close to the laser excitation wavelength (514.5 nm) and the threshold wavelength of the long pass filter (520 nm). Furthermore, a strong emission at wavelengths >1000 nm can be observed, which is very similar to bulk Si
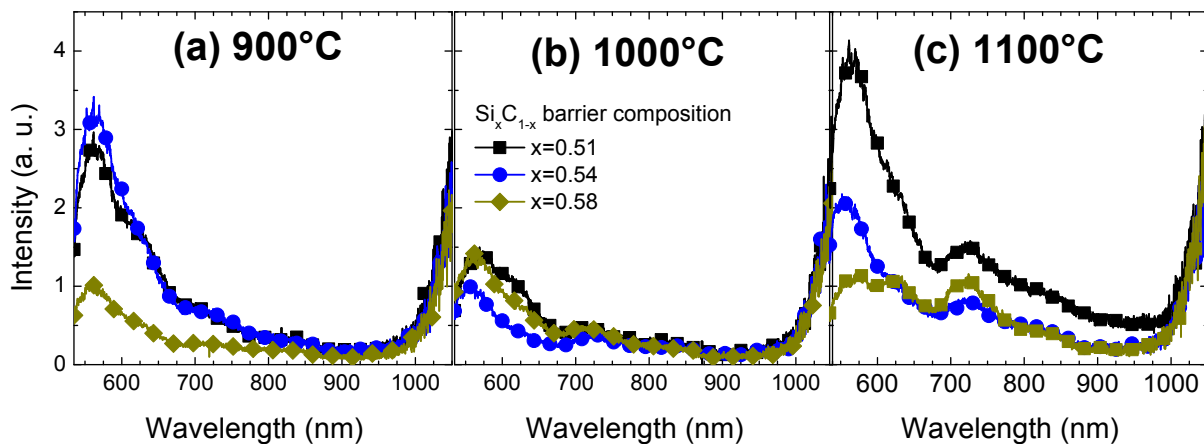
Fig. 5.21: Photoluminescence spectra of the samples presented in Tab. 5.5. Any surface oxide was etched off before the measurement in HF. The figures were adapted from [74].

PL. Only the onset can be seen because the Si CCD camera is not sensitive any more in this wavelength region. A third feature evolves around 720 nm for annealing temperatures of 1000°C and 1100°C.

Obviously, the PL is weakest for the samples annealed at 1000°C. However, it is difficult to derive a clear picture from the spectra. PL from amorphous a-Si_xC_{1-x} was intensively investigated by e.g. Siebert *et al*. [144], Carius *et al*. [145] and Tessler *et al*. [146], and consists of a broad Gaussian peak. The PL peak shifts towards the blue and becomes broader as the Si content is decreased from x=1 to x=0.5. A peak around 560 nm (2.2 eV) is frequently found in the PL spectra 3C-SiC [147] and attributed to band to band luminescence of the 2.4 eV band gap. Bearing in mind the 3C-SiC band gap is 2.4 eV and the partially amorphous structure, the broad peak around 560 nm most likely stems from band tail states luminescence. The peak at 720 nm could be ascribed to luminescence from Si NCs as they are most pronounced after annealing at >1000°C. However, defect luminescence e.g. from crystallite grain boundaries can not be ruled out.

5.7   Band gap characterization by optical absorption spectroscopy

The optical reflectance and transmittance in the ultraviolet and visible spectral range allow an access to valuable information on the elemental composition and the crystallinity of the film. Their detailed analysis was not subject of this thesis. Only a brief summary is presented here as the results affirm the statements made before, provide further insight to the energy band structure and thus complement the overall picture.

A detailed analysis for the characterization of SiC/Si NC films has been developed in the group of Summonte *et al*. at the Instituto per la microelettronica e microsistemi (CNR-IMM). The method relies on the simulation of experimental reflectance and transmittance spectra, measured in a conventional spectrophotometer. The simulation is performed by a computer code implementation (OPTICAL [148]) of a Fresnel coefficient approach applied to multilayers. The code is used to simulate composite materials approximated by an effective medium and arranged in any stack of coherent and incoherent layers. Summonte *et al*. [115, 149] analyzed SiC/Si NC multilayers that were prepared by PECVD and thermally annealed at a maximum temperature of 1100°C. The material is similar to the sample with the x=51% barrier layer discussed in this chapter (see Tab. 5.5). The reflectance and transmittance spectra are very well reproduced by modeling the SiC/Si NC layer as a Bruggeman effective medium [150] composed of amorphous and microcrystalline phases of SiC and Si. The optical functions for the amorphous phases were measured on reference

samples of the respective layers. The latter had been annealed at 600°C to effuse any hydrogen in order to resemble the electronic structure of the remaining amorphous phases in the multilayers. The microcrystalline SiC reference sample had been annealed at 1100°C, and the spectra of microcrystalline Si were taken from the literature. As the blue-shifted band gap of Si NCs changes fundamentally the optical spectra of the c-Si compound, it requires an adapted optical function for the latter to achieve agreement of the simulation with the experimental data.

However, the reflectance and transmittance spectra were very well reproduced with the effective medium approach described above, without the need to introduce any quantum effects. Due to the size-dependent quantum confinement in Si NCs, the optical gap should shift to higher photon energy for smaller crystals. Furthermore, smaller crystals can be expected for lower Si excess within the SiC/Si$_x$C$_{1-x}$ multilayer. Thus, with the presence of quantum size effects a higher gap is expected for lower Si excess and thus smaller NCs. Contrariwise, the opposite trend is evident. The band gap was defined here as the optical gap E_{04} (see section 13.2.3), and the discrepancy was shown to arise from the residual amorphous Si fraction still present in the layer. In detail, a positive correlation between the Si excess and the larger crystalline volume fraction (and larger crystallites) was found. Vice versa, the amorphous Si fraction is the larger, the smaller the Si excess is. As amorphous Si absorbs much more strongly than crystalline Silicon, the blue shift occurs because more Si crystallizes (larger Si crystalline volume fraction and Si NC size). In summary, while a red shift due to higher Si excess would be expected under the assumption of quantum confinement, the opposite trend was found experimentally and the blue shift explained with the higher Si crystalline volume fraction.

The crystallized volume fraction was compared to independently obtained values derived from Raman spectra of the Si TO mode and good agreement was found [109]. The results do not rule out quantum confinement in the Si NCs, but demonstrate that possibly present confinement effects are masked by defect absorption in the very defect-rich amorphous phases.

The analysis of the optical reflectance and transmittance spectra thus provides a complementary tool to GIXRD and Raman spectroscopy to track the structural changes in the SiC/Si NC film. A careful modeling has proven to be necessary to correctly identify the contributions of the different material phases to the optical absorption.

5.8   Chapter summary

This chapter is dedicated to the investigation of Si NCs in a SiC host matrix which is advantageous due to its electrical properties compared to SiO_2. The band offsets between silicon and silicon carbide ($E_{G, \, 3C\text{-}SiC}$ =2.4 eV) constitute only a small confining potential to electrons and holes compared to the SiO_2 matrix. The comparatively low barrier facilitates electrical transport for two reasons: Electrical conduction can take place through the matrix itself after absorption in the Si NC and subsequent thermionic or photon-assisted charge carrier emission into the matrix. Furthermore, wave function coupling and thus miniband formation is expected to be stronger for a smaller confining potential, providing a conductive path directly through the Si NC network even at higher NC separations of 3-4nm [41]. The possibility to dope SiC provides a means to introduce free carriers to the system without the need to dope the Si NCs (modulation doping). Common dopants are nitrogen and aluminum. Nitrogen incorporates to the C sites in the SiC lattice and forms an impurity level 50 meV below the conduction band.

The formation of Si NCs in SiC has been pursued using a multilayer approach in analogy to the SiO_2/Si NC system. The structural transformations of SiC/Si_xC_{1-x} multilayers due to thermal annealing had already been investigated by several authors [106, 114] using very high Si contents in the well layers. However, a systematic electrical characterization has so far been missing. The study presented here targets the further optimization of the material developed by Künle [114], a characterization of the electrical properties and their correlation to the structural characteristics.

SiC layers with varying composition can readily be deposited by PECVD. PECVD allows for a deposition rate low enough to prepare layers with a thickness of only a few nanometers, a compact and homogeneous layer growth and a variation of the layer composition by adjusting the precursor gas (silane and methane) ratio. The composition was determined for this study by Rutherford backscattering spectrometry. The microstructure of the amorphous as well as the crystallized layers was investigated by FTIR. FTIR is sensitive to the vibrational modes in the atomic network and allows us to determine the concentration of a particular chemical bond, the crystallinity of the corresponding compound and also the crystallinity of the surrounding material. In particular, the wave number of the Si-C stretching vibration was found to be a useful quantity. It was shown to be sensitive not only to the SiC but also to the Si crystallinity, and thus provides a good qualitative measure for the overall film crystallinity. As the Si-C stretching vibration can be measured

independent of the annealing state (amorphous or crystalline), it represents a valuable comparative parameter that is readily accessible for all samples.

The amorphous precursor layers contain large amounts of hydrogen. The hydrogen effuses as the films are heated to temperatures between 500°C and 800°C, causing the film to shrink by 30%. Crystallization starts at temperatures between 700°C and 900°C, depending on the Si content. Interestingly, also SiC NCs form once the crystallization of Si is detected [106, 114]. According to TEM investigations, the multilayer structure is preserved up to annealing temperatures of 900°C. After annealing at 1000°C, however, the individual layers are interrupted and the multilayer structure deteriorates. The loss of the multilayer structure was also evidenced by experiments according to which inter-diffusion between the barrier and the Si-rich layers occurs upon thermal annealing [79].

In order to avoid inter-diffusion, multilayer samples were prepared with varying Si content x (C content 1-x) in the barrier layer. The Si content was varied between a stoichiometric composition (51%) and 58%. The higher Si content in the barrier was shown to foster Si crystallization by lowering the Si crystallization temperature from 1100°C ($x = 51\%$) to 900°C ($x = 58\%$). For isothermally annealed samples, the crystalline volume fraction and the Si NC size are positively correlated with the barrier Si content. A different picture is obtained for the formation of SiC NCs: Neither the crystallization temperature, nor the SiC NC size is correlated with the barrier layer composition.

While the barrier composition does not influence SiC crystallization, a higher C content promotes the formation of Si-C bonds. The latter is observed by FTIR, which is also sensitive to Si-C bonds in the amorphous part of the material. These experimental results support the previous conclusions [79] based on TEM investigations that the compositional difference between the Si-rich layer and the stoichiometric barrier layer balance due to thermal annealing.

The electrical properties of the SiC/Si NC multilayers were characterized with dark DC conductivity, photoconductivity and temperature-dependent conductivity measurements. It was shown that SiC/Si NC multilayers with stoichiometric SiC barriers provides dark conductivities of $\approx 5 \times 10^{-4}$ Ω^{-1}cm^{-1}. The dark conductivity was found to increase for higher Si content of the barrier and for higher annealing temperature. The influence of both quantities can be summarized in the film crystallinity, concluding that the films are the more conductive the more crystalline they are. However, the opposite trend was observed for the samples with the highest barrier Si content that were annealed at temperatures ≥1000°C. The conductivity was found to decrease as the samples were annealed at higher

temperature. The same samples also exhibited a previously unidentified hump in the high-frequency wing of the FTIR Si-C(s) peak. According to its position in the FTIR spectrum, the hump can be explained with the asymmetric Si-N stretching vibration. The presence of N in the film was confirmed with SIMS. The N concentrations derived from SIMS and FTIR are both in the range of $10^{21}\,cm^{-3}$. Provided the approximations regarding the calibration standards both in SIMS and in FTIR, the two methods are in very good agreement. Comparison with the literature suggests that N incorporates as a Si_3N_4 phase at the Si phase boundaries at least within 10 nm beneath the film surface. As the Si_3N_4 phase represents a barrier to electrical conduction and is thermally grown by annealing in N_2, it explains the trend of decreasing dark conductivity for higher annealing temperatures. The incorporation of N to the SiC lattice as a dopant impurity is also a possible mechanism, but the results from nanocrystalline 3C-SiC grown by CVD give more evidence for SiC background doping due to oxygen impurities. Nitridation of the SiC surfaces to Si_3N_4 does not happen at the experimental conditions relevant to the present case.

The temperature dependent conductivity follows the Arrhenius law for temperatures >300 K. Activation energies between 180 meV and 370 meV were determined for this temperature range. A clear dependence on the structural properties could not be observed.

The photoconductivity was measured using the 514.5 nm Ar ion laser line. A photo response could be shown for all samples, and the photoconductivity was found to be approximately 1.1 to 1.5 times the dark conductivity. The photoconductivity resembles the same dependence on the structural properties as found for the dark conductivity. With the assumption that the mobility does not depend on the illumination, the photoconductivity values allow to derive an upper limit of the effective charge carrier lifetime of 10^{-2} s.

Furthermore, photoluminescence spectroscopy was employed to investigate the spontaneous emission using again the 514.5 nm Ar ion laser line. The PL intensity was found to be very low and comparable to the PL intensity of a native oxide on a Si (100) wafer or a partially oxidized SiC/Si NC film. However, a spectrum of the SiC/Si NC film could be measured for every sample. The PL consists of three components: One broad peak around 560 nm, e.g. right below the excitation wavelength, the Si bulk luminescence at wavelengths >1000 nm, and a small feature at 720 nm that appears only after annealing temperatures >1000°C. As the PL intensity was very low, the origin of the distinct emissions was not revealed.

The optical absorption was not investigated in detail in the framework of this thesis. However, comparable SiC/Si NC multilayers to those discussed here were studied by Summonte *et al*. [115, 149]. The optical spectra of the SiC/Si NC multilayers could be perfectly reproduced assuming a mix of amorphous and microcrystalline bulk SiC and Si phases. Noteworthy, a higher Si excess was shown to result in a larger optical gap (E_{04}), exactly the opposite trend as would be expected under the assumption of quantum confinement. The trend is readily explained by the residual amorphous volume fractions due to the incomplete crystallization of Si. However, as the amorphous volume fractions contain a huge defect density, possibly present quantum effects would be masked by the defect absorption. The clearest evidence for quantum confinement in Si NCs in a SiC matrix has so far been shown with electron energy loss spectroscopy [79].

In conclusion, silicon carbide with embedded Si NCs behaves very differently than the SiO_2/Si NC material. An independent control of Si NC formation, separate from crystallization of SiC, could not be proven. The multilayer structure is lost upon thermal annealing and the electrical properties are dominated by effects other than Si NC formation. Depending on the annealing conditions, the material is a mixture of four phases, which are Si and SiC both in the amorphous as well as the crystalline state.

6 Comparative discussion of silicon nanocrystals in SiO$_2$ and SiC

This chapter reviews the state of material development of the Si NC materials discussed in the preceeding two chapters on the background of their implementation to a solar cell. Based on a description of the requirements to the materials, the material properties are revisited and shortcomings are identified.

The research project presented here aims at the implementation of Si NC quantum dots as the absorber of a high-band gap solar cell. Owing to the discovery of their high band gap [13], Si nanostrutures were identified as the key material that could enable a crystalline tandem solar cell [151].

A Si NC material has to fulfill a number of criteria to be implemented as the top cell absorber in the c-Si tandem concept. The material should exhibit an optical band gap around 1.7 eV [152], electrical transport under illumination, and optical transparency for photons with less than band gap energy. The engineering of an appropriate band gap implies a control of the Si NC size. Moreover, a tight size distribution is mandatory to impede optical absorption or charge carrier trapping by states below the band gap. The requirements of high absorption and charge carrier transport furthermore imply a techonolgical optimization towards a high Si NC volume density. Finally, a high-quality interface to the surrounding matrix material is required, without the degradation effects found in amorphous materials [153].

The boundary conditions for material optimization can thus be summarized as "Si NCs with 1.7 eV band gap and tight size distribution, a high NC volume density and a high quality NC interface". An optimization conflict can be noted here between quantum confinement and maximized Si NC density. At some point of ever denser packed NCs, the quantum confinement is expected to break down. This trade-off will be commented on later.

As the Si NCs cannot be handled in vacuum, they have to be embedded in a matrix material. The matrix material is ideally also Si-based, but should at least be compatible with Si technology in order to stick to the principal objective of a c-Si tandem solar cell. Analogously to the criteria above, the matrix material has to ensure a low recombination and should foster charge carrier transport.

The growth of Si NCs in SiO$_2$ follows the scheme of Si clustering mediated by oxygen emission from the Si-rich phases and subsequent crystallization, and solid phase crystallization of amorphous multilayers [18] has been proven to be a powerful method to restrict the Si NC size distribution. An exact control over the optical band gap, measured as the photoluminescence emission peak, has been achieved and the band gap can be tuned up to around 2 eV. The size dispersion of Si NCs prepard by solid phase crystallization in bulk SiO$_x$ films follows a lognormal distribution with common sizes of 4.5±1.45 nm [154]. By means of the multilayer approach, a Gaussian size distribution could be obtained with very narrow size dispersions of for example 3.3±0.4 nm and 2.8±0.2 nm [154]. The multilayer approach has so far enabled the narrowest size dispersions among the available technologies [155].

Sub-band gap defect absorption was shown to be related to strained interface defects [58]. The sub-band gap absorption as well as the density of electrically active defects [156] were successfully minimized by a hydrogen treatment after high-temperature annealing. A microscopic analysis of the passivation mechanisms of the SiO$_2$/Si NC interface proved that the interface behaves comparable to the planar SiO$_2$/Si interface [63]. In detail, the SiO$_2$/Si NC hydrogen passivation kinetics obeys the same temperature and time dependence, and thus similar temperature stability as for the planar interface can be inferred. With the additional hydrogen passivation step the number of defective NCs can be reduced to 2% [157]. The SiO$_2$/Si NC interface is also enhanced by nitridation in analogy to the planar SiO$_2$/Si interface with a comparable nitrogen areal density [56]. An illumination-induced degradation as known from a-Si:H is therefore not expected to affect the Si NC solar cell performance negatively.

In contrast to the very good optical properties, the electrical properties of the SiO$_2$/Si NC material are not yet optimized. The reliable studies on electrical transport studies have all indicated extremely low conduction via the SiO$_2$ barrier. Charge carrier injection in MOS structures takes mostly place by Fowler-Nordheim tunneling [14]. Evidence for direct tunneling has also been reported [71], but the resistivities are still far too high for solar cell application.

Wave function coupling in the Si NC network has been investigated in this work by optical spectroscopy (chapter 4.3), and shown to be not sufficient for the formation of minibands. Recently, excellent agreement was reported between experimental spectra (photoluminescence and absorption) and those calculated with ab-initio DFT methods as a superposition of the emission from Si NCs with an empirical size distribution [67].

Moreover, Seino *et al.* [73] pointed out that miniband formation occurs only for NC separations smaller than 0.5 nm. Therefore, the density of states of Si NC ensembles realized so far has to be considered as the superposition of the density of states of the individual nanocrystals taking into account the Si NC size distribution.

It was reported by Luo *et al.* [45] that besides very dense packing, also a tight size control is necessary to achieve wave function coupling. The authors reported that for size variations of only 10% the wave function coupling is already severely affected. Luo *et al.* arrive at a similar conclusion as Seino *et al.* [73], reporting that miniband formation ceases at separations >0.5 nm, and that even at intimate contact of two neighboring nanocrystals the quantum confinement is reduced by only 50 meV. The trade-off between confinement and transport mentioned above is therefore not present in the SiO_2/Si NC system. Rather, the quantum confinement appears to be much stronger than expected at the outset of Si NC photovoltaic research. According to Luo *et al.* also the size distribution requirements are much stricter. In fact, the cease of miniband formation due to a variation of Si NC sizes can be interpreted in analogy to amorphous semiconductors (Anderson localization [36]). In amorphous solids, the disorder potential due to the lacking long range order leads to a localization of the energy states. Si NCs exhibit a periodic atom arrangement within each crystallite, but no coherence between different NCs. Interpreting the lacking coherence with a disorder potential, the size variation would localize the wave functions to the NCs. Luo *et al.* observed exactly this effect using atomistic calculations, thus supporting this interpretation. It has to pointed out however, that confirmation by other methods is still missing, and that the interaction of larger Si NC arrays has not been modeled yet due to the immense computation time.

Noteworthy, advances are recently being made towards increased Si NC areal densities and minimized barrier thicknesses [158], and the technological possibilities are not yet fully exploited. The challenging requirements to the electrical properties are also being tackled by novel approaches beyond the SiO_2/SiO_x or SiO_2/Si multilayer approach. The implementation of SiO_x barriers in a multilayer of Si quantum well layers (i.e. a SiO_x/Si multilayer) led to a conductivity increase by 10 orders of magnitude compared to the conventional SiO_2 barriers [72]. However, the current increase was achieved at the expense of quantum confinement and NC size control. A possibility could be the growth of SiO_2 monolayer shells around the Si NCs by e.g. atomic layer deposition.

The lack of charge carrier transport initially triggered the exploitation of alternative matrix materials such as silicon carbide. Multilayers consisting of silicon-rich layers sandwiched

between stoichiometric silicon carbide barrier layers were prepared in analogy to the SiO_2/Si NC multilayer system. However, the silicon carbide matrix fundamentally changes the crystallization mechanism as well as the optical and electrical properties. Indeed, electrical transport through the SiC matrix is possible. Conductivities as high as 10^{-4} $1/(\Omega cm)$ were reported in this thesis (Fig. 5.20) for non-intentionally doped SiC prepared by PECVD and thermal annealing. Non-intentional incorporation of nitrogen and oxygen turned out to occur under certain conditions similar as observed before for epitaxially grown 3C-SiC (section 5.6.4). Additionally, the unwanted formation of Si_3N_4 phases in Si-rich Si_xC_{1-x} layers during thermal annealing was shown. The formation of Si_3N_4 has to be avoided as it impedes electrical transport. However, doping of the SiC matrix by nitrogen incorporating already during layer deposition is a viable option to achieve a n-type matrix material. Thus, the requirement of charge carrier transport is apparently fulfilled by the SiC matrix.

Rather, the challenge has turned out to be the control of the crystallization mechanism. So far, a separation of Si and SiC NC formation has not yet been shown. As SiC NCs form simultaneously with Si NCs, the resulting film comprises a high density of SiC/Si grain boundaries. Even the inter-growth of Si and SiC crystals was reported based on high-resolution TEM studies [79].

According to TEM investigations, the SiC/Si_xC_{1-x} multilayer structure is preserved for thermal annealing up to 900°C for 30 min. At higher temperatures, however, the multilayer structure is gradually lost and the crystallization of Si and SiC proceeds continuously through the entire film. Si crystallites with sizes in the nm range have been proven by TEM-based methods. Evidence for quantum confinement in Si NCs embedded in SiC was shown on the basis of electron energy loss spectroscopy [79]. However, proof of quantum confinement by optical or electrical methods has not yet been given. Contrariwise, the optical and electrical properties could so far always be explained with the bulk properties of the involved materials, rendering the introduction of quantum effects for a description of the measured quantities superfluous. In particular, the optical reflection and transmission spectra in the ultraviolett, visible and near infrared spectral range can be described very well with a Bruggeman effective medium approximation [149, 159] consisting of c-SiC, a-SiC, c-Si and a-Si in their respective volume concentrations. The method has been successfully applied to study the multilayer composition and structural transformation and agrees with Raman spectroscopy with regard to the Si crystalline volume fraction. In most experiments, a fraction of a-Si is still present even after annealing

at 1100°C [149]. As this amorphous silicon volume fraction exhibits an extremely high defect density and thus considerable sub-band gap absorption, it masks eventual quantum confinement effects in the optical spectra.

In conclusion, if quantum effects are present in the SiC/Si NC material, they are not detectable in macroscopic quantities that are averaged over a larger sample volume such as reflectance, transmittace or photoluminescence. Rather, possibly present quantum confinement effects are masked by the large defect density that dominates the measured macroscopic quantities. A study of quantum confinement effects in the SiC/Si NC material therefore requires advanced analytical methods with sub-nm resolution such as STEM-EELS [79].

7 Development of a Si NC high-band gap device with full flexibility for contact formation

This chapter discusses several approaches to an optoelectronic characterization of Si NC films on device level. Several simple device structures are presented and a review of their experimental realizations and the characterization results obtained so far is given. The main obstacle to device fabrication is the high temperature of the Si NC solid phase crystallization. The objective of a solar cell device with a high quality Si NC absorber and full flexibility for contact formation imposes special requirements to device design and fabrication. A membrane-based device was developed in the framework of this thesis to meet this challenge. The membrane-based device provides full area access to the back side of the Si NC film and decouples the formation of selective contacts from high-temperature annealing. This chapter introduces the concept and discusses experimental realizations with SiC and SiO$_2$-based Si NC multilayers. The results were presented in parts in [160] and [161].

7.1 Concepts for silicon nanocrystal photovoltaic test devices

The necessity of using temperatures up to 1150°C for the fabrication of the Si NC layer imposes severe requirements on the thermal stability and the expansion coefficient of the substrate. Device fabrication is further complicated because the substrate hinders the access to the layer back side. The simplest possibility is to use a conductive substrate as shown in Fig. 7.1 (a), e.g. a Si wafer. The Si NC layer contribution to the IV curve can theoretically be distinguished from that of the wafer using monochromatic light with a penetration depth of less than the Si NC layer thickness. The penetration depth $1/\alpha$ for Si NCs in SiO$_2$ is about 10 µm at 3 eV and 1 µm at 4 eV, cf. Fig. 4.2. Technologically viable Si NC layers are usually thinner than 300 nm. Thus a large fraction of the incident light is transmitted through the Si NC film and generates charge carriers in the substrate wafer. This impedes the distinction between the Si NC contribution and that of the substrate wafer. A solution could be the choice of a substrate wafer with an optical band gap higher than that of the Si NC film, e.g. a silicon carbide wafer or epitaxial gallium nitride on a silicon carbide or sapphire wafer. However, the substrate wafer is also required to have suitable work function and electron affinity to establish a selective contact to electrons or
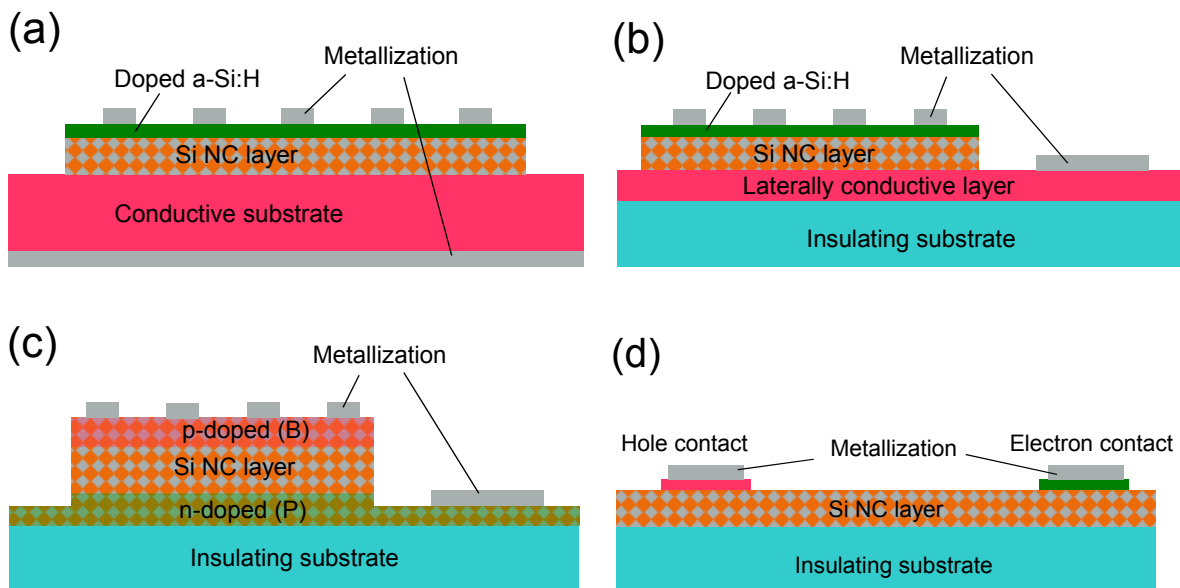
Fig. 7.1: *Test device concepts for the electrical characterization of Si NC solar cell absorbers. Structure (b) was used by Kurokawa et al. [164] and Yamada et al. [22], and structure (c) was employed by Perez-Wurfl et al. [165].*

holes. The device concept sketched in Fig. 7.1 (a) was implemented in a number of experiments by Park *et al*. [162], Cho *et al*. [21] and Song *et al*. [163] at the University of New South Wales with a Si wafer as a substrate. Due to mentioned shortcomings this approach was not pursued in the framework of this thesis.

A slightly more advanced concept is shown in Fig. 7.1 (b). The back contact to the Si NC layer is established by a laterally conductive layer on an insulating substrate. As the conductive layer can be made thin, the unwanted light absorption can be suppressed more easily than in concept (a). The conductive layer can be doped to achieve sufficient lateral conductivity. However, out-diffusion of dopants into the Si NC layer durresitsing the high-temperature annealing might affect Si NC formation and will blur the junction. Devices according to structure (b) were realized by Kurokawa *et al.* [164] and Yamada *et al.* [22]. They prepared p-i-n and n-i-p structures on quartz glass superstrates with heavily doped polycrystalline (poly) Si as back contact layer. Different kinds of Si NC films based on SiC were implemented as an absorber and doped amorphous silicon was used for the top contact. The poly Si layer was several hundred nm thick and is thus to be described by bulk properties. The devices were illuminated with an AM1.5G spectrum through the quartz glass substrate and the poly Si layer but the photovoltaic contribution of the poly Si layer was not discussed.

A variant of concept (b) is shown in Fig. 7.1 (c). This concept circumvents an additional

material as back contact and therefore also the unwanted absorption in the latter. Instead, the back contact is realized through the Si NC layer which is doped during deposition. Perez-Wurfl *et al.* [166] [165] presented experiments with this device structure. They fabricated SiO_2/Si-rich oxide multilayers on quartz glass and doped in-situ the lowermost bilayers with phosphorus and the top bilayers with boron. However, strong inter-diffusion of dopants was reported to occur during high-temperature annealing.

In all concepts mentioned so far (Fig. 7.1 (a, b, c)), the physical properties of the electrical back contact cannot be tuned independently from the solid phase crystallization process. Any change of the thermal annealing step will also affect the properties of the electrical contact. Furthermore, diffusion of dopants from the contact layer to the Si NC layer affects the electrical properties of the latter. To avoid dopants diffusion from the back contact layer, a conductive diffusion barrier or a high-temperature stable conductive layer would have to be implemented. Diffusion barriers are widely used in the microelectronics and also photovoltaics industry. Richards *et al*. [167] [168] employed TiO_2 as a barrier for phosphorous diffusion and reported at least partial suppression of diffusion. Alen *et al*. [169] compared TiO_2 and Ta2O5 and showed temperature stability of TiO_2 up to 650°C.

A possible high-temperature stable conductive layer is Al-Ti, which was reported by Dhote and Auciello *et al*. [170, 171] to be stable up to 600°C. Even better temperature stability is known for metal silicides. An early review was given by Chow *et al*. [172]. An overview on the temperature stability can be found in Murarka [173], who mentions temperature stabilities >1000°C for $MoSi_2$, $TaSi_2$ and WSi_2. Buried WSi_x layers were fabricated by Luo *et al*. [174] by annealing at temperatures between 800°C and 1000°C, and Park *et al*. [175] reported stability of $HfSi_x$ up to 950°C. Minami *et al*. [176] investigated a number of different transparent conductive oxides (TCOs) and found SnO_2 and SnO_2:Sb to be stable up to 900°C in Ar ambient. In_2O_3 and ITO were reported to be stable in air up to 800°C. Gregory *et al*. [177] conducted experiments with ITO at temperatures between 750°C and 1100°C and reported degradation for all temperatures. In conclusion, future Si NC devices can possibly be fabricated with a back contact realized by a high-temperature stable conductive material or a diffusion barrier in conjunction with a doped wafer. Peak Si NCs preparation temperatures of up to 900°C appear to be compatible with advanced conductive layers. However, the mentioned possibilities are not sufficiently mature at present to enable a reliable characterization of a Si NC film annealed at temperatures up to 1100°C.

A possibility of separating contact formation from the recrystallization process and the

substrate properties is to realize both contacts on the front side of the recrystallized layer, see Fig. 7.1 (d). First, Si NCs are formed by thermal annealing. Then, selective contacts to electrons and holes are established. Structuring of the selective contact materials is technologically challenging, but does not imply fundamental constraints on their physical properties. The realization of devices according to structure (d) was pursued within this work. Two different fabrication processes were developed and tested. Details were reported in [27]. Devices similar to structure (d) were also presented by Rölver *et al.* [20] and Berghoff *et al.* [178] with lateral Schottky contacts [20] or doped regions formed by ion implantation [178]. However, this approach requires much higher carrier diffusion lengths than any vertical structure. Device performance is likely to be limited by series resistance.

7.2 Development of a wafer-free membrane p-i-n test device

For the photovoltaic characterization of Si NC films without the flaws discussed above, a membrane-based device as shown in Fig. 7.2 was developed in this work. Its key feature is the local removal and then encapsulation of the substrate after solid phase crystallization of the Si NCs. After opening the electrically insulating encapsulation, the Si NC layer can be accessed freely from both sides. A Si wafer can be used as a substrate, and insulation and structuring can be realized with Si-based dielectric layers deposited by PECVD. Fabrication sequences for membrane devices with SiC- and with SiO_2-based absorbers are explained in the next section. This structure permits free choice for the selective contact material and the interface pretreatment. All electrically active materials can be chosen to have a band gap comparable to or higher than the Si NC film. This permits an unambiguous characterization of the Si NC material. The structure can be realized as p-i-n diode using an
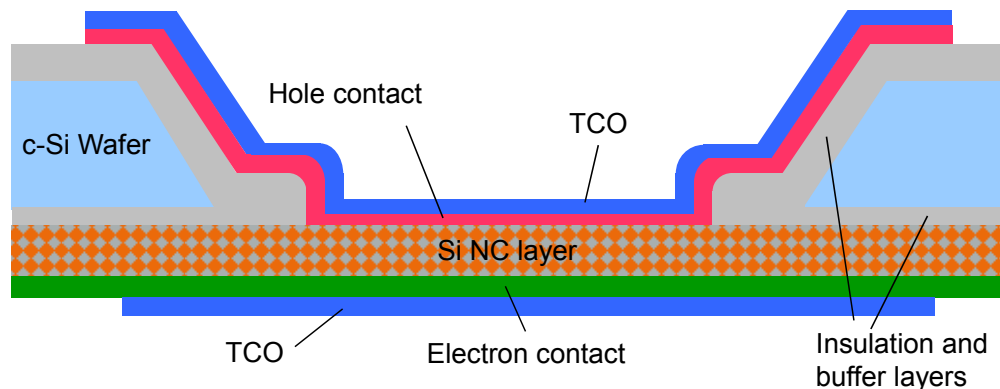

Fig. 7.2: *Structure of a membrane-based Si NC test device. The Si NC layer is prepared on the c-Si wafer by PECVD and high-temperature annealing. The wafer substrate is then removed locally.*

intrinsic and thin Si NC absorber. Photocurrent collection is thus enhanced by the electrical field between p- and n-contact [179]. Furthermore, device fabrication is compatible with standard Si process technology.

7.2.1 Selective contacts to SiC or SiO$_2$ with embedded Si NCs by doped a-Si$_x$C$_{1-x}$:H

Doped amorphous silicon has found widespread use in crystalline silicon heterojunction solar cells for the feasibility of very high open-circuit voltages (>700 mV, [180]). The advantage of doped amorphous silicon is an excellent surface passivation along with the possibility of setting the Fermi level very close to the c-Si band edges. Doped amorphous silicon carbide (a-Si$_x$C$_{1-x}$:H) was used within the framework of this thesis to establish selective contacts to Si NC embedded in SiC or SiO$_2$.

The introduction of carbon widens the band gap [181] and leads to a lower refractive index [84]. It is therefore interesting as a window layer, anti-reflection coating and for high-band gap solar cells. The band structure of bulk a-Si$_x$C$_{1-x}$:H thin films as well as the band lineup of c-Si(100)/a-Si$_x$C$_{1-x}$:H heterojunctions was investigated by Brown *et al.* [181] with photoelectron spectroscopy. They found that the widening of the band gap is mainly due to a valence band shift. Good agreement was reported for both techniques employed, the photothreshold of bulk a-Si$_x$C$_{1-x}$:H thin films as well as the valence band offset of c-Si(100)/a-Si$_x$C$_{1-x}$:H heterojunctions. The conduction band offset, however, showed only a minor compositional shift. Bittencourt *et al.* [182] presented a broader review of c-Si(100)/a-Si$_x$C$_{1-x}$:H band offsets confirming the results of Brown *et al.*.

In the following, the band alignment in a p-i-n structure with Si NCs as i-layer and doped a-Si$_x$C$_{1-x}$:H as selective contacts is deduced based on the electron affinity model introduced by Anderson [183, 184]. Values for the electron affinity of c-Si and a-Si$_x$C$_{1-x}$:H as well as the band gap of Si were taken from the literature. Tab. 7.1 summarizes the values and the data sources. The band gap was measured by spectral ellipsometry. The Fermi energy of phosphorous-doped a-Si$_x$C$_{1-x}$:H had been derived from photoelectron spectroscopy [85] and that of boron-doped a-Si$_x$C$_{1-x}$:H from activation energy measurements with a comparable sample [185, 186].

The band alignment, shown in Fig. 7.3 (a), was derived for intrinsic Si NCs assuming for simplicity a symmetric shift of the electron and hole energy levels by 0.2 eV each. This means that any effects of the embedding matrix are neglected. The band alignment for a specific Si NC size and embedding matrix is obtained by shifting the energy bands of the

Tab. 7.1: Band structure data used to derive the band structures shown in Fig. 7.3.

Material	Quantity	Value	Comment
c-Si	$q\chi$	4.05 eV	[42]
c-Si	E_G	1.12 eV	[42]
a-Si$_{0.95}$C$_{0.05}$:H	$E_{V,Si} - E_V$	0.56 eV	Photoelectron spectroscopy [181]
a-Si$_{0.95}$C$_{0.05}$:H	E_G	1.8 eV	Spectral Ellipsometry
a-Si$_{0.95}$C$_{0.05}$:H (n)	E_F-E_V	1.35 eV	[P]=$1\cdot10^{21}$ cm^{-3}, Photoelectron spectroscopy [85]
a-Si$_{0.95}$C$_{0.05}$:H (p)	E_F-E_V	0.5 eV	[B]=$4.4\cdot10^{20}$ cm^{-3} (SIMS) and [185]
3C-SiC	$q\chi$	4 eV	[187]
3C-SiC	E_G	2.4	[77]

Si NCs accordingly. Within the framework of this thesis most devices were realized with a partially crystalline 3C-SiC host matrix. Owing to the low band offsets to c-Si, the 3C-SiC matrix can in principle also contribute to charge carrier transport. Therefore, the band alignment for a 3C-SiC absorber is derived as a reference and shown in Fig. 7.3 (b). Small discontinuities can be seen in Fig. 7.3 at the Si NC/a-Si$_x$C$_{1-x}$:H(p) interface and the SiC/a-Si$_x$C$_{1-x}$:H(n) interface. In real systems, however, band alignment will depend on the interface band structure, i.e. on the size of the Si NC next to the interface, the interface matrix thickness and the surface conditioning. As all quantities are sensitive to experimental imponderables like the time between cleaning and selective contact
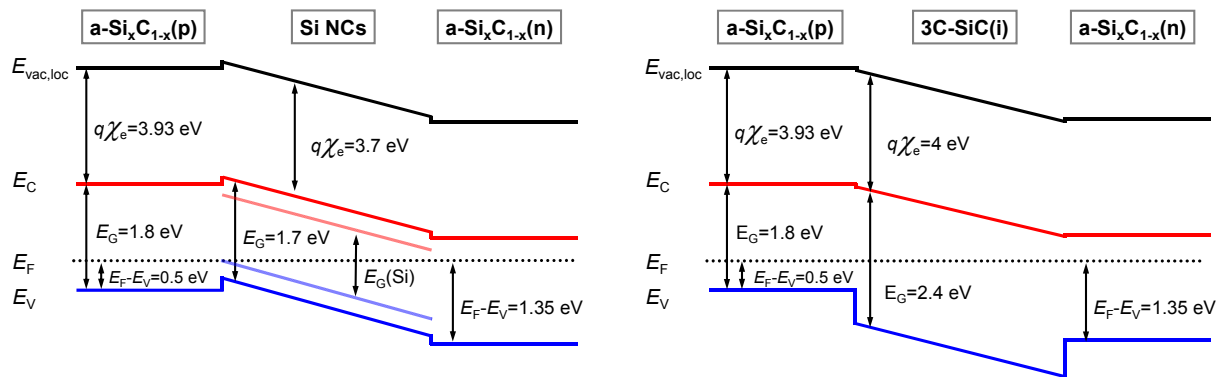
Fig. 7.3: (Left) Energy band diagram for a p-i-n structure with p- and n-doped a-Si$_x$C$_{1-x}$:H as selective contacts and an intrinsic Si NC absorber. The bulk Si conduction and valence bands are also indicated for orientation (light red and light blue). (right) Energy band diagram for a 3C-SiC absorber. The energy band diagrams were plotted based on the electron affinity model [183] and the values in Tab. 7.1. The exact course of the band bending was not calculated.

deposition, the band discontinuities are neglected in the framework of this thesis. According to Fig. 7.3 (a), transport barriers at the selective contact interfaces do not form for confinement energies of up to ±0.4 eV. Doped a-Si$_x$C$_{1-x}$:H therefore appears to be a viable material to selectively contact a Si NC superlattice.

The a-Si$_x$C$_{1-x}$:H layers used in the framework of this thesis had previously been developed for the passivation of Si wafers by Suwito within his doctoral thesis at Fraunhofer ISE [85]. An assessment of the Si passivation qualities as well as a characterization of structural (TEM, FTIR, SIMS) and electrical properties (surface photovoltage and photoelectron spectroscopy) can be found in his work. Furthermore, identical a-Si$_x$C$_{1-x}$:H thin films were employed in a-Si/c-Si heterojunction solar cells by Pysch [188, 189]. The a-Si$_x$C$_{1-x}$:H layers were prepared in the AK400M reactor shown in Fig. 5.2 with 30 sccm SiH$_4$, 30 sccm CH$_4$, 30 sccm Ar, 100 sccm H$_2$, 10 W RF power, 5 V bias voltage and a pressure of 0.3 mbar. For doped layers, H$_2$ was substituted with PH$_3$ (n-type) or B$_2$H$_6$ (p-type). The carbon content was determined by SIMS to be 5% (x=0.95) [85]. Before deposition of the doped layers, a very thin (few nm) intrinsic a-Si$_x$C$_{1-x}$:H layer was prepared on the surface of the Si NC film because intrinsic layers have much less deep defects [190, 191]. The i-layer is not included in the notation for simplicity, i.e. a-Si$_x$C$_{1-x}$:H(p) refers to the entire i-p stack hereinafter.

7.2.2 Sample preparation with a SiC-based absorber

All samples in this work were fabricated on 4 inch (100) oriented phosphorus-doped (1 Ωcm) FZ Si wafers as substrate. The basic cell process is illustrated in the flow chart in Fig. 7.4. It is applicable to absorbers that are not attacked by HF, such as SiC- or Si$_3$N$_4$-based materials. The process flow starts with a "RCA" cleaning sequence (for the definition of RCA and other cleaning processes see section 13.3) followed by growing a thermal SiO$_2$ in dichloroethylene at 1050°C and an annealing at 1070°C in nitrogen for 6 h. The resulting oxide thickness was 300 nm. The SiC/SRC multilayer is then deposited on the thermal oxide by plasma-enhanced chemical vapor deposition (PECVD) and then annealed at temperatures up to 1100°C in nitrogen atmosphere in a tube furnace. The wafer side with the multilayer is referred to as the front side hereinafter. Details on the SiC/SRC multilayer deposition and annealing as well as on other device specifics are reported in section 8.2.1. After thermal annealing, a-Si$_{0.49}$C$_{0.51}$ was deposited on the wafer rim as an etch mask. The wafers were then exposed to a remote hydrogen plasma for the passivation of defects in the multilayer stack. After a dip in HF (1%), a-Si$_x$C$_{1-x}$:H(n) was deposited on the front side. The thicknesses of all a-Si$_x$C$_{1-x}$:H layers (selective contacts as well as the SiC/SRC multilayer)

1.	Thermal oxidation (insulation A)
2.	PECVD multilayer
3.	Solid phase crystallization
4.	PECVD a-SiC:H Edge Mask
5.	Hydrogen passivation
6.	PECVD a-Si$_x$C$_{1-x}$:H(n)
7.	PECVD stabilization
8.	PECVD hard mask
9.	IJ structuring hard mask
10.	Structuring wafer
11.	IJ structuring hard mask
12.	PECVD insulation B
13.	IJ structuring insulation A and B
14.	PECVD a-Si$_x$C$_{1-x}$:H(p)
15.	IJ Removal stabilization
16.	SD ITO
17.	SD ITO

Fig. 7.4: Flow chart (left) for the basic cell process for membrane-based p-i-n devices with a SiC-based absorber and a-Si$_x$C$_{1-x}$:H as selective contacts. Plasma enhanced chemical vapor deposition (PECVD), sputter deposition (SD), inkjet printing (IJ) and wet chemical etching are used for deposition and structuring. The resulting structure (right) is indicated after specific process steps. The front side is facing down in this sketch.
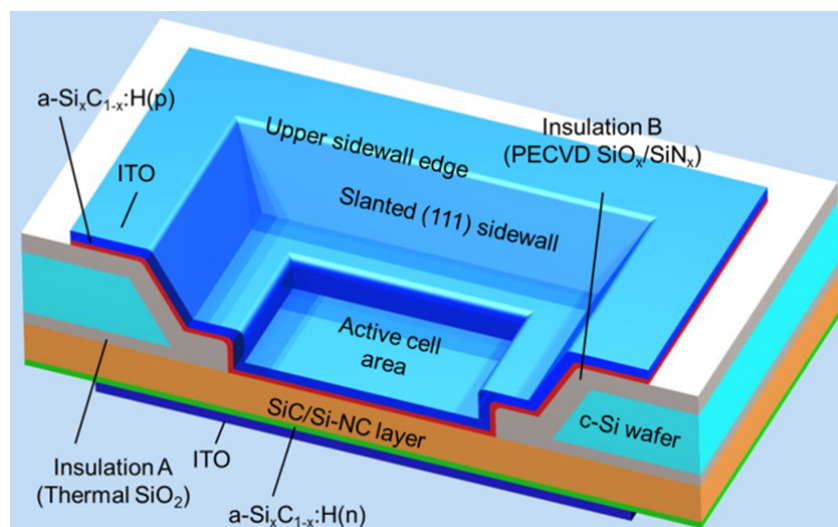
Fig. 7.5: Sketch of the membrane-based device. The figure was taken from [192].

were controlled by determining the deposition rate immediately before on trial samples. After the a-Si$_x$C$_{1-x}$:H(n), a 2 µm to 3 µm thick stabilization layer was deposited on the front side, followed by the deposition of a nitride layer as a hard mask on both sides. The layer stack on the back side (SiO$_2$/SiN$_x$) was then structured in buffered hydrofluoric acid (SiOETCH). All masking steps were done with as Schmid DoD 300 inkjet printer using a hydrocarbon wax hotmelt ink as masking material. The front side was fully protected by the hotmelt ink during all structuring steps with HF.

After structuring the back side layer stack and stripping the inkjet resist, the wafer is locally etched away in 30% potassium hydroxide (KOH) at 80°C. The device structure makes use of the anisotropic KOH etch character. KOH etches the <100> directions in c-Si 400 times faster and the <110> directions 600 times faster than the <111> directions. For the device structure used here, a 200 µm thick, (100) oriented Si wafer is used. All structures are of rectangular or square shape and aligned along <110>. With this alignment the shape is preserved during KOH etching. The anisotropy results in sidewalls that are 54.7° tilted towards the horizontal. This angle permits standard deposition techniques to be used in the subsequent process steps. The KOH etch stops at the thermal oxide between the wafer and the SiC/Si NC layer. In a further structuring step, the protruding SiO$_2$/SiN$_x$ hard mask on the front side was removed in buffered HF. In this step, the front side and also the membrane and the lower part of the sidewalls were protected with hotmelt resist to avoid etching of insulation layer A. Then, insulation layer B was deposited on the back side, i.e. on the wafer back surface, on the sidewalls and on the membrane. Insulation layer B consists of a stack of SiO$_x$ and SiN$_x$ deposited by PECVD. As the layers are slightly non-stoichiometric, they are denoted as SiO$_x$ and SiN$_x$. The insulation layers A and B were then opened locally on the membrane, again using inkjet printing. After cleaning with hot HNO$_3$ and an HF-Dip, a-Si$_x$C$_{1-x}$:H(p) was deposited on the back side. Then the stabilization layer on the front side was etched off in HF while the back side was protected with hotmelt resist. Afterwards, 70 nm indium tin oxide (ITO) was sputtered on the front and on the back. A shadow mask was used for the depositions of the a-Si$_x$C$_{1-x}$:H(p) and both ITO layers for lateral separation of different cells on the same wafer. Approximately 100 cells are realized on one 4 inch wafer, including test structures. At the end of the fabrication process, contact pads were formed on the ITO by silver ink.

The phosphorus-doped a-Si$_x$C$_{1-x}$:H(n) layers used in this work were chosen for their excellent thermal stability because after the deposition of a-Si$_x$C$_{1-x}$:H(n) further PECVD processes are carried out. Their temperature stability was analyzed by Suwito [85] by

monitoring the hydrogen content and the c-Si surface passivation quality after isochronal annealing at temperatures between 250°C and 500°C. He found that no degradation occurs up to 300°C, and only after annealing at 400°C for 30 min the effective charge carrier lifetime drops to 250 µs. As this is still a high value, an eventual degradation of the a-Si_xC_{1-x}:H(n) layer during the PECVD processes subsequent to its deposition can be neglected.

If the Si NC layer is not properly insulated from the wafer due to e.g. pinholes or a damaged insulation layer, the wafer might still contribute to the measured IV curve. The insulation layer stack B was chosen based on results with planar metal insulator semiconductor (MIS) test structures [193, 194]. The MIS structures in that work consisted of a shiny etched c-Si wafer, the dielectric layer under investigation (several different SiO_x and SiN_x) and an Al electrode prepared by electron beam evaporation. Thicknesses of 500 nm, 1000 nm and 1500 nm were chosen for investigation of the SiO_x layer. Furthermore, the effect of the preceding cleaning step on the insulation properties was investigated. Good insulation was achieved with 500 nm SiO_x on HNF cleaned surfaces. Several etch processes in HF are carried out after the deposition of insulation layer B. In two processes (No. 13 and 15 in Fig. 7.4) the insulation layer B is protected by inkjet resist during HF etching. However, if the masking property of the resist fails, the etchant will also attack the insulation layer B. Failure of the inkjet resist is discussed in the next section. At the end of processes No. 13 and 15 a dip in HF (1%) as a cleaning step is carried out. To minimize etching of insulation layer B, the SiN_x layer was prepared on top of the SiO_x layer.
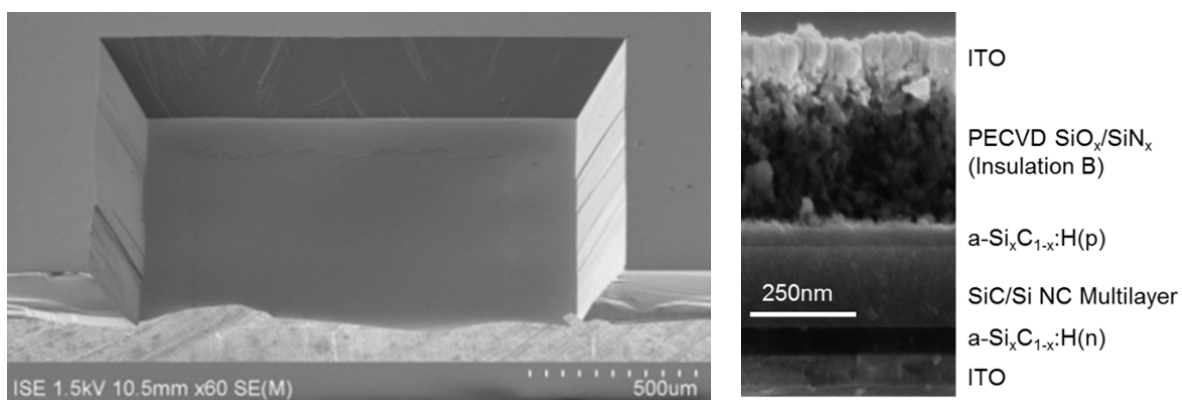
Fig. 7.6: (Left) SEM picture [195] of a trial sample with a 200 nm SiO_2 membrane. The opening of insulation layer B can clearly be distinguished. (Right) Layer sequence of the free-standing membrane in the region where the insulation layer is not opened [195]. For real devices, the a-Si_xC_{1-x}(p) layer was prepared after the insulation layer B.

7.2.3 Sample preparation with a SiO$_2$-based absorber

With the introduction of two additional process steps, the process flow described above (Fig. 7.4) is also suitable to prepare SiO$_2$-based devices. The two additional process steps are needed for selective etching of the insulation layer A (thermal SiO$_2$ in Fig. 7.4) over the SiO$_2$/Si NC layer.

For this means, an additional Si$_3$N$_4$ layer was implemented between the thermal oxide and the Si NC layer in the framework of this thesis. Si$_3$N$_4$ can be etched in boiling concentrated phosphoric acid (H$_3$PO$_4$), which does not etch SiO$_2$. After insulation layer B was opened in HF as described above (step 13 in Fig. 7.4), the inkjet resist was stripped and the Si$_3$N$_4$ layer opened in hot H$_3$PO$_4$. This implies 4 additional wet chemistry steps compared to the process flow for SiC/Si NC membranes (H$_3$PO$_4$ etch/rinse/HF/rinse). The Si$_3$N$_4$ was prepared by sputtering and optimized for minimized hydrogen content to avoid blistering during high-temperature annealing (1150°C, 60 min). Simple planar test structures were used to estimate the etch rate. However, the etch rate changes upon high-temperature annealing and possibly also due to the composition of the SiO$_2$/Si NC layer. Process control was therefore done with real samples using a scanning electron microscope. Fig. 7.7 depicts scanning electron micrographs of a membrane after partial etching of the Si$_3$N$_4$ intermediate layer. The original thickness was 100 nm. The Si$_3$N$_4$ layer can be well distinguished from the Si NC layer, the thermal SiO$_2$ and the PECVD SiO$_x$ layer. After the H$_3$PO$_4$ etch, 30 nm Si$_3$N$_4$ still persisted in this sample.
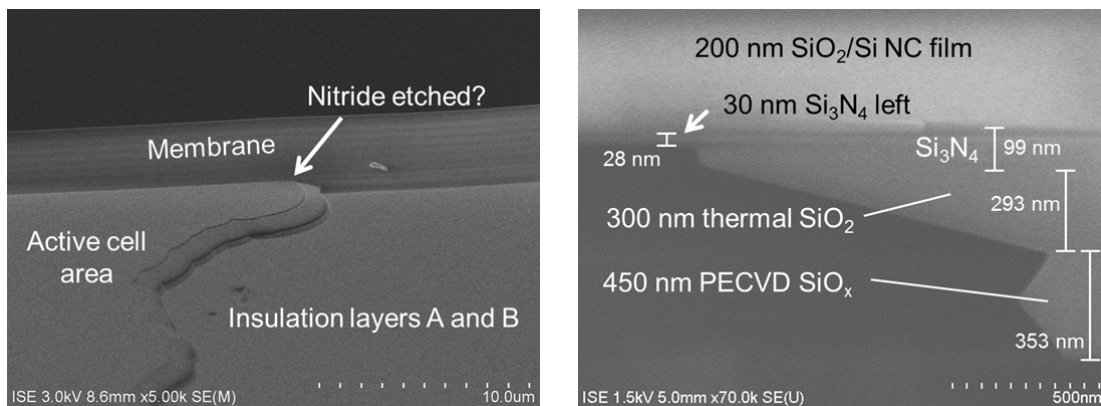
Fig. 7.7: (Left) Overview SEM picture of the free standing membrane at the rim of the insulation layers. In higher resolution (right), the micrograph reveals that the originally 100 nm thick Si$_3$N$_4$ layer was etched to about 30 nm. The insulation layer B (PECVD SiO$_x$) can clearly be distinguished from the insulation layer A (thermal SiO$_2$).

7.2.4 Modifications of the basic process flow

For a number of samples, several modifications to the basic cell process were made. They are summarized here in brief with reference to the basic process flow depicted in Fig. 7.4. Understanding of the modifications is no requirement for the lecture of the subsequent sections.

1. The amorphous SiC layer on the wafer rim (step 4) can as well be deposited after the nitride hard mask (step 8). In some cases this sequence demonstrated a better performance of the masking layer during the KOH etch (step 10). This is attributed to the masking layer step coverage.

2. As discussed below (section 0), the most critical issue besides mechanical stability is an unwanted etching of insulation layer B. A thicker SiO_x/SiN_x stack can be prepared to minimize this problem. However, the thickness is limited by the maximum etch time permitted of the inkjet resist. The use of two (instead of one) structuring steps circumvents this problem, but implies at least 4 more wet chemical processes (rinse/HF etch/rinse/strip). Additionally, a H_3PO_4 etch can be included between the two HF etches in the two-step sequence. This sequence allows the use of a $SiO_x/SiN_x/SiO_x$ layer stack as an insulation layer B by making use of the selectivity of H_3PO_4 over SiO_2.

3. The process steps 15 and 16 can be interchanged to enhance the mechanical stability of the membrane.

7.3   Chapter summary

In this chapter, the development of a device for the substrate-free characterization of Si NC films prepared by high-temperature annealing has been presented. The need for high-temperature annealing imposes severe requirements to the device design and fabrication technologies. Available device realizations have been reviewed and several limitations have been identified. The key challenge consists in establishing selective contacts to the Si NC film that extract the quasi-Fermi level splitting to the metal contacts, do not themselves contribute to the device IV characteristics, and do not affect adversely Si NC formation.

A membrane-based device has been presented that meets all requirements. Selective contacts can be established by doped a-Si_xC_{1-x}:H after the completion of all high-temperature processes, and the process route is applicable with slight modifications to SiC-Si_3N_4- and SiO_2-based membranes.

8 Detailed analysis of membrane-based p-i-n solar cells

This chapter covers the general characterization of the membrane-based cell structure as well as a detailed photovoltaic characterization of the SiC/Si NC material as the absorber layer in a membrane-based p-i-n solar cell. Prerequisites for using the device to investigate the Si NC materials are the mechanical stability of the membrane itself and the insulating properties of the insulation layers. Insulation layer failure renders a characterization of the Si NC membare practically impossible. Therefore, the overall device is characterized first with emphasis on proving the origin of the photovoltaic properties. Then, properly working devices are used to investigate the photovoltaic properties of the SiC/Si NC material. Optical modeling of the p-i-n layer stack is used in conjunction with a spectral response measurement to demonstrate that the photocurrent is generated in the Si NC layer. Illumination-dependent IV measurements are modeled with the uniform field approximation to determine the mobility lifetime product, which is the fundamental recombination and transport property. The general device analysis was published in [195] and [161]. The illumination-dependent IV analysis was published in [192].

8.1 Characterization of device functionality and failure

8.1.1 Mechanical stability

The concept of preparing free standing membranes that are insulated from the wafer substrate implies several technological challenges. The membranes are very thin and mechanically fragile. Furthermore, strain between the single layers of the membrane layer stack can reduce mechanical stability. The poor mechanical properties are especially critical as many wet-chemical cleaning steps are involved. Especially the membrane-devices with SiO_2-based NC layers turned out to be very critical. In this section the reason for their failure will be discussed.

To test the fabrication process for SiO_2-based membrane devices, standard PECVD SiO_2 layers were used in the beginning to substitute the SiO_2/Si NC layer. This led to a bunch of technological problems, most of which could be ascribed to the surface roughness of the

PECVD SiO_2 layer. More advanced samples were fabricated with SiO_2/Si NC multilayers that were to be employed as the solar cell absorber in a later Si QD solar cell. The SiO_2/Si NC multilayer preparation was described in Hartel *et al*. [196]. In the framework of this thesis, eight runs with oxide-based devices were processed. For six runs, SiO_2/Si NC multilayers were used. Even though each of these consisted of only a few wafers, several membrane structures were successfully processed. However, a photovoltaic response of the SiO_2/Si NC membrane could not be shown for any of these structures.

Breakage of the membrane during the very last process steps diminished the yield of the last and most optimized run critically. Fig. 8.1 shows a structure that survived at least until the structuring of the insulation layer B (seething H_3PO_4, step 13, cf. Fig. 7.4). The active cell area is missing; it was ripped out exactly along the rim of insulation layer B. The picture illustrates the fragility of the structures. The impact of the structuring step on the mechanical stability was evaluated with reference structures for which the insulation layer was not structured (step 13, cf. Fig. 7.4).

The numbers and statistical occurrences of mechanically faultless structures at the end of the cell process are summarized in Tab. 8.1. The result clearly demonstrates that the active cell area without the mechanical support of the insulation layer is extremely prone to breakage. As none of the very few mechanically faultless cells structures showed a photovoltaic response of the active cell area, these samples were not investigated further.
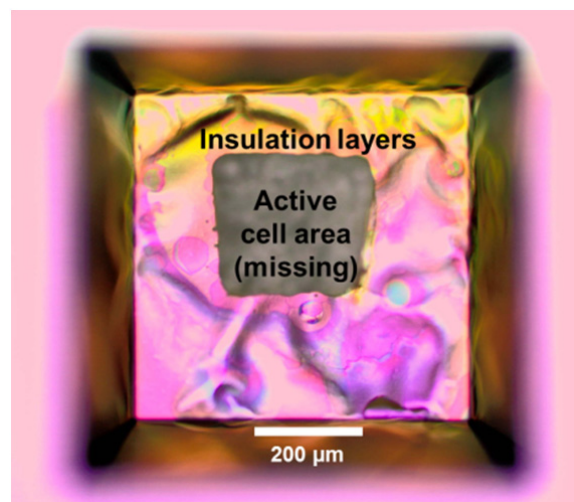
Fig. 8.1: Optical micrograph of a structure with a SiO_2/Si NC layer of the most optimized run at the end of the fabrication process. The active cell area was torn out of the membrane exactly along the rim of the insulation layers (A and B). The Figure was adapted from [197].

Tab. 8.1: Overview of mechanically faultless cells and reference structures at the end of the cell process. The reference structures are mechanically more stable because the insulation layer B is not opened (no active cell area).

Wafer No.	Mechanically faultless cells (No. / %)	Mechanically faultless reference structures (No. / %)
1	0 / 0 %	8 / 47 %
3	1 / 1.3 %	6 / 35.3 %
4	3 / 3.8 %	6 / 35.3 %
5	1 / 1.3 %	7 / 41.2 %
9	1 / 1.3 %	8 / 47 %
14	0 / 0 %	6 / 35.3 %
16	0 / 0 %	2 / 11.8 %
18	3 / 3.8 %	10 / 58.8 %

8.1.2 Insulation layer characterization

The concept of characterizing the Si NC film without any wafer influence depends crucially on the insulating properties of the insulation layers. The insulation layers where chosen carefully with appropriate thickness, see section 7.2.2. However, in many devices the insulation layer stack B was shunted and a large part of the signal was due to the wafer. To ensure reliable characterization of the Si NC p-i-n diode it first has to be proven electrically for each structure that the photovoltage and the photocurrent stem only from the "membrane diode" itself and not from the wafer. Then, further characterization can be carried out. A potential contribution of the wafer to the photovoltaic properties of the overall device can be thought of as an additional "wafer diode" parallel to the "membrane diode". In order to separate the membrane diode characteristics from the "wafer diode", the different device parts were separately illuminated and the overall IV curve was measured. In principle the device can be illuminated from either side. In order to demonstrate the device functionality, however, the structured and therefore critical side was illuminated to detect a possible contribution of the wafer more easily.

Fig. 8.2 shows IV curves of one membrane cell in dark (A), under illumination of the entire wafer (B) and with shadow masks (C, D). Mask C leaves only the membrane illuminated, but shadows the surrounding wafer and contacts. Under mask D, only the "wafer diode" is

illuminated and light can reach the membrane cell only by reflection at the slanted sidewalls. For the cell shown here, the IV curve with mask D reproduces the IV curve under full area illumination. This hints at a damaged insulation layer and a large wafer contribution to the overall IV curve. The spatially resolved charged carrier collection properties can be investigated with light beam induced current (LBIC) maps as described in section 13.2.10. Fig. 8.3 (a) shows an LBIC map along with the (mirrored) dark field micrograph of the same cell whose IV curves were shown in Fig. 8.2. A photocurrent from the slanted sidewalls can be seen in the LBIC image. Exactly in this area the dark field
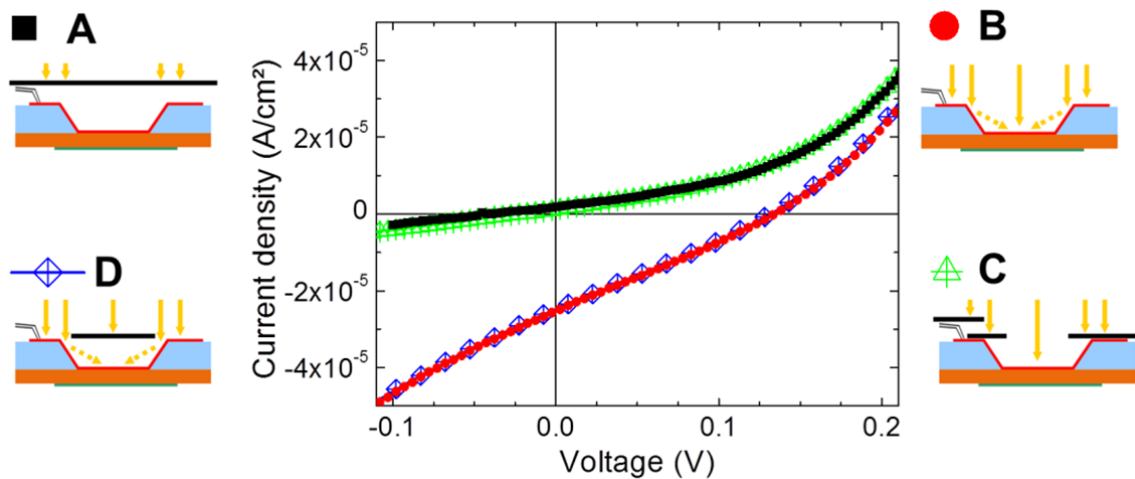
Fig. 8.2: *Current-voltage curves in dark (A), under full area illumination (B) and under illumination with shadow masks (C, D).*
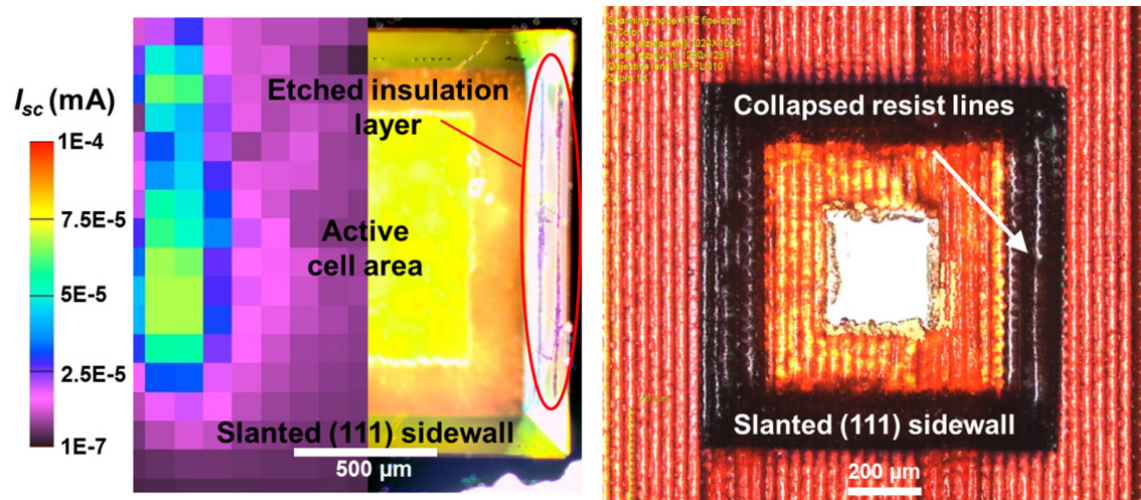
Fig. 8.3: *(Left) Light beam induced current (LBIC) map combined with the dark field micrograph of a finished membrane-based p-i-n solar cell, adapted from [197]. The LBIC map is mirrored along the vertical center line. The area of maximum current corresponds to the etched insulation layer. (Right) Optical micrograph of an inkjet printed membrane before structuring of insulation layer B (process step 13, cf. Fig. 7.4).*

image reveals two line shaped etch damages. The insulation layer B is damaged here, giving rise to photocurrent collection from the wafer substrate in this area. The line shaped etch damage can be attributed to failure of the inkjet resist during wet chemical etching in step 13 or 15 (flow chart in Fig. 7.4). Fig. 8.3 (b) depicts an optical micrograph of an identically processed structure in step 13 of the fabrication process. The inkjet resist is printed in lines as the print head moves in one dimension over the sample. The typical line pattern of the inkjet resist can be seen in Fig. 8.3 (b) on the wafer surface, the membrane, and the slanted sidewalls. However, the line pattern exhibits a different period on the right hand side slanted sidewall. Several ink lines merged here because the inkjet resist fell down the steep (54.7°) sidewalls. Therefore, the line pattern in Fig. 8.3 (a) suggests that the insulation layer damage seen was caused by a collapse of the inkjet resist lines on the slanted sidewalls as seen in Fig. 8.3 (b). For a more detailed characterization with higher spatial resolution, the insulation layer failure was investigated with electron beam induced current (EBIC). The working principle of EBIC is described in section 13.2.11. Fig. 8.4 shows optical micrographs, scanning electron micrographs and EBIC images for one structure. The
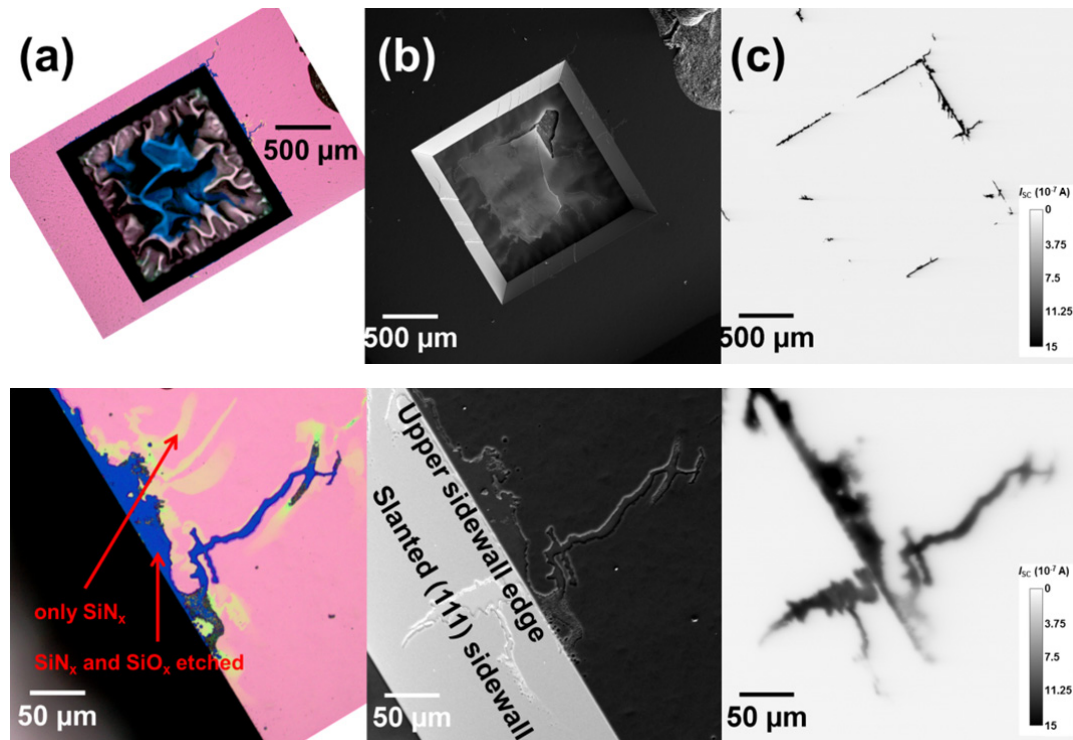
Fig. 8.4: (a) Optical micrograph, (b) scanning electron micrograph and (c) electron beam induced current (EBIC) micrograph of a finished membrane-based p-i-n solar cell with distinct damage of the insulation layer B along the upper sidewall edge. The lower row shows a detail of the overview picture shown in the upper row. The figure was adapted from [161].

lower row depicts details of the upper rim of the (111) sidewall. In the optical micrograph (Fig. 8.4 (a)) the insulation layer appears pink. It consists in this case of 450 nm SiO_x and 50 nm SiN_x. Along the upper sidewall edges, the insulation layer appears to be damaged (blue in the optical micrograph). Around the blue area, a blurred yellow region can be seen. The etch attack of the blue area is also seen in the scanning electron micrograph (SEM, Fig. 8.4 (b)). However, as the yellow region cannot be detected in the SEM image (b), only a very thin part of the insulation layer is etched here. The EBIC image (c) shows a clear current signal from the region that appears blue in the optical micrograph. No current is detected from the region that appears to be undamaged in the SEM and seen yellow in the optical micrograph. The images shown here do not permit to conclude to which extend a certain layer is etched. However, they demonstrate that once the etch damage gives rise to an EBIC signal, it is also clearly detectable in the optical micrograph. Furthermore, even minor damage which does not yet degrade the insulation properties is already clearly visible in the optical micrograph.

EBIC and LBIC are current-sensitive methods and consequently do not allow to draw conclusions on the magnitude of the photovoltage. The latter is provided with IV measurements employing shadow masks as shown in Fig. 8.2. and Fig. 8.5. However, the shadow mask method does not permit to measure a contribution from the slanted sidewalls due to the limited spatial resolution. Therefore, the IV characteristics of the entire structure were further analyzed with a network simulation for different cases of failing insulation layers as described in section 13.1. The results of the network simulation demonstrate that the measured voltage is affected to lesser extent than the current by
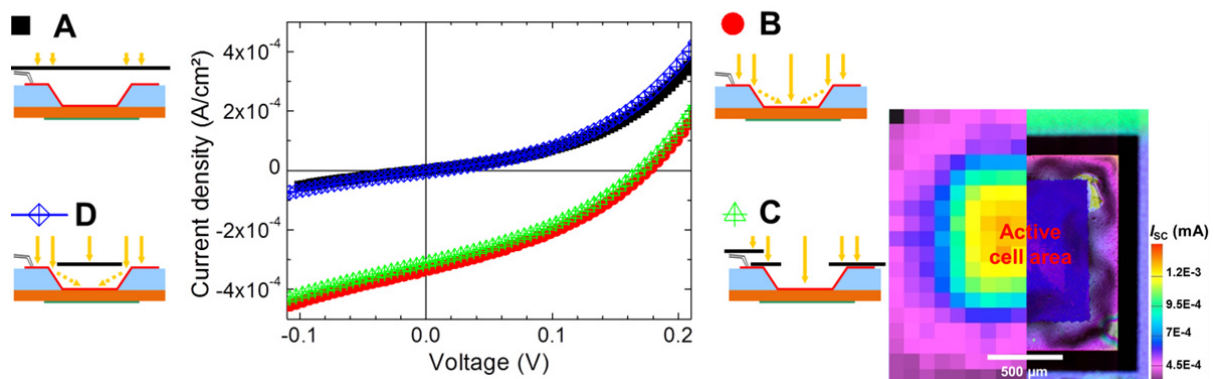

Fig. 8.5:   *(Left) Current-voltage curves in dark (A), under full area illumination (B) and under illumination with shadow masks (C, D).(Right) Light beam induced current map of the corresponding cell combined with an optical micrograph (mirrored). The LBIC map was taken from [197].*

insulation layer failure. Therefore, current-sensitive methods are viable to qualify the overall device performance and the simulation results in conjunction with the LBIC map permit a clear proof that the entire IV curve is free of any wafer contribution.

The exemplary study of individual structures with light microscopy, electron microscopy and electron beam induced current permits a clear assignment of defects that are visible in the light microscope to failure of the insulation layer. After selection of those structures that appeared to be free of defects in the light microscope, a clear correlation was established between the results of IV and light beam induced current measurements. When an IV curve was attributed to the membrane but not to the wafer based on the shadow mask procedure, LBIC measurements confirmed this behavior. An example of this behavior is shown in Fig. 8.5. The IV curve with shadow mask D resembles very well the dark IV curve and the application of mask C demonstrates that the IV curve is due to only the active cell area on the membrane. The LBIC map finally confirms this behavior.

The following procedure was established to qualify the overall device performance: In a first step, all devices are analyzed by optical microscopy with special emphasis on the upper sidewall rims (Fig. 8.4). Then, the insulation layer on the slanted sidewalls is checked with dark field microscopy (Fig. 8.3). If the structure appears to be free of defects, IV curves in dark, under full area illumination and with shadow masks C and D are measured (Fig. 8.2. and Fig. 8.5). If the IV curves demonstrate that the wafer does not influence the measurement, the structure is qualified as "good" and selected for further characterization. Within the framework of this thesis, an LBIC map was recorded for all "good" structures in this work and confirmed the result.

8.2   Photovoltaic characterization of membrane-based p-i-n devices

8.2.1 Sample description

Membrane-based p-i-n solar cells for a detailed photovoltaic analysis were fabricated with two groups of SiC/Si NC multilayers originating from the two institutes Fraunhofer ISE (Freiburg, Germany) and CNR-IMM (Bologna, Italy). The two groups are referred to as "CNR" and "ISE" hereinafter. Both multilayer materials (ISE and CNR) were prepared by PECVD with the precursor gases SiH_4, CH_4 and H_2 in a similar deposition process regime, and both were made up of alternating bilayers of stoichiometric SiC and Si-rich Si_xC_{1-x}. The two fabrication routes differ by the exact PECVD reactor geometry and the exact course of the annealing ramps. The material that was prepared at Fraunhofer ISE was described in detail in chapter 5. Details on the CNR multilayer fabrication and its structural

characterization can be found in [109, 111, 198]. Tab. 8.2 summarizes the PECVD processes for the precursor layers and reports their Si content. The thermal annealing was performed at 1050°C for 60 min in N_2 in case of the ISE material, and the CNR samples were annealed at 600°C for 4 h and then at 1100°C for 30 min in N_2. An encapsulation layer was used for the CNR material to protect the SiC multilayer during the high-temperature step. Details on the encapsulation layer and its removal were reported in [198]. Both material systems exhibit very similar structural properties. Apart from the Si content, the main differences arise from the higher annealing temperature of the CNR material and the encapsulation layer. Both materials lose their multilayer structure upon solid phase crystallization (see section 5.5) and the SiC/Si NC layer has to be considered a random mixture of Si and SiC NCs in both cases. Due to the higher annealing temperature, the CNR material exhibits a higher Si crystalline volume fraction. Moreover, the encapsulation layer prevents the formation of Si_3N_4 phases in the CNR material, and the nitrogen impurity concentration is limited to 1×10^{17} cm^{-3} as measured by SIMS. This value is not higher than expected based on the literature on 3C-SiC by CVD (see [126] and section 5.6.4) The in-depth characterization presented in this chapter was exclusively carried out with CNR multilayers. The ISE multilayer was only used for the first runs to test the device fabrication process and to establish a reliable characterization scheme. The cell results of all properly working devices are summarized in Tab. 8.3 together with the multilayer parameters (layer thicknesses, Si content, number of bilayers) at the end of this chapter.

Tab. 8.2: Overview of PECVD processes employed for multilayer fabrication. The RF frequency was 13.56 MHz in all cases.

Source	Composition x	SiH_4 (sccm)	CH_4 (sccm)	H_2 (sccm)	Pressure (mbar)	RF power (W)	Substrate temperature (°C)
ISE	0.77	10	10	100	0.3	65 W	280°C
ISE	0.63	7	20	100	0.3	65 W	280°C
ISE	0.51	7	60	100	0.3	65 W	280°C
CNR	0.65	6.1	70	10	0.95	4 W	350°C
CNR	0.65	6.1	70	10	0.8	4 W	350°C
CNR	0.5	1.6	70	10	0.95	4 W	350°C

8.2.2 Optical properties and external quantum efficiency

The external quantum efficiency (EQE) connects photon absorption and charge carrier collection and determines the short-circuit current of the solar cell [199]. It is thus the relevant optical quantity for solar cell operation. In the limit of ideal charge carrier collection, the external quantum efficiency equals the optical absorption.

As the contact layers also absorb part of the incident light and the SiC/Si NC layer is thinner than the absorption depth, the absorptance of the SiC/Si NC layer depends on the entire solar cell layer stack. Therefore, an optical simulation of the entire layer stack is required in order to quantify the absorptance of the SiC/Si NC and the other layers. The characterization of the p-i-n solar cell optical properties was carried out in three steps: The optical constants of the individual layers were determined by spectrophotometry and spectral ellipsometry. The entire p-i-n solar cell was then simulated using the previously determined optical constants to quantify the absorptance of each particular layer. In a third step, the external quantum efficiency was measured and compared to the absorptance.

For the ITO and a-Si$_{0.95}$C$_{0.05}$:H layers the optical constants were determined by variable angle spectral ellipsometry. The optical properties of the SiC/Si NC layer were obtained from a simulation [148] of measured reflection and transmission spectra using the effective medium approximation and the known compositional and structural data. The SiC/Si NC layer was treated as a mixture of SiC (77%) and Si (23%) with 10 nm SiC layers underneath and on top. All optical simulations were carried out using the open source program OPTICAL [148], an implementation of a Fresnel coefficient approach applied to multilayers. This program allows the simulation of composite materials that are approximated by an effective medium and arranged in any stack of coherent and incoherent layers.

The absorptance of each layer as well as the total absorptance, reflectance and transmittance is shown along with the device structure in Fig. 8.6. The maximum of the SiC/Si NC absorptance is at 500 nm. A maximum photo-generated current (optical limit) of $J_{\text{gen}} = 5.97 \, \text{mA/cm}^2$ was estimated from the integrated SiC/Si NC absorptance under the assumption of $EQE = 1$. Fig. 8.6 shows that the selective contact on the illuminated side (a-Si$_x$C$_{1-x}$:H(p)) absorbs considerably for wavelengths <520 nm. The ITO contribution in Fig. 8.6 is displayed as the sum of both layers. Besides absorption in the ultraviolet, the ITO also absorbs for wavelengths >750 nm. However, this
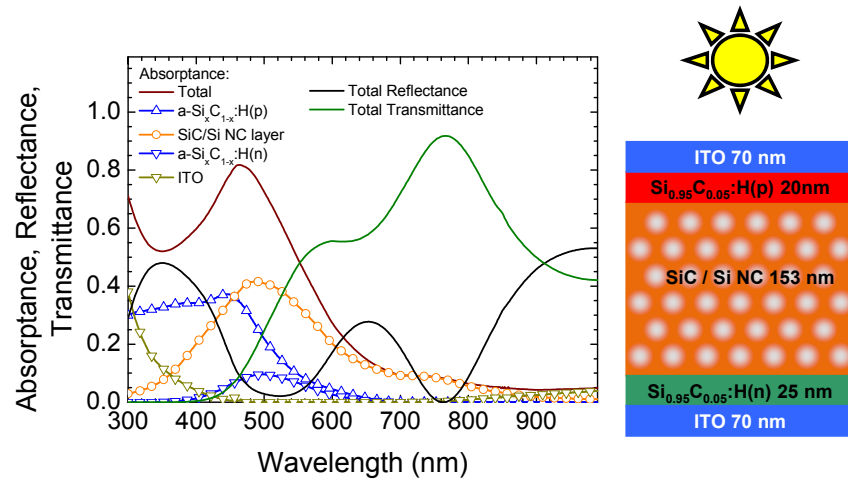
Fig. 8.6: Absorption, reflection and transmission of the entire structure (lines) and the absorption of the single device layers (lines with symbols). The simulated structure is shown right (taken from [192]).

contribution is attributed to free carrier absorption and therefore does not generate electron-hole pairs. The external quantum efficiency (EQE) is most commonly obtained from a measurement of the differential spectral response at a certain bias light level. For this means the device is held at constant operation conditions by bias light illumination and the differential spectral response is measured using monochromatic chopped light [200].

Because of the small device area (1 mm²) and the low light intensity of the monochromatic light spot this approach was not viable for the membrane-based solar cells. For this reason, Fourier transform photocurrent spectroscopy was employed as recently introcuded by Petermann *et al.* [201]. This method uses supercontinuum laser light, which is dispersed, chopped, collimated and then focused on the active cell area. The key element is a chopper wheel, which modulates each color of the dispersed laser beam with a different frequency. The photospectrum is obtained as the Fourier transform of the measured photocurrent time series. The wavelength calibration is established with monochromatic filters (600 nm, 700 nm, 800 nm, 900 nm, 1000 nm, 1200 nm). A reference measurement is made with a calibrated Si photodiode under identical illumination to calculate the spectral response. Details of the method and the setup employed for this experiment are described in [201]. As not all wavelengths can be selected at once, five measurements with a spectral width of about 100 nm were recorded around the center wavelengths 500 nm, 600 nm, 700 nm, 800 nm and 900 nm. A change of the spectral operation region implies slightly changed settings of several optical elements. As a consequence, each spectrum is recorded at a different bias light level and also at a slightly different spatial position on the active

cell area. For this reason, their absolute signal levels do not match. However, all spectra exhibit an exponential decrease with the wavelength,

$$SR_i(\lambda) = c_i e^{-\lambda}, \qquad (8.1)$$

with proportionality constants c_i. For further evaluation the spectra were scaled by a constant prefactor c_i with the constraint of minimized square deviation from $c_i=1$:

$$\sum_i (c_i - 1)^2. \quad (8.2)$$

A reference solar cell with known spectral response was measured in parallel as a consistency check. The qualitative agreement with the calibrated spectral response measured with standard solar cell characterization tools was very good. The error due to the non-constant illumination conditions is about 20%. The external quantum efficiency calculated from the scaled single spectral response spectra is shown in Fig. 8.7 (left) along with the absorption spectra of Fig. 8.6. Within the measured EQE range the SiC/Si NC and the a-Si$_x$C$_{1-x}$:H(p) layer exhibit a similar decay with the wavelength. However, the SiC/Si NC absorption is red-shifted respective to the a-Si$_x$C$_{1-x}$:H(p) absorption. The EQE also exhibits this red shift and the spectral shape of the EQE is very similar to the SiC/Si NC absorption spectrum. While above 680 nm the a-Si$_x$C$_{1-x}$:H(p) absorptance is zero, the EQE vanishes at 930±50 nm and the SiC/Si NC absorptance only at 1000 nm. This is being seen more clearly in the logarithmic representation in Fig. 8.7. As the EQE spectrum is proportional to the SiC/Si NC spectrum both below and above 700 nm it can be inferred that the a-Si$_x$C$_{1-x}$:H(p) absorption does not contribute to the EQE. The free carrier absorption in the ITO above
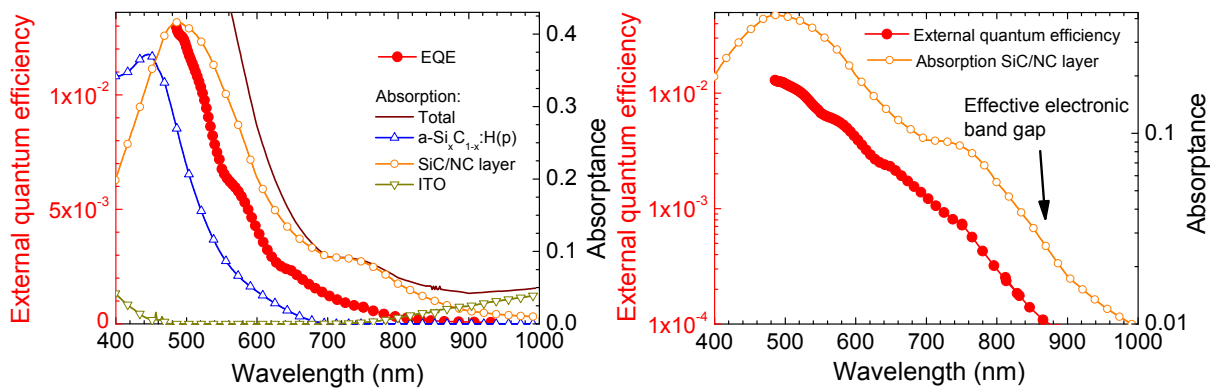
Fig. 8.7: *(Left) External quantum efficiency and absorption spectra of selected device layers of cell G193-E16 (see also Fig. 8.6). (Right) External quantum efficiency and absportion spectrum in logarithmic representation. No external quantum efficiency could be detected for wavelengths $\lambda >930±50$ nm. The error arises from the spatial distribution of the wavelengths at the chopper wheel position.*

750 nm does not contribute positively to the EQE either. The measured photocurrent therefore has to be ascribed to the SiC/Si NC membrane alone without contributions from the a-Si$_x$C$_{1-x}$:H or ITO layers. The absorption reaches further into the infrared, but the EQE is zero already for wavelengths λ >930±50 nm. According to the definition of the EQE as the ratio of detected photons per incident photons at a given wavelength, the EQE onset defines a threshold wavelength λ =930 nm for photon absorption and subsequent charge carrier collection. The EQE threshold wavelength constitutes an effective electronic band gap $E_{G,\text{electronic}} = 2\pi\hbar c/\lambda$ =1.33 eV of the absorber material. For lower photon energy, photons are absorbed but the charge carriers are not collected any more. This can be attributed to defect states with very inefficient transport, similar to band tail states in amorphous semiconductors.

8.2.3 Current-voltage analysis

Typical IV curves in dark and under illumination of a membrane p-i-n solar cell are shown in Fig. 8.8. The measurements were taken at 25°C sample temperature and illumination was set to 1000 W/m² if not otherwise specified. The open-circuit voltage of the cell shown in Fig. 8.8 is 282 mV and the short-circuit current density 0.339 mA/cm². The fill factor (FF) is 36.2%. The light IV curve in Fig. 8.8 exhibits a pronounced short-circuit conductance (slope at 0 V) which is not present in the dark curve. The dark and light curves are seen to cross over at V_{FB}=400 mV. The cross over is a common feature for Si and chalcopyrite thin film solar cells [202] and can be explained with a photo shunt or a voltage-dependent collection function as described in section 2.4. The experimental J_{SC} value is only 0.057×J_{gen}, indicating highly recombinative defects in the depletion region. The characteristics of the IV curves shown in Fig. 8.8 (shunt under illumination, cross over of light and dark IV curves, fill factor, J_{SC} and V_{OC} values) is typical of all devices investigated in the framework of this thesis. In the following, a detailed analysis is exemplarily performed for this cell. An overview of all properly working cells is given in Tab. 8.3.

The peculiar IV characteristics (shunting, high series resistance, low fill factor) do not permit an unequivocal fit of the one-diode model to the data as it is usually done for c-Si solar cells. Therefore, a detailed IV curve analysis was undertaken in two steps. First, the dark curve was analyzed to determine the series resistance, parallel resistance and the ideality factor. In a second step, the dark diode parameters were used to fit the light IV curve according to the uniform field approximation (Eq. (2.34) with the collection function
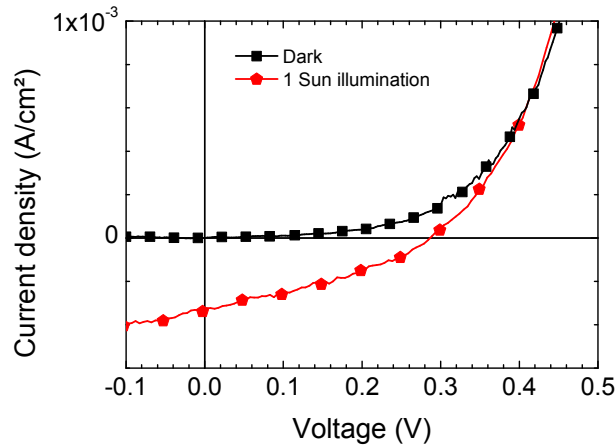
Fig. 8.8: Dark and light IV curve of cell G193-E16. The IV curve characteristics are representative of all devices investigated in the framework of this thesis. The Figure was adapted from [192].

of Eq. (2.35)). The dark parallel resistance R_P=11808 Ωcm² was calculated as the slope of the dark IV curve around 0 V (short-circuit resistance). The series resistance and diode ideality factor were then extracted using the small conductance method according to Werner [203]. This method makes use of three different representations of the same IV data, commonly referred to as "Werner plots", shown in Fig. 8.9 for cell G193-E16. Each of the three plots permits to determine a value for the series resistance and the ideality factor from the slope or the y-axes intercept of a linear regression. The mean value is regarded as a good estimate for the series resistance (or ideality factor) if all three plots yield consistent values (low standard error of the mean value). The majority of IV curves investigated in the framework of this thesis had consistent values both for the series resistance and the ideality factor.
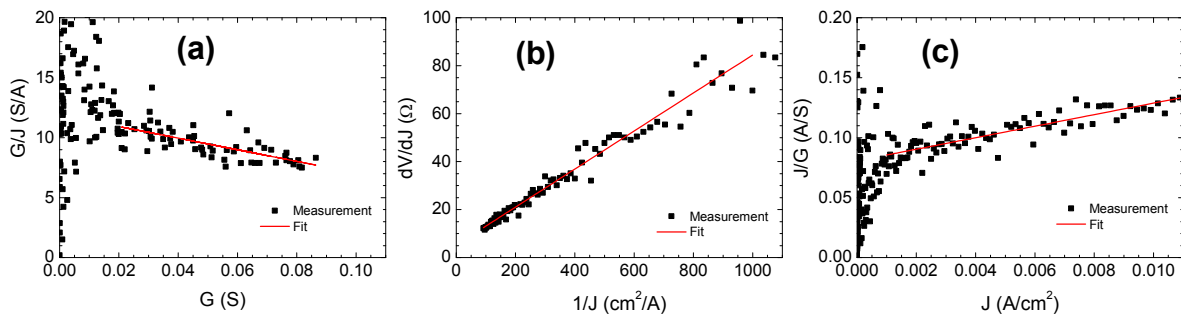
Fig. 8.9: Small conductance analysis (Werner plots) of the dark IV curve for the extraction of series resistance and ideality factor. The three plots are different representations of the same set of data. The resulting values of the IV curve shown here are R_S=4.5±0.5 Ωcm² and n=3.2±0.1.

8.2.4 Illumination-dependent current-voltage analysis

Illumination-dependent IV measurements were employed with the objective to determine the $(\mu\tau)_{\text{eff}}$ product, which is the fundamental transport and recombination property of the absorber material. The light IV curve in Fig. 8.8 exhibits a pronounced photo shunt indicating strong recombination in the absorber layer. The following analysis is governed by the idea of a thin, undoped, and recombinative absorber within the electrical field between the highly doped regions. This case can be described with reasonable simplifications with the uniform field approximation introduced by Crandall [34] as described in section 2.4 (Eqs. (2.34) and (2.35)). The advantage of the uniform field approximation is the analytical description of the entire light IV curve. "Entire light IV curve" refers to the curve between short-circuit and open-circuit or cross over conditions. The light IV function according to Eqs. (2.34) and (2.35) involves eight parameters $(J_{\text{gen}}, J_0, n, R_{\text{S}}, R_{\text{P}}, V_{\text{FB}}, (\mu\tau)_{\text{eff}}, d)$. The series resistance, parallel resistance and the ideality factor were determined from the dark curve analysis as described in the previous section (8.2.3). Furthermore, the flat-band voltage was obtained from the cross over voltage. The absorber layer thickness and the maximum short-circuit current were determined by the optical simulation discussed in section 8.2.1. This procedure allows to fix all parameters except J_0 and $(\mu\tau)_{\text{eff}}$, which are treated as free fit parameters. For an unequivocal determination of these two parameters, the illumination-dependent current-voltage (IV) measurements were fitted simultaneously with the same set of parameters according to Eqs. (2.34) and (2.35).

Complementary to the application of the uniform field approximation after Crandall [34], the variable illumination method after Merten *et al*. [35] was applied. The latter relies on a plot of the short-circuit resistance against the short-circuit current, see Eq. (2.38). As this method uses only directivly accesible IV curve parameters, a fit of the IV curve is not necessary. Eq. (2.38) illustrates that the recombination appears in the IV curve as an illumination-dependent short-circuit resistance and permits to extract the drift length from the slope of a plot of R_{SC} over $1/J_{\text{SC}}$. IV curves at illumination levels between 1 and 20 suns are shown in Fig. 8.10. One sun refers to an irradiation of 1000 W/m^2, which was realized with a sun simulator and adjusted with a calibrated c-Si solar cell. The illumination level was varied using a Frensel lens with variable distance to the sample. The illumination dependence of R_{SC} is depicted in Fig. 8.11. The experimental data obey very well Eq. (2.38), and a linear regression yields a slope of 0.39319 V. This corresponds to an effective drift length of 150 nm and an effective mobility lifetime product of
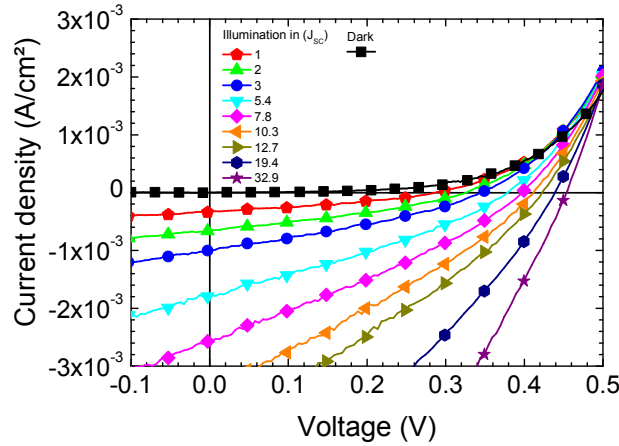
Fig. 8.10: Illumination-dependent current-voltage curves, taken from [192]. The cell was illuminated with a sun simulator and a Fresnel lens from the wafer side (cf. Fig. 8.6).
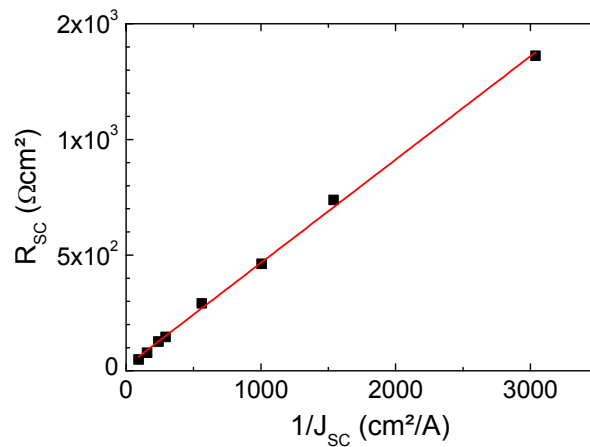
Fig. 8.11: Illumination-dependence of the short-circuit resistance (points) and fit of Eq. (2.38) to the data, taken from [192]. The slope of the linear regression is 0.3932 V. This corresponds (V = 0 V) to $(\mu\tau)_{eff}$ = 5.75·10^{-10} cm²/V and an effective drift length of 150 nm with V_{FB} = 0.4 V.

$(\mu\tau)_{\text{eff}}$ = 5.75·10^{10} cm²/V at short-circuit conditions and with V_{FB} determined as the cross over voltage (0.4 V). Simultaneous fits of Eqs. (2.34) and (2.35) (uniform field approximation) to IV curves at four different illumination levels are shown in Fig. 8.12. The illumination was set to $C \times J_{\text{gen}}$, C being the light concentration calculated from the ratio of the respective short-circuit current to that under 1 sun illumination. The optical limit (5.97 mA/cm², see section 8.2.2) was used for J_{gen} at 1 sun illumination. The flat-band voltage was set to 1.2×V_{FB} for the best fit, where V_{FB} refers to the cross over voltage determined from Fig. 8.10. An excellent fit is obtained for a wide range of illumination intensities with $(\mu\tau)_{\text{eff}}$ = 2.6×10^{-11} cm²/V and J_0 = 5.2×10^{-6} A/cm². The only parameter
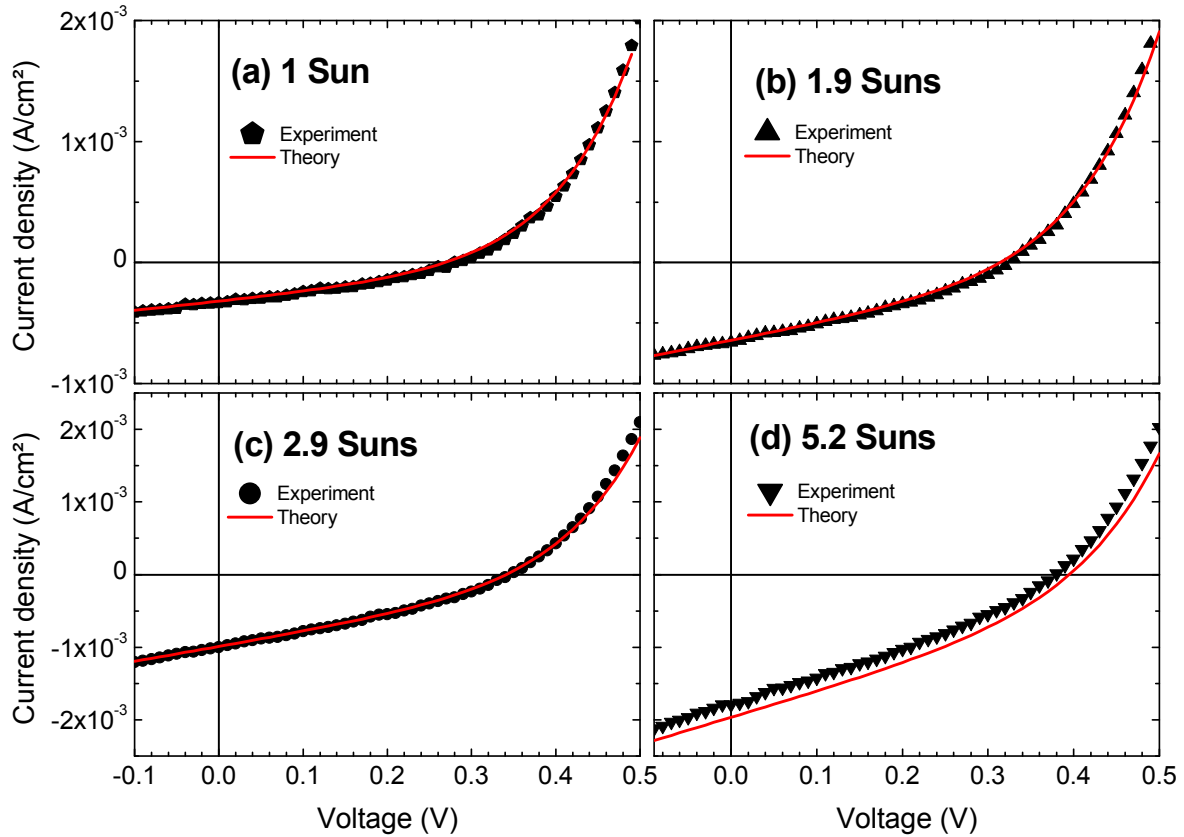
Fig. 8.12: Current-voltage curves of membrane-based p-i-n devices and the respective fits of the one-diode model with voltage dependent collection function in the uniform field approximation (Eqs. (2.34) and with the collection function of Eq. (2.35)) to the data. Series resistance, parallel resistance and ideality factor were fixed to the dark values.

that is not confirmed independently is the dark saturation current. However, Hegedus [202] analyzed data from a large variety of thin film solar cells and demonstrated that within a regime in which V_{OC} is linearly correlated with V_{FB}, the dark saturation current does not influence V_{OC}. As the IV curves presented here exhibit a linear dependence of V_{OC} on V_{FB} (not shown here), it was inferred that J_0 only has a minor impact on the overall IV curve.

The good agreement between the experimental data and the theory over a wide range of illumination densities (Fig. 8.12) strongly supports the validity of the presented analysis. Furthermore, the mobility lifetime product agrees approximately within one order of magnitude with the value of 5.75×10^{-10} cm²/V derived with the method after Merten *et al.* (Fig. 8.11). The latter method does not require knowledge of J_{gen} but utilizes only the directly accessible J_{SC}.

On the other hand, the optical limit was assumed for J_{SC} for the IV curve fitting, resulting in 2.6×10^{-11} cm²/V. As the optical limit is the ideal case it overestimates J_{gen}, and the procedure thus underestimates $(\mu\tau)_{eff}$ for a given short-circuit current. Thus, the analysis after Crandall is expected to yield a lower $(\mu\tau)_{eff}$ value than the method of Merten. Given the very limited foreknowledge about the Si NC material, both theories are in excellent agreement. Both methods employed here ascribe any recombination in the entire device to the effective mobility lifetime product. As losses can also occur in the other device parts apart from the Si NC absorber, e.g. by interface recombination or transport barriers, the value of $(\mu\tau)_{eff} \approx 10^{-10}$ cm²/V has to be seen as a lower limit to the electronic quality of the Si NC film itself.

8.2.5 Temperature dependence

The device performance was furthermore analyzed as a function of the cell temperature at different illumination levels. The temperature- and illumination-dependent IV measurements were made at temperatures between 5°C and 48°C and irradiances between 0.5 and 20 suns. A V_{OC} temperature coefficient of -2.04 mV/K at 1 sun was determined, which is comparable to values for c-Si solar cells [23]. After the IV measurements for the determination of the temperature coefficient, further measurements were done at 35°C and 48°C. These measurements yielded extraordinarily high V_{OC} values of 544 mV (35°C) and 525 mV (48°C) at an illumination of about 18 suns. Unfortunately, a detailed IV analysis as discussed above was not possible for the measurement at 35°C because the dark IV curve was not stable. Reliable results for the series resistance, the ideality factor and the parallel resistance were determined for the
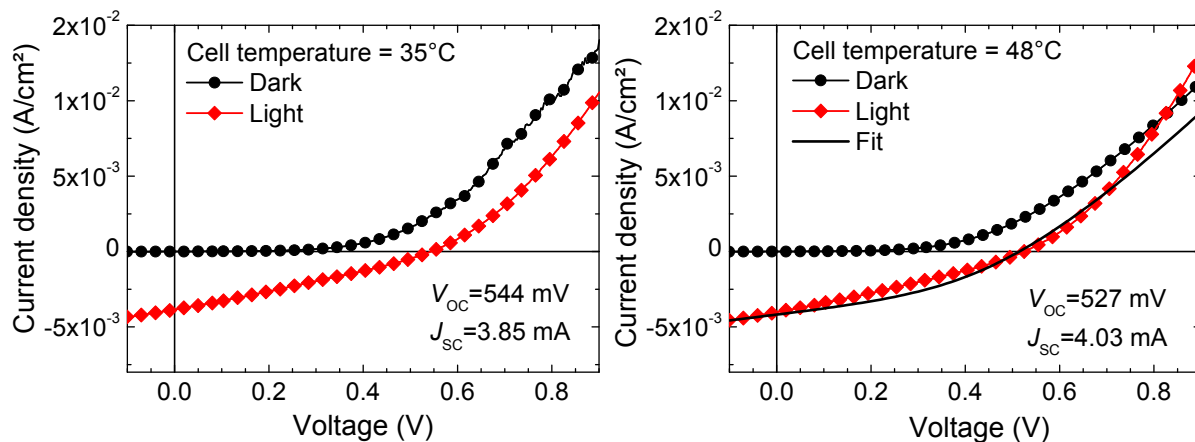

Fig. 8.13: Current-voltage curves at 35°C (left) and 48°C (right) at an irradiation of about 18 suns.

measurement at 48°C from the dark curve as described in 8.2.3 (R_S =28.3 Ωcm^2, n =3, R_P =10264 Ωcm^2). The measurement at 48°C had been performed before the one at 35°C. The IV curve at 48°C and 18 suns could be fitted with Eqs. (2.34) and (2.35) using the dark curve parameters and J_0 =5.2×10^{-6} A/cm^2, $(\mu\tau)_{eff}$ = 1.0×10^{-11} cm²/V, which are similar values as obtained for the fit in Fig. 8.12. However, the flat-band voltage had to be set to 1.152 V, which is 1.4 times the cross over voltage (0.823 V), to obtain a reasonable fit. The elevated temperature and prolonged exposure to concentrated light apparently caused an annealing effect leading to an increased flat-band voltage. The physical origin of the increased flat-band voltage could not be identified as the device degraded after further measurements.

8.2.6 Comparison of cell results

Four runs of membrane-based p-i-n solar cells were successfully processed. The earlier runs comprised ISE multilayers as the absorber and had a strong focus on the demonstration of the device functionality and cell process optimization (see section 8.1.) The optimized cell process was then used to fabricate devices with the CNR material. For a total number of 13 cells an IV curve was measured and shown to be exclusively due to the SiC/Si NC multilayer. The cell results of all properly functioning devices are summarized in Tab. 8.3. As the number of cells per wafer is low and most wafers were processed in different runs, a direct relation of the cell results to the compositional and structural properties of the SiC/Si NC layer has to be taken with care. However, a positive correlation between V_{OC} and the Si content x can be identified as a general trend.

The values for the effective mobility lifetime product determined on solar cell device level are around 10^{-10} cm²/V within one order of magnitude. Interestingly, values between 10^{-8} cm²/V and 10^{-5} cm²/V were obtained by photoconductivity measurements as discussed in section 5.6.5. The SiC/Si NC multilayer employed in the solar cells featured stoichiometric barrier layers and was annealed at 1100°C. The most similar sample in section 5.6 is thus the one that exhibits an effective mobility lifetime product of 10^{-7} cm²/V (Fig. 5.20, Si-C(s) central wave number 792 cm^{-1}). The remarkable difference of three orders of magnitude can be explained by the measurement technique. The current in a conductivity measurement is carried by the majority carriers. The solar cell photocurrent, on the other hand, is carried by the majority and the minority charge carriers. Consequently, the $(\mu\tau)_{eff}$ value determined with a solar cell device is sensitive not only to the majority charge carrier characteristics but also to those of the minority charge carriers. The mobility and the lifetime of the minority charge carriers is in most cases orders of magnitude lower.

Tab. 8.3: Overview over all cells whose photovoltaic properties were proven to stem only from the active membrane cell area.

ID	BL	SRC	SiC	V_{OC} (mV)	V_{FB} (mV)	J_{SC} (mA/cm²)	FF (%)	J_0 (mA/cm²)	n	R_S (Ωcm²)	$R_{SC,dark}$ (Ωcm²)	$R_{SC,light}$ (Ωcm²)	$(\mu\tau)_{eff}$ (cm²/(Vs))
QM7													
C4-4	20	4.5 nm x=0.77	3 nm	362	468	0.34	---[1]	---[1]	2.5	10	47923	1394	---[1]
C5-1				320	465	0.35		---[1]	2.7	3.8	29607	1209	---[1]
C5-3				370	480	0.37		---[1]	2	4.1	62614	1325	---[1]
QM17													
W4-G2	30	3 nm x=0.63	3nm	170	---[2]	0.073					---[2]		
W4-G4				212	---[2]	0.201					---[2]		
C4-A													
G197-E2	30	2.6 nm x=0.65	3 nm	176	326	0.334	35	1.2×10^{-5}	3	10.1	2068	963	5×10^{-11}
G197-F8				119	233	0.168	31	2×10^{-5}	3.8	4.6	1637	987	3.5×10^{-11}
G202-D10	bulk	---	98 nm	133	---[5]	0.215	28		---[3]		1774	761	
G202-F13				106	227	0.158	29	2.5×10^{-5}	3.8	2.2	1599	814	3×10^{-11}
C4-B													
G193-E16	30	2.6 nm x=0.65	3 nm	282	415	0.339	35	5.2×10^{-6}	3.2	4.9	11808	292	2.6×10^{-11}
G199-F13				81	≈150[4]	0.079	67		4.6	2.6	2009	995	
G199-F15				53	≈150[4]	0.110	40			---[3]	2620	396	
G199-F17				107	≈175[4]	0.138	39		4	2.5	2344	617	

[1] No illumination-dependent measurements.

[2] Dark and light IV data too noisy for further analysis.

[3] Dark IV curve analysis not reliable. Fit of light IV curve not possible.

[4] Dark and light IV data very noisy, error ±30mV

[5] Dark and light IV curves do not intersect

The large discrepancy between the $(\mu\tau)_{\mathrm{eff}}$ values determined by photoconductivity on the one hand and from a solar cell device measurement on the other hand thus stresses the importance of a suitable characterization device, which is sensitive to the relevant material properties.

8.3   Chapter summary

In this chapter, a detailed analysis of membrane-based Si NC p-i-n solar cells has been presented. The analysis comprised membrane-based p-i-n solar cells with SiO_2/Si NC and SiC/Si NC multilayers as absorber. The fabrication process yield and the insulation layer failure were analyzed. A method was presented to identify properly working devices and to prove the origin of the photovoltaic properties. A detailed characterization of the spectral and illumination-dependent properties was presented and the effective mobility lifetime product of SiC/Si NC films was determined on device level.

The membranes are very fragile and prone to breakage. It was shown that the structuring of the insulation layer stack on the membrane (step 13 in Fig. 7.4) and the subsequent final fabrication steps are especially critical for the process yield. The additional Si_3N_4 layer that is required for the devices with Si NCs in SiO_2 leads to at least 4 more wet chemistry steps in comparison to the device for Si NCs in SiC. The yield of the finished SiO_2/Si NC cells was compared to the yield of reference structures fabricated on the same wafer but with unstructured insulation layer. The comparison suggests that after structuring the insulation layer, the membrane is not stable enough to survive the rest of the cell process.

In contrast to devices with SiO_2/Si NC absorber and the additional Si_3N_4 layer, an acceptable yield was obtained with SiC/Si NC devices. The biggest technological challenge in this case was the characterization and optimization of the insulation layer performance. Insulation layer failure arises from unsufficient adhesion of the inkjet resist on the 54.7° steep slanted sidewalls. As individual inkjet resist lines slide down the sidewall, the resist locally loses its masking behavior and the insulation layer is etched.

A device process with a robust insulation layer was developed and a reliable method was presented to identify properly working SiC/Si NC devices. The method consists of a pre-charaterization by optical bright- and dark-field microscopy, followed by IV measurements employing shadow masks and light beam induced current measurements. It was shown that once appropriate criteria for the microscopy and IV characterization are established, and the process flow is characterized as a whole, the tedious light beam induced current measurements can be omitted.

After having shown the functionality of the overall device, a detailed characterization of the optical and electrical properties was carried out. The optical properties of the cell were simulated with an optical model of the entire ITO/a-Si_xC_{1-x}:H(p)/(SiC/Si NC)/a-Si_xC_{1-x}:H(n)/ITO stack system using previously determined optical functions of the individual layers. The model was applied to calculate the spectrally resolved absorptance within each layer in the stack.

Spectral response measurements were not viable with standard solar cell equipment (grating monochromator) because of the small absolute current values. Therefore, a Fourier transform photocurrent spectroscopy technique was employed to measure the spectral response between 500 nm and 900 nm. It was shown, that the spectral behavior of the external quantum efficiency resembles the optical absorption spectrum of the SiC/Si NC absorber. Therefore, it was inferred that the cell performance is indeed caused by the SiC/Si NC layer and not other device parts like e.g. the doped a-Si_xC_{1-x}:H layers.

The external quantum efficiency vanished for wavelengths of $\lambda >$930 nm, corresponding to a threshold energy of 1.33 eV. The absorption spectrum extended up to 1000 nm, but the charge carriers generated from these low-energy photons were not collected and measured as an external current. Hence, the threshold energy of 1.33 eV was interpreted in terms of an effective electronic band gap in analogy to amorphous semiconductors. Electronic states extend into the band gap giving rise to optical transitions. However, electrical transport through these states is very inefficient and the photogenerated charge carriers are thus not detected any more.

The cell results obtained with several different SiC/Si NC absorber layers were compared. Due to the high membrane breakage rate and the insulation layer failure of the remaining mechanically faultless devices, the number of cells for each SiC/Si NC absorber layer was very limited. A statistically sound comparison is therefore impossible. However, a positive correlation of the open-circuit voltage with the Si content can tentatively be indentified.

Furthermore, an approach was developed to determine the effective mobility lifetime product, which is the fundamental transport and recombination parameter. The approach makes use of a dark IV curve analysis, illumination-dependent current-voltage measurements and optical modeling of the p-i-n device layer stack. The dark IV curve was evaluated according to the small conductance method according to Werner [203] to extract the series resistance and the ideality factor. The parallel resistance is obtained from the slope of the dark IV curve at zero bias. The dark IV curve parameters are then used to model the IV curves under illumination under the premise of the superposition principle.

The device is described within the uniform field approximation after Crandall [34], which provides a means to model illumination-dependent IV curves with an analytical voltage-dependent collection function. Very good agreement was found between the experimental data and the theory for illumination levels between 1 and 5 suns. An effective mobility lifetime product of 2.6×10^{-11} cm^2/V was derived from this procedure. Supplementary to the analytical modeling of the entire IV curve, the mobility lifetime product was also determined using the simplified method of Merten $et\ al.$ [35]. This method requires only the direct accessible IV curve parameters R_{SC} and J_{SC} and V_{FB}. A mobilitiy lifetime product of 5.75×10^{-10} cm^2/V was determined with this method. As the fit according to Crandall tends to underestimate the mobility lifetime product, the two values are found to be in good agreement. A mobility lifetime product in the range of 10^{-10} cm^2/V is three orders of magnitude lower than in "device quality" amorphous silicon for solar cell absorbers [153]. The low photocurrent even without any external bias, as mentioned above, indicates a high defect density in the depletion region, i.e. the absorber bulk. In earlier studies on planar structures [118], the Si/SiC interface was found to be very recombination active. The high recombination in the absorber bulk can thus be related to mainly two causes: The interfaces between the Si and SiC NCs and the dangling bond defects in the residual amorphous volume fractions.

The discrepance between the effective mobility lifetime product determined on solar cell device level (10^{-10} cm²/V) with the majority carrier value from photoconductivity measurements (10^{-7} cm²/V) stresses the importance of material characterization on device level.

The device performance was furthermore analyzed as a function of the cell temperature at different illumination levels and very high open-circuit voltages of 544 mV and 525 mV were measured at about 18 suns at 35°C and 48°C, respectively. The temperature coefficient was shown to be -2.04 mV/K at 1 sun. The high voltages were ascribed to an annealing effect, but the physical origin of this effect could not be elucidated.

The solar cell characterization presented in this chapter impressively demonstrates the capabilities of membrane-based solar cell devices. A method for an unequivocal indentification of properly working devices has been developed. The devices have been employed for a thorough analysis of the SiC/Si NC material, and important material parameters such as the effective electronic band gap and the effective mobility lifetime product were determined.

The work presented here constitutes the first characterization of SiC-based Si NC materials in a minority carrier device and has demonstrated for the first time the voltage potential of Si NCs embedded in SiC.

9 Critical review of the crystalline silicon tandem solar cell concept

This chapter revisits the most important properties of the Si NC materials in the light of a crystalline Si tandem solar cell. Three tandem device structures are derived from the device point of view and the main implications for the material are discussed.

The concept of a crystalline Si tandem solar cell relies on the electrical exploitation of the high band gap of Si NCs. The Si NC material serves as the absorber in the top solar cell in this concept, and has thus to be designed for a band gap of approximately 1.7 eV.

The present project is focused on Si NCs prepared by the approach of amorphous multilayer deposition and subsequent high-temperature thermal annealing, as this approach has shown excellent optical properties for the SiO_2-based material, a comparatively narrow Si NC size distribution and is compatible with large area production.

The importance of the matrix material and also the assets and drawbacks implied by a SiO_2 or SiC matrix were discussed in chapter 6. In brief, the SiO_2 matrix is very efficient in impeding electrical transport and the SiC matrix results in a high density of structural and electrical defects.

At the present stage of material development, wave function coupling of Si NCs in SiO_2 is not strong enough to provide an electrical transport mechanism apart from tunneling. Such a material is not suitable as a solar cell absorber due to the immense series resistance losses. Luo *et al*. pointed out that the NC size variation is extremely critical for NC-NC interaction and thus miniband formation. It was argued in chapter 4, that this effect might be a fundamental problem arising from the disorder introduced by the NC size variation.

By partially abandoning the multilayer structure, however, electrical transport enhanced by 10 orders of magnitude was shown. In this specific case, quantum confinement was present only in one dimension (1D, Si quantum wells). As the NCs merged across the barriers, the quantum confinement was lost also in this direction. Evidently, the technological limits of arranging Si NCs in SiO_2 and achieving a higher volume and areal NC density are far from exhausted. A careful exploitation of the apparent tradeoff between quantum confinement and coalescence is thus still to be carried out to achieve optimum material properties.

With regard to the SiC matrix, a reduction of the defect density is the prerequisite for an investigation of quantum confinement effects. The focus is thus not on maximizing the Si NC density, but on growing Si NCs whilst ensuring a low defect density within the SiC matrix and at the SiC/Si NC interface. A ternary SiC/SiO$_x$ superlattice has already been employed to tackle this challenge, but the SiC matrix has been found to be extremely defect-rich [204, 205]. The addition of O- [164] or N- [206] impurities to the SiC matrix proved to suppress SiC crystallization and resulted in enhanced device results. However, the supposed defect reduction was not investigated in detail. Finally, a combination of direct Si NC synthesis with matrix embedding techniques is a candidate for size-control in conjunction with electrical transport. In detail, plasma or wet chemically synthesized Si NCs could be deposited to a substrate and covered by a monolayer of silicon oxide using atomic layer deposition (ALD).

So far, material characterization has mostly been done with optical methods or using majority carrier devices. However, a conclusive assessment of Si NC materials as a solar cell absorber implies a material analysis on solar cell device level.

A systematic study of the photovoltaic properties of SiC/Si NC layers on solar cell device level was presented in chapter 8. Open-circuit voltages of up to 370 mV were shown at 1 sun illumination. The spectral properties of the SiC/Si NC absorber layer have revealed an effective electronic band gap of 1.33 eV. The largest room for improvement was found for the recombination properties. An effective mobility lifetime product of approximately 10^{-10} cm^2/V was determined (section 8.2.4), which is three orders of magnitude below the value considered "device quality" for amorphous silicon. Against the background of thicker absorbers (chapter 6) required for a Si NC solar cell compared to an a-Si:H solar cell, this value stresses the importance of advanced defect engineering for SiC/Si NC films. Mobility lifetime products between 10^{-8} cm^2/V and 10^{-5} cm^2/V were derived in this theis from photoconductivity measurements for a comparable material (section 5.6.5). These values were measured using a majority carrier device and are thus not sensitive to minority carrier recombination. They cannot be compared to the value determined on solar cell level due to the different experimental conditions, but the large discrepancy stresses the need for a systematic material characterization with properly designed devices, i.e. on solar cell device level.

The thickness of the Si QD solar cell that is required to achieve current matching was calculated by Summonte *et al.* [149, 207]. A thickness of approximately 5 μm was calculated for Si NCs in SiO$_2$ [207], but 500 nm were found to be sufficient for Si NCs in SiC

[149]. While the exact numbers are subject to the Si NC density, the general trend that Si NCs in SiC absorb stronger can be explained with the additional absorption by the matrix.

Provided the shortcomings of the different Si NC materials are remedied, various tandem solar cell device concepts are possible. A cost-efficient fabrication process practically implies the monolithic growth and interconnection of the bottom and top solar cell. This leads to the three tandem device structures sketched in Fig. 9.1. (a) A high-efficiency approach with a monocrystalline Si wafer bottom solar cell, (b) a low cost approach based on an encapsulated foreign substrate and (c) a low cost approach with superstrate configuration.

The three device structures are conceptually guided by (a) high-efficiency solar cells such as passivated emitter and rear contact (PERC) solar cells [208], (b) recrystallized wafer equivalent (RexWE) solar cells [209], and (c) the crystalline Si on glass (CSG) approach [210].

The implications of the three structures for the Si QD material and the feasibility of a tandem device shall be briefly described here. The structure (a) has to compete with already commercialized wafer solar cells. Industrial high-efficiency wafer solar cells are already exceeding 20% efficiency, and it might be inferred that the tandem concept of Fig. 9.1 (a) can only be competitive if the tandem efficiency clearly exceeds the wafer "technological limit" of 26% [1]. However, if one additional PECVD step (for QD cell fabrication) is sufficient to increase the efficiency of a simple standard wafer solar cell (Al back surface field) by e.g. 2% absolute, this concept would be very attractive.
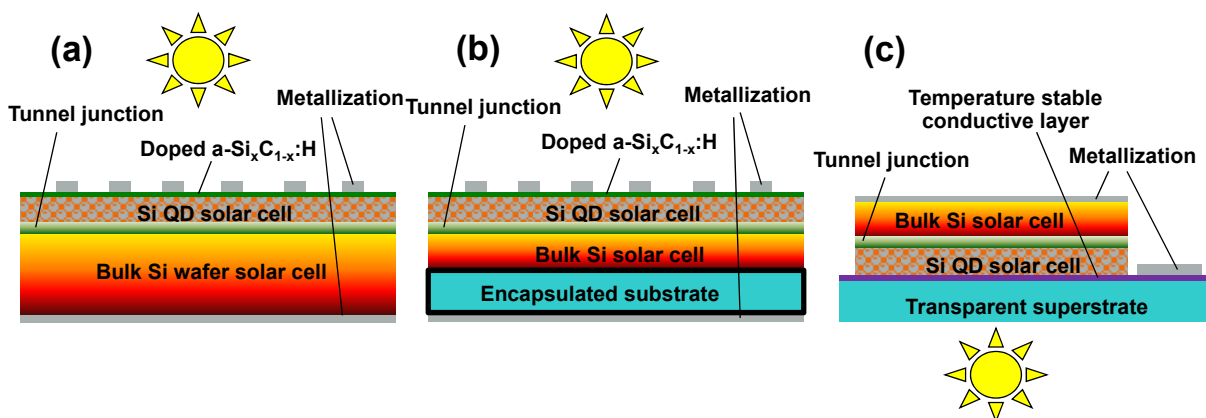

Fig. 9.1: Tandem solar cell structures for the c-Si tandem concept: (a) High-efficiency concept with a wafer-based bottom solar cell, (b) thin-film approach using an encapsulated low-cost substrate and (c) thin film superstrate approach for a reduced thermal budget on the bottom solar cell.

In any case, the bottom solar cell and also the tunnel junction have to stand the thermal budget needed to fabricate the Si QD top solar cell.

Structure (b) is subject to the same requirements, although less severely applied because of the comparatively less elaborated bottom cell and the greater cost potential. It is noted, however, that texturing of structure (b) will be challenging if a superlattice QD cell is to be grown on top. Moreover, the surface roughness of the encapsulation layer and the polycrystalline bulk Si solar cell might adversely affect the multilayer structure of the Si QD solar cell. Consequently, the development of a Si QD material without multilayer arrangement is desireable for approach (b).

On the other hand, structure (a) is usually textured with random pyramids. As their period and height is in the range of several μm and their surface consists of flat (111) planes, this texture could be compatible with the multilayer approach and could even be advantageous to increase the effective light path through the QD layer.

Structure (c) is distinguished by a flat surface for Si NC growth and no thermal impact to the bulk Si solar cell, but the need for a transparent conductive layer. The challenges are thus shifted away from the bulk Si cell that has to stand the thermal budget in structures (a) and (b) and converted to requirements to the transparent conductive layer. Possibilities were pointed out in section 7.1. Realistic options include tungsten silicide, which provides a stable contact up to 900°C. Unless novel materials permit higher temperatures, the feasibility of structure (c) critically depends on a reduction of the Si QD thermal budget. A lower thermal budget could be achieved by rapid thermal or flash annealing followed by a prolonged thermal anneling step at lower temperature.

In summary, each tandem structure implies a different emphasis to the Si QD properties. Structure (a) is compatible with the superlattice approach but imposes the highest requirements to the absorption as well as recombination and transport properties. In structure (b), the multilayer approach interferes with the surface roughness of the bulk Si solar cell. However, for Si QD materials beyond the multilayer approach this structure appears to be the most feasible. Structure (c) is viable only for peak temperatures up to 900°C involved in Si QD fabrication.

In any of the three structures, the Si QD cell has to deliver and to conduct 15 mA/cm^2 to 20 mA/cm^2 current in order to be current matched to the bottom solar cell. Such high currents stress even more the need for efficient electric transport through the QD material.

At the present stage, the Si NC materials are not yet developed enough to render a crystalline tandem solar cell viable. Provided the present material shortcomings are remedied, a reduction of the peak annealing temperature has to be achieved to ensure compatability with tandem solar cell technology. Furthermore, abandoning the strict multilayer configuration will most probably facilitate tandem solar cell integration.

10 Conclusion

The basic motivation of this thesis has been to explore a path beyond the 29% fundamental efficiency limit [1] of crystalline silicon (Si).

Motivated by the tunable optical band gap, the project has pursued the implementation of Si nanocrystals (NCs) as a solar cell absorber with the overall goal to realize a crystalline Silicon tandem solar cell. After the project had been motivated and outlined in chapter 1, basic theoretical concepts for Si NCs and solar cells were introduced in chapter 2. The maximum open-circuit voltage of Si NC materials was estimated theoretically in chapter 3. Chapter 4 was dedicated to the optical properties of Si NCs embedded in SiO_2 and the determination of the maximum open-circuit voltage by optical spectroscopy. Chapter 5 covered the preparation of Si NCs embedded in silicon carbide (SiC) and a characterization of the structural and electrical properties. The two materials, the oxide- and the carbide-based material, were put in contrast to each other in chapter 6 and their respective properties were discussed in the light of their application as a solar cell absorber. In chapter 7, the available Si NC device structures were discussed, and a lack of device structures for a material characterization on solar cell device level was identified. A novel membrane-based device structure has been developed in the framework of this thesis that copes with the specific requirements of Si NC characterization. In chapter 8, a general characterization of the device functionality was carried out and a procedure was developed to demonstrate the origin of the photovoltage. The membrane-based device was applied to Si NCs embedded in SiC with a systematic characterization of the photovoltaic properties. Finally, chapter 9 reviewed the tandem solar cell device concepts on the background of the material development status and the requirements to the materials arising from different tandem solar cell concepts.

The <u>first step towards a Si NC solar cell</u> is the demonstration that <u>photovoltages above the bulk Si level</u> are attainable with Si NCs. Therefore, the maximum open-circuit voltage of an idealized Si NC solar cell was assessed in **chapter 3** based on a theoretical model. The open-circuit voltage was approximated by the quasi-Fermi level splitting in the Si NC absorber assuming ideal charge separation. The <u>Si NCs were modeled as a cubic superlattice of cubic monodisperse NCs and described theoretically with the envelope function approximation to calculate the band structure and the density of states</u>. The three most prominent host matrices, SiO_2, Si_3N_4 and SiC, were considered including variations of the Si NC size, density, and illumination. A charge carrier density of $10^{16}\,cm^{-3}$ was

determined based on optical absorption and transient photoluminescence measurements for Si NCs embedded in SiO$_2$. As the number of states in the first miniband is much higher than the excess charge carrier density, the quasi-Fermi level splitting follows approximately the band gap as the Si NC size or density is varied. According to this theoretical model, open-circuit voltages >1 V are attainable with Si NCs embedded in any of the three host matrices.

Experimental investigations were performed with two material systems in the framework of this thesis, Si NCs embedded in SiC (SiC/Si NC) and Si NCs embedded in SiO$_2$ (SiO$_2$/Si NC). Both materials were prepared according to the multilayer approach and high-temperature thermal annealing as originally proposed by Zacharias [18] for SiO$_2$/Si NC. The multilayer approach comprises the deposition of alternating amorphous Si-rich and stoichiometric layers. During the subsequent thermal annealing step, the Si excess clusters and crystallizes, confined by the stoichiometric layers that act as growth barriers.

In **chapter 4**, the optical properties of Si NCs in SiO$_2$ were examined. The size-dependent blue shift of the band gap was shown with optical absorption and photoluminescence spectroscopy. After having shown theoretically in chapter 3 the feasibility of quasi-Fermi level splittings >1 eV, this chapter aimed at an experimental demonstration of a high quasi-Fermi level splitting. For this means, calibrated photoluminescence and absorption measurements were analyzed with the generalized Planck law of radiation.

If the wave functions in adjacent Si NCs interact sufficiently strong so as to establish chemical equilibria between the electrons and between the holes in different NCs, the luminescence spectrum has to obey the generalized Planck law of radiation. However, charge carrier temperatures of >500 K had to be assumed to achieve agreement between the experimental data and the theory. As a hot carrier population could be ruled out, it was inferred that the generalized Planck law is not valid for this material. Rather, the spectrum was explained as a superposition of independent light emitters, broadened by the Si NC size distribution. Consequently, wave function coupling is not strong enough at the present stage of development for the formation of minibands. This argument is also supported by the very weak electrical transport through Si NCs embedded in SiO$_2$ reported by other authors. According to theoretical studies [45], the NC-NC interaction ceases as the NC sizes deviate by more than 20%. It has been argued in this thesis that the loss of NC-NC interaction can be seen in analogy to the Anderson localization in amorphous solids. According to this explanation, a superior size control would be the key for enhanced transport properties by minimizing the disorder potential.

 Chapter 5 was devoted to the <u>development and characterization of the SiC-based</u> <u>material</u>. The SiC matrix as alternative to SiO_2 was motivated by the challenge to achieve electrical conduction through the Si NC network. SiC exhibits a small band gap (2.3 eV) compared to SiO_2 and can be doped. The NC-NC interaction is expected to be more pronounced due to the lower barrier, and a doped matrix would provide free charge carriers to the Si NCs (modulation doping).

In previous studies the formation of Si NCs in SiC multilayers had been evidenced, but it had also been found that <u>SiC nanocrystals form simultaneously with the formation of</u> <u>Si NCs</u>. Thus, an <u>experiment</u> was conducted that aimed at <u>separating the formation of SiC</u> <u>and Si NCs</u> by means of Si-rich barrier layers. In this experiment, the <u>Si crystalline volume</u> <u>fraction and the Si NC size</u> were shown to be <u>positively correlated with the barrier Si</u> <u>content</u>. A different picture was obtained for the formation of SiC NCs: Neither the crystallization temperature, nor the SiC NC size was found to be correlated with the barrier layer composition. However, the barrier layer composition did indeed influence the formation of Si-C bonds. Thus, <u>more Si-C bonds form, but the SiC nanocrystals do not grow</u> <u>to larger size as the barrier is more stoichiometric (less Si rich)</u>. This result strongly supports the conclusion as pointed out by Künle [79] that <u>upon thermal annealing Si and C</u> <u>inter-diffuse</u>. In contrast to the SiO_x system, the thermal annealing causes an alloying in spite of a phase separation before the system crystallizes. Only upon crystallization the phases separate again.

In all cases, a residual amorphous Si phase remains. In the SiC/Si NC multilayers characterized in chapter 5, also a part of the SiC remains amorphous. Consequently, the SiC/Si NC material has to be considered as a <u>mixture of SiC and Si phases, which are both</u> <u>present in the amorphous as well as the crystalline state</u> depending on the annealing conditions. The multilayer structure is increasingly lost as the material is annealed longer and at higher temperatures.

It was <u>demonstrated in this thesis that the frequency of the Si-C stretching vibration</u> is a suitable parameter to <u>represent the</u> <u>overall film crystallinity qualitatively</u>, accounting for the crystallization of the SiC as well as the Si phases. As this quantity is available independently of the annealing state, it provides a practical parameter to relate other properties to the overall crystallinity.

The <u>electrical conductivity</u> of the SiC/Si NC multilayer was found to <u>increase with the Si</u> <u>content and the overall crystallinity</u>. However, the <u>contrary</u> was observed for samples with the <u>highest total Si content</u> (70%). In these samples, the conductivity decreased by 3

orders of magnitude as the film was more crystalline. <u>Nitrogen incorporation</u> in these samples was proven by SIMS and FTIR and related to the formation of <u>Si_3N_4</u> in the film volume during thermal annealing. By comparison with literature results, the Si_3N_4 was inferred to grow around the Si domain interfaces. As in these samples the conduction takes place through the Si phases, a Si_3N_4 shell around or between the Si phases constitutes an electrical transport barrier. This <u>explains the reduced conductivity in spite of the higher crystallinity</u>.

The photoconductivity was measured, and the effective mobility lifetime product was determined to be between 10^{-8} cm^2/V and 10^{-5} cm^2/V. Compared to the amorphous Si device quality value of $>10^{-7}$ cm^2/V [153], the values obtained with the SiC/Si NC multilayers are very reasonable. However, the relative photo response is only 10% of the dark conductivity. It is important to note that photoconductivity is not sensitive to minority carriers, while the minority carrier transport and recombination characteristics are crucial for solar cell operation. Therefore, photoconductivity is only of limited use to assess the performance of the material as a solar cell absorber.

The comparative discussion of the Si NC materials in **chapter 6** arrived at very different conclusions for the oxide- and the carbide-based materials. Si NCs in SiO_2 provide a band gap that is tunable due to quantum confinement. The SiO_2/Si NC interface is comparable to the planar SiO_2/Si interface, with similar hydrogen passivation kinetics and comparable nitrogen areal densities. Therefore, <u>SiO_2</u> as the embedding matrix provides a <u>high-quality interface</u> to the Si NCs with a <u>very low defect density</u>. <u>However</u>, all theoretical and experimental results, including these presented in this thesis, <u>speak against miniband formation</u> for the material in its present stage.

<u>Conduction through the SiC</u>-based material has been proven in this work to be <u>very efficient</u> ($\approx 5 \times 10^{-4}$ Ω^{-1}cm^{-1}). Moreover, nitrogen doping of the matrix can be exploited to enhance electrical transport even further. <u>However, the crystallization mechanisms are more complex</u> than for the SiO_2/Si NC material, and at the present stage the density of structural and electronic defects is too high to allow an investigation of quantum confinement effects. Approaches have been pointed out to improve both materials. SiC/SiO_x multilayers have been pursued to combine the superior surface passivation of SiO_2 with the conduction through the SiC matrix [204] [205].

For Si NCs in SiO_2, one bridging oxygen atom between adjacent NCs is enough to provide quantum confinement according to theoretical calculations [45]. The implementation of an atomic layer deposited monolayer of SiO_2 could be a way to achieve conduction while not

losing confinement. Moreover, conductive SiO$_x$ barrier layers are a noteworthy attempt for advanced oxide-based multilayers [72].

In **chapter 7,** the available <u>device structures</u> for a <u>characterization of Si NC films on solar cell level</u> were reviewed. In all device structures presented so far, <u>either the Si NC or the device performance is adversely affected</u> by the device structure and the required <u>fabrication processes</u>, or the <u>structure does not allow for a separation of the Si NC and substrate contributions</u> to the measurement. <u>This thesis has been aiming at</u> filling the gap between high-quality NCs with full flexibility to tune the multilayer properties, and the requirements of a device structure that permits to <u>extract the quasi-Fermi level splitting</u> within the Si NC absorber <u>to the external contacts</u>.

To go beyond the limitations of previous devices, a <u>membrane-based p-i-n device</u> has been developed in this work. For this structure, the Si NC film is deposited on a substrate wafer. After high-temperature annealing and Si NC formation, the substrate wafer is locally removed and then encapsulated with insulating layers. After structuring the insulating layers, the Si NC film can be accessed from both sides, providing full flexibility for the choice of selective contacts. In the framework of this thesis, <u>fabrication processes were developed for oxide- as well as carbide-based NC layers</u>. They differ in the need for an additional intermediate layer and thus more structuring steps for the oxide-based NC films. Doped a-Si$_x$C$_{1-x}$:H was shown to be an appropriate selective contact material for Si NC films. <u>Si NC solar cells</u> were prepared with a planar <u>ITO/a-Si$_x$C$_{1-x}$:H(p)/(SiC/Si NC)/a-Si$_x$C$_{1-x}$:H(n)/ITO</u> device design with active cell areas of about 1 mm^2 and channel lengths as low as 100 nm. The entire active cell area is illuminated and contacted from both sides.

The <u>device structure relies on insulating layers</u> to permit a characterization of the Si NC layer without any wafer influence. A procedure was presented in **chapter 8** to <u>identify reliably the functionality</u> of the Si NC p-i-n solar cell and to prove that the <u>origin of the measured quantities</u> is indeed the active <u>SiC/Si NC cell area</u>. In order to quantify the absorptance in each layer of the solar cell layer stack, the optical properties of the entire layer stack were modeled using the previously determined optical functions of the individual layers. The external quantum efficiency was measured in this thesis by means of Fourier transform photocurrent spectroscopy and illumination with a supercontinuum light source. <u>Comparison of the external quantum efficiency spectrum with the SiC/Si NC layer absorption</u> demonstrated that the <u>photovoltaic action</u> is indeed <u>caused by the SiC/Si NC layer</u>.

Thus, methods have been developed in this thesis that allow to implement the Si NC layer to a p-i-n solar cell, directly compare the photovoltaic performance of different NC materials on device level, and that characterize the spectra of Si NC materials. The external quantum efficiency measurement presented here constitutes the only spectrally resolved characterization of Si NCs by an electrical method so far.

The dark current-voltage (IV) characteristics of the Si NC p-i-n membrane solar cells were analyzed with the small conductance method according to Werner [203]. This method was found to be well suitable to extract the series resistance and the ideality factor. The dark parallel resistance, determined from the slope of the IV curve at zero bias, was typically in the range of 10^4 Ωcm. Under illumination, however, the parallel resistance decreases to about 10^2 Ωcm, the exact value depending on the illumination level.

An illumination-dependent device analysis was performed to determine the fundamental transport and recombination properties, the effective mobility lifetime product, on device level. For this means, the device was modeled assuming a uniform electric field [34] over the SiC/Si NC absorber. Within this model, the photocurrent is a function of the applied voltage and the effective mobility lifetime product. The illumination-dependent IV curves were fitted simultaneously with one parameter set and the knowledge of the previously determined dark IV curve parameters. Excellent agreement between the theoretical description and the experimental data was shown and an effective mobility lifetime product of 2.6×10^{-11} cm²/V was determined. Complementary to this method, a simplified parametric analysis [35] was carried out, yielding a value of 5.75×10^{-10} cm²/V. Taking into account the restricted validity of the latter model to zero bias, both values are in good agreement. As the effective mobility lifetime product in the two methods accounts for any losses in the entire device, the value of approximately $\approx 10^{-10}$ cm²/V constitutes a lower limit to the SiC/Si NC mobility lifetime product. This value is three orders of magnitude smaller than for amorphous Si device quality ($>10^{-7}$ cm²/V [153]). Interestingly, it is even 5 orders of magnitude below the value determined from photoconductivity measurements. Photoconductors are not sensitive to the minority charge carrier transport and recombination properties and hence overestimate the effective mobility lifetime product. The discrepancy stresses the need for more advanced structures such as the membrane-based p-i-n solar cell developed in this thesis for a systematic material characterization.

Membrane-based solar cells were fabricated employing different SiC/Si NC layers. As a general trend, a positive correlation between the total Si content of the Si NC layer and the solar cell parameters was observed. Moreover, extraordinary high open-circuit voltages

were measured after prolonged light exposure and heating to ≈50°C. An open-circuit voltage of <u>544 mV</u> was measured at 35°C and 18 suns. The value could be explained with an increased flat-band voltage caused by a thermal annealing effect.

The characterization of the photovoltaic properties on solar cell device level has revealed an urgent need for an electronically enhanced SiC/Si NC material. The <u>characterization scheme presented in this thesis</u> can be applied to a <u>comparative material characterization</u>, and therefore <u>enables a systematic material optimization</u>.

According to the dark conductivity measurements presented in chapter 5, the SiC/Si NC material indeed provides electrical transport ($\sigma_{\text{dark}} = 10^{-4}\,(\Omega\text{cm})^{-1}$). However, the recombination properties are not satisfying, and at the current stage <u>devices are limited</u> by the very <u>low effective mobility lifetime</u> values of about 10^{-10} cm²/V. As the <u>SiC matrix crystallizes simultaneously</u> with the formation of Si NCs, a very <u>high grain boundary density</u> evolves. The separation of Si NC formation from the crystallization of SiC is therefore identified as one key issue towards enhanced device performance.

In **chapter 9,** the tandem solar cell concept was revisited and three different realization approaches were presented and discussed in the light of the current status of material development. The <u>three tandem solar cell realizations</u> are inspired by (a) <u>c-Si wafer</u> solar cells, (b) <u>recrystallized Si thin film</u> solar cells and (c) the <u>Si on glass</u> approach. All tandem cell concepts envisage a monolithic interconnection of the two cells in order to cope with cost restrictions. It was pointed out that concept (a) implies the strictest requirements to the Si QD conductivity and absorption due to the high photocurrent required for current matching. This boundary condition and also the thermal budget restrictions are less severe for concept (b), as the bottom cell is less developed and the process provides more cost flexibility. The feasibility of concept (c) depends on a temperature-stable transparent conductive layer, which is not available to date. <u>All tandem solar cell concepts urge a reduction of the thermal budget</u>, as the high-temperature QD preparation route employed in this thesis implies a performance degradation of the other device parts.

Electrical transport through Si NCs embedded in SiO_2 has turned out to be much more challenging than anticipated at the beginning of this project. For the implementation of Si NCs embedded in SiO_2 as solar cell absorber, enhanced electrical transport through the Si NC network is indispensable. As material research has so far been focusing on the understanding of the quantum confined band gap, the technological possibilities have still not been fully exploited.

The membrane-device structure and also the selective contact scheme developed in this thesis are suitable for the characterization of SiO_2/Si NC layers on solar cell device level and can thus be used as a powerful tool for future material optimization. The characterization results presented in chapter 8 demonstrate the striking capabilities of the membrane-based solar cell. The unequivocal indentification of properly working devices has allowed for the separation of the contributions of the individual device parts to the global measurement quantities. Hence, this approach has successfully been employed for a thorough characterization of the SiC/Si NC material. Important material parameters such as the effective electronic band gap and the effective mobility lifetime product were determined by the use of the membrane-based device. The results presented in this thesis constitute the first characterization of SiC-based Si NC materials in a minority carrier device. The membrane-based p-i-n device and the demonstration of the voltage potential of Si NCs embedded in SiC provide a sound base for ongoing material characterization and optimization.

11 Deutsche Zusammenfassung

Die weltweite Energieversorgung beruht heute auf den fossilen Primärenergieträger Erdöl, Kohle und Gas. Bei der Konversion der in chemischer Form in Erdöl, Kohle und Gas gespeicherten Energie in elektrische Energie werden große Mengen klimawirksamer Emissionen freigesetzt. Eine Konsequenz ist der globale Klimawandel, der immer folgenschwerere Auswirkungen zeigt. Zur Erhaltung unserer natürlichen Lebenswelt und für ein friedliches Zusammenleben ist ein radikales Umdenken mit einer Wende hin zu erneuerbaren Energien dringend erforderlich.

Innerhalb der erneuerbaren Energien nimmt die Photovoltaik eine Schlüsselrolle ein. Die direkte Konversion der Sonnenstrahlung in elektrische Energie birgt entscheidende Vorteile gegenüber anderen erneuerbaren Energien. Im Gegensatz zu Wind- und Wasserkraft steht Sonnenstrahlung praktisch unbegrenzt zur Verfügung. Zum anderen sind Photovoltaikanlagen durch ihre hohe Modularität fast beliebig skalierbar und können gleichermaßen auf Einfamilienhausdächern wie auch in Großkraftwerken eingesetzt werden. Innerhalb der photovoltaischen Technologien kommt kristallinen Siliciumsolarzellen mit einem Marktanteil von 86% eine eindeutige Vorreiterrolle zu. Silicium ist ungiftig, in praktisch unbegrenzten Mengen auf der Erdoberfläche vorhanden und durch seine breite Verwendung in der Elektronikindustrie technologisch weit ausgereift. Mittels Massenproduktion und optimierter Fertigungstechnologien konnte in der vergangenen Dekade eine beeindruckende Reduzierung der Produktionskosten erreicht werden. Für einen langfristig geringeren Materialeinsatz und damit niedrigere Kosten pro Kilowatt installierter Leistung sind höhere Wirkungsgrade durch neue Solarzellenkonzepte erforderlich.

Somit ist die zugrundeliegende Motivation dieser Arbeit die Steigerung des **fundamentalen** Wirkungsgradgrenzwertes Silicium-basierter Solarzellen. Aufgrund der inhärenten Thermalisierungs- und Transmissionsverluste ist der Wirkungsgrad von Siliciumsolarzellen auf 29% beschränkt [1]. Dieses fundamentale Limit lässt sich erhöhen indem die bestehende Siliciumsolarzelle um eine zweite Solarzelle mit größerer Energiebandlücke erweitert wird. Materialien mit hoher Bandlücke sind unter Ausnutzung des Quantenbeschränkungseffekts mit Silicium-Nanokristallen (Si NCs für „silicon nanocrystals") realisierbar.

In dieser Arbeit werden Silicium-Nanokristalle eingebettet in Siliciumcarbid- (SiC) und Siliciumdioxid- (SiO$_2$) Wirtsmatrizen auf ihre Eignung als Solarzellenabsorbermaterial untersucht. Sowohl für das SiC- als auch für das SiO$_2$-basierte Material wird zunächst ein amorphes Multischichtsystem per plasma-unterstützter Gasphasenabscheidung (PECVD) hergestellt. In einer anschließenden Temperung bei Temperaturen bis zu 1100°C werden die Silicium-Nanokristalle dann per Festphasenkristallisation ausgebildet.

Die vorliegende Arbeit umfasst zum einen grundlegende Materialuntersuchungen, bei der die strukturellen Eigenschaften in Bezug zu den optischen und elektrischen Eigenschaften gesetzt werden. Zum anderen wird die Eignung von Silicium-Nanokristall-Materialien als Solarzellenabsorber untersucht.

Nachdem das Thema in Kapitel 1 motiviert und die Gliederung der Arbeit vorgestellt wird, werden in Kapitel 2 grundlegende theoretische Konzepte von Silicium-Nanokristallen und Solarzellen vorgestellt. In Kapitel 3 wird die maximale Offenklemmenspannung anhand theoretischer Methoden abgeschätzt. Kapitel 4 behandelt die optischen Eigenschaften von in SiO$_2$ eingebetteten Si NC und die Bestimmung der maximalen Offenklemmenspannung mittels optischer Spektroskopie. In Kapitel 5 wird die Präparation von in SiC eingebetteten Si NCs vorgestellt sowie eine detaillierte strukturelle und elektrische Charakterisierung des Materials diskutiert. Kapitel 6 stellt die zwei Materialsysteme, Si NCs in SiC und Si NCs in SiO$_2$, vergleichend gegenüber und erörtert ihre Eigenschaften vor dem Hintergrund ihrer Anwendung als Absorber in einer Solarzelle. Kapitel 7 stellt die verfügbaren und bisher verwendeten Si NC-Bauteile vor und bewertet ihre Eignung als Teststruktur zur Charakterisierung der Offenklemmenspannung einer Si NC-Solarzelle. Es wird ein Mangel an geeigneten Teststrukturen festgestellt, welcher aus der gegenseitigen störenden Beeinflussung des zur Präparation der Nanokristalle notwendigen Hochtemperaturschrittes und der selektiven Kontakte herrührt. Eine neuartige, im Rahmen dieser Arbeit entwickelte Membran-Teststruktur entkoppelt den Hochtemperaturschritt von der Ausbildung der selektiven Kontakte und ermöglicht somit erstmalig eine Charakterisierung und Beurteilung der photovoltaischen Eigenschaften (Offenklemmenspannung) der Nanokristallschicht. In Kapitel 8 wird eine allgemeine Bauteilcharakterisierung sowie eine Methode zur Identifizierung fehlerhafter Bauteile vorgestellt. Kapitel 8 stellt Ergebnisse von Membran-Solarzellen mit einem Absorber aus Si NCs eigebettet in SiC vor und erörtert eine systematische Charakterisierung der Materialeigenschaften anhand beleuchtungsabhängiger Solarzellenmessungen. In Kapitel 9 werden   verschiedene   Tandemsolarzellenkonzepte   vor   dem   Hintergrund   des

Materialentwicklungsstands und der durch das jeweilige Zellkonzept bedingten Anforderungen an das Si NC-Material bewertet.

Der erste Schritt hin zu einer Si NC-Solarzelle ist der Beleg, dass mit Si NCs höhere Offenklemmenspannungen als mit ausgedehnten („bulk") Si-Kristallen möglich sind. Die maximal mögliche Offenklemmenspannung wird in Kapitel 3 anhand eines theoretischen Modells für verschiedene Materialsysteme abgeschätzt. Dafür wird die Offenklemmenspannung als der Potentialunterschied der quasi-Fermi-Niveaus unter der Annahme idealer Ladungsträgerseparation angenähert. Die Silicium-Nanokristalle werden als kubisches Übergitter kubischer monodisperser Nanokristalle modelliert und theoretisch mittels der „envelope function approximation" beschrieben um die Bandstruktur und die Zustandsdichte zu berechnen. Es werden die drei gängigsten Wirtsmaterialien, SiO_2, Si_3N_4 und SiC, behandelt und eine Variation der Nanokristallgröße und -dichte sowie der Beleuchtungsstärke vorgenommen. Die Überschussladungsträgerdichte wird mittels optischer Absorptionsmessungen und transienter Photolumineszenzmessungen an Si NCs in SiO_2 zu 10^{16} cm^{-3} bestimmt. Da die Zustandsdichte im ersten Miniband deutlich größer als die Überschussladungsträgerdichte ist, folgt die Aufspaltung der quasi-Fermi-Niveaus bei Variation der Nanokristallgröße oder -dichte in guter Näherung der Bandlücke. Anhand dieses Modells sind Offenklemmenspannungen >1 eV mit jeder der drei betrachteten Wirtsmatrizen erreichbar.

Experimentell wurde im Rahmen dieser Arbeit das SiO_2-basierte (SiO_2/Si NC) sowie das SiC-basierte (SiC/Si NC) Material untersucht. Zur Herstellung beider Materialien wurde die Methode nach Zacharias [18] angewandt, bei der zunächst eine amorphe Multischicht abgeschieden wird, in der anschließend durch einen Hochtemperaturschritt die Si NCs gebildet werden. Die Multischicht besteht aus sich abwechselnden Si-reichen und stöchiometrischen Schichten, sodass während des Hochtemperaturschrittes die stöchiometrischen Schichten als Diffusionsbarriere wirken und somit das Wachstum der Si-Kristalle beschränken.

In Kapitel 4 werden Si NCs in SiO_2 mit optischen Methoden untersucht. Die größenabhängige Blauverschiebung der Bandlücke wird anhand optischer Absorptions- und Photolumineszenzspektroskopie gezeigt. Während in Kapitel 3 die Möglichkeit einer quasi-Fermi-Niveau-Aufspaltung von >1 eV mit einer theoretischen Modellierung gezeigt wurde, strebt Kapitel 4 die experimentelle Bestimmung der quasi-Fermi-Niveau-Aufspaltungen an.

Zu diesem Zweck werden kalibrierte Photolumineszenz- und Absorptionsmessungen gemäß des verallgemeinerten Planckschen Strahlungsgesetzes analysiert. Sofern die Wellenfunktionen in benachbarten Si NCs so stark wechselwirken dass sich ein chemisches Gleichgewicht zwischen den Elektronen und den Löchern in verschiedenen NCs einstellen kann, müsste das Lumineszenzspektrum dem Planckschen Strahlungsgesetz gehorchen. Um die experimentellen Daten mit dem Planckschen Strahlungsgesetzes zu reproduzieren müssen jedoch Temperaturen von >500 K angenommen werden. Aus der Tatsache, dass eine Population heißer Ladungsträger ausgeschlossen werden kann, lässt sich folgern, dass das Plancksche Strahlungsgesetz für dieses Material nicht gültig ist. Vielmehr ist das Lumineszenzspektrum als Superposition einzelner Strahler und die Breite des Spektrums als Resultat der Nanokristall-Größenverteilung zu sehen. Folglich ist die Kopplung der Wellenfunktionen bei dem derzeitigen Materialentwicklungsstand nicht stark genug zur Ausbildung von Minibändern. Diese Schlussfolgerung wird auch von Ergebnissen anderer Autoren unterstützt, welche einen nur sehr schwach ausgeprägten elektrischen Transport durch Si NCs in SiO$_2$ berichten. Nach theoretischen Studien verschwindet die Wechselwirkung zwischen benachbarten NCs bereits bei Größenunterschieden von mehr als 20%. Wie in dieser Dissertation dargelegt wird, kann der Verlust der NC-NC Wechselwirkung in Analogie zur Anderson-Lokalisierung in amorphen Festkörpern gesehen werden. Nach dieser Erklärung wäre eine bessere Größenkontrolle der Schlüssel zu einer Verringerung des Unordnungspotenzials um eine NC-NC Wechselwirkung zu ermöglichen.

Kapitel 5 ist der Entwicklung des SiC-basierten Nanokristallmaterials gewidmet. Die SiC-Matrix als Alternative zu SiO$_2$ ist motiviert durch die Notwendigkeit elektrischen Transports durch das Nanokristall-Netzwerk. Im Gegensatz zu SiO$_2$ weist SiC eine deutlich geringere Bandlücke (2.3 eV) auf und kann darüber hinaus dotiert werden. Aufgrund der geringeren Bandlücke ist eine deutlich ausgeprägtere Inter-Nanokristall-Wechselwirkung zu erwarten, und durch eine dotierte Matrix liessen sich freie Ladungsträger in den Si-Nanokristallen bewirken (Modulationsdotierung).

Die Ausbildung von Si NCs in SiC ist bereits in vorhergehenden Studien gezeigt worden. Darüber hinaus wurde jedoch auch beobachtet dass sich simultan zu Nanokristallen aus Si auch Nanokristalle aus SiC bilden. Daher wurde im Rahmen dieser Arbeit ein Experiment durchgeführt, welches die Bildung von Si NCs ohne gleichzeitiges Entstehen von SiC-Nanokristallen beabsichtigt, indem Si-reiche Barrierenschichten verwendet werden. Die Ergebnisse lassen eine klare positive Korrelation sowohl des kristallinen Si-Volumenanteils als auch der Si-Nanokristallgröße mit dem Si-Gehalt der Barrieren erkennen. Für SiC-

Nanokristalle ergibt sich jedoch ein anderes Bild: Weder die Kristallisationstemperatur noch die SiC-Nanokristallgröße stehen in Zusammenhang mit der Barrierenkomposition. Allerdings beeinflusst die Zusammensetzung der Barriere das Entstehen von Si-C-Bindungen: während ein geringerer Si-Gehalt der Barriere (näher an der stöchiometrischen Zusammensetzung) zwar eine höhere Si-C-Bindungsdichte bedingt, führt dies nicht zu größeren SiC Kristalliten. Dieses Ergebnis unterstützt die Folgerungen von Künle [79], dass die Si- und C-Atome während des Hochtemperaturschrittes diffundieren und die Schichten sich somit vermischen. Im Gegensatz zu dem SiO$_x$-System ist der Temperschritt also eher als Legieren denn als Phasenseparation zu betrachten und erst durch die Kristallisierung trennen sich die Si- und die SiC-Phase wieder.

Der Siliciumüberschuss kristallisiert nicht vollständig, sondern es wird in allen Fällen ein Rest amorphen Siliciums beobachtet. In den in Kapitel 5 behandelten SiC/Si NC-Multilagen bleibt auch ein Teil der SiC-Phase amorph. Folglich ist das SiC/Si NC-Material als Gemisch aus SiC- und Si-Phasen zu betrachten, welche je nach Temperbedingungen beide sowohl in der amorphen als auch in der kristallinen Phase vorliegen. Außerdem geht die Multilagenstruktur zunehmend verloren wenn das Material länger oder bei höheren Temperaturen getempert wird.

In dieser Arbeit wird gezeigt, dass die Frequenz der Si-C Streckschwingung auf die Kristallisierung beider Phasen (Si und SiC) empfindlich ist und somit einen geeigneten Parameter zur qualitativen Erfassung der insgesamten Kristallinität darstellt. Da dieser Parameter unabhängig vom Temperzustand, also auch für amorphe Schichten, verfügbar ist, bietet er ein praktisches und leicht zugängliches Maß um andere Eigenschaften in Bezug zur insgesamten Kristallinität der Schicht zu setzen.

Die elektrische Leitfähigkeit der SiC/Si NC-Schichten steigt mit dem Si-Gehalt und der insgesamten Kristallinität der Schicht. Das Gegenteil ist jedoch bei den Proben mit dem höchsten totalen Si-Gehalt (70%) zu sehen. In diesen Proben geht die Leitfähigkeit um drei Größenordnungen zurück wenn die Schichten kristallisieren. Anhand von Sekundärionen-Massenspektroskopie (SIMS) und Fourier-transformierter Infrarotspektroskopie (FTIR) wird nachgewiesen, dass sich Stickstoff in den SiC/Si NC-Schichten befindet. Unter Zuhilfenahme von Literaturergebnissen wird dies mit der Bildung einer Si$_3$N$_4$-Phase um die Si-Bereiche herum während des Tempervorgangs begründet. Da der elektrische Transport vornehmlich durch die Si-Phasen stattfindet stellt die Nitridphase eine Leitfähigkeitsbarriere dar und erklärt somit die verringerte Leitfähigkeit trotz der höheren Kristallinität.

Anhand von Photoleitfähigkeitsmessungen wird das effektive Produkt von Ladungsträgermobilität und -lebensdauer ($(\mu\tau)_{\text{eff}}$, „effective mobility lifetime product") berechnet und es werden für die vorliegende Probenserie Werte zwischen 10^{-8} cm^2/V und 10^{-5} cm^2/V bestimmt. Im Vergleich zu dem Richtwert für „device quality" bei amorphem Silicium von $>10^{-7}$ cm^2/V [153] stellen die Werte für SiC/Si NC Multilagen bereits günstige Werte dar. Die Photoleitfähigkeit beträgt jedoch nur etwa 10% der Dunkelleitfähigkeit. An dieser Stelle muss bemerkt werden, dass die Photoleitfähigkeit nicht sensitiv auf die Eigenschaften der Minoritätsladungsträger ist, während deren Transport- und Rekombinationseigenschaften jedoch ausschlaggebend für den Einsatz als Absorber einer Solarzelle sind. Daher erlauben Photoleitfähigkeitsmessungen nur bedingt Aussagen über die Eignung des Materials in einer Solarzelle.

Die vergleichende Diskussion der Si NC-Materialien in Kapitel 6 kommt zu sehr unterschiedlichen Schlüssen für die Oxid- und Carbid-basierten Materialien. Die Bandlücke von Si NCs in SiO$_2$ kann durch die Quantenbeschränkung eingestellt werden. Die SiO$_2$/Si NC-Grenzfläche ist vergleichbar mit der planaren Si/SiO$_2$-Grenzfläche, und weist eine ähnliche Kinetik der Wasserstoffpassivierung sowie vergleichbare Stickstoff-Flächendichten auf. SiO$_2$ als einbettende Wirtsmatrix bietet daher eine hochwertigen Grenzfläche zu den Si Nanokristallen mit einer sehr geringen Defektdichte. Andererseits sprechen alle theoretischen und experimentellen Daten gegen die Ausbildung von Minibändern in dem Material in seinem derzeitigen Entwicklungsstand.

Für das SiC-basierte Material wurde eine sehr gute elektrische Leitung gezeigt ($\approx 5\times10^{-4}$ Ω^{-1}cm^{-1}). Darüber bietet SiC die Möglichkeit, durch eine Dotierung der SiC-Matrix mit Stickstoff den elektrischen Transport weiter zu begünstigen. Die Kristallisierungsmechanismen sind jedoch deutlich komplexer als im Falle des SiO$_2$/Si NC-Materials, und bei derzeitigem Stand ist die strukturelle und elektronische Defektdichte zu groß um Quantenbeschränkungseffekte zu untersuchen. Für beide Materialsysteme wurden bereits Verbesserungsansätze vorgeschlagen. Beispielsweise wurden SiC/SiO$_x$-Multilagen realisiert um die guten Oberflächenpassivierungseigenschaften von SiO$_2$ mit der Leitfähigkeit des SiC zu kombinieren [204] [205].

Bei Si NCs in SiO$_2$ reicht nach theoretischen Rechnungen [45] bereits ein Sauerstoffatom zwischen zwei benachbarten Nanokristallen bereits aus, um Quantenbeschränkung in den Nanokristallen zu erreichen. Eine per Atomic layer deposition (ALD) abgeschiedene SiO$_2$-Monolage könnte daher einen Weg darstellen um elektrische Leitfähigkeit zu erreichen

ohne die Quantenbeschränkung zu aufzugeben. Ein weiterer vielsprechender Ansatz für fortgeschrittene Oxid-basierte Multilagen sind leitfähige SiO_x-Barriereschichten [72].

In Kapitel 7 werden die verfügbaren Bauteilstrukturen zur Charakterisierung von Si NC-Schichten auf Solarzellenebene erörtert. In allen bisher veröffentlichten Strukturen wird entweder die Si NC- oder die Bauteilperformance nachteilig von der Bauteilstruktur und dem Herstellungsprozess beeinflusst, oder die Bauteilstruktur ermöglicht es nicht, zwischen dem Beitrag der Si NCs und jenem des Substrates zu unterscheiden. Daher beabsichtigt die vorliegende Arbeit die Lücke zu füllen, die bisher besteht zwischen hoch optimierten Si NC mit voller Flexibilität bezüglich der Multilageneigenschaften einerseits, und den Anforderungen einer Bauteilstruktur zur Extraktion der quasi-Fermi-Niveau-Aufspaltung im Si NC-Material zu den externen Kontakten, andererseits.

Um die Beschränkungen vorheriger Bauteile zu überwinden, wurde im Rahmen dieser Arbeit ein Membran-basiertes p-i-n Bauteil entwickelt. Zur Herstellung dieser Struktur wird zunächst die Si NC-Schicht auf einen Substratwafer abgeschieden. Nach dem Hochtemperaturschritt zur Ausbildung der Si NCs wird der Substratwafer lokal entfernt und dann mit elektrisch isolierenden Schichten verkapselt. Nach Strukturierung der Isolierschichten ist die Si NC-Schicht von beiden Seiten frei zugänglich, was volle Flexibilität bei der Wahl des selektiven Kontaktmaterials gewährleistet. Im Rahmen dieser Arbeit wurden Herstellungsprozesse sowohl für Oxid- als auch für Carbid-basierte Membran-Solarzellen entwickelt. Die zwei Prozessrouten unterscheiden sich durch die Notwendigkeit einer zusätzlichen Zwischenschicht und somit mehr Strukturierungsschritten für die Oxid-basierten Schichten. Dotiertes amorphes Siliciumcarbid (a-Si_xC_{1-x}:H) ist ein geeignetes Material um selektive Kontakte zu Si NC-Schichten zu präparieren. Es wurden Si NCs mit planarem ITO/a-Si_xC_{1-x}:H(p)/(SiC/Si NC)/a-Si_xC_{1-x}:H(n)/ITO Bauteildesign, aktiven Zellflächen von etwa 1 mm² und Messlängen >100 nm hergestellt. Die gesamte aktive Zellfläche wird beleuchtet und von beiden Seiten kontaktiert.

Die Funktionalität der Bauteilstruktur beruht auf dielektrischen Schichten zur elektrischen Isolierung des Substratwafers, welche die Charakterisierung der Si NC-Schicht ohne Wafereinfluss ermöglichen. In Kapitel 8 wird eine Vorgehensweise erörtert anhand derer die Funktionalität der Si NC p-i-n Solarzellen verlässlich überprüft werden kann, und welche belegt, dass die gemessenen Größen tatsächlich aus der aktiven SiC/Si NC-Zellfläche herrühren. Zur Bestimmung des Absorptionsgrades jeder einzelnen Schicht des Solarzellenschichtstapels wird eine optische Modellierung des Schichtstapels mit den vorher bestimmten optischen Funktionen der einzelnen Schichten vorgenommen. Die

externe Quanteneffizienz wird mit Fourier-transformierter Photostromspektroskopie unter Anregung mit einer Superkontinuums-Lichtquelle gemessen. Aus dem Vergleich des spektralen Verlaufs der externen Quanteneffizienz mit der Absorption der SiC/Si NC-Schicht lässt sich folgern, dass der photovoltaische Effekt wirklich aus der SiC/Si NC-Schicht herrührt.

Zusammenfassend werden im Rahmen dieser Arbeit Methoden entwickelt welche erstens die Implementierung der Si NC-Schicht in eine p-i-n-Solarzelle ermöglichen, zweitens einen direkten Vergleich verschiedener Si NC-Schichten auf Solarzellenebene erlauben und drittens das Spektrum der Si NC-Schicht bestimmen. Die hier vorgestellten Messungen der externen Quanteneffizienz stellen die bisher einzige spektral aufgelöste Charakterisierung von Si NCs mittels einer elektrischen Methode dar.

Die Strom-Spannungs- (IV) Charakteristik der Si NC-p-i-n-Solarzellen im Dunkeln wurde mit der „small conductance method" nach Werner [203] ausgewertet. Diese Methode erwies sich als gut anwendbar um den Serienwiderstand und den Idealitätsfaktor zu bestimmen. Der Parallelwiderstand im Dunkeln, bestimmt aus der Steigung der IV-Kurve ohne angelegte Spannung, war typischerweise im Bereich von 10^4 Ωcm. Unter Beleuchtung sinkt der Parallelwiderstand jedoch auf etwa 10^2 Ωcm, wobei der genaue Wert auch von der Beleuchtungsstärke abhängt. Es wird eine beleuchtungsstärken-abhängige Bauteilanalyse durchgeführt um die fundamentalen Transport- und Rekombinationseigenschaften, das effektive Mobilitäts-Lebensdauer-Produkt, auf Solarzellen-Ebene zu bestimmen. Dazu wird angenommen, dass die eingebaute Spannung als gleichmäßiges elektrisches Feld (uniform electric field [34]) über dem SiC/Si NC-Absorber anliegt. Innerhalb dieses Modells wird der Photostrom als eine Funktion der angelegen Spannung und des effektiven Mobilitäts-Lebensdauer-Produkts ausgedrückt. Es wird eine simultane Kurvenanpassung des Modells an die Beleuchtungsstärken-abhängigen IV-Kurven vorgenommen wobei viele Parameter durch die vorher bestimmten Dunkelparameter festgelegt sind. Die theoretische Beschreibung zeigt eine exzellente Übereinstimmung mit den experimentellen Daten, wodurch $(\mu\tau)_{\text{eff}}$=2.6×10^{-11} cm²/V bestimmbar ist. Komplementär zu dieser Methode wurde eine vereinfachte parametrische Analyse [34] vorgenommen, welche einen Wert von $(\mu\tau)_{\text{eff}}$=5.75×10^{-10} cm²/V ergibt. In Anbetracht der Tatsache dass die Gültigkeit der letzteren Methode auf angelegte Spannungen von Null beschränkt ist, sind beide Werte in guter Übereinstimmung. Da sich der Wert von ≈10^{-10} cm²/V in beiden Methoden auf die Verluste im gesamten Bauteil bezieht, kann dies als untere Schranke für die SiC/Si NC-Schicht angesehen werden. Dieser Wert liegt drei Größenordnungen unter dem „device

quality"-Wert für amorphes Silicium ($>10^{-7}$ cm^2/V [153]). Interessanterweise ist er fünf Größenordnungen kleiner als das anhand von Photoleitfähigkeitsmessungen an vergleichbarem Material bestimmte Mobilitäts-Lebensdauer-Produkt. Da Photoleiter Majoritätsladungsträgerbauteile sind, zeigen sie keine Empfindlichkeit gegenüber den Transport- und Rekombinationseigenschaften der Minoritätsladungsträger und überschätzen folglich das effektive Mobilitäts-Lebensdauer-Produkt. Dieser Unterschied unterstreicht die Notwendigkeit fortgeschrittener Zellstrukturen für eine systematische Materialcharakterisierung wie etwa der im Rahmen dieser Arbeit entwickelten Membran-basierten p-i-n-Solarzelle.

Membran-Solarzellen wurden mit mehreren unterschiedlichen SiC/Si NC-Schichten hergestellt. Es wird ein positiver Zusammenhang zwischen dem gesamten Si-Gehalt der Si NC-Schicht und den Solarzellenparametern als allgemeiner Trend festgestellt. Darüber hinaus wurden außergewöhnlich hohe Offenklemmenspannungen nach ausgedehnter Beleuchtung und Temperung bei ≈50°C gemessen. Es konnte eine Offenklemmenspannung von 544 mV bei 35°C und einer Beleuchtungsstärke von 18 Sonnen gezeigt werden. Dieses Ergebnis wurde mit einer durch einen Ausheileffekt gesteigerten Flachbandspannung erklärt.

Die Charakterisierung der photovoltaischen Eigenschaften auf Solarzellenebene lässt einen dringenden Handlungsbedarf für ein elektronisch optimiertes SiC/Si NC-Material erkennen. Das in dieser Arbeit dargelegte Charakterisierungsschema ermöglicht einen direkten Materialvergleich und somit eine systematische Materialoptimierung. Nach den in Kapitel 5 behandelten Dunkelleitfähigkeitsmessungen ermöglicht das SiC/Si NC-Material elektrischen Transport ($\sigma_{\mathrm{dark}} = 10^{-4}$ (Ωcm)$^{-1}$). Die Rekombinationseigenschaften des Materials sind jedoch noch nicht zufriedenstellend, und bei dem derzeitigen Materialentwicklungsstand sind die Bauteile durch die sehr geringen Werte des effektiven Mobilitäts-Lebensdauer-Produkts von ≈10^{-10} cm²/(Vs) limitiert. Dadurch dass die SiC-Matrix während der Ausbildung von Si-Nanokristallen ebenfalls kristallisiert, entsteht eine hohe Dichte an Korngrenzen. Die Separation der Ausbildung von Si-Nanokristallen von der Kristallisierung des SiC wird daher als ein Schlüssel zu einem besseren Bauteilergebnis angesehen.

Kapitel 9 kommt auf das Tandemsolarzellenkonzept zurück und erörtert drei Realisierungsansätze vor dem Hintergrund des derzeitigen Materialentwicklungsstatus. Die drei Realisierungsansätze sind angelehnt an (a) c-Si Wafer-Solarzellen, (b) rekristallisierte Si-Dünnschicht-Solarzellen und (c) den Ansatz „Si auf Glas". Alle Ansätze sehen aus

Kostengründen eine monolithische Integration der zwei Zellen vor. Es wird festgestellt das Konzept (a) aufgrund der notwendigen Stromanpassung die höchsten Anforderungen an die Leitfähigkeit und Absorption der Si NCs stellt. In Konzept (b) sind diese Rahmenbedingung als auch die Beschränkung des thermischen Budgets weniger streng da die untere Solarzelle weniger optimiert ist und der Herstellungsprozess mehr Kostenflexibilität bietet. Die Machbarkeit von Konzept (c) hängt von einer temperaturstabilen leitfähigen transparenten Schicht ab, welche bisher nicht verfügbar ist. Alle drei Tandemsolarzellenansätze legen eine Reduktion des thermischen Budgets dringend nahe, da die Hochtemperatur-Route zur Herstellung des Si NC-Materials eine Degradation der anderen Teile der Tandemzelle nach sich zieht.

Elektrischer Transport durch Si NCs in SiO_2 hat sich als deutlich schwieriger als zu Beginn des Projektes vermutet herausgestellt. Zur Verwendung von in SiO_2 eingebetteten Si NC als Solarzellenabsorber ist eine deutliche Verbesserung der elektrischen Transporteigenschaften unabdingbar. Dadurch dass die Materialforschung bisher auf das Verständnis der quantenbeschränkten Bandlücke konzentriert war, sind die technologischen Möglichkeiten noch nicht ausgeschöpft.

Die Membran-Struktur und die Art der selektiven Kontakte, die in dieser Arbeit entwickelt wurden, sind auch zur Charakterisierung von SiO_2/Si NC-Schichten auf Solarzellenebene geeignet und bieten ein machtvolles Werkzeug für die zukünftige Materialoptimierung.

Die in Kapitel 8 vorgestellten Charakterisierungsergebnisse illustrieren eindrucksvoll die Möglichkeiten der Membran-Solarzellen.

Die eindeutige Identifizierung korrekt funktionierender Bauteile ermöglicht die Separation der Beiträge einzelner Bauteilelemente zu den gemessenen globalen Werten. Darauf aufbauend wurde der Ansatz erfolgreich zu einer umfassenden Charakterisierung des SiC/Si NC-Materials angewendet. Grundlegende Materialparameter wie die effektive elektronische Bandlücke und das effektive Mobilitäts-Lebensdauer-Produkt konnten mittels der Membran-Solarzelle bestimmt werden. Mit dieser Arbeit werden erstmals Charakterisierungsergebnisse von SiC-basierten Si NC-Schichten in einem Minoritätsladungsträgerbauelement vorgestellt. Das Membran-basierte p-i-n-Bauteil und die Demonstration des Spannungspotenzials von Si NC eingebettet in SiC stellt eine fundierte Basis für die weiterführende Materialcharakterisierung- und Optimierung dar.

12 Bibliography

[1]   R. M. Swanson, "Approaching the 29% limit efficiency of silicon solar cells," in *Proceedings of the 31st IEEE Photovoltaic Specialists Conference*, Orlando, USA, 2005, pp. 889-94.

[2]   R. A. Muller, J. Curry, D. Groom, R. Jacobsen, S. Perlmutter, R. Rohde, A. Rosenfeld, C. Wickham, and J. Wurtele, "Decadal variations in the global atmospheric land temperatures," in *Berkeley Earth Project*, ed. Berkeley, CA, USA, 2011.

[3]   D. King, K. Richards, and S. Tyldesley, *International climate change negotiations: Key lessons and next steps*. Oxford, United Kingdom, 2011, http://www.smithschool.ox.ac.uk/wp-content/uploads/2011/03/Climate-Negotiations-report_Final.pdf.

[4]   IEA, "International Energy Agency World Energy Outlook 2012," 2012, http://www.worldenergyoutlook.org.

[5]   Greenpeace, "Point of no return," 2013, http://www.greenpeace.de/fileadmin/gpd/user_upload/themen/klima/20130122-Studie-Point-Of-No-Return-Erderwaermung.pdf.

[6]   SEMI, "International Technology Roadmap for Photovoltaics (ITRPV)," 2012, http://www.itrpv.net/.cm4all/iproc.php/Reports%20downloads/roadmap_itrpv_march_2012_full_web.pdf?cdp=a.

[7]   S. W. Glunz , R. Preu, and D. Biro, "Crystalline silicon solar cells: state-of-the-art and future developments," in *Comprehensive renewable energy*. vol. 1, A. Sayigh, Ed., ed Oxford: Elsevier, 2012, pp. 353-87.

[8]   M. A. Green, K. Emery, Y. Hishikawa, W. Warta, and E. D. Dunlop, "Solar cell efficiency tables (version 41)," *Progress in Photovoltaics: Research and Applications,* vol. 21, pp. 1-11, 2013 2013.

[9]   C. Wadia, A. P. Alivisatos, and D. M. Kammen, "Materials availability expands the opportunity for large-scale photovoltaics deployment," *Environmental Science and Technology,* vol. 43, pp. 2072-7, 2009.

[10]   D. L. Staebler and C. R. Wronski, "Reversible conductivity changes in discharge-produced amorphous Si," *Applied Physics Letters,* vol. 31, pp. 292-4, 1977.

[11]   D. L. Staebler and C. R. Wronski, "Optically induced conductivity changes in discharge-produced hydrogenated amorphous silicon," *Journal of Applied Physics,* vol. 51, pp. 3262-8, 1980.

[12]   R. A. Street, *Hydrogenated amorphous silicon*. Cambridge: Cambridge University Press, 1991.

[13]   L. T. Canham, "Silicon quantum wire array fabrication by electrochemical and chemical dissolution of wafers," *Applied Physics Letters,* vol. 57, pp. 1046-8, 1990.

[14]   Z. Yuan, A. Anopchenko, N. Daldosso, R. Guider, D. Navarro-Urrios, A. Pitanti, R. Spano, and L. Pavesi, "Silicon nanocrystals as an enabling material for silicon photonics," *Proceedings of the IEEE,* vol. 97, pp. 1250-68, 2009.

[15]   O. Jambois, F. Gourbilleau, A. J. Kenyon, J. Montserrat, R. Rizk, and B. Garrido, "Towards population inversion of electrically pumped Er ions sensitized by Si nanoclusters," *Optics Express,* vol. 18, pp. 2230-2235, 2010/02/01/ 2010.

[16]   S. Tiwari, F. Rana, H. Hanafi, A. Hartstein, E. F. Crabbé, and K. Chan, "A silicon nanocrystals based memory," *Applied Physics Letters,* vol. 68, pp. 1377-9, 1996.

[17]   P. Löper, A. Hartel, M. Künle, D. Hiller, S. Janz, M. Hermle, M. Zacharias, and S. W. Glunz "Silicon quantum dot absorber layers for all-silicon tandem solar cells: optical and electrical characterisation," in *Proceedings of the 24th European Photovoltaic Solar Energy Conference*, Hamburg, Germany, 2009, pp. 434-8.

[18]   M. Zacharias, J. Heitmann, R. Scholz, U. Kahler, M. Schmidt, and J. Bläsing, "Size-controlled highly luminescent silicon nanocrystals: A SiO/SiO_2 superlattice approach," *Applied Physics Letters,* vol. 80, pp. 661-3, 2002.

[19]   Y. Kurokawa, S. Tomita, S. Miyajima, A. Yamada, and M. Konagai, "Observation of the photovoltaics effect from the solar cells using silicon quantum dots superlattice as a light absorption layer," in *Proceedings of the 33rd IEEE Photovoltaic Specialists Conference*, San Diego, CA, USA, 2008, pp. 1-6.

[20]   R. Rölver, B. Berghoff, D. L. Bätzner, B. Spangenberg, and H. Kurz, "Lateral Si/SiO_2 quantum well solar cells," *Applied Physics Letters,* vol. 92, p. 212108, 2008.

[21]   E.-C. Cho, S. Park, X. Hao, D. Song, G. Conibeer, S.-C. Park, and M. A. Green, "Silicon quantum dot/crystalline silicon solar cells," *Nanotechnology,* vol. 19, p. 245201, 2008.

[22]   S. Yamada, Y. Kurokawa, S. Miyajima, A. Yamada, and M. Konagai, "High open-circuit voltage oxygen-containing silicon quantum dots superlattice solar cells," in *Proceedings of the 35th IEEE Photovoltaic Specialists Conference*, Honolulu, Hawaii, USA, 2010, pp. 766-9.

[23]   P. Würfel, *Physics of solar cells - from basic principles to advanced concepts*, 2nd ed. Weinheim: Wiley-VCH Verlag GmbH & Co. KGaA, 2009.

[24]   N. W. Ashcroft and N. D. Mermin, *Solid state physics*. Tokyo; Philadelphia: Holt-Saunders, 1976.

[25]   O. L. Lazarenkova and A. A. Balandin, "Miniband formation in quantum dot crystal," *Journal of Applied Physics,* vol. 89, pp. 5509-15, 2001.

[26]   G. Bastard, "Superlattice band structure in the envelope-function approximation," *Physical Review B,* vol. 24, pp. 5693-7, 1981.

[27]   R. Müller, "Elektrische und photovoltaische Eigenschaften von Silicium-Nanokristallen in einer dielektrischen Matrix," Masterarbeit, Technische Fakultät. Institut für Mikrosystemtechnik, Universität Freiburg, Freiburg, Germany, 2011.

[28]   T. Roth, "Analysis of electrically active defects in silicon for solar cells," Dr. rer. nat Dissertation, Fachbereich Physik, Universität Konstanz, Konstanz, 2008.

[29]   G. Kirchhoff, "Ueber das Verhältniss zwischen dem Emissionsvermögen und dem Absorptionsvermögen der Körper für Wärme und Licht," *Annalen der Physik,* vol. 185, pp. 275-301, 1860 1860.

[30]   M. A. Weinstein, "On the Validity of Kirchhoff's Law for a Freely Radiating Body," *American Journal of Physics,* vol. 28, 1960 1960.

[31]   G. Lasher and F. Stern, "Spontaneous and stimulated recombination radiation in semiconductors," *Physical Review,* vol. 133, pp. 553-63, 1964.

[32]   P. Würfel, "The chemical potential of radiation," *Journal of Physics C: Solid State Physics,* vol. 15, pp. 3967-3985, 1982.

[33]   P. Würfel, S. Finkbeiner, and E. Daub, "Generalized Planck's radiation law for luminescence via indirect transitions," *Applied Physics A (Materials Science Processing),* vol. 60, pp. 67-70, 1995.

[34]   R. S. Crandall, "Modeling of thin film solar cells: Uniform field approximation," *Journal of Applied Physics,* vol. 54, pp. 7176-7186, 1983/12/01/ 1983.

[35]   J. Merten, J. M. Asensi, C. Voz, A. V. Shah, R. Platz, and J. Andreu, "Improved equivalent circuit and analytical model for amorphous silicon solar cells and modules," *IEEE Transactions on Electron Devices,* vol. 45, pp. 423-429, 1998/02// 1998.

[36]   P. W. Anderson, "Absence of diffusion in certain random lattices," *Physical Review,* vol. 109, pp. 1492-1505, 1958.

[37]   J. Tauc, R. Grigorovici, and A. Vancu, "Optical properties and electronic structure of amorphous germanium," *Physica Status Solidi B,* vol. 15, pp. 627-37, 1966.

[38]   G. D. Cody, T. Tiedje, B. Abeles, B. Brooks, and Y. Goldstein, "Disorder and the optical-absorption edge of hydrogenated amorphous silicon," *Physical Review Letters,* vol. 47, pp. 1480-3, 1981.

[39]   G. D. Cody, "Urbach edge, disorder, and absorption on-set in a-Si:H," in *Proceedings of the Materials Research Society Spring Meeting*, Warrendale, PA, USA, 2005, pp. A1.3.1-13.

[40]   P. Löper, R. Müller, D. Hiller, T. Barthel, E. Malguth, S. Janz, J. C. Goldschmidt, M. Hermle, and M. Zacharias, "Quasi-Fermi-level splitting in ideal silicon nanocrystal superlattices," *Physical Review B,* vol. 84, p. 195317, 2011.

[41]   C.-W. Jiang and M. A. Green, "Silicon quantum dot superlattices: Modeling of energy bands, densities of states, and mobilities for silicon tandem solar cell applications," *Journal of Applied Physics,* vol. 99, p. 114902, 2006.

[42]   S. M. Sze, *Semiconductor devices, Physics and Technology. ,* 2nd ed. New York, NY, USA: John Wiley & Sons Inc. , 2002.

[43]   G. Lehmann and M. Taut, "On the numerical calculation of the density of states and related properties," *Physica Status Solidi B,* vol. 54, pp. 469-77, 1972.

[44]   E. Yablonovitch and G. D. Cody, "Intensity enhancement in textured optical sheets for solar cells," *IEEE Transactions on Electron Devices,* vol. 29, pp. 300-5, 1982.

[45]   J.-W. Luo, P. Stradins, and A. Zunger, "Matrix-embedded silicon quantum dots for photovoltaic applications: a theoretical study of critical factors," *Energy & Environmental Science,* vol. 4, pp. 2546-57, 2011.

[46]   Y. Chao, L. Šiller, S. Krishnamurthy, P. R. Coxon, U. Bangert, M. Gass, L. Kjeldgaard, S. N. Patole, L. Lie, N. O'Farrell, T. A. Alsop, A. Houlton , and B. R. Horrocks, "Evaporation and deposition of alkyl-capped silicon nanocrystals in ultrahigh vacuum," *Nature Nanotechnology,* vol. 2, pp. 486-9, 2007.

[47]   M. Ehbrecht, B. Kohn, F. Huisken, M. A. Laguna, and V. Paillard, "Photoluminescence and resonant Raman spectra of silicon films produced by size-selected cluster beam deposition," *Physical Review B,* vol. 56, pp. 6958-6964, 1997/09/15/ 1997.

[48]   A. Bapat, C. Anderson, C. R. Perrey, C. B. Carter, S. A. Campbell, and U. Kortshagen, "Plasma synthesis of single crystal silicon nanoparticles for novel electronic device applications," *Plasma Physics and Controlled Fusion,* vol. 46, pp. 97-109, 2004.

[49]   D. Jurbergs, E. Rogojina, L. Mangolini, and U. Kortshagen, "Silicon nanocrystals with ensemble quantum yields exceeding 60%," *Applied Physics Letters,* vol. 88, pp. 233116/1-3, 2006.

[50]   J. Heitmann, R. Scholz, M. Schmidt, and M. Zacharias, "Size controlled nc-Si synthesis by SiO/SiO2 superlattices," *Journal of Non-Crystalline Solids,* vol. 299–302, Part 2, pp. 1075-1078, 2002/04// 2002.

[51]   P. D. Persans, A. Ruppert, and B. Abeles, "Crystallization kinetics of amorphous Si/SiO_2 superlattice structures," *Journal of Non-Crystalline Solids,* vol. 102, pp. 130-5, 1988.

[52]   R. Rölver, B. Berghoff, D. Bätzner, B. Spangenberg, H. Kurz, M. Schmidt, and B. Stegemann, "Si/SiO_2 multiple quantum wells for all silicon tandem cells: Conductivity and photocurrent measurements," *Thin Solid Films,* vol. 516, pp. 6763-6, 2008.

[53]   B. Stegemann, A. Schoepke, and M. Schmidt, "Structure and photoelectrical properties of SiO_2/Si/SiO_2 single quantum wells prepared under ultrahigh vacuum conditions," *Journal of Non-Crystalline Solids,* vol. 354, pp. 2100-4, 2008.

[54]   J. Heitmann, F. Müller, M. Zacharias, and U. Gösele, "Silicon nanocrystals: size matters," *Advanced Materials,* vol. 17, pp. 795-803, 2005.

[55]   D. Hiller, "The Influence of Interface Defects on the Optical Properties of Silicon Nanocrystals," Dissertation, Technische Fakultät, Universität Freiburg, Freiburg, 2011.

[56]   D. Hiller, S. Goetze, F. Munnik, M. Jivanescu, J. W. Gerlach, J. Vogt, E. Pippel, N. Zakharov, A. Stesmans, and M. Zacharias, "Nitrogen at the Si-nanocrystal/SiO_2 interface and its influence on luminescence and interface defects," *Physical Review B,* vol. 82, p. 195401, 2010.

[57]   D. Kovalev, H. Heckler, G. Polisski, and F. Koch, "Optical properties of Si nanocrystals," *Physica Status Solidi B,* vol. 215, pp. 871-932, 1999.

[58]   B. G. Lee, D. Hiller, J.-W. Luo, O. E. Semonin, M. C. Beard, M. Zacharias, and P. Stradins, "Strained Interface Defects in Silicon Nanocrystals," *Advanced Functional Materials,* vol. 22, pp. 3223-3232, 2012 2012.

[59]   D. König, J. Rudd, M. A. Green, and G. Conibeer, "Role of the interface for the electronic structure of Si quantum dots," *Physical Review B,* vol. 78, p. 035339, 2008.

[60]   S. Godefroo, M. Hayne, M. Jivanescu, A. Stesmans, M. Zacharias, O. I. Lebedev, G. Van Tendeloo, and V. V. Moshchalkov, "Classification and control of the origin of photoluminescence from Si nanocrystals," *Nature Nanotechnology,* vol. 3, pp. 174-8, 2008.

[61]   M. Jivanescu, A. Stresmans, and M. Zacharias, "Inherent paramagnetic defects in layered nanocrystalline Si/SiO$_2$ superstructures," *Physica E,* p. published online, 2008.

[62]   S. Cheylan and R. G. Elliman, "Effect of hydrogen on the photoluminescence of Si nanocrystals embedded in a SiO2 matrix," *Applied Physics Letters,* vol. 78, pp. 1225-1227, 2001/02/26/ 2001.

[63]   A. R. Wilkinson and R. G. Elliman, "Kinetics of H$_2$ passivation of Si nanocrystals in SiO$_2$," *Physical Review B,* vol. 68, p. 155302, 2003.

[64]   A. Stesmans, "Interaction of Pb defects at the (111) Si/SiO$_2$ interface with molecular hydrogen: simultaneous action of passivation and dissociation," *Journal of Applied Physics,* vol. 88, pp. 489-97, 1 July 2000 2000.

[65]   W. S. Pelouch, R. J. Ellingson, P. E. Powers, C. L. Tang, D. M. Szmyd, and A. J. Nozik, "Comparison of hot-carrier relaxation in quantum wells and bulk GaAs at high carrier densities," *Physical Review B,* vol. 45, pp. 1450-3, 15 Jan 1992.

[66]   B. Feuerbacher and P. Würfel, "Verification of a generalised Planck law by investigation of the emission from GaAs luminescent diodes," *Journal of Physics: Condensed Matter,* vol. 2, pp. 3803-10, 1990.

[67]   R. Guerra, F. Cigarini, and S. Ossicini, "Optical absorption and emission of silicon nanocrystals: from single to collective response," *Journal of Applied Physics,* vol. submitted, 2013.

[68]   R. J. Walters, G. I. Bourianoff, and H. A. Atwater, "Field-effect electroluminescence in silicon nanocrystals," *Nature Materials: Letters,* vol. 4, pp. 143-6, 2005.

[69]   Y. Berencén, J. M. Ramírez, O. Jambois, C. Domínguez, J. A. Rodríguez, and B. Garrido, "Correlation between charge transport and electroluminescence properties of Si-rich oxide/nitride/oxide-based light emitting capacitors," *Journal of Applied Physics,* vol. 112, pp. 033114-033114-5, 2012/08/14/ 2012.

[70]   A. Anopchenko, A. Marconi, E. Moser, S. Prezioso, M. Wang, L. Pavesi, G. Pucker, and P. Bellutti, "Low-voltage onset of electroluminescence in nanocrystalline-Si/SiO2 multilayers," *Journal of Applied Physics,* vol. 106, pp. 033104-033104-8, 2009/08/11/ 2009.

[71]   A. Marconi, A. Anopchenko, M. Wang, G. Pucker, P. Bellutti, and L. Pavesi, "High power efficiency in Si-nc/SiO2 multilayer light emitting devices by bipolar direct tunneling," *Applied Physics Letters,* vol. 94, pp. 221110-221110-3, 2009/06/04/ 2009.

[72]   B. Berghoff, S. Suckow, R. Rölver, B. Spangenberg, H. Kurz, A. Sologubenko, and J. Mayer, "Improved charge transport through Si based multiple quantum wells with substoichiometric SiO$_x$ barrier layers," *Journal of Applied Physics,* vol. 106, p. 083706, 2009.

[73]   K. Seino, F. Bechstedt, and P. Kroll, "Tunneling of electrons between Si nanocrystals embedded in a SiO_{2} matrix," *Physical Review B,* vol. 86, 2012/08/16/ 2012.

[74]   A. Witzky, "Elektrische und optische Charakterisierung von Silicium-Carbid-Schichten mit eingebetteten Silicium-Nanokristallen für Silicium-basierte Solarzellen mit hoher Bandlücke," Diplomarbeit, Fakultät für Physik, Universität Freiburg, Freiburg, 2012.

[75]   R. Gradmann, "Charakterisierung von Silizium-Nanokristallen in einer Siliziumkarbid-Matrix," Diplomarbeit, Institut für Kristallographie, Universität zu Köln, Köln, 2010.

[76]   R. Gradmann, P. Loeper, M. Künle, M. Rothfelder, S. Janz, M. Hermle, and S. Glunz, "Si and SiC nanocrystals in an amorphous SiC matrix: Formation and electrical properties," *Physica Status Solidi C,* vol. 8, pp. 831-4, 2011.

[77]   G. L. Harris, *Properties of silicon carbide*. London, UK: INSPEC, the Institution of Electrical Engineers, 1995.

[78]   M. Künle, S. Janz, K. G. Nickel, and O. Eibl, "Changes in chemical composition and nanostructure of SiC thin films prepared by PECVD during thermal annealing," *physica status solidi (a),* vol. 208, pp. 1885-95, 2011.

[79]   M. T. Künle, "Silicon carbide single and multilayer thin films for photovoltaic applications," Dissertation, Mathematisch-Naturwissenschaftliche Fakultät, Universität Tübingen, Tübingen, Germany, 2011.

[80]   P. G. Neudeck, "Silicon carbide technology," in *The VLSI Handbook*, W.-K. Chen, Ed., 2nd ed Boca Raton, FL, USA: CRC Press and IEEE Press, 2007, pp. 5.1-5.34.

[81]   N. F. Mott, "Conduction in non-crystalline materials " *Philosophical Magazine,* vol. 19, pp. 835-52, 1969.

[82]   R. C. Chittick, J. H. Alexander, and H. F. Sterling, "The preparation and properties of amorphous silicon," *Journal of the Electrochemical Society,* vol. 116, pp. 77-81, 1969.

[83]   D. A. Anderson and W. E. Spear, "Electrical and optical properties of amorphous silicon carbide, silicon nitride and germanium carbide prepared by the glow discharge technique," *Philosophical Magazine,* vol. 35, pp. 1-16, 1977.

[84]   J. Bullot and M. P. Schmidt, "Physics of amorphous silicon-carbon alloys," *Physica Status Solidi B,* vol. 143, pp. 345-418, 1987.

[85]   D. Suwito, "Intrinsic and doped amorphous silicon carbide films for the surface passivation of silicon solar cells," Dissertation, Fakultät für Physik, Universität Konstanz, Konstanz, 2011.

[86]   M. P. Rothfelder, "Spektrale Ellipsometrie zur optischen und strukturellen Charakterisierung von amorphen Siliciumkarbid-Schichtsystemen," Diplom, Fakultät für Mathematik und Physik, Universität Freiburg, Freiburg, 2010.

[87]   M. Mayer, "SIMNRA User's Guide," 1997.

[88]   M. H. Brodsky, M. Cardona, and J. J. Cuomo, "Infrared and Raman spectra of the silicon-hydrogen bonds in amorphous silicon prepared by glow discharge and sputtering," *Physical Review B,* vol. 16, pp. 3556-71, 1977.

[89]   G. Lucovsky, R. J. Nemanich, and J. C. Knights, "Structural interpretation of the vibrational spectra of a-Si:H alloys," *Physical Review B,* vol. 19, pp. 2064-73, 1979.

[90]   H. Wieder, M. Cardona, and C. R. Guarnieri, "Vibrational spectrum of hydrogenated amorphous Si-C films " *Physica Status Solidi B,* vol. 92, pp. 99-112, 1979.

[91]   Y. Catherine, G. Turban, and B. Grolleau, "Reaction mechanisms in plasma deposition of SixC1-x:H films," *Thin Solid Films,* vol. 76, pp. 23-34, 1981/01/30/ 1981.

[92]   Y. Tawada, S. Tsuge, M. Kondo, H. Okamoto, and Y. Hamakawa, "Properties and structure of a-SiC:H for high-efficiency a-Si solar cell," *Journal of Applied Physics,* vol. 53 pp. 5273-81, 1982.

[93]   R. A. C. M. M. van Swaaij, A. J. M. Berntsen, W. G. J. H. M. van Sark, H. Herremans, J. Bezemer, and W. F. van der Weg, "Local structure and bonding states in a-Si$_{1-x}$C$_x$:H," *Journal of Applied Physics,* vol. 76, pp. 251-6, 1994.

[94]   W. Beyer and H. Mell, "Composition and thermal stability of glow-discharge a-Si:C:H and a-Si:N:H alloys," in *Disordered Semiconductors*, 1987, pp. 641-58.

[95]   P. I. Rovira and F. Alvarez, "Chemical (dis)order in a-Si$_{1-x}$C$_x$:H for x<0.6," *Physical Review B,* vol. 55, pp. 4426-34, 1997.

[96]   D. R. Mckenzie, "Infrared absorption and bonding in amorphous hydrogenated silicon-carbon alloys," *Journal of Physics D: Applied Physics,* vol. 18, pp. 1935-48, 1985.

[97]   J. A. Borders, S. T. Picraux, and W. Beezhold, "Formation of SiC silicon by ion implantation," *Applied Physics Letters,* vol. 18, pp. 509-11, 1971.

[98]   L. Calcagno, P. Musumeci, F. Roccaforte, C. Bongiorno, and G. Foti, "Crystallization process of amorphous silicon-carbon alloys," *Thin Solid Films,* vol. 411, pp. 298-302, 2002.

[99]   K. Schillinger, S. Janz, and S. Reber, "Atmospheric Pressure Chemical Vapour Deposition of 3C-SiC for Silicon Thin-Film Solar Cells on Various Substrates," *Journal of Nanoscience and Nanotechnology,* vol. 11, pp. 8108-8113, 2011 2011.

[100]   W. G. Spitzer, D. A. Kleinman, and C. J. Frosch, "Infrared properties of cubic silicon carbide films," *Physical Review,* vol. 113, pp. 133-6, 1959.

[101]   G. Lucovsky, P. D. Richard, D. V. Tsu, S. Y. Lin, and R. J. Markunas, "Deposition of silicon dioxide and silicon-nitride by remote plasma enhanced chemical vapor deposition," *Journal of Vacuum Science & Technology A,* vol. 4, pp. 681-8, 1986.

[102]   D. K. Basa and F. W. Smith, "Annealing and crystallization processes in a hydrogenated amorphous Si-C alloy film," *Thin Solid Films,* vol. 192, pp. 121-33, 1990.

[103]   H. Kuzmany, *Solid-State Spectroscopy: An Introduction*: Springer, 1998.

[104]   M. Schnabel, P. Löper, S. Gutsch, P. R. Wilshaw, and S. Janz, "Thermal oxidation and encapsulation of silicon–carbon nanolayers," *Thin Solid Films,* vol. 527, pp. 193-199, 2013/01/01/ 2013.

[105]   D. Song, E.-C. Cho, G. Conibeer, Y.-H. Cho, and Y. Huang, "Fabrication and characterization of Si nanocrystals in SiC matrix produced by magnetron cosputtering," *Journal of Vacuum Science Technology B,* vol. 25, pp. 1327-35, 2007.

[106]   D. Song, E.-C. Cho, G. Conibeer, Y. Huang, C. Flynn, and M. A. Green, "Structural characterization of annealed Si1–xCx /SiC multilayers targeting formation of Si nanocrystals in a SiC matrix," *Journal of Applied Physics,* vol. 103, p. 083544, 28 Apr 2008.

[107]   M. Künle, T. Kaltenbach, P. Löper, A. Hartel, S. Janz, O. Eibl, and K.-G. Nickel, "Si-rich a-SiC:H thin films: structural and optical transformations during thermal annealing," *Thin Solid Films,* vol. 519, pp. 151-7, 2010.

[108]   Y. Kurokawa, S. Miyajima, A. Yamada, and M. Konagai, "Preparation of nanocrystalline silicon in amorphous silicon carbide matrix," *Japanese Journal of Applied Physics,* vol. 45, pp. 1064-6, 2006.

[109]   J. López-Vidrier, S. Hernández, J. Samà, M. Canino, M. Allegrezza, M. Bellettato, R. Shukla, M. Schnabel, P. Löper, L. López-Conesa, S. Estradé, F. Peiróa, S. Janz, and B. Garrido, "Structural, optical and electrical properties of silicon nanocrystals embedded in SixC1–x/SiC multilayer systems for photovoltaic applications," *Materials Science and Engineering B,* pp. 1-6, 2012.

[110] C. Summonte, S. Mirabella, R. Balboni, A. Desalvo, I. Crupi, F. Simone, and A. Terrasi, "Growth and characterization of Si nanodot multilayers in SiC matrix," in *Proceedings of the 23rd European Photovoltaic Solar Energy Conference*, Valencia, Spain, 2008, pp. 730-3.

[111] C. Summonte, M. Allegrezza, M. Bellettato, F. Liscio, M. Canino, and A. Desalvo, "Silicon nanodots in silicon carbide matrix," *in preparation,* 2013.

[112] A. M. Hartel, M. Künle, P. Löper, S. Janz, and A. W. Bett, "Amorphous Si_xC_{1-x}:H single layers before and after thermal annealing: correlating optical and structural properties," *Solar Energy Materials & Solar Cells,* vol. 94, pp. 1942-6, 2010.

[113] C. Spinella, S. Lombardo, and F. Priolo, "Crystal grain nucleation in amorphous silicon," *Journal of Applied Physics,* vol. 84, pp. 5383-414, 1998.

[114] M. Künle, P. Löper, M. Rothfelder, S. Janz, K.-G. Nickel, and O. Eibl, "Structural and optical characterization of Si quantumdots in a SiC matrix," in *Proceedings of the Materials Research Society Spring Meeting*, San Francisco, CA, USA, 2010.

[115] C. Summonte, M. Canino, M. Allegrezza, M. Bellettato, R. Shukla, A. Desalvo, A. Terrasi, S. Mirabella, I. Crupi, S. Janz, P. Löper, M. Schnabel, J. Lopez-Vidrier, L. Lopez-Conesa, S. Hernandez, S. Estrade, F. Peiro, B. Garrido, and J. Valenta, "Optical absorption of silicon nanocrystals in silicon carbide matrix," in *Proceedings of the E-MRS Spring Meeting*, Strasbourg, France, 2012.

[116] S. Schamm, C. Bonafos, H. Coffin, N. Cherkashin, M. Carrada, G. Ben Assayag, A. Claverie, M. Tencé, and C. Colliex, "Imaging Si nanoparticles embedded in SiO2 layers by (S)TEM-EELS," *Ultramicroscopy,* vol. 108, pp. 346-357, 2008/03// 2008.

[117] C. M. Wang, Y. Zhang, W. J. Weber, W. Jiang, and L. E. Thomas, "Microstructural Features of Al-Implanted 4H–SiC," *Journal of Materials Research,* vol. 18, pp. 772-779, 2003 2003.

[118] C. W. Liu and J. C. Sturm, "Low temperature chemical vapor deposition growth of β-SiC on (100) Si using methylsilane and device characteristics," *Journal of Applied Physics,* vol. 82, pp. 4558-4565, 1997/11/01/ 1997.

[119] S. E. Hicks, A. G. Fitzgerald, S. H. Baker, and T. J. Dines, "The structural, chemical and compositional nature of amorphous silicon carbide films," *Philosophical Magazine B,* vol. 62, pp. 193-212, 1990.

[120] C. Droz, "Thin film microcrystalline silicon layers and solar cells: microstructure and electrical performances," Dissertation, Faculté des Sciences, Neuchatel, 2003.

[121] Z. Iqbal and S. Veprek, "Raman scattering from hydrogenated microcrystalline and amorphous silicon," *Journal of Physics C: Solid State Physics,* vol. 15, p. 377, 1982.

[122] D. Beeman, R. Tsu, and M. F. Thorpe, "Structural information from the Raman spectrum of amorphous silicon," *Physical Review B,* vol. 32, pp. 874-8, 1985.

[123] A. Morimoto, S. Oozora, M. Kumeda, and T. Shimizu, "Raman studies on local structural disorder in silicon-based amorphous semiconductor films," *Solid State Communications,* vol. 47, pp. 773-7, 1983.

[124] N. F. Mott and E. A. Davis, *Electronic processes in non-crystalline materials*. Cambridge: Oxford University Press 1971.

[125] M. Yamanaka, H. Daimon, E. Sakuma, S. Misawa, and S. Yoshida, "Temperature dependence of electrical properties of n- and p-type 3C-SiC," *Journal of Applied Physics,* vol. 61, pp. 599-603, 1987/01/15/ 1987.

[126] M. Eickhoff, H. Moller, J. Stoemenos, S. Zappe, G. Kroetz, and M. Stutzmann, "Influence of crystal quality on the electronic properties of n-type 3C-SiC grown by low temperature low pressure chemical vapor deposition," *Journal of Applied Physics,* vol. 95, pp. 7908-17, 2004.

[127] A. Gali, D. Heringer, P. Deák, Z. Hajnal, T. Frauenheim, R. P. Devaty, and W. J. Choyke, "Isolated oxygen defects in 3C- and 4H-SiC: A theoretical study," *Physical Review B,* vol. 66, 2002/09/27/ 2002.

[128] A. Suzuki, A. Uemoto, M. Shigeta, K. Furukawa, and S. Nakajima, "Temperature dependence of electrical properties of nondoped and nitrogen doped betaSiC single crystals grown by chemical vapor deposition," *Applied Physics Letters,* vol. 49, pp. 450-2, 1986.

[129] D. V. Tsu, G. Lucovsky, and M. J. Mantini, "Local anatomic structure in thin films of silicon nitride and silicon diimide produced by remote plasma-enhanced chemical-vapor deposition," *Physical Review B,* vol. 33, pp. 7069-76, 1986.

[130] E. Bustarret, M. Bensouda, M. C. Habrard, and J. C. Bruyere, "Configurational statistics in a-SixNyHz alloys: A quantitative bonding analysis," *Physical Review B,* vol. 38, pp. 8171-84, 15 Oct 1988.

[131] D. J. Larkin, P. G. Neudeck, J. A. Powell, and L. G. Matus, "Site-competition epitaxy for superior silicon carbide electronics," *Applied Physics Letters,* vol. 65, pp. 1659-1661, 1994/09/26/ 1994.

[132] M. B. J. Wijesundara, D. Gao, C. Carraro, R. T. Howe, and R. Maboudian, "Nitrogen doping of polycrystalline 3C-SiC films grown using 1,3-disilabutane in a conventional LPCVD reactor," *Journal of Crystal Growth,* vol. 259, pp. 18-25, 2003/11// 2003.

[133] S. Miyagawa, S. Nakao, K. Saitoh, M. Ikeyama, H. Niwa, S. Tanemura, and Y. Miyagawa, "Formation of β-Si_3N_4 by nitrogen implantation into SIC " *Journal of Applied Physics,* vol. 78, pp. 7018-21, 1995.

[134] V. van Elsbergen, M. Rohleder, and W. Mönch, "Formation of nitride layers on 6H-SiC surfaces," *Applied Surface Science,* vol. 134, pp. 197-201, 1998.

[135] V. M. Bermudez, "Study of the initial adsorption of nitrogen on SiC (1OO)-(2 x 1)," *Surface Science,* vol. 276, pp. 59-68, 1992.

[136] H. N. Waltenburg and J. T. Yates, "Surface chemistry of silicon," *Chemical Reviews,* vol. 95, pp. 1598-673, 1995.

[137] T. Ito, S. Hijiya, T. Nozaki, H. Arawaka, M. Shinoda, and Y. Fukukawa, "Very thin silicon nitride films grown by direct thermal reaction with nitrogen," *Journal of Electrochemical Society: Solid-State Science and Technology,* vol. 125, pp. 448-52, 1978.

[138] A. G. Schrott and S. C. Fain Jr, "Nitridation of Si(111) by nitrogen atoms," *Surface Science,* vol. 111, pp. 39-52, 1981/10/02/ 1981.

[139] A. G. Schrott, Q. X. Su, and S. C. Fain Jr, "Reaction of Si(100) single crystals with nitrogen atoms," *Surface Science,* vol. 123, pp. 223-230, 1982/12/02/ 1982.

[140] H. Zhu, D. Yang, L. Wang, and D. Due, "Thermal nitridation kinetics of silicon wafers in nitrogen atmosphere during annealing," *Thin Solid Films,* vol. 474, pp. 326-9, 2005.

[141] H. M. Jennings, "Review - on reactions between silicon and nitrogen," *Journal of Materials and Science,* vol. 18, pp. 951-67, 193.

[142] L. Barbadillo, M. J. Hernández, M. Cervera, P. Rodriguez, and J. Piqueras, "Low-energy carbon and nitrogen ion implantation in silicon," *Journal of Vaccum Science & Technology B,* vol. 19, pp. 1124-32, 2001.

[143] L. Barbadillo, M. J. Hernández, M. Cervera, P. Rodriguez, J. Piqueras, S. I. Molina, F. M. Morales, and D. Araujo, "Structural characterization of high-dose C^+ + N^+ ion-implanted," *Nuclear Instruments and Methods in Physics Research B,* vol. 184, pp. 361-70, 2001.

[144] W. Siebert, R. Carius, W. Fuhs, and K. Jahn, "Photoluminescence in a-$Si_{1-x}C_x$:H films," *Physica Status Solidi B,* vol. 140, pp. 311-21, 1987.

[145] R. Carius, K. Jahn, W. Siebert, and W. Fuhs, "Photoluminescence in amorphous alloys: a-SiO$_x$:H, a-SiN$_x$:H, a-Si$_x$C$_{1-x}$:H," *Journal of Luminescence,* vol. 31-32, pp. 354-6, 1984.

[146] L. R. Tessler and I. Solomon, "Photoluminescence of tetrahedrally coordinated a-Si$_{1-x}$C$_x$:H," *Physical Review B,* vol. 52, pp. 10962-71, 1995.

[147] J. Y. Fan, X. L. Wu, and P. K. Chu, "Low-dimensional SiC nanostructures: Fabrication, luminescence, and electrical properties," *Progress in Materials Science,* vol. 51, pp. 983-1031, 2006.

[148] E. Centurioni, "Generalized matrix method for calculation of internal light energy flux in mixed coherent and incoherent multilayers," *Applied Optics,* vol. 44, pp. 7532-7539, http://www.bo.imm.cnr.it/users/centurioni/optical.html, 2005.

[149] C. Summonte, M. Canino, M. Allegrezza, M. Bellettato, A. Desalvo, S. Mirabella, and A. Terrasi, "Systematic characterization of silicon nanodot absorption for third generation photovoltaics," in *Proceedings of the 26th European Photovoltaic Solar Energy Conference*, Hamburg, Germany, 2011, pp. 361-6.

[150] D. A. G. Bruggeman, "Berechnung verschiedener physikalischer Konstanten von heterogenen Substanzen. I. Dielektrizitätskonstanten und Leitfähigkeiten der Mischkörper aus isotropen Substanzen.," *Annalen der Physik,* vol. 416, pp. 636-64, 1935.

[151] M. A. Green, "Potential for low dimensional structures in photovoltaics," *Materials Science and Engineering B,* vol. 74, pp. 118-24, 2000.

[152] F. Meillaud, A. Shah, C. Droz, E. Vallat-Sauvain, and C. Miazza, "Efficiency limits for single-junction and tandem solar cells," *Solar Energy Materials & Solar Cells,* vol. 90, pp. 2952-9, 2006.

[153] R. E. I. Schropp and M. Zeman, *Amorphous and microcrystalline silicon solar cells: modeling, materials and device technology*. Boston/Dordrecht/London: Kluwer Academic Publishers, 1998.

[154] M. Zacharias, J. Heitmann, L. X. Yi, E. Wildanger, and R. Scholz, "Silicon technology used for size-controlled silicon nanocrystals," in *Towards the first silicon laser*, L. Pavesi, Ed., ed: Kluwer academic publishers, 2003, pp. 131-8.

[155] O. Debieu, "Optical characterization of luminescent silicon nanocrystals embedded in glass matrices," Dissertation, Physikalisch-Astronomische Fakultät, Universität Jena, 2008.

[156] D. Hiller, M. Jivanescu, A. Stesmans, and M. Zacharias, "P$_{b(0)}$ centers at the Si-nanocrystal/SiO$_2$ interface as the dominant photoluminescence quenching defect," *Journal of Applied Physics,* vol. 107, p. 084309, 2010.

[157] D. Hiller, S. Goetze, and M. Zacharias, "Rapid thermal annealing of size-controlled Si nanocrystals: Dependence of interface defect density on thermal budget," *Journal of Applied Physics,* vol. 109, pp. 054308-054308-5, 2011/03/10/ 2011.

[158] S. Gutsch, A. M. Hartel, D. Hiller, and M. Zacharias, "Transport Regimes in Silicon Nanocrystal/SiO2 Superlattices," in *Proceedings of the E-MRS Spring Meeting*, Strasbourg, France, 2012.

[159] R. Shukla, C. Summonte, M. Canino, M. Allegrezza, M. Bellettato, A. Desalvo, D. Nobili, S. Mirabella, N. Sharma, M. Jangir, and I. P. Jain, "Optical and electrical properties of Si nanocrystals embedded in SiC matrix," *Advanced Materials Letters,* vol. 3, pp. 297-304, 2012.

[160] P. Löper, A. Witzky, A. Hartel, S. Gutsch, D. Hiller, J. C. Goldschmidt, S. Janz, S. W. Glunz, and M. Zacharias, "Photovoltaic properties of silicon nanocrystals in silicon carbide," in *Proceedings of SPIE*, San Francisco, California, USA, 2012, pp. 82560G-1-6.

[161] P. Löper, M. Canino, J. Lopez-Vidrier, M. Schnabel, F. Schindler, F. Heinz, A. Witzky, Bellettato, M. Allegrezza, D. Hiller, A. Hartel, S. Gutsch, S. Hernandez, R. Guerra, S. Ossicini, B. Garrido, S. Janz, and M. Zacharias, "Silicon nanocrystals from high-temperature annealing: Characterization on device level," *Physica Status Solidi A,* 2013.

[162] S. Park, E. Cho, D. Song, G. Conibeer, and M. A. Green, "n-Type silicon quantum dots and p-type crystalline silicon heteroface solar cells," *Solar Energy Materials & Solar Cells,* vol. 93, pp. 684-90, 2009.

[163] D. Song, E.-C. Cho, G. Conibeer, Y. Huang, and M. A. Green, "Fabrication and electrical characteristics of Si nanocrystal/c-Si heterojunctions," *Applied Physics Letters,* vol. 91, p. 123510, 2007.

[164] Y. Kurokawa, S. Yamada, S. Miyajima, A. Yamada, and M. Konagai, "Effects of oxygen addition on electrical properties of silicon quantum dots/amorphous silicon carbide superlattice," *Current Applied Physics,* vol. 10, pp. S435-8, 2010.

[165] I. Perez-Wurfl, L. Ma, D. Lin, X. Hao, M. A. Green, and G. Conibeer, "Silicon nanocrystals in an oxide matrix for thin film solar cells with 492 mV open circuit voltage," *Solar Energy Materials and Solar Cells,* vol. 100, pp. 65-8, 2012.

[166] I. Perez-Wurfl, X. Hao, A. Gentle, D.-H. Kim, G. Conibeer, and M. A. Green, "Si nanocrystal p-i-n diodes fabricated on quartz substrates for third generation solar cell applications," *Applied Physics Letters,* vol. 95, p. 153506, 2009.

[167] B. S. Richards, J. E. Cotter, C. B. Honsberg, and S. R. Wenham, "Novel uses of TiO_2 in crystalline silicn solar cells," in *Proceedings of the 28th IEEE Photovoltaic Specialists Conference*, Anchorage, Alaska, 2000, pp. 1-4.

[168] B. S. Richards, "Comparison of TiO2 and other dielectric coatings for buried-contact solar cells: a review," *Progress in Photovoltaics: Research and Applications,* vol. 12, pp. 253-81, 2004.

[169] P. Alen, M. Vehkamaki, M. Ritala, and M. Leskela, "Diffusion barrier properties of atomic layer deposited ultrathin Ta2O5 and TiO2 films," *Journal of the Electrochemical Society,* vol. 153, pp. G304-G308, 2006 2006.

[170] A. M. Dhote, O. Auciello, D. M. Gruen, and R. Ramesh, "Studies of thin film growth and oxidation processes for conductive Ti–Al diffusion barrier layers via in situ surface sensitive analytical techniques," *Applied Physics Letters,* vol. 79, pp. 800-802, 2001/08/06/ 2001.

[171] O. Auciello, "Science and technology of thin films and interfacial layers in ferroelectric and high-dielectric constant heterostructures and application to devices," *Journal of Applied Physics,* vol. 100, pp. 051614-051614-15, 2006/09/19/ 2006.

[172] T. P. Chow and A. J. Steckl, "Refractory metal silicides: thin-film properties and processing technology," *IEEE Tansactionson Electron Devices,* vol. ED-30, pp. 1480-97, 1983.

[173] S. P. Murarka, "Silicide thin-films and their applications in microelectronics," *Intermetallics,* vol. 3, pp. 173-86, 1995.

[174] S. H. Luo, W. L. Liu, M. Zhang, Z. F. Di, S. Y. Wang, Z. T. Song, C. L. Lin, and S. C. Zou, "Buried tungsten silicide layer in silicon on insulator substrate by Smart-Cut®," *Semiconductor Science and Technology,* vol. 19, pp. 1329-32, Nov 2004.

[175] C. S. Park, B. J. Cho, and D.-L. Kwong, "Thermally stable fully silicided Hf-silicide metal-gate electrode," *IEEE Electron Device Letters,* vol. 25, pp. 372-4, 2004.

[176] Minami1999, "Stability of transparent conducting oxide films for use at high temperatures," *Journal of Vaccum Science & Technology A,* vol. 17, pp. 1822-6, 1999.

[177] O. J. Gregory, X. Chen, and E. E. Crisman, "Strain and temperature effects in indium–tin-oxide sensors," *Thin Solid Films,* vol. 518, pp. 5622-5, 2010.

[178] B. Berghoff, S. Suckow, R. Rölver, N. Wilck, B. Spangenberg, and H. Kurz, "Si/SiO2 quantum well solar cells based on lateral charge carrier transport," in *Proceedings of the 24th European Photovoltaic Solar Energy Conference and Exhibition*, Hamburg, Germany, 2009, pp. 388 - 390.

[179] S. S. Hegedus and W. N. Shafarman, "Thin-film solar cells: device measurements and analysis," *Progress in Photovoltaics: Research and Applications,* vol. 12, pp. 155-76, 2004.

[180] T. Kinoshita, D. Fujishima, A. Yano, A. Ogane, S. Tohoda, K. Matsuyama, Y. Nakamura, N. Tokuoka, H. Kanno, H. Sakata, M. Taguchi, and E. Maruyama, "The approaches for hig efficiency HIT^{TM} solar cell with very thin (<100µm) silicon wafer over 23%," in *Proceedings of the 26th European Photovoltaic Solar Energy Conference and Exhibition*, Hamburg, Germany, 2011, pp. 871-4.

[181] T. M. Brown, C. Bittencourt, M. Sebastiani, and F. Evangelisti, "Electronic states and band lineups in c-Si(100)/a-Si$_{1-x}$C$_x$:H heterojunctions," *Physical Review B,* vol. 55, pp. 9904-09, 1997.

[182] C. Bittencourt and F. Alvarez, "Valence band offsets of a-Si$_{1-x}$C$_x$ on c-Si and a-Si:H," in *Properties of amorphous silicon and its alloys*, T. Searle, Ed., ed: Institution of Engineering and Technology, 1998, pp. 174-80.

[183] R. L. Anderson, "Experiments on Ge-GaAs Heterojunctions," *Solid-State Electronics,* vol. 5, pp. 341-51, 1962.

[184] E. T. Yu, J. O. McCaldin, and T. C. McGill, "Band offsets in semiconductor heterojunctions," in *Solid State Physics*. vol. 46, H. Ehrenreich and D. Turnbull, Eds., ed Cambridge: Academic Press, 1992, pp. 1-146.

[185] F. Demichelis, C. F. Pirri, E. Tresso, G. Della Mea, V. Rigato, and P. Rava, "Physical properties of undoped and doped hydrogenated amorphous silicon carbide," *Semiconductor Science and Technology,* vol. 6, pp. 1141-6, 1991.

[186] M. N. P. Carreno and I. Pereyra, "p-Type doping in a-Si$_{1-x}$C$_x$:H obtained by PECVD," *Journal of Non-Crystalline Solids,* vol. 266-269, pp. 699-703, 2000.

[187] M. J. Bozack, "Surface studies on SiC as related to contacts," *Physica Status Solidi B,* vol. 202, pp. 549-80, 1997.

[188] D. Pysch, J. Ziegler, J.-P. Becker, D. Suwito, S. Janz, S. W. Glunz, and M. Hermle, "Stretched-exponential increase in the open-circuit voltage induced by thermal annealing of amorphous silicon-carbide heterojunction solar cells," *Applied Physics Letters,* vol. 94, pp. 093510/1-3, 2009.

[189] D. Pysch, M. Bivour, M. Hermle, and S. W. Glunz "Amorphous silicon carbide heterojunction solar cell on p-type substrates," *Thin Solid Films,* vol. 519, pp. 2550-4, 2011.

[190] M. Tanaka, M. Taguchi, T. Matsuyama, T. Sawada, S. Tsuda, S. Nakano, H. Hanafusa, and Y. Kuwano, "Development of new a-Si / c-Si heterojunction solar cells: ACJ-HIT (Artifically constructed junction-heterojunction with intrinsic thin-layer)," *Japanese Journal of Applied Physics,* vol. 31, pp. 3518-22, 1992.

[191] Y. Tsunomura, Y. Yoshimine, M. Taguchi, T. Baba, T. Kinoshita, H. Kanno, H. Sakata, E. Maruyama, and M. Tanaka, "Twenty-two percent efficiency HIT solar cell," *Solar Energy Materials & Solar Cells,* vol. 93, pp. 670-3, 2009.

[192] P. Löper, M. Canino, D. Qazzazie, M. Schnabel, M. Allegrezza, C. Summonte, S. W. Glunz, S. Janz, and M. Zacharias, "Silicon nanocrystals embedded in silicon carbide: Investigation of charge carrier transport and recombination," *Applied Physics Letters,* vol. 102, pp. 1-4, 2013.

[193] C. Reichel, "Decoupling charge carrier collection and metallization geometry of back-contacted back-junction silicon solar cells," Dissertation, Technische Fakultät, Universität Freiburg, Freiburg, Germany, 2012.

[194] C. Reichel, F. Granek, M. Hermle, and S. W. Glunz, "Back-contacted back-junction n-type silicon solar cells featuring an insulating thin film for decoupling charge carrier collection and metallization geometry," *Progress in Photovoltaics: Research and Applications,* pp. n/a-n/a, 2012 2012.

[195] P. Löper, D. Stüwe, M. Künle, M. Bivour, C. Reichel, R. Neubauer, M. Schnabel, M. Hermle, O. Eibl, S. Janz, M. Zacharias, and S. W. Glunz, "A membrane device for substrate-free photovoltaic characterization of quantum dot based p-i-n solar cells," *Advanced Materials,* vol. 24, pp. 3124-9, 2012.

[196] A. M. Hartel, D. Hiller, S. Gutsch, P. Löper, S. Estradé, F. Peiró, B. Garrido, and M. Zacharias, "Formation of size-controlled silicon nanocrystals in plasma enhanced chemical vapor deposition grown SiO_xN_y/SiO_2 superlattices," *Thin Solid Films,* vol. 520, pp. 121-5, 2011.

[197] D. M. Qazzazie, "Modellierung und Charakterisierung von Silizium-basierten Nanokristall-Membransolarzellen," M.Sc. Masterarbeit, Technische Fakultät, Universität Freiburg, Freiburg, Germany, 2012.

[198] M. Canino, C. Summonte, M. Allegrezza, R. Shukla, I. P. Jain, M. Bellettato, A. Desalvo, F. Mancarella, M. Sanmartin, A. Terrasi, P. Löper, M. Schnabel, and S. Janz,

"Identification and tackling of a parasitic surface compound in SiC and Si-rich carbide films," *Materials Science and Engineering: B,* 2013.

[199] M. A. Green, *Silicon solar cells: advanced principles and practice*. Sydney, Australia: Centre for Photovoltaic Devises and Systems UNSW, 1995.

[200] J. O. Schumacher, "Numerical simulation of silicon solar cells with novel device structures," Dissertation, Fakultät für Physik, University of Konstanz, Konstanz, 2000.

[201] C. Petermann, R. Beigang, and P. Fischer, "Fourier-transform photocurrent spectroscopy using a supercontinuum light source," *Applied Physics Letters,* vol. 100, p. 061108, 2012.

[202] S. S. Hegedus, "Current–Voltage Analysis of a-Si and a-SiGe Solar Cells Including Voltage-dependent Photocurrent Collection," *Progress in Photovoltaics: Research and Applications,* vol. 5, pp. 151-168, 1997 1997.

[203] J. H. Werner, "Schottky barrier and pn-junctionI/V plots — Small signal evaluation," *Applied Physics A,* vol. 47, pp. 291-300, 1988/11/01/ 1988.

[204] K. Ding, U. Aeberhard, W. Beyer, O. Astakhov, F. Köhler, U. Breuer, F. Finger, R. Carius, and U. Rau, "Annealing induced defects in SiC, SiO_x single layers, and SiC/SiO_x hetero-superlattices," *physica status solidi (a),* p. published online, 2012.

[205] K. Ding, U. Aeberhard, O. Astakhov, U. Breuer, M. Beigmohamadi, S. Suckow, B. Berghoff, W. Beyer, F. Finger, R. Carius, and U. Rau, "Defect passivation by hydrogen reincorporation for silicon quantum dots in SiC/SiO_x hetero-superlattice," *Journal of Non-Crystalline Solids,* p. published online, 2012.

[206] Y. Kurokawa, S. Tomita, S. Miyajima, A. Yamada, and M. Konagai, "Effects of nitrogen on the electrical properties of Si quantum dots superlattice using a-SiC Matrix," in *Proceedings of the 24th European Photovoltaic Solar Energy Conference*, Hamburg, Germany, 2009, pp. 398-403.

[207] S. Summonte, E. Centurioni, A. Desalvo, M. Canino, S. Mirabella, R. Agosta, F. Simone, A. Terrasi, M. A. Di Stefano, S. Di Marco, S. Ravesi, and S. Lombardo, "Optical Properties of Silicon Nanoparticles for Photovoltaic Applications," in *24th European Photovoltaic Solar Energy Conference*, Hamburg, Germany, 2009, pp. 317 - 321.

[208] A. Mohr, P. Engelhart, C. Klenke, S. Wanka, A. A. Stekolnikov, M. Scherff, R. Seguin, S. Tardon, T. Rudolph, M. Hofmann, F. Stenzel, J. Y. Lee, S. Diez, J. Wendt, W. Brendle, S. Schmidt, J. W. Müller, P. Wawer, M. Hofmann, P. Saint-Cast, J. Nekarda, D. Erath, J. Rentsch, and R. Preu, "20%-efficient rear side passivated solar cells in pilot series designed

for conventional module assembling," in *Proceedings of the 26th European Photovoltaic Solar Energy Conference and Exhibition*, Hamburg, Germany, 2011, pp. 2150-3.

[209] I. Kuzma-Filipek, K. V. Nieuwenhuysen, J. V. Hoeymissen, M. R. Payo, E. V. Kerschaver, J. Poortmans, R. Mertens, G. Beaucarne, E. Schmich, S. Lindekugel, and S. Reber, "Efficiency (>15%) for thin-film epitaxial silicon solar cells on 70cm^2 area offspec silicon substrate using porous silicon segmented mirrors," *Progress in Photovoltaics: Research and Applications,* vol. 18, pp. 137-43, 2010.

[210] Z. Ouyang, O. Kunz, A. B. Sproul, and S. Varlamov, "Influence of the absorber doping for p-type polycrystalline silicon thin-film solar cells on glass prepared by electron beam evaporation and solid-phase crystallization," *Journal of Applied Physics,* vol. 109, p. 054510, 2011.

[211] S. W. Glunz, C. Hebling, W. Warta, and W. Wettling, "Comparison of spatially resolved carrier lifetimes in mc-Si with solar cell and material characteristics," in *Proceedings of the 1st World Conference on Photovoltaic Energy Conversion*, Hawaii, USA, 1994, pp. 1625-8.

[212] S. Fischer, "Photonenmanagement für neuartige Silizium-Solarzellen," Diplomarbeit, Fakultät für Mathematik und Physik, Universität Freiburg, Freiburg, Germany, 2009.

[213] S. J. Wawilow, "Die Fluoreszenzausbeute von Farbstofflösungen als Funktion der Wellenlänge des anregenden Lichtes. II," *Zeitschrift für Physik,* vol. 42, pp. 311-8, 1927.

[214] M. Künle, S. Janz, O. Eibl, C. Berthold, V. Presser, and K.-G. Nickel, "Thermal annealing of SiC thin films with varying stoichiometry," *Materials Science and Engineering B,* vol. 159-160, pp. 355-60, 2009.

[215] R. Tsu, J. Gonzalez-Hernandez, S. S. Chao, S. C. Lee, and K. Tanaka, "Critical volume fraction of crystallinity for conductivity percolation in phosphorus-doped Si:F:H alloys," *Applied Physics Letters,* vol. 40, p. 534, 1982.

[216] E. Bustarret and M. A. Hachicha, "Experimental determination of the nanocrystamne volume fraction in sincon thin films from Raman spectroscopy," *Applied Physics Letters,* vol. 52, pp. 1675-7, 1988.

[217] P. Scherrer, *Göttinger Nachrichten Gesellschaft,* vol. 2, p. 98, 1918.

[218] A. L. Patterson, "The Scherrer formula for X-ray particle size determination," *Physical Review,* vol. 56, pp. 978-982, 1939.

[219] G. Nitsche, "Elektronenstrahlinduzierte Strommessungen in Silicium: Untersuchung laserchemisch prozessierter Proben sowie temperaturabhängige Messungen von mc-

Silicium zum Vergleich mit Mikro-Photolumineszenzspektroskopie," Diplom Diplomarbeit, Universität Karlsruhe, Karlsruhe, Germany, 2011.

[220] P. J. Mohr and B. N. Taylor, "CODATA Recommended Values of the Fundamental Physical Constants:1998," *Journal of Physical and Chemical Reference Data,* vol. 28, 1999.

13 Appendix

13.1 Network simulation of membrane-based solar cells

The influence of insulation layer breakdown on the global IV characteristics was estimated with a network simulation of the equivalent circuit shown in Fig. 13.1. Insulation layer breakdown was approximated as an ohmic contact, denoted as R_4 and R_6 in Fig. 13.1. The Si NC p-i-n solar cell and the Si wafer solar cell were both modeled by a diode and a parallel resistance. The parallel resistances (R_1, R_5 in Fig. 13.1) were assumed to be 10 kΩcm² and weighted with the corresponding area. The different ITO parts were treated as ohmic series resistances R_2, R_3, R_7 and calculated for each particular cell geometry from the known ITO resistivity $\rho = 4\times10^{-4}\,\Omega$cm. Three cases were considered: High (700 mV), medium (500 mV) and very low (300 mV) open-circuit voltage of the wafer diode. The open-circuit voltage of the Si NC membrane cell was set to 300 mV as this is the relevant voltage range for devices discussed here. Open-circuit voltages were set by choosing the corresponding values for the dark saturation current density. The short-circuit currents were assumed to be 40 mA/cm² (wafer diode) and 1 mA/cm² (Si NC solar cell) and the diode ideality factors were set to 1. In this model, the insulation shunt resistances (R_4, R_6) are the only two free parameters. As they influence the global IV curve identically, one was set to zero and the other treated as a free parameter modeling the shunt resistance. A parameter variation for the structures with the smallest (0.09 mm²) and the largest (25 mm²) active cell area is shown in Fig. 13.2 plotted against the shunt resistance.
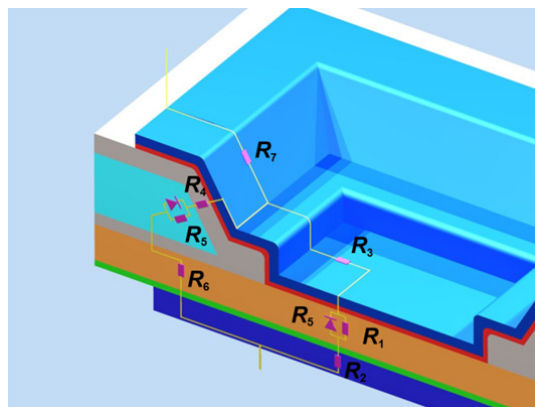

Fig. 13.1:Sketch of the equivalent circuit for the network simulation. Failure of insulation layers A and B is represented by the ohmic shunt resistances R_6 and R_4, respectively. Both have identical effect on the global IV curve. The figure was taken from [197].

Fig. 13.2 illustrates that small structures ((a) and (c)) are much more affected by conduction through the insulation layers than larger structures ((b) and (d), note the different x-axes). The green line marks a 10% deviation from the values of the membrane only ($V_{OC} = 300$ mV, $J_{SC} = 1$mA/cm²). It can be seen that insulation layer failure is readily seen in the short-circuit current ((a) and (b)) while the open-circuit voltage ((c) and (d)) is largely unaffected. This result stresses that the structure is suitable as a voltage device. Furthermore, current-sensitive methods are viable to detect insulation layer failure and allow for a spatially resolved device failure analysis. If no current contribution from the wafer substrate is detected, the entire IV curve is free of wafer influence.
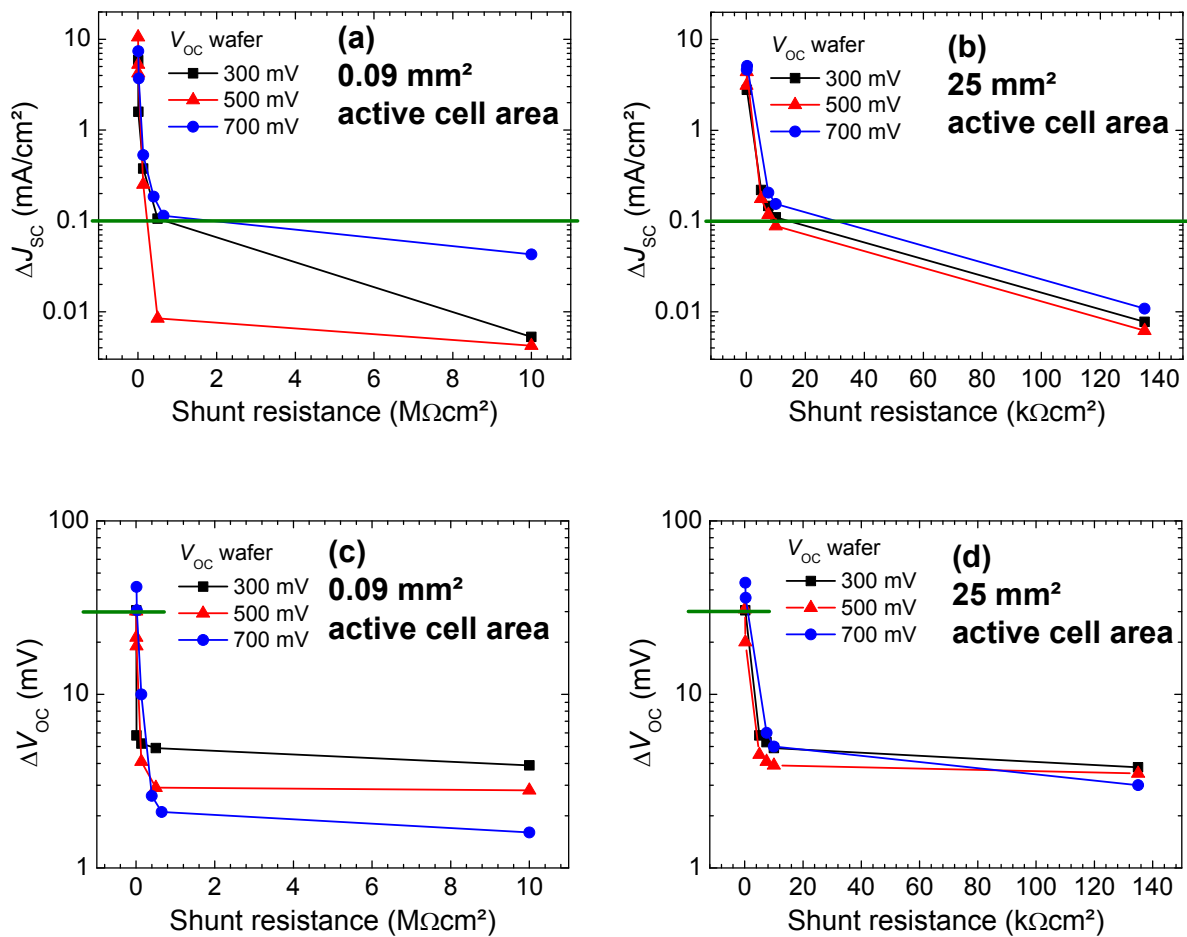
Fig. 13.2: Simulated deviation of the short-circuit current (upper row) and the open-circuit (lower row) voltage due to insulation breakdown. The device was simulated with a numerical network simulation of the equivalent circuit shown in Fig. 13.1. Insulation breakdown is modeled as an ohmic shunt resistance. The figure was taken from [197].

13.2 Characterization methods

13.2.1 Conductivity measurements

Conductivity measurements were done with a Hewlett Packard HP4041B picoammeter. The sample was mounted in an evacuated cryostat to avoid influences of surface adsorbates and for electric shielding. The current noise level was around 5×10^{-15} A. The setup is described in detail in [74]. The resistivity was determined in the following way: Current-voltage curves were measured for six different electrode distances on the device structure shown in Fig. 13.3. A linear regression was then performed for every current-voltage curve to determine the resistance. The resistance R is the sum of the electrode contact resistances R_C and the film resistance R_{Film}, $R = R_{Film} + 2R_C$. The film resistance is proportional to the electrode distance S with the constant offset $2R_C$. A plot of the total resistance against the distance permits to separate R_C and R_{Film} and thus to extract the the specific conductivity σ:

$$R_{Film} = \frac{S}{\sigma dw}.$$ (13.1)

The film thickness is denote as d and the electrode width w.
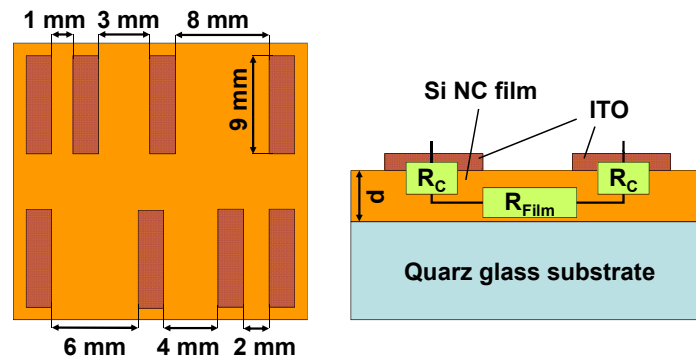
Fig. 13.3: Device structure employed for electrical characterization. The contacts were defined by ITO sputtering through a shadow mask. The figures were taken from [74].

For temperature-dependent conductivity measurements, the temperature of the chuck in the cryostat was controlled with liquid nitrogen and resistive heating. The sample temperature was measured with a resistance thermometer (PT100) that was pressed to the film surface. A current-voltage curve was recorded for one pair of electrodes after temperature stabilization.

Photoconductivity measurements were performed with a fiber coupled Ar ion laser as light source. A fiber collimator and a rotatable cylindrical lens were used to shape a

homogeneous illumination of the area between the contacts. The irradiance was measured with a solar cell with known spectral response. The effective mobility lifetime product was calculated according to Eq. (2.43).

13.2.2 Fourier transform infrared spectroscopy

Infrared (IR) spectroscopy is an optical spectroscopic technique that is sensitive to vibrational modes of two or more bonded atoms (molecules). The selection rule for IR spectroscopy is that the electric dipole moment changes during vibration [103]. For this reason neither symmetric vibration modes cannot be detected by IR spectroscopy because their dipole moment does not change nor homonuclear bonds are detected as they do not have a dipole moment at all.
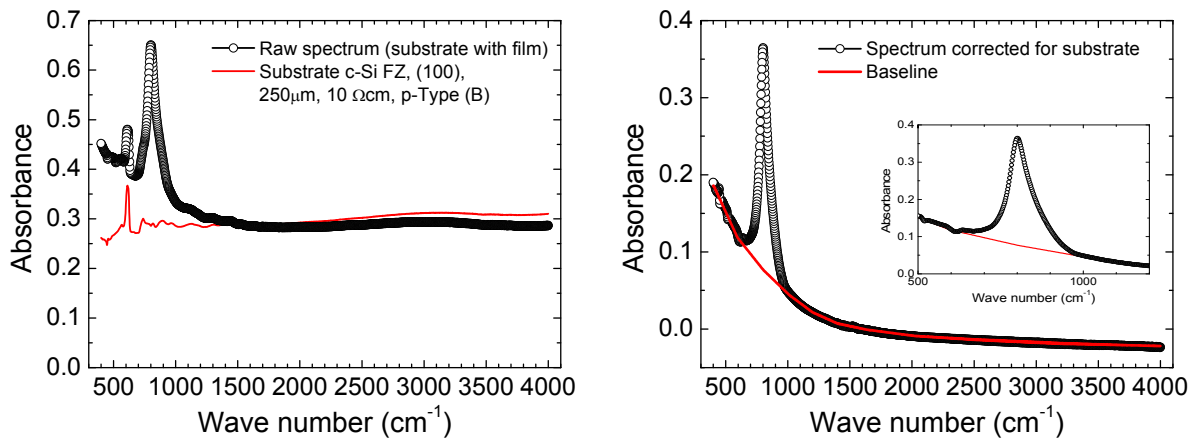
Fig. 13.4:(Left) IR absorbance spectrum of the sample consisting of a FZ c-Si wafer substrate with a SiC/Si NC multilayer film. (Right) After substraction of the reference, the spectrum is corrected for the baseline.

Fourier transform infrared spectroscopy makes use of the Fourier transform to calculate the infrared spectrum of a sample from the experimentally generated interferogramm. In this thesis, a Bruker IFS-113v FTIR spectrometer was used, which operates in transmission mode. A spectrum is generated by first measuring the spectrum of the apparatus itself, followed by the spectrum of the sample. The devision of these two spectra,

$$T = \frac{I}{I_0},$$
(13.2)

yields the transmittance T of the sample. I is the incident, and I_0 the transmitted intensity. A substrate wafer is measured together with every sample as a reference. Fig. 13.4 (a) shows an example of a spectrum of an annealed SiC/Si NC film on the substrate along with the reference substrate spectrum. After substraction of the reference, the spectrum

usually contains non-linear baseline. The baseline is caused by various wavelength dependent measurement artifacts such as the imperfect infrared transparency of the film, interface reflections due to discontinuities of the refreactive index or scattering due to surface roughness. Therefore, a baseline correction has to be performed to extract the experimental spectrum as shown in Fig. 13.4 (b).

13.2.3 Spectrophotometry

Reflection and transmission spectra were measured with a Varian 500i spectrophotometer. The operating principle is depicted in Fig. 13.5. The light of a broad band source is monochromatized with a grating monochromator and guided by means of an optical chopper and mirrors either via the sample or through a reference entrance to an integrating sphere. For a transmission measurement, the sample is placed at position A, and for a reflection measurement, the sample is placed at position B. The detector records the intensity in the integrating sphere and is read out with a lock-in technique using the frequency of the optical chopper as reference. The intensity is related to the reflectance of a reflection standard and to zero signal which are measured before the sample (baseline measurement).

Neglecting multiple reflections, the absorption coefficient can be calculated from the reflectance R and the transmisstance T as

$$\alpha = \frac{1}{d} \mathrm{Ln}\left(\frac{1-R}{T}\right), \qquad (13.3)$$

As the determination of the optical band gap defines on the assumed model, frequently the optical band gap is expressed as E_{04} or E_{04}. The value E_{03} (E_{04}) refers to the photon energy at which the absorption coefficient is $\alpha = 10^3$ cm^{-1} (10^3 cm^{-1}).
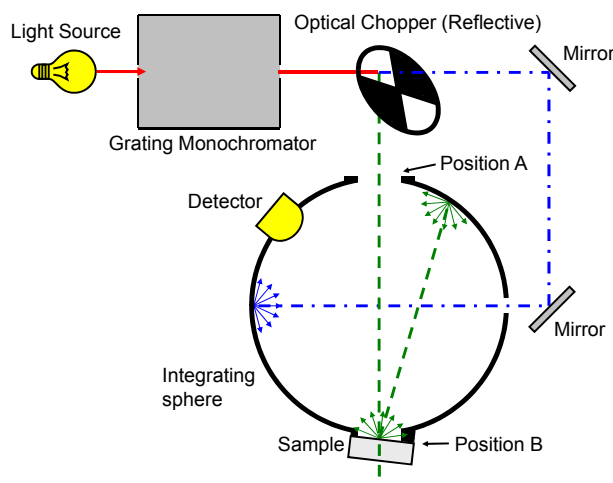
Fig. 13.5: Schematic of a Varian 500i spectrophotometer. The figure was adapted from [212].

13.2.4 Photoluminescence

Photoluminescence (PL) was measured with two setups. The operating principle was the same and is sketched in Fig. 13.6. One setup was calibrated to measure the photoluminescence in absolute units (power per area per spectral interval). For the other setup, the relative transmission function was determined, and the spectra are therefore given in arbitrary units of power per spectral interval. In both setups, an Ar ion laser was used as light source (488 nm line for the calibrated setup, 514.5 nm line for the other setup), and a grating monochromator and a Si CCD camera as detection system. For calibrated measurements, the excitation light area and intensity were defined with a pinhole and photodiode and the sample was positioned to the focus of the detection system with the help of two crossed alignment lasers.
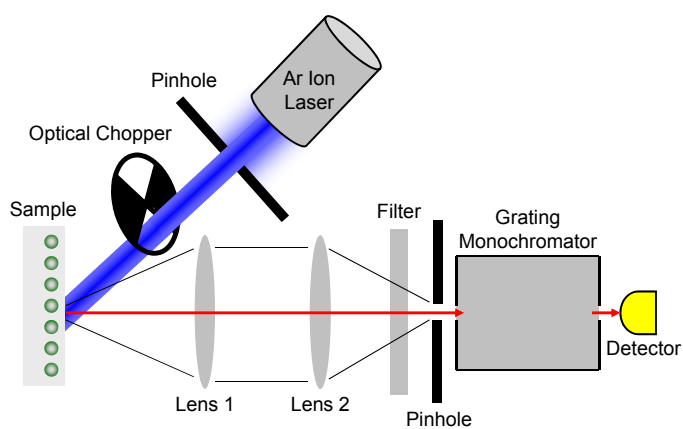

Fig. 13.6: Schematic of the photoluminescence setup. The figure was adapted from [27].

13.2.5 Photoluminescence excitation

Photoluminescence excitation (PLE) measures the ratio of photons emitted at the photoluminescence peak per incident photons. As the luminescence quantum yield is independent of the excitation wavelength (Kasha-Vavilov rule [213]), the PLE signal is a direct measure of the absorption. In contrast to other absorption measurements like spectrophotometry or photothermal deflection spectroscopy, only optical transitions at the probed wavelength contribute to the PLE signal.

13.2.6 Raman spectroscopy

Raman spectroscopy measures the wave number shift (Raman shift) due to inelastic scattering of monochromatic light at Raman active phonon modes in the probed material.

Raman spectra were measured under excitation with an Ar ion laser operating at 488 nm and the signal was detected using a grating monochromator. In annealed Si-rich SiC films, the silicon-related features between 50 cm^{-1} and 600 cm^{-1} are the most prominent modes. SiC modes occur between 750 cm^{-1} and 1000 cm^{-1} [119, 214], but have a much weaker intensity. In the framework of this thesis, Raman spectroscopy was used to examine the structural transformations of Silicon from the amorphous phase to the crystalline state. For this means, the spectrum was analyzed in the wave number range 300 cm^{-1} to 600 cm^{-1}. Characteristic for crystalline Si is the narrow peak due to the transversal optical (TO) phonon at 520 cm^{-1} [120]. This mode shifts to lower wave numbers as the crystallite size is reduced and appears as a broad Gaussian peak at 480 cm^{-1} for amorphous Si [121]. Furthermore, amorphous Si exhibits a longitudinal acoustical mode at 300 cm^{-1} and a longitudinal optical mode at 400 cm^{-1} [122, 123]. Characteristic for microcrystalline Si is another peak at 500 cm^{-1}, showing up as a hump in the low wave number shoulder of the c-Si TO phonon peak.

The Raman spectra analyzed in this work were fitted by a superposition of 5 peaks: Gaussian peaks at 300 cm^{-1}, 400 cm^{-1}, and 480 cm^{-1}, for the amorphous components, and a Gaussian peak at 500 cm^{-1} as well as a Lorentzian peak at 510 cm^{-1} for the crystalline components. Tsu et $al.$ [215] and Bustarret et $al.$ [216] introduced procedures to derive the crystalline volume fraction from the relative intensity of the amorphous and crystalline modes. In this work, the Raman crystalline volume fraction RCVF was calculated from the peak areas of the modes at 480 cm^{-1}, 500 cm^{-1} and 510 cm^{-1}, I_{480}, I_{500}, I_{510}, respectively, as

$$\text{RCVF} = \frac{I_{500} + I_{510}}{I_{500} + I_{510} + I_{480}}. \tag{13.4}$$

A linear baseline was taken into account. An exemplary fit is shown in Fig. 13.7. In order to reproduce all experimental spectra, a variation of the center wave number of up to 5 cm^{-1} was permitted.
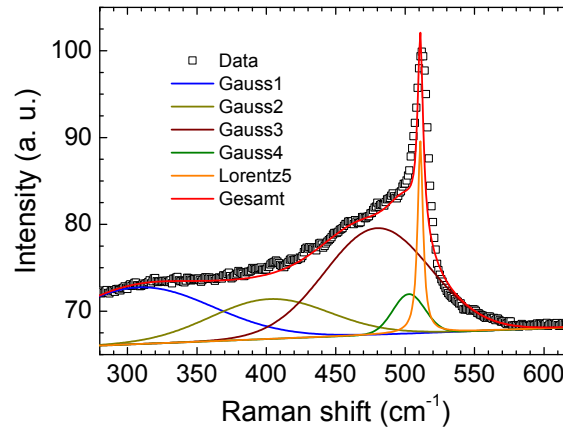

Fig. 13.7: Raman spectrum of an annealed Si-rich SiC film. The spectrum was fitted with 3 Gaussians for the modes in amorphous Si (centered at 300 cm^{-1}, 400 cm^{-1}, 480 cm^{-1}), and a Gaussian at 500 cm^{-1} to account for the crystallite grain boundaries and a Lorentzian at 510 cm^{-1} to account for the TO mode in crystalline Si.

13.2.7 X-ray diffraction

X-ray diffractograms were measured in grazing incidence configuration with a Philips X`Pert MRD system with Cu Kα_1 radiation (λ=1.541 Å). The angle of incidence was set to 0.3°C. The samples were irradiated with a line focus narrowed by a 1/32° horizontal slit in front of the X-ray source. A long-plate collimator (0.27°) was used for detection. The detector scna sthe detection angle 2θ from 20° to 100°. When the Bragg condition

$$2d_{hkl}\sin(\theta) = k\lambda, \quad k = 1,2,3 \dots \tag{13.5}$$

is fulfilled, reflection from the lattice planes (hkl) occurs. The spacing between two adjacent (hkl) lattice planes is d_{hkl}. A mean crystalline domain size L can be calculated from the width (full width at half maximum, FWHM) of the diffraction peak by means of the Scherrer formula [217], [218]

$$L = \frac{0.9\lambda}{\text{FWHM}(2\theta)\cos(\theta)}. \quad n = 1,2,3 \dots \tag{13.6}$$

13.2.8 Rutherford backscattering spectrometry

Rutherford backscatterering spectrometry (RBS) utilizes the relation between the kinetic energy of an incident ion beam to the kinetic energy of the backscattered ions. The RBS analysis was done at the Helmholtzzentrum Dresden Rossendorf with an incident He$^+$ ion

beam with 1.7 MeV beam energy from a van de Graaff accelerator. The mass of the target ion determines the energy loss due to the elastic scattering. The kinematic factor k_i is defined as the energy ratio of the backscattered and incident He ions, E_i and E_0, respectively, and depends on the mass of the target atoms M_i, the mass of the incident ions M_{He}, and the scattering angle θ,

$$k_i(M_i) = \frac{E_i}{E_0} = \left(\frac{\sqrt{M_i^2 - M_{He}^2 \sin^2(\theta)} + M_{He}\cos(\theta)}{M_{He} + M_i} \right)^2. \qquad (13.7)$$

As all parameters except the target atom mass M_i are known, the target atoms can be identified by the energy loss $\Delta E_i = E_i - E_0$. Apart from this elastic energy loss, the electronic stopping of the incident and the backscattered ions along their path through the probed material leads to an additional energy loss, resulting in a continuous peak downshift in the RBS spectrum.

13.2.9 Solar cell IV characteristics

Solar cell IV measurements were done with 4-point wiring using a Keithley 2611A source meter. A Wacom solar simulator was used as light source. The irradiance was set to 1000 W/m^2 using a calibrated c-Si wafer reference solar cell. For intensity-dependent measurement, the irradiance was tuned by means of a Fresnel lens in variable height above the device under test. The temperature of the device under test was set by the temperature-controlled measurement chuck.

13.2.10 Light beam induced current

Light beam induced current (LBIC) refers to a spatially resolved short-circuit current measurement by scanning the excitation light spot over the device. The setup is sketched in Fig. 13.8. The light of a halogen lamp is chopped by an optical chopper and coupled to a fiber bundle. A focusing optics focuses the light to a spot of approximately 200 µm light to the solar cell. The optics is mounted on a xyz translational stage. An current sensitive preamplifier (EG&G) is used to provide a low input resistance to the device under test and convert the current signal to a voltage signal. The voltage signal is detected with a lock-in amplifier (EG&G) and the frequency reference of the optical chopper. As for all short-circuit current measurements, a charge separating junction is required.
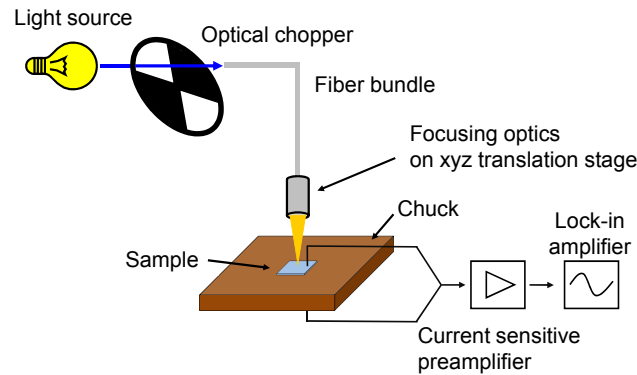
Fig. 13.8: Scheme of the light beam induced current setup. The figure was adapted from [197].

13.2.11 Electron beam induced current

In analogy to light beam induced current, electron beam induced current (EBIC) is another technique for a spatially resolved short-circuit current measurement. The main difference between the two techniques is that EBIC uses an electron beam for the generation of excess charge carriers instead of a light beam. The spatial resolution is thus superior to LBIC and the information depth depends on the electron scattering as the beam penetrates the sample. The measurements presented here were recorded with an EBIC stage integrated to a Hitachi SU-70 scanning electron microscope. Details on the EBIC method and the SEM employed here can be found in [219].

13.3 Cleaning processes

Several cleaning processes were employed in the sample preparation, each adapted to the requirements of the specific samples.

The fabrication process for the membrane cells starts with a so-called RCA clean which is done immediately prior to the thermal oxidation. The RCA clean employed here consists of the following of wet chemical treatments:

Rinse in deionized (DI) water, seething HNO_3 (70%) for 10min, rinse in DI water, HF (1%) for 25s, rinse in DI water, NH_4OH (8% 10l) with H_2O_2 (30%, 100ml) for 10min at 85°C, rinse in DI water, HF (1%) for 25s, rinse in DI water, HCl (8%, 10l) in H_2O_2 (30%, 100ml), rinse in DI water, HF (1%) for 25s, rinse in DI water.

If the temperature is not explicitly specified the process is done at room temperature.

Prior to depositing the SiC/Si NC multilayers, all Si substrates were cleaned with the "HNF" sequence, which is the first part of the RCA sequence:

Rinse in DI water, seething HNO_3 (70%) for 10min, rinse in DI water, HF (1%) for 25s, rinse in DI water.

The HNF sequence was also used as pretreatment before the deposition of the a-Si_xC_{1-x}:H selective contact layers.

All cleaning procedures for Si are based on oxidizing the Si surface and then removing the chemically grown oxide to prepare a Si surface of high purity. This mechanism does not work for quartz glass substrates, as in this case the surface cannot be further oxidized. For this reason, an adapted sequence was employed for quartz glass surfaces. It relies on the oxidation of organic adsorbates in hot HNO_3 followed by the oxidation of metals with HCl in combination H_2O_2 and a back etch of a few nm of the quartz glass surface.

Rinse in DI water, seething HNO_3 (70%) for 10min, rinse in DI water, HF (1%) for 60s, rinse in DI water, HCl (35%, 50ml) in H_2O_2 (30%, 50ml) diluted in 500 ml DI water, rinse in DI water, HF (1%) for 60s, rinse in DI water.

For special sample geometries, this sequence was not available and a "piranha" clean was used instead:

Acetone, isopropyl alcohol, H_2SO_4 (30%) with H_2O_2 at 80°C for 15min, rinse in DI water.

13.4 Abbreviations

Acronym	Meaning
2H, 3C, 4H, 6H	SiC polytypes
a	amorphous
AC	Alternate current
AM1.5G	Air mass 1.5 global
Al	Aluminum
Ar	Argon
B	Boron
c	crystalline
C	Carbon
CNR-IMM	Instituto per la microelettronica e microsistemi
CSG	Crystalline Si on glass
CVD	Chemical vapor deposition
D	Dimensional
DC	Direct current
DI	deionized
e	Electron
EBIC	Electron beam induced current
EFTEM	Energy filtered transmission electron microscopy
EELS	Electron energy loss spectroscopy
EQE	External quantum efficiency
ESR	Electron spin resonance
F	Fluor
FGA	Forming gas anneal
FTIR	Fourier transform infrared
FZ	Float zone
Ge	Germanium
GIXRD	Grazing incidence X-ray diffraction
γ	Photon

h	Hole
H	Hydrogen
He	Helium
HF	Hydrofluoric acid
Hf	Hafnium
HOMO	Highest occupied molecular orbital
In	Indium
IR	Infrared
ISE	Fraunhofer Institute for Solar Energy Systems
ITO	Indium tin oxide
IV	Current-voltage
KOH	potassium hydroxide
N	Nitrogen
NC	Nanocrystal
LBIC	Light beam induced current
LUMO	Lowest unoccupied molecular orbital
MIS	Metal insulator semiconductor
MOS	Metal oxide semiconductor
O	Oxygen
P	Phosphorus
PECVD	Plasma enhanced chemical vapor deposition
PERC	Passivated emitter and rear contact
PL	Photoluminescence
QD	Quantum dot
RBS	Rutherford backscattering spectrometry
RCA	Radio Corporation of America (Standard cleaning sequence)
RexWE	Recrystallized wafer equivalent
RF	Radio frequency
RPHP	Remote plasma hydrogen passivation
Si	Silicon

SiC	Silicon carbide
Si_xC_{1-x}	Non-stoichiometric silicon carbide
SiCN	Silicon carbo nitride
SiN_x	Non-stoichiometric silicon nitride
Si_3N_4	Stoichiometric silicon nitride
SIMS	Secondary ion mass spectrometry
SiO_x	Non-stoichiometric silicon oxide
SiO_2	Silicon dioxide
SiOETCH	Buffered hydrofluoric acid
SEM	Scanning electron microscope
Sn	Tin
stripeSTEM	Stripe scanning electron transmission microscope
Ta	Tantal
TEM	Transmission electron microscope
Ti	Titanium
TO	Transversal optical
W	Tungsten

13.5 Glossary

Variable	Dimension	Meaning
A		Absorptance
α	cm^{-1}	Absorption coefficient
β	$m^3 s^{-1}$	Coefficient of radiative recombination
c_i		Proportionality constant i
d	m	Thickness
d_{hkl}	m	Distance between lattice planes (hkl)
$q\chi$	eV	Electron affinity
N	$m^{-3}eV^{-1}$	Density of states
E	eV	Energy
EQE		External quantum efficiency
E_C	eV	Lowest energy in the conduction band
E_G	eV	Band gap
E_V	eV	Highest energy in the valence band
E_{03}	eV	Energy at which the absorption coefficient is 10^3 cm^{-1}
E_{PL}	eV	Photoluminescence peak energy
ε_F	eV	Fermi level
$\varepsilon_{F,e}$	eV	Electron quasi-Fermi level
$\varepsilon_{F,h}$	eV	Hole quasi-Fermi level
G	$m^{-3}s^{-1}$	Generation rate
G^0	$m^{-3}s^{-1}$	Equilibrium generation rate
ε_F	eV	Fermi level
$\Delta\varepsilon_F$	eV	Separation of quasi-Fermi levels
i		Iterative index
I_{PL}		Intensity (arbitrary units of power per area)
dj_γ	$m^{-2}s^{-1}eV^{-1}$	Photon current density
dj_γ^0	$m^{-2}s^{-1}eV^{-1}$	Photon current density
$dj_{\gamma,em}$	$m^{-2}s^{-1}eV^{-1}$	Emitted photon current density

$dj_{\gamma,\text{abs}}$	$\text{m}^{-2}\text{s}^{-1}\text{eV}^{-1}$	Absorbed photon current density
J	Acm^{-2}	Current density
J_0	Acm^{-2}	Saturation current density
J_h	Acm^{-2}	Hole current density
J_SC	Acm^{-2}	Short-circuit current density
J_gen	Acm^{-2}	Generation current density
J_dark	Acm^{-2}	Dark current density
J_light	Acm^{-2}	Light current density
	m^{-1}	Extinction coefficient
k	m	wave vector absolute value
		Iterative number
$\boldsymbol{k}$	m	wave vector
L	m	Nanocrystal size
L_coll	m	Effective drift length
L_D	m	Effective drift length
λ	m	Wavelength
m_0	kg	Electron invariant mass
m_{QP}^*	kg	Electron or hole effective mass in quantum dot
m_M^*	kg	Electron or hole effective mass in the matrix
μ	$\text{m}^2\,\text{V}^{-1}\,\text{s}^{-1}$	Charge carrier mobility
$(\mu\tau)_\text{eff}$		Effective mobility lifetime product
N	$\text{m}^{-3}\text{eV}^{-1}$	Density of states
N_k	m^{-3}	Integrated density of states in band k
N_C	m^{-3}	Effective density of states in the conduction band
N_V	m^{-3}	Effective density of states in the valence band
	m^{-3}	Charge carrier density,
n		Quantum number,
		Ideality factor
		Refractive index,

n_e	m^{-3}	Electron density
n_e^0	m^{-3}	Electron density in thermal equilibrium
n_i	m^{-3}	Intrinsic carrier density
Ω	sr	Solid angle
Δn	m^{-3}	Electron excess carrier density
n_h	m^{-3}	Hole density
n_h^0	m^{-3}	Hole density in thermal equilibrium
P	m	Periodicity of a periodic array
π		Number Pi
φ		Envelope function
ψ		Wave function
$\boldsymbol{r}$	m	Space vector
R		Reflectance; Resistance
R_S	Ωm^{-2}	Series resistance
$R_{SC,dark}$	Ωm^{-2}	Short-circuit resistance in dark
$R_{SC,light}$	Ωm^{-2}	Short-circuit resistance under illumination
R_{shunt}	Ωm^{-2}	Shunt resistance
S	m^2	Area
S	m	Distance
ρ	m	Specific resistance
σ	Ω^{-1}m^{-1}	Conductivity
σ_{dark}	Ω^{-1}m^{-1}	Dark conductivity
σ_{ext}	Ω^{-1}m^{-1}	Conductivity through extended states
$\sigma_{ext,0}$	Ω^{-1}m^{-1}	Average conductivity through states above the mobility edge
σ_{light}	Ω^{-1}m^{-1}	Conductivity under illumination
θ	°	Angle
T	K	Absolute temperature,
	°C	Temperature

T		Transmittance
t	s	Time
τ_{eff}	s	Effective excess carrier lifetime
U	$m^{-3}s^{-1}$	Net recombination rate
V	V	Potential, Voltage
V_{BI}	V	Built-in voltage
V_{ext}	V	External voltage
V_{FB}	V	Flat-band voltage
V_{OC}	V	Open-circuit voltage
w	m	Width
x		Compositional parameter, Carthesian coordinate
y, z		Carthesian coordinates

13.6 Physical constants

Variable	Value [220]	Dimension	Meaning
c	299 792 458	$m\ s^{-1}$	Speed of light in vacuum
$\hbar$	6.58211928×10^{-16}	eV s	Planck constant
k_B	$1.380\ 6504\times10^{-23}$	$J\ K^{-1}$	Boltzmann constant
m_0	$9.109\ 382\ 15\times10^{-31}$	kg	Electron rest mass
q	$1.602\ 176\ 462(63)\times10^{-19}$	C	Elementary charge

14 List of publications

14.1 Peer reviewed journal papers

P. Löper, M. Canino, D. Qazzazie, M. Schnabel, M. Allegrezza, C. Summonte, S. W. Glunz, S. Janz, and M. Zacharias, "Silicon nanocrystals embedded in silicon carbide: Investigation of charge carrier transport and recombination," *Applied Physics Letters,* vol. 102, pp. 1-4, 2013.

P. Löper, M. Canino, J. Lopez-Vidrier, M. Schnabel, F. Schindler, F. Heinz, A. Witzky, Bellettato, M. Allegrezza, D. Hiller, A. Hartel, S. Gutsch, S. Hernandez, R. Guerra, S. Ossicini, B. Garrido, S. Janz, and M. Zacharias, "Silicon nanocrystals from high-temperature annealing: Characterization on device level," *Physica Status Solidi A,* 2013.

M. Canino, C. Summonte, M. Allegrezza, R. Shukla, I. P. Jain, M. Bellettato, A. Desalvo, F. Mancarella, M. Sanmartin, A. Terrasi, P. Löper, M. Schnabel, and S. Janz, "Identification and tackling of a parasitic surface compound in SiC and Si-rich carbide films," *Materials Science and Engineering: B,* 2013.

M. Schnabel, P. Löper, S. Gutsch, P. R. Wilshaw, and S. Janz, "Thermal oxidation and encapsulation of silicon–carbon nanolayers," *Thin Solid Films,* vol. 527, pp. 193-199, 2013/01/01/ 2013.

P. Löper, D. Stüwe, M. Künle, M. Bivour, C. Reichel, R. Neubauer, M. Schnabel, M. Hermle, O. Eibl, S. Janz, M. Zacharias, and S. W. Glunz, "A membrane device for substrate-free photovoltaic characterization of quantum dot based p-i-n solar cells," *Advanced Materials,* vol. 24, pp. 3124-9, 2012.

J. López-Vidrier, S. Hernández, J. Samà, M. Canino, M. Allegrezza, M. Bellettato, R. Shukla, M. Schnabel, P. Löper, L. López-Conesa, S. Estradé, F. Peiróa, S. Janz, and B. Garrido, "Structural, optical and electrical properties of silicon nanocrystals embedded in SixC1–x/SiC multilayer systems for photovoltaic applications," *Materials Science and Engineering B,* pp. 1-6, 2012.

S. Fischer, H. Steinkemper, P. Löper, M. Hermle, and J. C. Goldschmidt, "Modeling upconversion of erbium doped microcrystals based on experimentally determined Einstein coefficients," *Journal of Applied Physics,* vol. 111, p. 013109, 2012.

P. Löper, D. Pysch, A. Richter, M. Hermle, S. Janz, M. Zaccharias, and S. W. Glunz, "Analysis of the temperature dependence of the open-circuit voltage," *Energy Procedia,* vol. 27, pp. 135-42, 2012.

S. Janz, M. Schnabel, and <u>P. Löper</u>, "Silicon nanocrystals produced by solid phase crystallisation of superlattices for photovoltaic applications," *Materials Science and Engineering B,* 2012.

<u>P. Löper</u>, R. Müller, D. Hiller, T. Barthel, E. Malguth, S. Janz, J. C. Goldschmidt, M. Hermle, and M. Zacharias, "Quasi-Fermi-level splitting in ideal silicon nanocrystal superlattices," *Physical Review B,* vol. 84, p. 195317, 2011.

J. López-Vidrier, S. Hernández, A. M. Hartel, D. Hiller, S. Gutsch, <u>P. Löper</u>, L. López-Conesa, S. Estradé, F. Peiró, M. Zacharias, and B. Garrido, "Structural and optical characterization of size controlled silicon nanocrystals in SiO_2/SiO_xN_y multilayers," *Energy Procedia,* vol. 10, pp. 43-8, 2011.

R. Gradmann, <u>P. Löper</u>, M. Künle, M. Rothfelder, S. Janz, M. Hermle, and S. Glunz, "Si and SiC nanocrystals in an amorphous SiC matrix: Formation and electrical properties," *Physica Status Solidi C,* vol. 8, pp. 831-4, 2011.

J. C. Goldschmidt, S. Fischer, <u>P. Löper</u>, K. W. Krämer, D. Biner, M. Hermle, and S. W. Glunz "Experimental analysis of upconversion with both coherent monochromatic irradiation and broad spectrum illumination," *Solar Energy Materials and Solar Cells,* vol. 95, pp. 1960-3, 2011.

A. M. Hartel, D. Hiller, S. Gutsch, <u>P. Löper</u>, S. Estradé, F. Peiró, B. Garrido, and M. Zacharias, "Formation of size-controlled silicon nanocrystals in plasma enhanced chemical vapor deposition grown SiO_xN_y/SiO_2 superlattices," *Thin Solid Films,* vol. 520, pp. 121-5, 2011.

M. Künle, T. Kaltenbach, <u>P. Löper</u>, A. Hartel, S. Janz, O. Eibl, and K.-G. Nickel, "Si-rich a-SiC:H thin films: structural and optical transformations during thermal annealing," *Thin Solid Films,* vol. 519, pp. 151-7, 2010.

A. M. Hartel, M. Künle, <u>P. Löper</u>, S. Janz, and A. W. Bett, "Amorphous Si_xC_{1-x}:H single layers before and after thermal annealing: correlating optical and structural properties," *Solar Energy Materials & Solar Cells,* vol. 94, pp. 1942-6, 2010.

S. Fischer, J. C. Goldschmidt, <u>P. Löper</u>, G. H. Bauer, R. Brüggemann, K. Krämer, D. Biner, M. Hermle, and S. W. Glunz "Enhancement of silicon solar cell efficiency by upconversion: Optical and electrical characterization," *Journal of Applied Physics,* vol. 108, p. 044912, 2010.

M. Peters, J. C. Goldschmidt, <u>P. Löper</u>, B. Groß, J. Üpping, F. Dimroth, R. B. Wehrspohn, and B. Bläsi, "Spectrally-selective photonic structures for PV applications," *Energies,* vol. 3, pp. 171-93, 2010.

D. Hiller, R. Zierold, J. Bachmann, M. Alexe, Y. Yang, J. W. Gerlach, A. Stesmans, M. Jivanescu, U. Müller, J. Vogt, H. Hilmer, <u>P. Löper</u>, M. Künle, F. Munnik, K. Nielsch, and M. Zacharias, "Low temperature silicon dioxide by thermal atomic layer deposition: investigation of material properties," *Journal of Applied Physics,* vol. 107, p. 064314, 2010.

M. Peters, J. C. Goldschmidt, P. Löper, B. Bläsi, and A. Gombert, "The effect of photonic structures on the light guiding efficiency of fluorescent concentrators," *Journal of Applied Physics,* vol. 105, p. 014909, 2009.

B. Ahrens, <u>P. Löper</u>, J. C. Goldschmidt, S. W. Glunz , B. Henke, P.-T. Miclea, and S. Schweizer, "Neodymium-doped fluorochlorozirconate glasses as an upconversion model system for high efficiency solar cells," *Physica Status Solidi A,* vol. 205, pp. 2822-30, 2008.

A. Goetzberger, J. C. Goldschmidt, M. Peters, and <u>P. Löper</u>, "Light trapping, a new approach to spectrum splitting," *Solar Energy Materials & Solar Cells,* vol. 92, pp. 1570-8, 2008.

14.2 Papers presented at international conferences

<u>P. Löper</u>, M. Canino, J. Lopez-Vidrier, M. Schnabel, F. Schindler, F. Heinz, A. Witzky, Bellettato, M. Allegrezza, D. Hiller, A. Hartel, S. Gutsch, S. Hernandez, R. Guerra, S. Ossicini, B. Garrido, S. Janz, and M. Zacharias, "Silicon quantum dots in photovoltaic devices: device fabrication, characterization and comparison of materials," in *Proceedings of the 28th European Photovoltaic Solar Energy Conference and Exhibition*, Frankfurt, Germany, 2012.

C. Summonte, M. Canino, M. Allegrezza, M. Bellettato, R. Shukla, A. Desalvo, A. Terrasi, S. Mirabella, I. Crupi, S. Janz, <u>P. Löper</u>, M. Schnabel, J. Lopez-Vidrier, L. Lopez-Conesa, S. Hernandez, S. Estrade, F. Peiro, B. Garrido, and J. Valenta, "Optical absorption of silicon nanocrystals in silicon carbide matrix," in *Proceedings of the E-MRS Spring Meeting*, Strasbourg, France, 2012.

S. Janz, <u>P. Löper</u>, M. Schnabel, M. Zacharias, D. Hiller, S. Gutsch, A. Hartel, C. Summonte, A. Canino, M. Allegrezza, S. Ossicini, R. Guerra, I. Marri, B. Garrido, S. Hernandez, J. López-Vidrier, J. Valenta, T. Kubera, M. Foti, and C. Gerardi, "The NASCEnT project," in *Proceedings of the 26th European Photovoltaic Solar Energy Conference and Exhibition*, Hamburg, Germany, 2011, pp. 22-7.

M. Schnabel, A. Witzky, <u>P. Löper</u>, R. Gradmann, M. Künle, and S. Janz, "Electrical properties of recrystallised SiC films from PECVD precursors for silicon quantum dot solar cell applications," in *Proceedings of the 26th European Photovoltaic Solar Energy Conference and Exhibition*, Hamburg, Germany, 2011, pp. 454-60.

R. Müller, <u>P. Löper</u>, D. Hiller, S. Gutsch, R. Keding, C. Reichel, M. Bivour, M. Hermle, S. Janz, J. C. Goldschmidt, M. Zacharias, and S. W. Glunz "Calculation of the quasi fermi-level splitting in an ideal superlattice of silicon nanocrystals," in *Proceedings of the 26th European Photovoltaic Solar Energy Conference and Exhibition*, Hamburg, Germany, 2011, pp. 465-9.

<u>P. Löper</u>, D. Hiller, M. Künle, R. Gradmann, S. Janz, M. Hermle, M. Zacharias, and S. W. Glunz "Silicon quantum dot superstructures for all-silicon tandem solar cells: electrical and optical characterization," in *Proceedings of the 22nd Workshop on Quantum Solar Energy Conversion*, Brigels, Switzerland, 2010.

<u>P. Löper</u>, D. Hiller, M. Künle, R. Gradmann, M. Rothfelder, S. Janz, M. Hermle, M. Zacharias, and S. W. Glunz "Carrier confinement and transport in high band gap materials with embedded Si quantum dots," in *Proceedings of the 25th European Photovoltaic Solar Energy Conference and Exhibition*, Valencia, Spain, 2010, pp. 269-73.

<u>P. Löper</u>, "Silicon nanostructures for photovoltaics," in *Stipendientag der Reiner Lemoine Stiftung*, Berlin, Germany, 2010.

F. Hallermann, J. C. Goldschmidt, S. Fischer, <u>P. Löper</u>, and G. von Plessen, "Calculation of up-conversion photoluminescence in Er^{3+} ions near noble-metal nonoparticles," in *Proc. SPIE Vol. 7725, 77250Y*, Brussels, Belgium, 2010.

<u>P. Löper</u>, A. Hartel, M. Künle, D. Hiller, S. Janz, M. Hermle, M. Zacharias, and S. W. Glunz "Silicon quantum dot absorber layers for all-silicon tandem solar cells: optical and electrical characterisation," in *Proceedings of the 24th European Photovoltaic Solar Energy Conference*, Hamburg, Germany, 2009, pp. 434-8.

J. C. Goldschmidt, S. Fischer, <u>P. Löper</u>, M. Peters, L. Steidl, M. Hermle, and S. W. Glunz "Photon management with luminescent materials," in *Proceedings of the 21st Workshop on Quantum Solar Energy Conversion*, Rauris, Austria, 2009.

M. Künle, A. Hartel, <u>P. Löper</u>, S. Janz, and O. Eibl, "Preparation of Si-quantumdots in SIC: single layer vs multi layer approach," in *Proceedings of the 24th European Photovoltaic Solar Energy Conference*, Hamburg, Germany, 2009, pp. 191-5.

A. Hartel, M. Künle, <u>P. Löper</u>, S. Janz, and A. W. Bett, "Amorphous Si_xC_{1-x}:H single layers before and after thermal annealing: correlating optical and structural properties," in *Proceedings of the E-MRS Spring Meeting*, Strasbourg, France, 2009.

M. Künle, A. Hartel, P. Löper, S. Janz, and O. Eibl, "Nanostructure and phase formation in annealed a-Si$_{1-x}$C$_x$:H thin films for advanced silicon solar cells," in *Proceedings of the 21st Workshop on Quantum Solar Energy Conversion*, Rauris, Salzburg, Austria, 2009.

P. Löper, M. Künle, A. Hartel, J. C. Goldschmidt, M. Peters, S. Janz, M. Hermle, S. W. Glunz , and M. Zacharias, "Silicon quantum dot superstructures for all-silicon tandem solar cells," in *Proceedings of the 21st Workshop on Quantum Solar Energy Conversion*, Rauris, Salzburg, Austria, 2009.

M. Peters, J. C. Goldschmidt, P. Löper, and B. Bläsi, "Photonic structures and solar cells," in *Proceedings of the 21st Workshop on Quantum Solar Energy Conversion*, Rauris, Austria, 2009.

J. C. Goldschmidt, P. Löper, S. Fischer, S. Janz, M. Peters, S. W. Glunz, G. Willeke, E. Lifshitz, K. Krämer, and D. Biner, "Advanced Upconverter Systems with Spectral and Geometric Concentration for high Upconversion Efficiencies," in *Proceedings IUMRS International Conference on Electronic Materials*, Sydney, Australia, 2008, pp. 307-11.

M. Peters, J. C. Goldschmidt, P. Löper, B. Bläsi, and G. Willeke, "Lighttrapping with angular selective filters," in *Proceedings of the 23rd European Photovoltaic Solar Energy Conference*, Valencia, Spain, 2008, pp. 353-7.

S. Fischer, J. C. Goldschmidt, P. Löper, S. Janz, M. Peters, S. W. Glunz, A. Kigel, E. Lifshitz, and K. Krämer, "Material characterization for advanced upconverter systems," in *Proceedings of the 23rd European Photovoltaic Solar Energy Conference*, Valencia, Spain, 2008, pp. 620-3.

M. Peters, J. C. Goldschmidt, P. Löper, C. Ulbrich, T. Kirchartz, S. Fahr, B. Bläsi, S. W. Glunz, and A. Gombert, "Photonic structures for the application on solar cells," in *Proceedings of the 20th Workshop on Quantum Solar Energy Conversion*, Salzburg, Austria, 2008.

M. Peters, J. C. Goldschmidt, P. Löper, L. Prönneke, B. Bläsi, and A. Gombert, "Design of photonic structures for the enhancement of the light guiding efficiency of fluorescent concentrators," in *Proceedings of SPIE*, Straßburg, France, 2008, pp. 70020V-1-11.

C. Ulbrich, S. Fahr, M. Peters, J. Upping, T. Kirchartz, C. Rockstuhl, J. C. Goldschmidt, P. Löper, R. Wehrspohn, A. Gombert, F. Lederer, and U. Rau, "Directional selectivity and light-trapping in solar cells," presented at the Proceedings of the SPIE - The International Society for Optical Engineering, 2008.

J. C. Goldschmidt, M. Peters, <u>P. Löper</u>, O. Schultz, F. Dimroth, S. W. Glunz, A. Gombert, and G. Willeke, "Advanced fluorescent concentrator system design," in *Proceedings of the 22nd European Photovoltaic Solar Energy Conference* Milan, Italy, 2007, pp. 608-12.

<u>P. Löper</u>, J. C. Goldschmidt, M. Peters, D. Biner, K. Krämer, O. Schultz, S. W. Glunz, and J. Luther, "Efficient upconversion systems for silicon solar cells," in *Proceedings of the 22nd European Photovoltaic Solar Energy Conference*, Milan, Italy, 2007, pp. 589-94.

M. Peters, J. C. Goldschmidt, <u>P. Löper</u>, B. Blaesi, and A. Gombert, "Photonic crystals for the efficiency enhancement of solar cells," in *EOS Topical Meeting on Diffractive Optics* Barcelona, Spain, 2007.

J. C. Goldschmidt, M. Peters, <u>P. Löper</u>, S. W. Glunz , A. Gombert, and G. Willeke, "Photon management for full spectrum utilization with fluorescent materials," in *Proceedings of the 19th Workshop on Quantum Solar Energy Conversion*, Bad Hofgastein, Salzburg, Austria, 2007.

M. Peters, J. C. Goldschmidt, <u>P. Löper</u>, A. Gombert, and G. Willeke, "Application of photonic structures on fluorescent concentrators," in *Proceedings of the 22nd European Photovoltaic Solar Energy Conference*, Milan, Italy, 2007, pp. 177-81.

14.3 Oral presentations

<u>P. Löper</u>, "Silicon quantum dots in photovoltaic devices: device fabrication, characterization and comparison of materials," *28th European Photovoltaic Solar Energy Conference and Exhibition, Frankfurt, Germany,* 2012.

<u>P. Löper</u>, "Photovoltaic properties of silicon nanocrystals in silicon carbide," *SPIE, San Francisco, CA, USA,* 2012.

<u>P. Löper</u>, "Aufspaltung der quasi-Fermi Niveaus in Silicium-Quantenpunkt-Strukturen," *Silicon Forest, Falkau,* 2012.

<u>P. Löper</u>, "Silicon quantum dot superstructures for all-silicon tandem solar cells: electrical and optical characterization," *22nd Workshop on Quantum Solar Energy Conversion, Brigels, Switzerland,* 2010.

<u>P. Löper</u>, "Carrier confinement and transport in high band gap materials with embedded Si quantum dots," *25th European Photovoltaic Solar Energy Conference and Exhibition, Valencia, Spain,* 2010.

P. Löper, J. C. Goldschmidt, M. Peters, S. Fischer, and S. W. Glunz, "Quantum Efficiency in Photovoltaics: From Basic Concepts to Practical Results," *Physikalisches Kolloquium, Freiburg, Germany,* 2010.

P. Löper, "Silicon quantum dot absorber layers for all-silicon tandem solar cells: optical and electrical characterisation," *24th European Photovoltaic Solar Energy Conference, Hamburg, Germany,* 2009.

P. Löper, "Silicon quantum dot superstructures for all-silicon tandem solar cells," *21st Workshop on Quantum Solar Energy Conversion, Rauris, Austria,* 2009.

P. Löper, "Upconversion for silicon solar cells: material and system characterisation," *23rd European Photovoltaic Solar Energy Conference, Valencia, Spain,* 2008.

14.4 Supervised Diploma, Master and Bachelor thesis

D. M. Qazzazie, "Modellierung und Charakterisierung von Silizium-basierten Nanokristall-Membransolarzellen," M.Sc. Masterarbeit, Technische Fakultät, Universität Freiburg, Freiburg, Germany, 2012.

C. Gredy, "Optimierung und Charakterisierung des Herstellungsprozesses von Silizium-Quantenpunkt-Solarzellen," Bachelorarbeit, Hochschule Karlsruhe – Technik und Wirtschaft, Karlsruhe, Germany, 2012.

A. Witzky, "Elektrische und optische Charakterisierung von Silicium-Carbid-Schichten mit eingebetteten Silicium-Nanokristallen für Silicium-basierte Solarzellen mit hoher Bandlücke," Diplomarbeit, Fakultät für Physik, Universität Freiburg, Freiburg, 2012.

R. Müller, "Elektrische und photovoltaische Eigenschaften von Silicium-Nanokristallen in einer dielektrischen Matrix," Masterarbeit, Technische Fakultät. Institut für Mikrosystemtechnik, Universität Freiburg, Freiburg, Germany, 2011.

R. Gradmann, "Charakterisierung von Silizium-Nanokristallen in einer Siliziumkarbid-Matrix," Diplomarbeit, Institut für Kristallographie, Universität zu Köln, Köln, 2010.

14.5 Book chapters

P. Löper, M. Canino, M. Schnabel, C. Summonte, S. Janz, and M. Zacharias, "High-band gap silicon nanocrystal solar cells - Device fabrication characterization and modelling," in *High-Efficiency Solar Cells - Physics, Materials and Devices*, Y. Shi, Ed., ed Heidelberg: Springer, to be published 2013.

P. Löper, M. Schnabel, and S. Janz, "Prototype PV cells with Si nanoclusters," in *Nanotechnology and Photovoltaic Devices: Light Energy Harvesting with Group IV Nanostructures*, J. Valenta and S. Mirabella, Eds., ed: Pan Stanford Publishing, to be published 2013.

M. Peters, A. Bielawny, B. Bläsi, R. Carius, S. W. Glunz, J. C. Goldschmidt, H. Hauser, M. Hermle, T. Kirchartz, P. Löper, J. Üpping, R. Wehrspohn, and G. Willeke, "Photonic Concepts for Solar Cells," in *Physics of Nanostructured Solar Cells*, V. Badescu and M. Paulescu, Eds., ed Hauppauge, NY, USA: Nova Science Publishers, 2010.

14.6 Patent Applications

P. Löper, R. Müller, S. Janz, M. Hermle, S. W. Glunz , and J. C. Goldschmidt, "Verfahren zur Herstellung eines Halbleiterbauelements und Halbleiterbauelement," Bundesrepublik Deutschland Patent, 2012.

J. C. Goldschmidt, M. Peters, M. Hermle, P. Löper, and B. Bläsi, "Lumineszenzkollektor mit mindestens einer photonischen Struktur mit mindestens einem lumineszenten Material sowie diesen enthaltendes Solarzellenmodul," Bundesrepublik Deutschland Patent, 2010.

J. C. Goldschmidt, P. Löper, and M. Peters, "Solarelement mit gesteigerter Effizienz und Verfahren zur Effizienzsteigerung," Bundesrepublik Deutschland Patent, 2007.

A. Götzberger, J. C. Goldschmidt, M. Peters, and P. Löper, "Photovoltaik-Vorrichtung und deren Verwendung," Germany Patent, 2007.

14.7 Diploma thesis

Philipp Löper, "Spektral aufgelöste Lumineszenzmessungen an Systemen zum Photonenmanagement", Universität Freiburg, Februar 2008

15 Danksagung